Time-Resolved Pump-Probe X-ray Absorption Fine Structure Spectroscopy of Gaq3

Dissertation
zur Erlangung des Doktorgrades
des Department Physik
der Universität Hamburg

vorgelegt von

Benjamin Dicke

aus Wickede

Hamburg

2013

Gutachter der Dissertation:	Prof. Dr. Edgar Weckert Prof. Dr. Markus Drescher
Gutachter der Disputation:	Prof. Dr. Edgar Weckert Dr. Alke Meents
Datum der Disputation:	28.10.2013
Vorsitzender des Prüfungsausschusses:	Prof. Dr. Michael A. Rübhausen
Vorsitzender des Promotionsausschusses:	Prof. Dr. Peter Hauschildt
Leiterin des Departments Physik:	Prof. Dr. Daniela Pfannkuche
Dekan der Fakultät Mathematik, Informatik und Naturwissenschaften:	Prof. Dr. Heinrich Graener

Kurzfassung

Gallium(tris-8-hydroxychinolin) (Gaq3) gehört zu einer Klasse metallorganischer Verbindungen, die als Elektronentransport- und Emissionsschicht in organischen Leuchtdioden Verwendung finden. Viele bisherige Forschungsaktivitäten beschäftigten sich mit den optischen und elektronischen Eigenschaften insbesondere denen des homologen Moleküls Aluminium(tris-8-hydroxychinolin) (Alq3). Die Kenntnis über die Struktur des ersten angeregten Zustands S_1 dieser Moleküle könnte einen tieferen Einblick in die Prozesse bieten, die mit dem Betrieb elektronischer Geräte wie zum Beispiel organischer Leuchtdioden verbunden sind. Damit könnten deren Effizienz und optischen Eigenschaften weiter verbessert werden. Bis heute jedoch konnte die Struktur des angeregten Zustandes nicht experimentell bestimmt werden. Die meisten Informationen über diese Struktur resultieren aus theoretischen Berechnungen.

Röntgenabsorptions-Feinstruktur-Spektroskopie (X-ray Absorption Fine Structure (XAFS) spectroscopy) ist eine weit entwickelte Technik, um sowohl die elektronischen als auch die geometrischen Eigenschaften einer Probe zu bestimmen. Die Kombination von ultrakurz gepulsten Röntgenstrahlquellen und gepulsten Lasersystemen bietet die Möglichkeit, XAFS Spektroskopie zur Untersuchung von laserinduzierten transienten Änderungen einer Probe zu verwenden.

Im Rahmen dieser Doktorarbeit wurde ein neuer Aufbau für zeitaufgelöste „Pump-Probe“ XAFS Spektroskopie an der PETRA III Strahlführung P11 entwickelt, um Proben in flüssiger Form zu messen. Bei diesem Aufbau wird die Probe durch einen femtosekunden langen Laserpuls mit einer Wellenlänge von $343\,\mathrm{nm}$ in einen optisch angeregten Zustand befördert und nach einem bestimmten Zeitabstand von einem Röntgenstrahlpuls abgefragt. Auf diese Weise wurde der erste angeregte Singulett Zustand S_1 von Gaq3, aufgelöst in Benzylalkohol, untersucht. Ein Strukturmodell für den angeregten Zustand des Gaq3-Moleküls wird auf Grundlage der mehrmals reproduzierten Ergebnisse der Röntgenabsorptions-Experimente vorgeschlagen. Gemäß dieses Modells wurde herausgefunden, dass sich als Konsequenz der optischen Anregung die $Ga - N_A$ Bindung verlängert, während die $Ga - O_A$ Bindung verkürzt wird.

Die Dynamik dieser strukturellen Änderungen waren nicht Fokus dieser Arbeit. Dennoch wurde die Lebensdauer des angeregten Zustands von Gaq3 analysiert. Diese stellt eine der ersten zeitaufgelösten Messungen an PETRA III dar. Zur Analyse und Diskussion dieser Ergebnisse sei der Leser an [1] verwiesen.

In Ergänzung zur Pump-Probe XAFS Spektroskopie wurden verschiedene Phasen von Gaq3 und Alq3 in Form von Pulver, Kristall, Film und Lösung mithilfe von Fluoreszenz-Spektroskopie untersucht. Dabei konnten elektronische und optische Unterschiede der Moleküle in Abhäng-

igkeit der jeweiligen Form identifiziert werden. Hierbei wiesen Gaq3, gelöst in Benzylalkohol und in kristalliner Form sehr ähnliche optische Eigenschaften auf, die ein Hinweis auf gleichartige, strukturelle Eigenschaften sind. Die unterschiedlichen Techniken, die zur Herstellung dieser Probenformen verwendet wurden, werden in der vorliegenden Arbeit vorgestellt. Die Analyse der Unterschiede zwischen den verschiedenen Probenformen könnte bei Beantwortung der Frage helfen, inwieweit Rückschlüsse, die aus dem Probensystem in flüssiger Form gezogen wurden, übertragbar sind auf das Probensystem in Kristall- oder Filmform, wie sie in organischen Leuchtdioden vorkommt.

Das zukünftige Ziel dieses Forschungsprojekts liegt in der direkten Vermessung des angeregten Zustands von Alq3 und Gaq3 und ähnlichen Probensystemen mithilfe zeitaufgelöster Kristallographie. Dafür müssen die Probenkristalle spezielle Anforderungen erfüllen, insbesondere für den laserinduzierten Anregungsprozess. In dieser Arbeit wird eine neu entwickelte Präparationsmethode für die Erzeugung dünner Einkristallschichten mit geringer Rauhigkeit vorgestellt. Diese Kristallschichten können in zukünftigen, zeitaufgelösten Kristallographie-Experimenten verwendet werden.

Abstract

Gallium(tris-8-hydroxyquinoline) (Gaq3) belongs to a class of metal organic compounds, used as electron transport layer and emissive layer in organic light emitting diodes. Many research activities have concentrated on the optical and electronic properties, especially of the homologue molecule aluminum(tris-8-hydroxyquinoline) (Alq3). Knowledge of the first excited state S_1 structure of these molecules could provide deeper insight into the processes involved into the operation of electronic devices, such as OLEDs and, hence, it could further improve their efficiency and optical properties. Until now the excited state structure could not be determined experimentally. Most of the information about this structure mainly arises from theoretical calculations.

X-ray absorption fine structure (XAFS) spectroscopy is a well developed technique to determine both, the electronic and the geometric properties of a sample. The connection of ultrashort pulsed X-ray sources with a pulsed laser system offers the possibility to use XAFS as a tool for studying the transient changes of a sample induced by a laser pulse.

In the framework of this thesis a new setup for time-resolved pump-probe X-ray absorption spectroscopy at PETRA III beamline P11 was developed for measuring samples in liquid form. In this setup the sample is pumped into its photo-excited state by a femtosecond laser pump pulse with $343\ \mathrm{nm}$ wavelength and after a certain time delay probed by an X-ray probe pulse. In this way the first excited singlet state S_1 of Gaq3 dissolved in benzyl alcohol was analyzed. A structural model for the excited state structure of the Gaq3 molecule based on the several times reproduced results of the XAFS experiments is proposed. According to this model it was found that the $Ga - N_A$ bond length is elongated, while the $Ga - O_A$ bond length is shortened upon photoexcitation.

The dynamics of the structural changes were not the focus of this thesis. Nevertheless the excited state lifetime of Gaq3 was analyzed and presents one of the first time-resolved measurements at PETRA III. For the analysis and discussion of these results the reader is referred to [1].

In addition to pump-probe XAFS spectroscopy, different phases of Gaq3 and Alq3 in form of powder, crystal, film and solution were analyzed by means of UV-VIS and fluorescence spectroscopy. Electronic and optical differences of the molecules related to the particular form could be revealed. Gaq3 in benzyl alcohol solution and Gaq3 in crystalline form exhibit very similar optical features, indicating similar structural properties. The various preparation techniques used to obtain the sample forms are presented in this thesis. Analyzing the differences among the diverse sample forms helps to answer the question on how the conclusions extracted from sample systems in liquid form can be transferred to the ones in crystal form or film form, the latter

appearing in organic light emitting diodes.

The future goal of this research project is the direct measurement of the excited state structure of Alq3 as well as Gaq3, and similar sample systems by time-resolved X-ray crystallography. The sample crystals have to fulfill specific requirements especially for the laser induced photoexcitation process. In this thesis a newly developed preparation method for low roughness singe crystal slices is presented. These crystal slices can be used for future perspective time-resolved X-ray crystallography experiments.

Contents

1. Introduction

Semiconductors such as silicon (Si) and germanium (Ge) are key materials for all microelectronic based devices. Their electronic properties in combination with the ability of the industry to employ them for fabrication of microelectronic devices has led to a large variety of electronic products based on semiconducting technology in our daily life.

1.1. Organic Semiconductors

In the last years another class of materials as a promising alternative for classical semiconductors has emerged, known as *Organic Semiconductors*. Intensive research has been made to understand the fundamental properties of these materials [2, 3] in order to apply them for electronic and optoelectronic devices such as *Organic Light Emitting Diodes (OLEDs)* [4, 5, 6], *Organic Solar Cells* [7] and *Organic Thin Film field-effect Transistors (OTFTs)* [8]. Especially OLEDs have a great potential for a new kind of illumination techniques in form of large area light sources and for a flexible and high brightness displays. With the rapidly developing smartphone and tablet market in recent years, the interest into OLEDs and OTFTs has increased. The majority of mobile phones from a major smartphone developer and producer Samsung are already completely based on the *Super-Active-Matrix-Organic Light Emitting Diode (Super-AMOLED)* technique. These developments point into direction of very thin and flexible OLED based displays and efficient large area TV-displays.

1.1.1. Principles

The principle of organic semiconductors is based on the ability of carbon to create a so called *delocalized π-electron system* by conjugated double and triple bonds. The term "conjugated" refers to alternating single and multiple bonds [3]. The electrons are not located at a specific π-orbital of a single carbon atom, but are extended over several carbon atoms like in an electron cloud, which means they are delocalized. Due to its valency carbon is flexible in formation of molecular orbitals, which lead to many different forms (allotropes) and physical properties. The electronic configuration of the ground state of carbon is $1s^2 2s^2 2p^2$ [3]. In some hybridizations it is energetically more efficient when one of the $2s$-electrons is excited into a $2p$-orbital, which leads to the creation of four equivalent bonds. This is the case for diamond, where all carbon atoms are sp^3-hybridized. This means one s-orbital and three p-orbitals (p_x, p_y, p_z) of a carbon atom build four sp^3-hybridized atomic orbitals [3]. Overlap of these atomic orbitals of two adjacent carbon atoms produce a strong covalent bond, which is the cause of the hard diamond structure. In this case, the configuration of carbon is $1s^2 sp^3 sp^3 sp^3 sp^3$. Another bonding opportunity originates

from sp^2-hybridization. Here the $2s$-orbital combines with two of the three p-orbitals creating three sp^2-orbitals oriented in the same plane with the third p_z-orbital arranged perpendicular to this plane. The simplest example for sp^2-hybridization of carbon is the ethene molecule (C_2H_4), where the two carbon atoms are linked by a double bond, shown in figure 1.1. Overlap of two

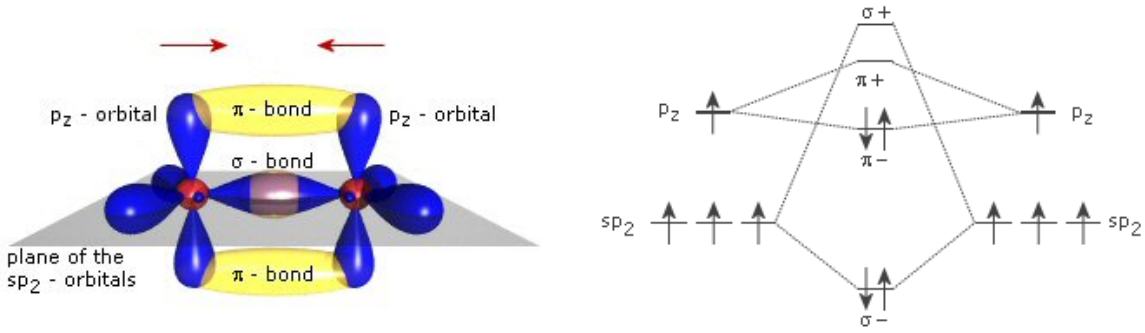

Figure 1.1.: *Left: A graphical presentation of the ethene molecule. Carbon atom cores are shown in red, Electron orbitals in blue and the $\pi-bonds$ in yellow. Right: Energy niveau scheme of ethene. Each arrow represents electrons with spin up (arrow up) or spin down (arrow down). Both figures were taken from [9].*

sp^2-hybrid orbitals results into a so called *σ-bond* [3]. The second bond originates from overlap of the two vertical p_z-orbitals and is referred to as a *π-bond*. As it can be seen in figure 1.1, the overlap of the p_z-orbitals is smaller than of the sp^2-orbitals and, thus, the π-bonding is less strong compared to the σ-bonding. Both, σ- and π-bonds, have a bonding and an antibonding component. In comparison to the σ-bond the π-bond is weaker and, hence, the bonding π-orbital and the antibonding π^*-orbital are energetically closer to each other [10].

In larger molecules such as aromatics in which several sp^2-hybridized carbon atoms bond together, a conjugated delocalized π-electron system is generated. A classical example for such an aromat is the benzene molecule, shown in figure 1.2. With increasing number of carbon atoms involved in the delocalized electron system, the energy gap between bonding and antibonding orbitals becomes smaller. Values in the range of $1.5 - 3\,\mathrm{eV}$ between the *Highest Occupied Molecular Orbital (HOMO)* and the *Lowest Unoccupied Molecular Orbital (LUMO)* allow $\pi-\pi^*$ transitions by light absorption in the ultraviolet (UV) or even visible (VIS) spectral range [10]. A delocalized π-electron system is, therefore, a requirement for the semi-conductive character of such organic materials.

In principle, organic semiconductors are classified into two groups: Small molecules and conjugated polymers [10, 8]. In polymers, the π-electron system is located along the molecular chain and a large number of overlapping π-bonds results in a band structure similar to that of classical in-organic semiconductors. Here, the HOMOs build the valence band E_v, while the LUMOs correspond to the conduction band E_c. The degree of conjugation, which depends on the number of carbon atoms, directly influences the energy gap and, thereby, the optical as well as electronic properties of the molecular system. As a basic rule, one can say the larger the molecule is, the smaller the spacing between successive energy levels becomes. This fact is for example well known from polyacenes. The wavelength of the main absorption peak of the polyacenes increases

from benzene over anthracene to pentacene [10, 3]. Hence, it is possible to accurately change the optical and electronic properties of a semiconducting material by controlling its chemical structure. The same obeys to small molecules such as Aluminum(tris-8-hydroxyquinoline) (Alq3), which was the material chosen for the worldwide first OLED and organic solar cell [7, 4]. Here, the electronic and optical properties can be controlled either by exchange of the central metal atom, leading to a homologous molecule such as Gallium(tris-8-hydroxyquinoline) (Gaq3), or by substitution of chemical groups at the ligands [11, 12, 13]. Since it is desirable to produce devices with specified emission properties, tuning of color emission is one of the largest research areas of OLEDs. One important difference between conjugated polymers and small molecules

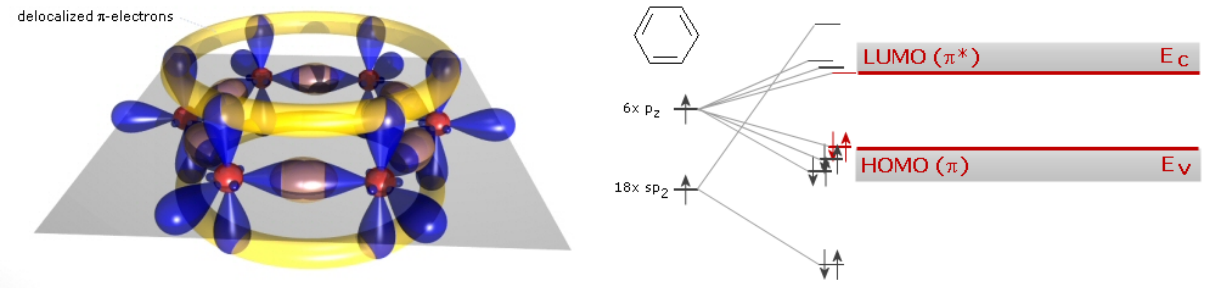

Figure 1.2.: *Left: A graphical presentation of the benzene molecule. The carbon atoms are circularly arranged and the $\pi - bonds$ in yellow form a delocalized π-electronsystem. Right: Energy niveau scheme of benzene. The HOMOS and LUMOS form energy bands comparable to the valence band E_v and conduction band E_c of classical semiconductors. Both figures were taken from [9].*

is the processing method employed for thin film generation. While small molecule layers can be generated by vapor deposition techniques, conjugated polymers can be only processed by wet techniques like spin-coating or ink-jet processing/spraying [10, 8]. The fabrication processes are in both cases more straight forward compared to that of their in-organic counterparts. The reason for this are the lower melting points of the Van-der-Waals based organic materials compared to the covalently bound in-organic materials which require high-temperature and high-vacuum conditions for processing. This allows cost efficient fabrication of large area devices. Furthermore, organic materials are softer, which makes them applicable for flexible displays.

1.1.2. Functioning Principle of an OLED

A typical OLED device is shown in figure 1.3 (adapted from [10]). It consists of multiple thin layers, which are embedded in a sandwich like structure between an anode and a cathode. A voltage applied between these two results in a current. The anode is the lowest layer and directly placed on top of the glass substrate. It injects holes [1] into the structure and is usually made of Indium-tin-oxide (ITO) due to its high work function and transparency for light. The cathode,

[1] "Hole" is a model particle and it is created when an electron leaves the HOMO of a molecule caused by the attracting force of the anode. This HOMO of the positive charged molecule can then be populated with an electron from the HOMO of an adjacent molecule. In this way the positive charge referred to as "hole" is

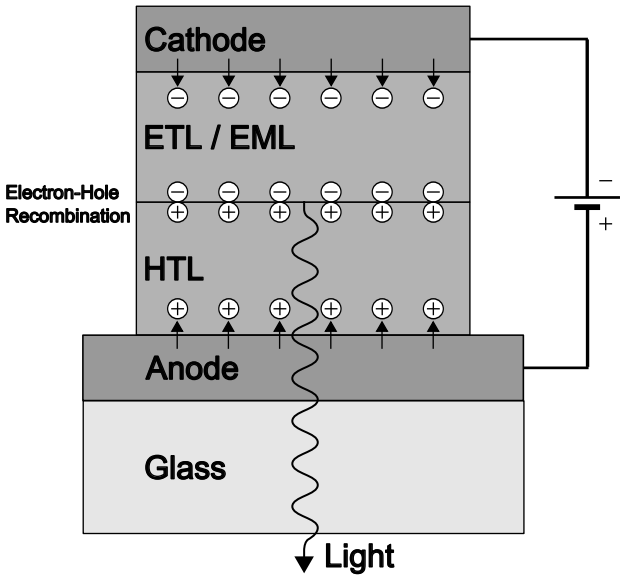

Figure 1.3.: *Working principle of an OLED consisting of several thin film layers. Light emission occurs via electron-hole recombination in the emission layer (EML) (further details see text). The figure is adapted from [10].*

made of aluminum or calcium is the top layer and used for electron injection. In between anode and cathode the *hole transport layer (HTL)* and the *electron transport layer (ETL)* carry holes and electrons, respectively, to the *emission layer (EML)*. Transport thereby occurs along the HOMOs for holes and along the LUMOs for electrons. In the emission layer electron-hole recombination takes place under formation of an exciton. Decay of this exciton leads to emission of light in the visible region. The first OLED was invented by Tang et al. [4], with the metalorganic compound Alq3 as emission layer. Even today Alq3 is widely used as emission as well as electron transport material in small molecule based OLEDs. Beside small molecules, conjugated polymers are also employed for OLED devices. Nowadays OLED research aims to increase efficiency, optimize the spectral range and prolong the durability of the devices. Small molecules and conjugated polymers are promising materials for this purpose due to their low costs, tunable emission wavelength, and flexibility in processing. Further improvements require knowledge of the fundamental structural, electronic, and optical properties of the materials involved in the processes of such devices. Especially, the excited state structure occurring in the excitation processes remains still unknown.

1.2. Photo-Excited States of Atoms and Molecules

Modern quantum mechanics describes the electrons of an atom or molecule via the wavefunction which gives the probability density of finding an electron in a specific atomic or molecular orbital.

transferred to another molecule. When many molecules are involved into this process the hole moves through the device into direction of the cathode [14].

These orbitals are described by a set of four quantum numbers whereas the electrons can occupy quantized energy states. A molecule is excited into an excited state when an electron moves from its actual energy state to a higher lying energy state. This process can occur by the absorption of light when the wavelength of the photon matches the energy difference between the two states, given by the Planck relation as [15]

$$E = h \cdot \nu = h \cdot c/\lambda \ , \tag{1.1}$$

where h is the planck constant, ν and λ are the frequency and wavelength of the photon with energy E, and c is the speed of light. The transitions must obey selection rules which describe how the quantum numbers change upon the transition between two energy states. Allowed transitions occur usually on fast time scales and those, which are forbidden by the selection rules are long-living. The absorption process occurs on a time scale faster than 10^{-15} s [3]. The excited state is not stable, and hence, the molecule relaxes after a specific time, called *lifetime*, back to the ground state. This relaxation can occur via different ways which depend on the electronic and structural properties of the molecule. Molecules capable to emit light as a consequence of the electronic transitions are called fluorochromes or dyes. Figure 1.4 illustrates the processes involved into the optical excitation and subsequent relaxation of such a molecule. This diagram is called *Jablonski-diagram*. The thick horizontal lines refer to electronic energy states which are degenerated into smaller vibrational levels denoted by the thinner lines. The vibrational levels occur as a consequence of nuclei movements. Because of the large disparity between nucleus mass and electron mass, the electrons are considered to follow any movement of the nucleus instantaneously resulting in vibrations. The *Vibrational Relaxation (VR)* within an electronic energy state occurs in ≤ 1 ps and it is non-radiative [15, 16]. The timescale of VR is much shorter than the fluorescence lifetime and as a consequence the molecule is most probable in its lowest vibrational niveau of the excited state before fluorescence takes place (Kasha's rule) [17, 15, 3]. In the Jablonski-diagram the energy states denoted by S are singlet states with total spin 0. The transitions between singlet states are allowed and, thus, they are most probably. When an excited molecule existing for a lifetime of the order of nanoseconds in the S_1 state relaxes to the ground state S_0 the most probably transition is given by the emission of fluorescence light. Since also the ground state S_0 has vibrational energy levels, the fluorescence light is shifted towards higher wavelengths with respect to the absorbed light. This shift is called *Stoke's shift* [15, 3]. In addition, the several closed packed vibrational states have a broadening effect on the fluorescence emission band. A competing process to fluorescence is the radiation from the first excited triplet state T_1. The transitions from singlet states to this state are spin forbidden and, therefore, less probable. But due to so called *Intersystem Crossing (ISC)* the process becomes possible. In this radiationless transition, occurring within 10^{-6} s to 10^{-9} s [3], the spin of the excited electron changes, though it is quantum mechanically forbidden. This happens when the spin of the electron couples to the orbital angular momentum, a process named *Spin-Orbit Coupling*. The relaxation from T_1 to S_0 under light emission is called *Phosphorescence*. The transition $T_1 \rightarrow S_0$ is also spin forbidden and it explains why phosphorescence with lifetimes of 10^{-3} s $- 10^{2}$ s [15] is much longer-living than the spin allowed fluorescence. It is important to mention that radiationless relaxation is not only responsible for the decay of vibrational states within a specific

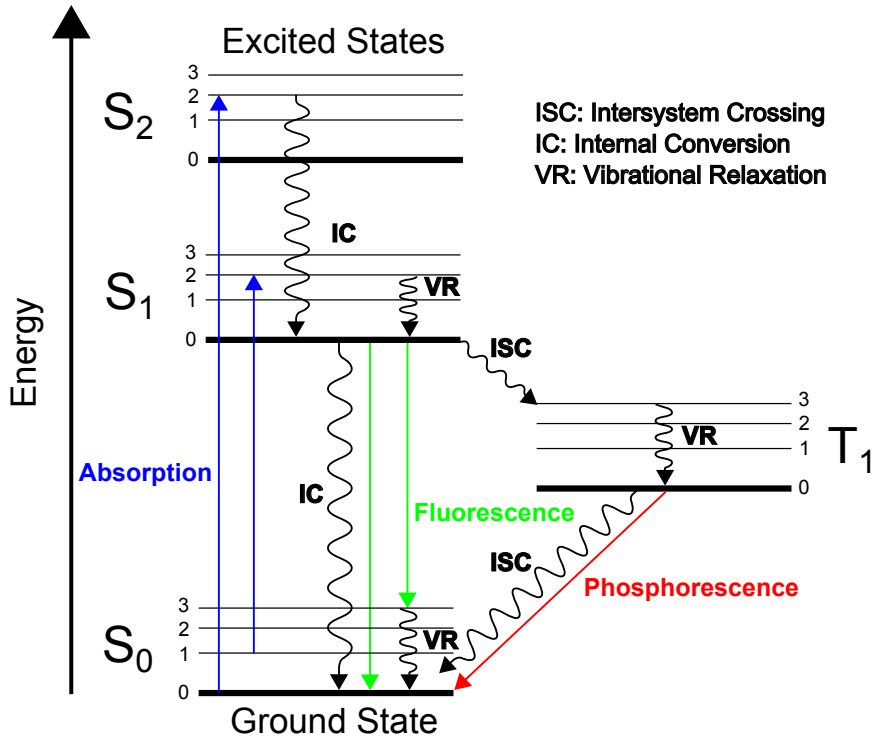

Figure 1.4.: *A Jablonski-diagram shows the processes involved in the photo-excitation and subsequent relaxation of a dye molecule. Transitions between energy levels are illustrated by arrows, whereas straight arrows represent radiative processes and curled arrows stand for non-radiative processes.*

electronic energy state, but it is also a possible pathway for deactivation from electronic excited states S_1 and S_2 to the ground state S_0 and termed *Internal Conversion (IC)* [3, 15]. In the case of the triplet state T_1, ISC is even the favored relaxation process. That is the reason that triplet states are often not easily detectable since phosphorescence signals are very low. One approach to overcome this problem is to cool down the sample in order to restrict molecular motions and make phosphorescence more competitive with respect to ISC [15]. Figure 1.5 shows typical absorption and fluorescence spectra as function of wavelength. For an efficient excitation and subsequent measurement of the fluorescence spectrum, the dye molecule is usually excited with an ideal excitation wavelength defined as the maximum of the absorption spectrum. The spectra reveal the before mentioned broadening and Stoke's shift as a consequence of the degeneration of the electronic states into vibrational modes. An experiment, in which the sample is pumped into an photo-excited state by a pump pulse and probed by a subsequently following probe pulse, is referred to as *pump-probe experiment*. This is the main experimental technique used in this thesis and it is introduced in chapter 1.4. For such an experiment it is important to know all energy states involved in the excitation and decay processes. The measurement and analysis of absorption and emission spectra allow the characterization of these energy states of a sample molecule and they are widely used methods. Furthermore the occupation densities of the energy states at a specific instant of time are important to know. The case, in which all molecules are in

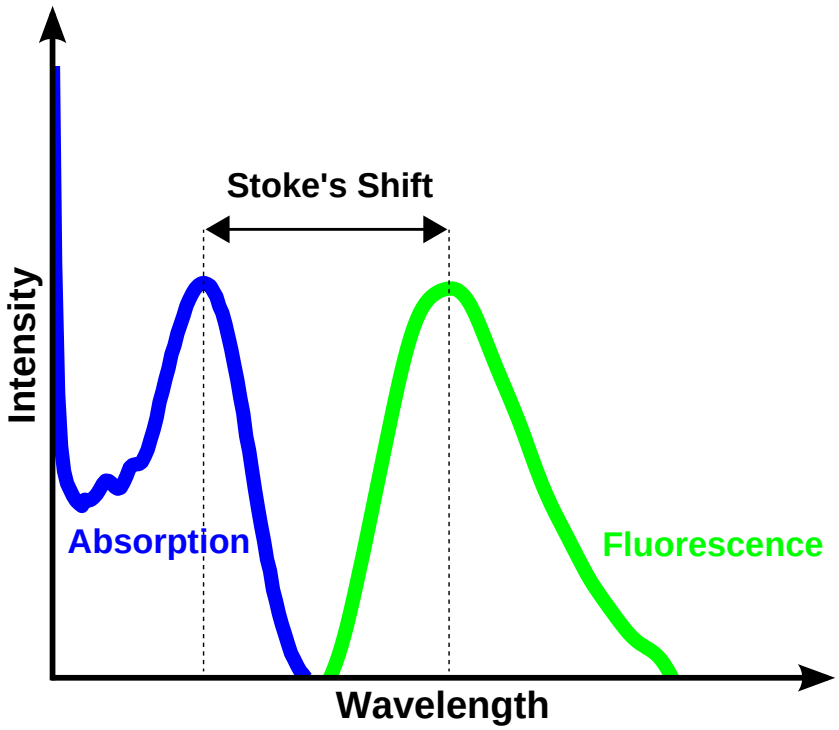

Figure 1.5.: *Typical absorption and fluorescence spectra of a dye molecule. As a result of energy losses within the excited molecule for example into vibrational motions, the emitted fluorescence spectrum is shifted towards higher wavelengths in comparison to the excitation absorption spectrum (Stoke's shift).*

the same energy state is unlikely to occur due to many processes taking place between the different states. Consequently, also the excitation and decay processes and their specific rates have to be characterized for the sample system. This is usually done by performing optical pump-probe experiments [18].

1.3. Metal-Quinolines Mq3

A very promising group of small organic molecules are the metal-chelates of quinolines. This section gives a brief overview of the most important research results from recent years.

1.3.1. Optical and Structural Properties of Mq3

In metal-hydroxyquinolines Mq3, where M is a metal (Al, Ga, In) with formal oxidation state +3, the 8-hydroxyquinoline molecule C_9H_7NO is used as ligand. The carbon atoms are connected to a cyclic compound with a delocalized π-electron system. Figure 1.6 shows as an example the Alq3 molecule where the central metal atom is coordinated by three hydroxyquinoline-rings, named A, B and C showing slight variations in bond lengths.

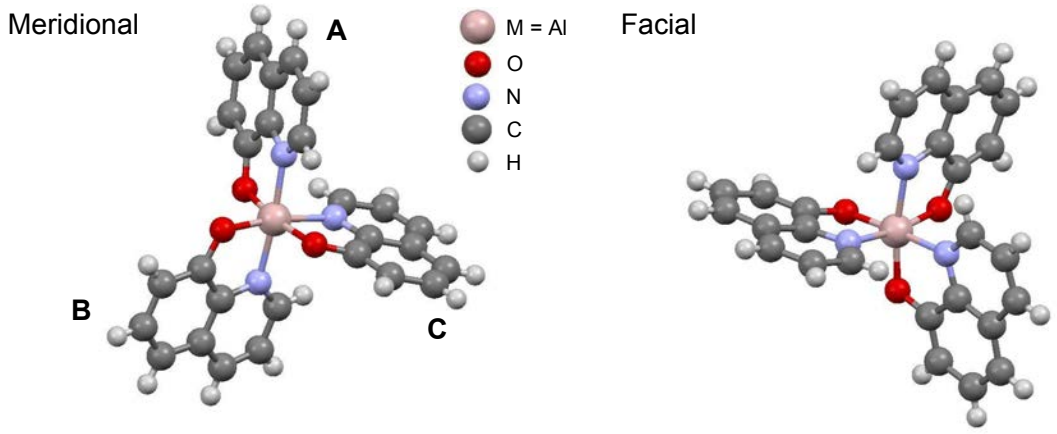

Figure 1.6.: *Left side: Meridional form of Alq3 (data taken from [19]) coordinated by three hydroxyquinoline-rings, named A, B and C. Right side: Facial form of Alq3 (data taken from [20]).*

Emission of these metal-chelates occurs from the hydroxyquinoline-ligands. The fact that absorption and emission spectra of Mq3 with different metal centers and spectra of 8-hydroxyquinoline show the same unique features, suggests that the excited state is concentrated on the ligand [21, 22]. Nevertheless, also the central metal atom plays an important role for the electronic and optical properties. The effect of the choice of the metal atom can be investigated by comparing the absorption and emission spectra of Mq3 for different metal atoms. In this thesis this was done for Alq3 and Gaq3 and it is presented in details in chapter 4.2.1. The electronic and optical properties can be controlled either by an exchange of the central metal atom, or by substitution of electron-donating or -withdrawing chemical groups at specific ligand positions. The energetic levels involved in the $\pi - \pi^*$ transition are affected, which allows tuning of the absorption and emission wavelengths [11, 12, 13, 23].

Two isomeric forms of Mq3 are known and are shown in figure 1.6. The meridional form is the more stable one and it appears in most phases, while the facial form can be only found in one particular crystalline phase [24, 25, 26]. The isomers display strong variations concerning the optical properties due to different HOMO-LUMO levels [24, 19, 27]. The facial isomer exhibits blue shifted *photoluminescence (PL)*, which makes it potentially interesting for blue light emitting diodes. For both Alq3 and Gaq3, the meridional phase can be converted into the facial phase by annealing between $380 - 400\ ^\circ\mathrm{C}$ [25, 24].

Another factor which defines specific optical, structural and electronic properties of metal-quinolines is the molecular packing within different phases. For OLEDs, the film form is the most interesting form and the mechanism, which influences charge injection and transport is crucial. It is not clear that the morphology of a film is purely amorphous. The first OLED publication reported about a micro-crystalline Alq3-film with grain sizes of 500 Å [4]. Brinkmann et al. highlighted the intrinsic amorphous nature of sublimed Alq3 films, whereas different molecular packings are possible and under special conditions a crystalline phase can be observed [19]. Emission spectra of different Gaq3 phases obtained by fluorescence spectroscopy are presented

in chapter 4.2.3. In case of Alq3, four different crystalline phases are known. The meridional form appears in the phases α, β, γ. The fourth phase, called δ-phase, was obtained by sublimation and consists of the facial isomer [24]. For the homologous Gaq3, three phases have been identified which are isomorphous to those of the Alq3 molecule: α, β-phase for the meridional form and the δ-phase for the facial isomer [25]. The facial isomer can be found in 1D-nanostructures and nanospheres [26]. The phases exhibit different photoluminescence properties, which can be attributed to density variations in the crystal structure [25]. In a solvent system the optical properties of the metal-quinoline $Mq3$ can also depend on the particular solvent [21]. Solvent effects were also analyzed in this thesis and are described in chapter 4.2.1 and discussed in more detail in chapter 6.1.1. In summary, the optical properties of metal-quinolines depend on the following factors:

- Central metal atom;
- Chemical groups substituted to proper locations on the ligands;
- Symmetry;
- Morphology of the particular phase.

In this context, the question on how far knowledge gained by investigation of crystalline or dissolved systems can be transferred to systems in film form is arising and it will be addressed in chapter 6.1.

1.3.2. Energy States and Transitions in Mq3

Light emission from metal-quinolines Mq3 is related to the before mentioned delocalized π-electron-system which causes a suitable energy gap between HOMO and LUMO. The emission of light is a consequence of the decay of an excited state in which a photon with an energy corresponding to the energy gap is emitted. The transfer of the molecule from its ground state to the excited state can be either achieved by applying an electric field or by irradiation with light. The corresponding emission is named electroluminescence or photoluminescence, respectively. The main mechanism of electron transfer from the HOMO to the LUMO is similar for both effects.

UV-VIS absorption spectra of Mq3 films show two characteristic peaks indicating two main excitations. Figure 1.7 shows, as an example, the UV-VIS absorption spectrum[2] of a Gaq3 thin film[3], which is in good agreement with other experimental data [29, 30]. The first peak at $266\ \mathrm{nm} (\sim 4.66\ \mathrm{eV})$ of the absorption spectrum is referred to as a transition from the $4p$ orbital of the metal center to the LUMO of the ligand ($4p \rightarrow \pi^*$ transition) [29]. The second peak at around $394\ \mathrm{nm} (\sim 3.15\ \mathrm{eV})$ is referred to as $\pi \rightarrow \pi^*$ transition from the ground singlet state to its first excited singlet state (also called $S_0 \rightarrow S_1$ transition) [29, 31]. Results from theoretical

[2]Fluorescence and absorption spectroscopic measurements conducted for this thesis are described in details in chapter 4.2.

[3]The setup used for thin film growth of metal-quinolines is described in chapter 3.2.

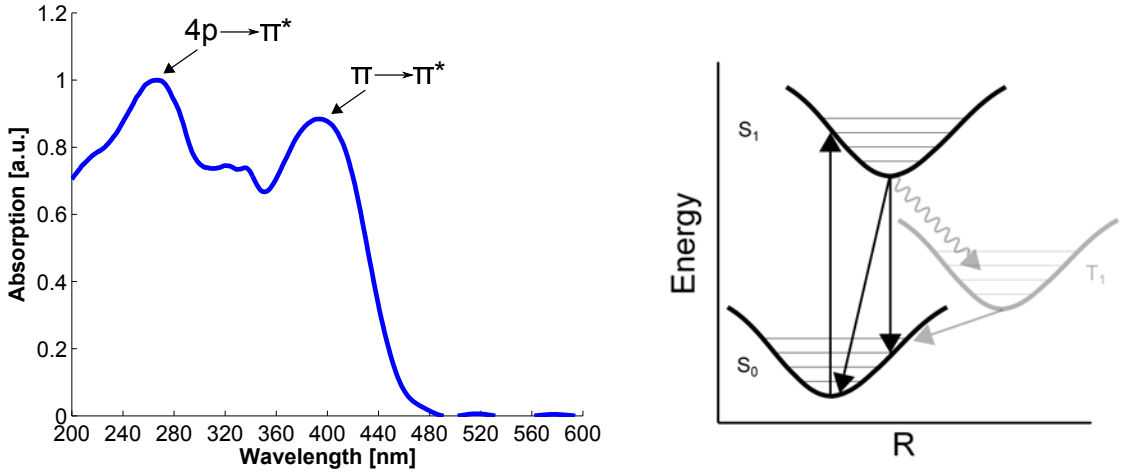

Figure 1.7.: *Left: Gaq3 UV-VIS absorption spectrum of a Gaq3 thin film. Right: Proposed energy niveau scheme of Mq3 with energy states S_0, S_1 and T_1 and vibrational states (illustrated by the straight lines) based on [28]. R is the configuration coordinate.*

calculations[4] for the absorption wavelength are not unique and strongly depend on the particular method and basis set which are used (compare [31, 32, 28]). In figure 1.7 an energy diagram of Mq3 is presented. The relaxation energy from S_1 to S_0 is lower than the excitation energy from S_0 to S_1, which is shown by a large shift of $126 - 148$ nm for Alq3 and of $133 - 165$ nm for Gaq3 between absorption and emission wavelengths, observed in experimental studies [30, 21] and confirmed in experiments of this thesis (see chapter 4.2). The above mentioned theoretical calculations qualitatively show the same shift, which is thought to arise from significant structural differences between the S_0 and S_1 state [28]. In the energy diagram R is the configuration coordinate. The change of this coordinate describes the different positions of the nuclei constituting the Mq3 molecule in the S_0 ground state structure and the S_1 excited state structure and thus illustrates the structural shift occurring between the two states. In addition, photoluminescence spectra of Alq3 thin-films showed a vibronic structure associated with the $S_1 \rightarrow S_0$ transition [33]. A vibronic structure was also observed from Alq3 single crystal and polycrystalline samples [19]. These observations agreed with theoretical calculations on the vibronic Alq3 structure [28, 33]. Decay from vibrational states takes place first non-radiatively to the lowest vibrational level of the S_1 state, and then the $S_1 \rightarrow S_0$ transition to the ground state occurs under emission of light (fluorescence). Hence, the wavelength of the fluorescence line is increased and so is the Stoke's shift. The lifetime of the S_1 singlet excited state in Alq3 decays exponentially and was measured to be about 10 ns to 16 ns [34, 24, 21, 35, 5]. The lifetime of the fluorescence decay of Alq3 and Gaq3 in different sample forms was also analyzed within this research project and it is presented in [1]. The results are in good agreement with the literature.

[4]The expression "theoretical calculation" is a relative general expression and is used throughout this thesis to refer to quantum chemical and computational calculations based on the *Density Functional Theory (DFT)*, the ab initio *Hartree-Fock* (HF) method and the *single Configuration-Interaction (CIS)* method. Where applicable the particular method will be specified.

In addition, the energy diagram in figure 1.7 shows a triplet state. The triplet state of Alq3 and Gaq3 is of importance to OLEDs, because light emission proceeds via electron-hole recombination leading to the generation of about $75\ \%$ excited triplet states and about $25\ \%$ excited singlet states. Thus, the maximum internal efficiency of an OLED can be increased by promoting emission from the triplet state [36, 10, 14]. However, detailed information of this state is harder to access because direct phosphorescence is hard to observe. The $T_1 \rightarrow S_0$ transition from the first triplet state, shown in the energy diagram of figure 1.7, is a quantum mechanically forbidden transition and, thus, the T_1 state has a much longer lifetime than the S_1 state. It is populated by ISC from the S_1 excited state (illustrated by the curled arrow in figure 1.7). The S_1 state preferably decays by emission of a photon causing the population of the T_1 state by ISC to be low, especially for light metals such as aluminum with a weak *heavy-atom* effect. The heavy-atom effect refers to the increase of spin-orbit coupling and thus the increase in the rates of spin-forbidden transitions for atoms with a high atomic number [37]. However, the triplet state of Alq3 was investigated by transient PL measurements [24] and by direct measurement of phosphorescence [36, 24]. The lifetime of the Alq3 triplet state in various forms at different temperatures was measured ranging from about $25\ \mu\mathrm{s}$ to $15\ \mathrm{ms}$ [36, 24, 38, 39, 35], indicating that population and decay of the Alq3 triplet state strongly depend on temperature as well as on the form. This thesis concentrates only on the first excited singlet state S_1 which can be directly populated by photoexcitation.

1.3.3. First Excited Singlet State of Mq3

Results from theoretical calculations show that the HOMOs are mainly localized on the phenoxide sides, while the LUMOs are mainly localized on the pyridyl sides of the ligand-rings [31, 40, 28] (see also figure 1.8). Hence, the $\pi \rightarrow \pi^*$ transition involves partial charge transfer from the phenoxide to the pyridyl side.

Upon the $S_0 \rightarrow S_1$ transition from HOMO to LUMO, primarily the A-ligand is involved [40]. Furthermore, it is predicted that a structural shift occurs which predominantly affects the bonds of the A-ligand, while the two other ligands nearly remain unchanged [31]. Especially the two bonds, which connect the A-ligand to the metal atom change. For Gaq3, the Ga-N bond is predicted to be shortened by 0.099 Å, while the Ga-O bond is elongated by 0.090 Å. This alternate bond change is explained by an increase of electron population on the N-atom causing an increase of the Ga-N attraction, while in the opposite side the electron population on the oxygen is reduced and the Ga-O bond weakened. In addition, C-C, C-N and C-O bonds of the A-ligand undergo changes of different extent [31]. The bond length changes upon the $S_0 \rightarrow S_1$ transition are examined in more detail in chapter 5.2.7. The structure related aspects of the excited state of Mq3 make the molecule very interesting for time-resolved pump-probe experiments. Until now the excited state structure of the Mq3 molecule has not been determined experimentally. Main insights into the molecule is based on both laser spectroscopic analysis and computational calculations. Laser spectroscopy provides important information related to the energy states and possible energetic transitions in the molecule, but this information cannot be directly translated into structural information in most cases. Theoretical calculations provide information on the structure and energetic states, but the results of these calculations often differ

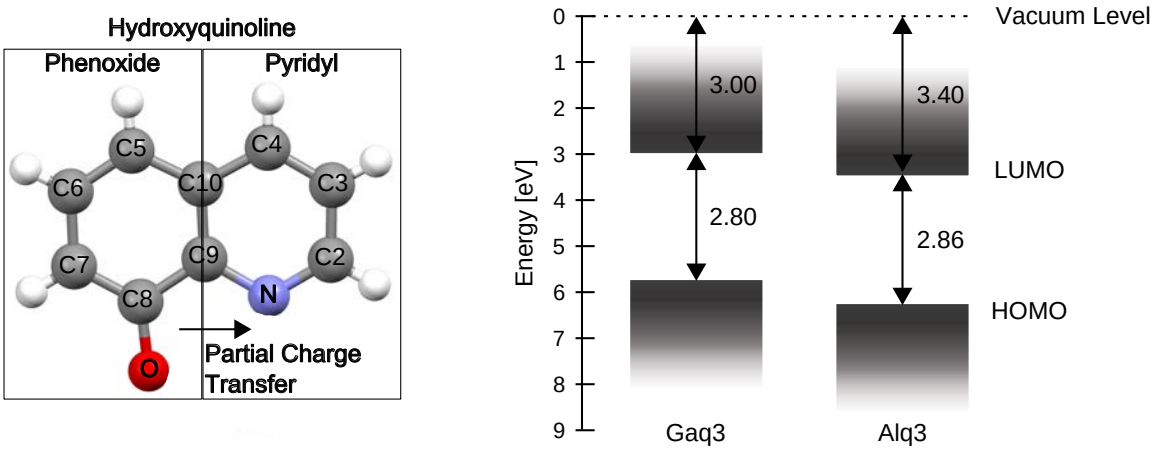

Figure 1.8.: *Left: One of three hydroxyquinoline ligands coordinated to the metal atom in Mq3. HOMOs and LUMOs are mainly located on the phenoxide and pyridyl side, respectively. Upon $\pi \rightarrow \pi^*$ transition, charge is partially transferred from the phenoxide side to the pyridyl side. Right: Energy niveau scheme with bandgaps between HOMOs and LUMOs of Alq3 and Gaq3. This figure is redrawn. It is based on [29].*

from experimental results especially regarding the energy transitions.

1.4. Pump-Probe Techniques

In nature, function is always linked to structure. By investigation of the structure of molecules we can understand their function. In most cases function is not static but related to dynamical processes. These processes like bond formation and breakage, chemical reactions, dynamics in proteins, atomic motion in lattices (phonons), phase transitions, melting and electron excitations occur on fast to ultrafast time scales. The time resolution required to study such processes is defined by the speed of atoms in matter, which is of the same order as the speed of sound, from $300\ \mathrm{m/s}$ to $1000\ \mathrm{m/s}$ [41]. For length scales of $0.3 - 1.0$ Å this corresponds to a time of 100 fs.

1.4.1. Ultrafast Spectroscopy

With the development of pulsed laser systems, which deliver femtosecond pulses the necessary instrumentation was made available to investigate such fast physical processes. In 1999 A. H. Zewail received the Nobel prize for his pioneering work on femtochemistry. In an experiment he used a femtosecond laser pulse to induce a chemical change in the I-CN sample molecule and after a certain time delay he monitored this change with a second femtosecond laser pulse. In this way it was possible to observe the bond change of the I-CN molecule upon chemical transition [42]. This method opened the field of femtochemistry. In the following years more complex systems such as retinal proteins were investigated by use of this technique [41]. In the

pump-probe scheme an ultrashort pump pulse is used to excite the sample into a non-equilibrium state and a second probe pulse is used to monitor the changes induced by the pump pulse. By measuring the changes as a function of time delay between pump and probe pulse, it is possible to access information on the time dependent decay of the electronic states. Ultrafast spectroscopy provides access to optical transition energies of a sample but for most systems this does not allow to draw conclusions about structural changes.

1.4.2. Ultrafast X-ray Absorption Spectroscopy

With the discovery of X-rays by Wilhelm Roentgen in 1895 [43] a new field in physics was opened and the determination of structure of matter became possible. The development of X-ray diffraction and X-ray absorption techniques allowed to retrieve structural information on the atomic scale. However, until recently, information, retrieved by X-ray techniques offered only a static picture of the structure. It is the combination of ultrashort laser pulses and X-ray pulses, which overcame the limitation of the two individual techniques. In ultrashort X-ray absorption and ultrashort X-ray diffraction experiments the same previously described pump-probe scheme is applied with the distinction that X-rays are used as probe pulse. This technique, illustrated in figure 1.9, facilitates access to both transient electronic and structural changes. It highly depends on intense, tunable, and pulsed sources of X-rays. These requirements are given quite recently by the development of 3rd generation synchrotrons such as ESRF, APS, Spring8, SLS and PETRA III. Their pulse duration is determined by the length of the electron bunches in the storage ring, of about 100 ps FWHM. For a better temporal resolution there are solutions to overcome this 100 ps-time limitation e.g. by laser generated X-ray pulses from plasmas [44] or by the slicing technique, which allows a pulse width reduction down to several hundred femtoseconds [45, 46]. However, both techniques suffer from limited photon-flux. Light sources of the 4th generation are Free electron lasers such as FLASH, LCLS and the future European XFEL, whose operation will presumably start at the end of 2015. Key features of these sources are the extreme short pulse duration of the order of 100 fs and the high pulse energy of the order of mJ. This results in a very high brilliance, exceeding that one of synchrotrons by several orders of magnitude.
Because of the high dependence on high quality X-ray sources, ultrafast X-ray absorption and diffraction experiments are a relatively young field of study. One of the first time-resolved X-ray absorption experiments examined the structural evolution of the iron atom in a myglobin-carbon monoxide complex after photoexcitation [47]. In 1993 Thiel et al. [48] analyzed structural changes of the photoexcited state of a platinum complex ($Pt_2(P_2O_5H_2)_4^{4-}$), with a lifetime of 4 μs by using a liquid jet system. However, these experiments were all limited to a nanosecond or longer time scale. In 2003 Saes et al. [49] reported the detection of transient chemical changes of $[Ru(bpy)_3]^{2+}$ which occur upon photoexcitation by ultrashort laser pulses. The excitation induces a charge transfer and leads to the formation of an excited state of 300 ns lifetime. In this experiment the synchrotron limited time resolution of 100 ps was reached. In recent years the ultrafast X-ray absorption spectroscopy on transition-metal complexes was established as a routine technique [50]. These complexes named $M(bpy)_3$ are formed by a central metal atom (where $M = Fe^{2+}, Ru^{2+}$), which is bonded to a tris-bipyridine ligand system $(bpy)_3$. In these complexes such as $[Ru^{II}(bpy)_3]^{2+}$ and $[Fe^{II}(bpy)_3]^{2+}$ the photoexcitation has strong influence

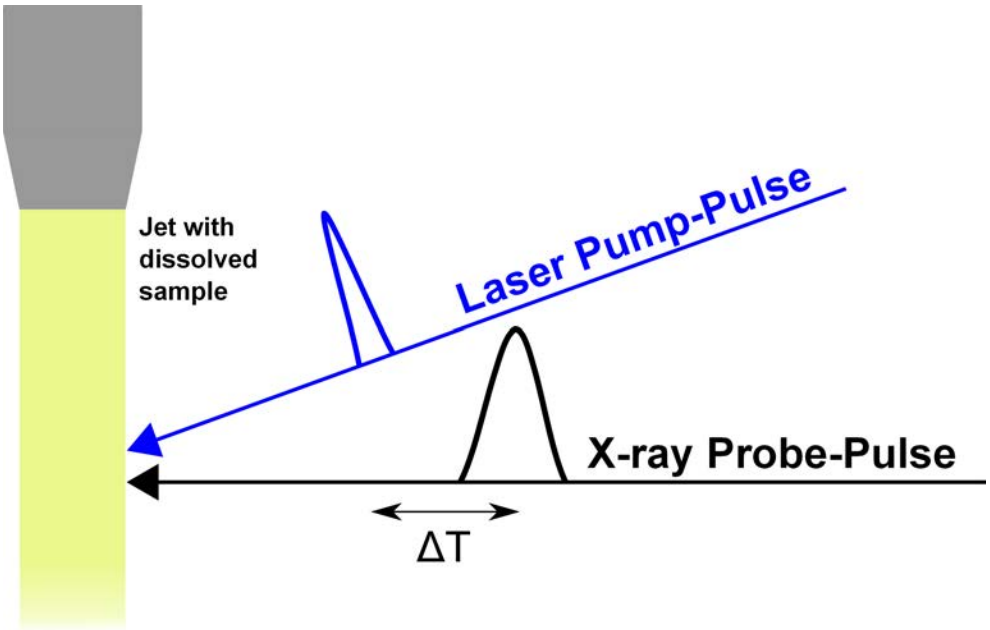

Figure 1.9.: *Pump-Probe scheme used for ultrafast X-ray absorption spectroscopy. In this example the sample is dissolved and thus provided in form of a liquid stream (so called jet). A laser pump-pulse excites the sample into a non-equilibrium excited state. After a certain time delay Δt a X-ray probe pulse hits the excited sample and probes the induced structural changes. In ultrafast laser spectroscopic experiments both, pump and probe pulses are laser pulses.*

on the transient molecular structure of their excited states. The compounds undergo bond length changes between the central metal atoms and the ligands of about 0.03 Å and 0.2 Å, respectively, which could be resolved by X-ray absorption spectroscopy conducted at synchrotrons with picosecond resolution [51, 52, 53]. In 2009 Bressler et al. used the slicing technique at the Swiss Light Source (SLS) in order to carry out time-resolved pump-probe XANES studies of $[Fe^{II}(bpy)_3]^{2+}$ on a femtosecond time scale. With this much faster processes of about 150 fs, involved into the population mechanisms of the energy states, could be resolved [54]. Femtosecond time-resolved X-ray absorption spectroscopy measurements of $[Fe^{II}(bpy)_3]^{2+}$ were very recently also conducted at a Free Electron Laser [55].

2. X-ray Absorption Fine Structure Spectroscopy

This chapter describes the *X-ray Absorption Fine Structure (XAFS)* phenomenon, which is analyzed in XAFS spectroscopy[1]. First a brief introduction into the theoretical background of XAFS and the computational methods for the data analysis are given. It is mainly based on the book by D.C. Koningsberger and R. Prins [59], the book by G. Bunker [60], and the review article of J.J. Rehr and R.C. Albers [61]. Afterwards important experimental basics, used for the XAFS experiments of this thesis, are introduced.

2.1. Introduction to XAFS

In *X-ray Absorption Fine Structure (XAFS) spectroscopy*, X-ray absorption by matter is measured as function of energy E. The basic physical measured quantity is the X-ray absorption coefficient μ(E) near or above the core binding energy of a particular atomic species [60]. It is related to the light intensity and the thickness of a sample through which the light is transmitted by the *Lambert-Beer Law* [62]

$$I = I_0 e^{-\mu(E)d} \ , \tag{2.1}$$

where I is the transmitted intensity of the X-rays and I_0 is the incident X-ray intensity onto the sample of thickness d. XAFS spectroscopy is a technique used to determine the geometrical and electronic structure of a sample. During the measurement the energy is changed stepwise and μ(E) is recorded for each energy step. The outcome of this is a characteristic absorption spectrum as shown in figure 2.1 [61]. Apart from resonance regions the X-ray absorption curve decreases continuously with increasing energy, because the X-rays become more penetrating. The absorption coefficient is a function of energy E and also depends on the sample density ρ, the atomic number Z and the atomic mass A [63]:

$$\mu(E) \approx \frac{\rho Z^4}{A E^3} \ . \tag{2.2}$$

[1]The expression "XAFS" was first introduced by F.W. Lytle [56]. Often "XAS", standing for X-ray Absorption Spectroscopy, is used in publications instead of XAFS spectroscopy. Both terms generally describe the same technique. However, in the following the term XAFS is used, since it refers more precisely to the analysis presented in this thesis. An overview of the historical development of XAFS and the nomenclature can be found in [57] and [58].

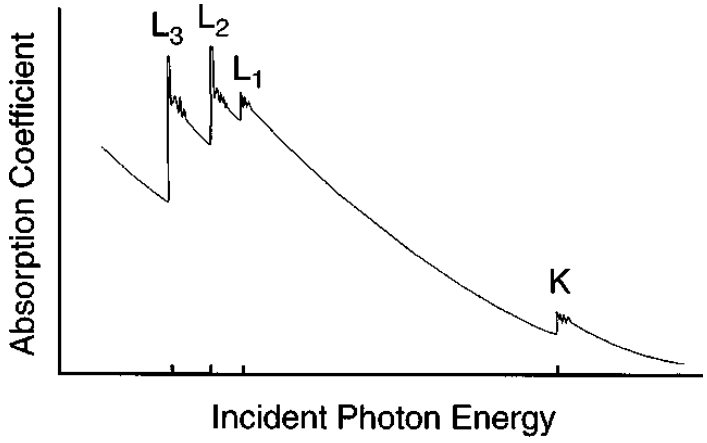

Figure 2.1.: *X-ray absorption coefficient as function of the X-ray energy. The overall decrease in absorption is discontinued by four sharp step-like peaks. The L edge is subdivided into three smaller edges. Above each single edge, oscillatory so called wiggles appear which are the EXAFS. The figure is taken from [61].*

The Z^4 dependence translates into a broad range of absorption coefficients for different elements leading to a strong contrast. Therefore, X-ray absorption spectroscopy is a very element sensitive technique [63]. At specific energies discontinuities can be observed. These are called absorption edges and they occur at energies equal to the excitation electron energy of a specific core shell. In these cases the electron is excited into the continuum, which means that the core shell is ionized. Since the core binding energies are element specific, the element to probe can be selected by tuning the X-ray energy to a certain absorption edge [63]. The core binding energies are commonly known and stored in look-up tables [64]. When an electron from the most tightly bound shell with principle quantum number n=1 is excited, the edge is called K-edge. The next most tightly bound shell is the n=2 shell and the corresponding edge is the L-edge. In fact the L-edge is split into further L_1-, L_2- and L_3-edges. L_1 corresponds to an excitation of a $2s$ electron while the L_2- and L_3-edges correspond to an excitation from the $2p_{1/2}$ and $2p_{3/2}$ orbitals which are a consequence of the spin-orbital coupling. For most of the elements the energy for the K- and L-edges ranges from $5\ \mathrm{keV}$ to $35\ \mathrm{keV}$ [63] and these two edges are the only ones which are observed by XAFS spectroscopy (though in some cases also the n=3 shell presenting the M-edge can be used) [59]. Around the edge energy of an element the absorption spectrum shows an oscillatory structure, which is referred to as XAFS [65]. The XAFS has an unique signature of a particular material because it reflects the atomic structure as well as the electronic and vibrational features of the material. It provides information on interatomic distances and coordination numbers. The XAFS spectrum can be divided into two main parts: The *X-ray Absorption Near Edge Structure (XANES)* is defined as the region around $\pm 30\ \mathrm{eV}$ of the main absorption edge. The *Extended X-ray Absorption Fine Structure (EXAFS)* describes the

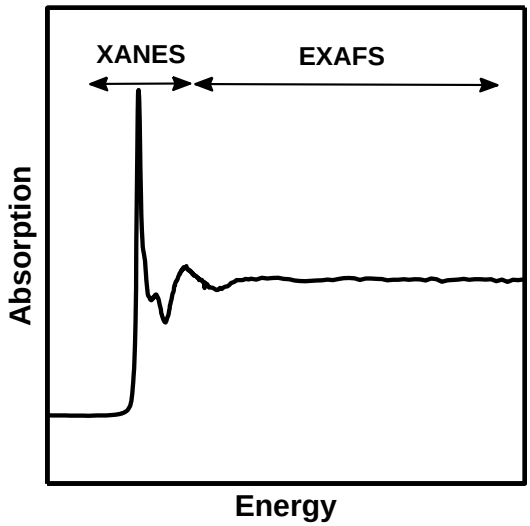

Figure 2.2.: *Absorption spectrum of Gallium tris-8(hydroxyquinoline) with XANES region, which is within* $50\ \mathrm{eV}$ *of the edge, and EXAFS region ranging up to* $800\ \mathrm{eV}$ *above the edge.*

remaining region above the absorption edge [56]. The boundary between these two regions is not well defined and there is generally an overlap of several tens of eV. According to Bianconi [66], the energy which separates the XANES from the EXAFS is that energy at which the wavelength of the excited electron corresponds to the distance between the absorbing atom and the closest neighboring atoms [59]. Both XANES and EXAFS are based on the same physical principle: The scattering of the photoelectron by the neighboring atoms of the absorber.

2.1.1. Physics of XAFS

The physical description of the quantum mechanical XAFS process is based on the photoelectric effect: An X-ray photon is absorbed by an atom of the sample and it rejects an electron of an inner shell, which is called *photoelectron*. Since XAFS is a quantum mechanical effect the photoelectron can be viewed as a spherical wave which spreads out over the sample and it is scattered from the electrons of the neighboring atoms (backscatterer). This scattering process of the photoelectron's wave is illustrated in figure 2.3. The scattered waves interfere with the outgoing wave and cause an energy dependent change of the absorption coefficient. The wavelength λ of the photoelectron can be calculated using the *de Broglie* relation [62]

$$\lambda = \frac{h}{p} = \frac{h}{m_e v_e} \ , \tag{2.3}$$

where h is the Planck constant, m_e is the photoelectron mass, v_e the velocity and p the momentum of the photoelectron. Assuming that the energy of the absorbed photon is completely used for the excitation of a single core electron the resulting kinetic energy E_{kin} of the photoelectron is

then the difference between the electron binding energy $E_{binding}$ and the X-ray photon's energy. It can be determined by the following relation [59]:

$$E_{kin} = \frac{p^2}{2m_e} = h\omega - E_0 \ , \tag{2.4}$$

where the X-ray photon of frequency ω has the energy $h\omega$. Absorption due to a given core level can only take place if there is an available state for the photoelectron that means a final quantum state with both, the right energy and the right angular momentum [63]. For example if the energy of the X-ray photon is below a particular electron binding energy of a core level, an electron of this level can only be excited to a higher lying valence level (e.g. 1s to 2p). If this valence level is filled with valence electrons, no final state is available for the photoelectron and thus no absorption can occur [63]. Once the energy of the x-ray is large enough to excite an electron to the continuum a sharp rise in the absorption spectrum appears. The absorption coefficient

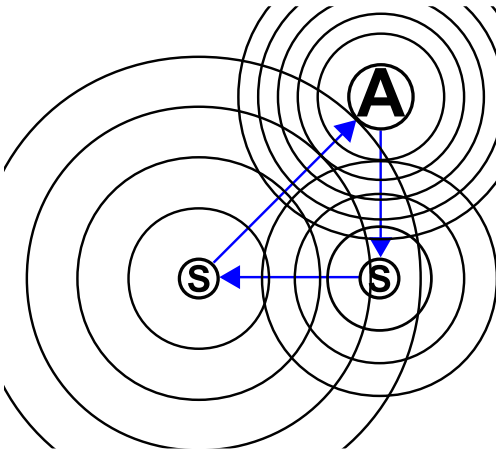

Figure 2.3.: *Illustration of the scattering of an outgoing photoelectron wave off the next neighboring atoms. The A atom is the central absorber atom and the source of the wave. The first scatterer is the S atom on the right side and the last scatterer is the S atom on the left side. The figure is adapted from [61].*

of XAFS is formed by the interference between the outgoing and the back scattered waves of the photoelectron. The total amplitude of the electron final wave function can be enhanced or reduced depending on the phases of the outgoing and backscattered waves [67]. If the two waves are in phase they interfere constructively which leads to a local maximum in the XAFS spectrum, whereas a minimum occurs if the waves are not in phase. As the energy of the photoelectron changes, its wavelength changes too, according to equation 2.3 and hence the relative phase varies. The change of the phase with respect to the wavelength depends on the distance between absorber and backscatterer. The strength of the backscattering wave depends on the type of

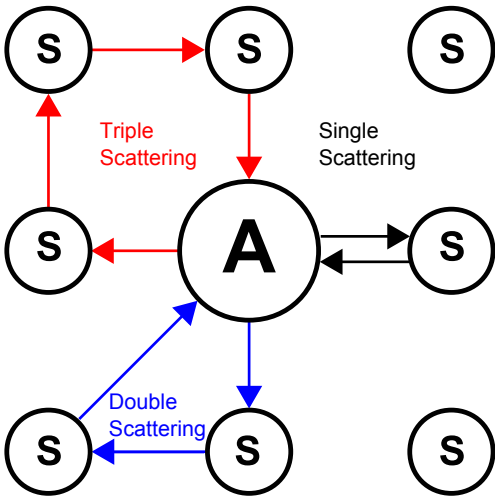

Figure 2.4.: *Scattering pathways for single scattering (black), double scattering (blue) and triple scattering (red). A represents the absorber atom while the neighboring atoms are marked by S. The arrows illustrate the path of the photoelectron's wave.*

backscatterer. This means the variation of XAFS is a direct consequence of the wave nature of the photoelectron and it contains information about the neighboring atoms of the absorber.

Scattering paths describe the trajectory of the photoelectron's wave, when it escapes from the central absorber atom followed by scattering off the neighboring atoms before it returns to the absorber atom. At high energies in the EXAFS region, where the photoelectron has a lower wavelength *single scattering (SS)* processes are dominating [68]. In contrast, at low energies in the XANES region of about 10 eV above the absorption edge only, the photoelectron wavelength λ is much larger than in the EXAFS region. At very low wavevectors k (see definition next page), also the mean free path is increased which implies that the photoelectron can scatter off many neighboring atoms present within the molecular cluster before it returns to the absorber [61]. This more complicated electron scattering process is called *multiple scattering (MS)* and has a strong angular dependency. MS is enhanced when two scatterers are almost collinear due to the forward scattering direction of the photoelectron [67]. Many different MS geometries are possible. Figure 2.4 shows as an example path geometries for scattering off one, two and three atoms.

2.1.2. EXAFS Spectrum

With increasing energy SS dominates the scattering process and beyond a certain energy only paths in which the electron is scattered once by a single backscattering atom contribute to the final wave function of the photoelectron (SS approximation). For energies above 50 eV it was found out that MS effects are weak enough to be neglected [68]. However, this is correct only, if just nearest-neighbor structural information has to be extracted. For more general and more accurate calculations, which also take into account longer distance contributions for the first shell signal it is important to include MS effects into the calculation. As it will be described later in

this chapter this is what modern XAFS theory can provide. For a given absorption spectrum, where the absorption coefficient $\mu(E)$ is measured, the EXAFS spectrum $\chi(E)$ is defined as the normalized, oscillatory part above the absorption edge [61, 63]

$$\chi(E) = \frac{\mu(E) - \mu_0(E)}{\Delta\mu_0(E)} \ , \tag{2.5}$$

where $\mu_0(E)$ is the smooth background absorption, representing the absorption of an isolated atom without any EXAFS effects, and $\Delta\mu_0$ is the measured edge jump in the absorption $\mu(E)$ at the energy E_0. It is typical to express the EXAFS in terms of the photoelectron wavevector k, which is proportional to the inverse photoelecton wavelength and can be calculated via [60]

$$k = \sqrt{2m_e(E - E_0)/\hbar^2} \ . \tag{2.6}$$

The oscillations in the EXAFS $\chi(k)$, now a function of k, often have low amplitudes (see for example EXAFS region in figure 2.2). In order to emphasize these oscillations the EXAFS is usually multiplied with a weighting factor k, k^2, or k^3. The classical EXAFS equation introduced by Stern, Sayers and Lytle [69, 68] is defined by:

$$\chi(k) = S_0^2 \sum_j \frac{N_j e^{-2\sigma_j^2 k^2} e^{-2R_j/\lambda(k)} f_j(k)}{kR_j^2} \sin[2kR_j + 2\delta_c + \Phi] \ . \tag{2.7}$$

The structural parameters for N atoms of group j are:

- the interatomic distances R_j;
- the number of equivalent scatterers which give the coordination number N_j;
- the temperature dependent root-mean-square fluctuation in bond length σ_j, which also contains effects due to structural disorder;
- the backscattering amplitude $f_j(k)$;
- the central atom partial wave phase shift of the final state δ_c;
- the phase factor Φ which presents the wavelike nature of the backscattering photoelectron;
- the photoelectron mean free path $\lambda(k)$, which is energy dependend;
- the overall amplitude factor S_0^2.

The overall amplitude factor S_0^2 factor did not appear in the original formula but was later added by Rehr et al. who obtained the final equation from a more detailed many body theory which also includes MS effects [61]. Although this factor shows a slight energy dependence, it is normally approximated to be constant. Besides the single scattering approximation it is also inadequate to consider the photoelectron as a plane wave. Thus in many body theory the wave

scattering amplitude $f(k)$ was replaced by an effective scattering amplitude $f_{eff}(k, r)$ where the r dependence reflects the spherical wave character of the photoelectron's wave. These corrections, which were introduced later do not affect the basic structure of the original EXAFS equation.

The oscillatory structure of EXAFS is clearly represented by the $sin(2kR)$ term and it is based on the interatomic distance and energy. δ_c and $f_j(k)$ are the energy dependent amplitude and phase parameters, respectively and contain the information necessary to identify the scattering atoms. The decay of the photoelectron wave is due to the $e^{-2R/\lambda(k)}$ term. It causes a relative short range of the wave of a few tens of Å only. The exponential term $e^{-2\sigma_j^2 k^2}$ is in good approximation the Debye-Waller factor and is due to thermal oscillations of the atoms around their equilibrium positions and due to effects of structural disorder [61]. The effect of the Debye-Waller factor increases with increasing energy and beyond a certain energy of $k \approx 1/\sigma$ which means about 10 Å^{-1} the EXAFS is cut off [61]. These exponential damping factors limit the EXAFS oscillations for atoms to be within about 5 Å around the absorber atom [67].
Equation 2.7 provides all important parameters to fit the local atomic structure around the absorbing atom to an experimental EXAFS spectrum and it allows the determination of interatomic distances and coordination numbers of a given sample [61].

2.1.3. XANES Spectrum

The XANES region is localized at the lower energies and it is hence much more sensitive to low-lying states than EXAFS where scattering by atoms is weak due to high energies. These low-lying states are the states, which are responsible for the binding and the electronic structure of the atoms. A XANES spectrum shows several main features which allow a direct qualitative interpretation of the absorbing atom. These features can be referred to electronic transitions. The number and intensity of the features appearing in a XANES spectrum, therefore, depend on the particular electronic structure of the absorbing atom. The strongest feature is the absorption edge indicating the most pronounced XANES transition. It is often referred to as "whiteline"[2]. There is no general definition for the absorption edge energy E_0. Some spectra show unresolved transitions, which overlap on the rising edge and hence do not allow an unique energy definition. However, it is typically taken as the maximum of the first derivative of the absorption as function of the energy [67].

The edge defines the ionization threshold to the continuum and its position and shape depend on the formal valence state and coordination environment as well as on the type of ligand [63]. That is why XANES spectra can be very useful to determine the oxidation state of the absorbing atom. The edge energy increases when the oxidation state of the absorber increases. The reason lies in the fact that atoms with a higher oxidation state usually have a higher electrical charge causing a higher attraction of the core electrons. That means that X-rays of higher energy are needed to eject such a core electron and absorbing atoms with different oxidation states will reflect this feature in spectra with shifted energy edges [67].

Another feature is the pre-edge peak. One can simply define that any edge below E_0 is a pre-edge. Because it is below the ionization energy it is a good indicator for transitions to empty

[2]In the following the expression "whiteline" is used in order to describe the maximum of the main absorption peak.

bound states and it depends also on the coordination symmetry around the absorber atom. For example first row transition metals with unfilled $3d$ electrons and filled $3p$ states show pre-peaks whose intensity decreases with progressing filling of the $3d$ band. Zinc (Zn) with a complete filled $3d$ band has no pre-peak. The transition $1s \rightarrow 3d$ is formally forbidden but becomes possible due to quadrupolar coupling [67]. Transition metals of groupVIII show transitions from $2p$ to $5d$ states. Also here the intensity of the L-edge peaks depends on the number of empty d states which can be filled. Gold (Au) which has no free d states shows a very small peak [59]. All transitions are defined by the selection rules and this way XANES directly probes the angular momentum of the electronic states. The primary transitions for K-edge with a $1s$ core electron and L_1-edge with a $2s$ core electron are: $s \rightarrow p$ while for the L_2- and L_3- edges the primary transitions are $p \rightarrow d$ [60, 67]. Other formally dipole forbidden transitions are possible due to mixing of molecular orbitals ($3d$ and $4p$) and quadrupolar coupling [67]. As it was already mentioned before, XANES is highly dominated by multiple scattering events. This provides detailed information on the sensitivity to the details of the geometrical arrangement of the absorber and its neighboring atoms including bond distances, bond angles and orientation among the atoms. In summary one can say that in general three different applications of XANES spectra can be found: Determination of the oxidation state, the electronic structure, and the three dimensional geometrical structure.

XANES is much more difficult to interpret than EXAFS. Until now there is no phenomenological formula similar to equation 2.7 for XANES, which would allow a straight forward quantitative analysis and the development of theoretical and computational methods is still ongoing. In principle, XANES includes all information of the three dimensional structure in the vicinity of the absorbing atom because it is highly based on the multiple scattering effects between the absorber and its neighboring atoms. This way it is also sensitive even to small structural variations which can change the multiple scattering signal. However, the interpretation of these results remains problematic. This fact can be easily understood by considering the EXAFS equation 2.7: For low k there is an increase in the mean free path $\lambda(k)$ and the equation becomes invalid due to the $1/k$ term [63]. That means the XANES region is more sensitive to longer distance absorber-scatterer interactions than those regions, which are typically sampled by EXAFS. Furthermore, the e^{-k^2} dependence of the Debye-Waller factor, which is a damping factor, becomes negligible in the XANES region [61]. As a consequence of these two effects there is no useful XANES equation to fit data and extract structural information from the sample [63]. Therefore, the interpretation and simulation of XANES structures is complicated since there are many interactions and a large number of multiple scattering pathways which need to be taken into account.

2.2. Theoretical Approaches to XAFS

2.2.1. Multiple Scattering Theory

This section gives a brief summary of the most important theoretical approaches which have led to the actual XAFS theory and it is based on the review article of J.J. Rehr and R.C. Albers [61]. A drawback of equation 2.7 is that it accounts only for SS, representing the basic and normally

most dominant form of scattering. For precise quantitative calculations of the absorption coefficient also MS paths have to be taken into account. The theory of XAFS has continuously improved over the last decades. XAFS is a quantum mechanical problem and for both, XANES and EXAFS the same quantum interference effects are involved so that the theoretical description is to a certain extent valid for both. Nevertheless, the theory fails for XANES for many reasons especially due to atomic, chemical, and many-body corrections, so that the quantitative analysis of XANES is still a generally unsolved problem [61]. The X-ray absorption process can be described as a transition between two quantum states. The initial state is represented by a deep core electron and an X-ray and the final state is presented by a core hole and a photoelectron [63]. The absorption coefficient is proportional to the transition rate and can be calculated via Fermi's golden rule [61]:

$$\mu \propto \sum_f | < \psi_f | \hat{\epsilon} \cdot \vec{r} | \psi_i > |^2 \delta(E_f - E_i - \hbar\omega) \ . \tag{2.8}$$

The wave functions ψ_i and ψ_f are the initial and final eigenstates for the effective one-electron Hamiltonian H for the initial state and H' for the final state with energies E_i and E_f. $\hat{\epsilon} \cdot \vec{r}$ is the dipole operator for the incident electromagnetic wave interacting with the atom. The initial state is mostly the $1s$ state for the K-edge or the $2s$ or $2p$ state for the L-edge. The description of XAFS is mainly based on the quantum interference of these two states where the initial state is very much localized at the position around the absorber atom, whereas the final state is a superposition of outgoing and backscattered electron waves. There are two general approaches to solve equation 2.8. The first is the direct calculation of the wavefunctions, which is done in the *Molecular Orbital Theory*, while the second one avoids the calculation of the wavefunctions and calculates the spectrum directly from the Green's function. In addition it incorporates inelastic losses and other quasiparticle effects [61]. Therefore, the Green's function formulation is very utile for XAFS. In position space the one-particle Green's function can be written in terms of the wavefunctions ψ_f of energy E_f [61]:

$$G(\vec{r}, \vec{r}'; E) = \sum_f \frac{\psi_f(\vec{r'}) \psi_f^*(\vec{r'})}{E - E_f + i\Gamma} \ , \tag{2.9}$$

where Γ is a net lifetime which includes effects of extrinsic and intrinsic losses. The photoelectron escaping from the absorber atom can take various paths as it scatters off several neighboring atoms. The oscillatory structure in the XAFS results from the interference of photoelectron wave contributions from these different paths. The moving photoelectron is influenced by an effective optical potential which differs from that used in ground state calculations because of the excited state nature of the electron. The effective potential $V(E)$, for the photoelectron passing through the molecule, consists of a net Coulomb potential, V_{coul}, and a self-energy term, $\Sigma(E)$ [61]:

$$V(E) = V_{coul} + \Sigma(E) \ . \tag{2.10}$$

Muffin-tin Potential

XAFS calculations usually employ the so called *muffin-tin geometry* approach (see figure 2.5) [61]. In this approach the potential consists of a spherical scattering potential centered on each atom and a constant value in the interstitial region between the atoms. The muffin tins provide atomic phase shifts which are calculated from spherically atomic like potentials inside the muffin tins. For the region near the center of each atom this is a highly precise approximation. But in the outer regions of the atom and the interstitial region between the atoms the potential is highly determined by the bonding properties. Therefore, it depends strongly on the type of the bonds and the type of atoms which are bonding. With increasing energy these effects become less important because the kinetic energy of the photoelectron is so high that it is less sensitive to small variations of the potential in these region. This explains why the muffin tin approach works well especially for EXAFS.

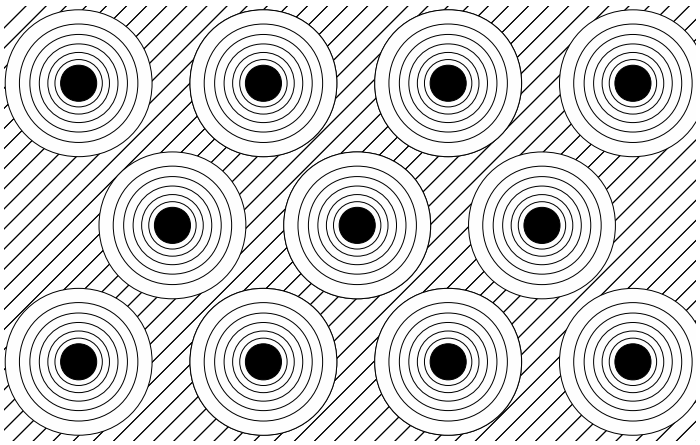

Figure 2.5.: *Scheme of muffin-tin approximation. A spherical scattering potential is centered on each atom which is presented by the black circle. The interstitial region where the potential is constant is illustrated by the diagonal stripes. The figure is adopted from [61].*

Multiple Scattering Expansion

We now come back to equation 2.9. The one-particle final state Hamiltonian for the final states ψ_f with energies E_f includes the potential $V(E)$ from 2.10. The one particles Green's function can be written as $G = 1/(E - H + i\Gamma)$. The absorption from a given core level c is given by [61]:

$$\mu = -\frac{1}{\pi} Im < c|\hat{\epsilon} \cdot \vec{r} G(\vec{r}, \vec{r'}; E) \hat{\epsilon} \cdot \vec{r'}|c > \Theta(E - E_F) \ , \tag{2.11}$$

where $\Theta(E - E_f)$ is a broadened step function which makes sure that the absorption coefficient is non-zero only above the fermi energy E_F. The Green's function can be expanded to a Dyson

series [61, 60]:

$$G = G^0 + G^0 t G^0 + G^0 t G^0 t G^0 + ... \tag{2.12}$$

$$G = 1/[1 - G^0 t] G^0 \ , \tag{2.13}$$

where G^0 is the free-electron propagator which describes how the electron propagates between two points in space and t is a function which describes how a photoelectron scatters from neighboring atoms. As it is explained in chapter 2.1.1 the scattering of the photoelectron can include a huge number of different types of paths. G considers all these paths within the cluster of the atom and solving equation 2.12 analysis the interaction between the photoelectron and all its surrounding atoms. That means that equation 2.12 is the sum over the contributions from different orders of electron scattering . $G^0 t G^0$ describes single scattering paths, $G^0 t G^0 t G^0$ is sum of all double scattering path and so on. Multiple scattering events of 3rd, 4th or even higher order can be simply added as a sum of every possible path of that order.

Full Multiple Scattering and Path-by-Path Expansion

This summation over all paths is called the path-by-path expansion approach. As it can be seen from equations 2.12 and 2.13 the term $1/[1 - G^0 t] G^0$ includes all scattering events. Thus solving equation 2.13 is a an exact method and corresponds to the path-py-path approach to infinite order. To solve this equation the multiple scattering matrix $[1 - G^0 t]$ has to be inverted. This approach is called the *Full Multiple Scattering (FMS)* approach [61, 60]. Since the photoelectron has a limited mean free path, FMS calculations have to be done only for a cluster of atoms near the absorber atom. The cluster size corresponds to the order of the photoelectrons mean free path. A typical calculation requires about 50 to 150 atoms in the cluster [70] and can be - depending on the cluster size - very time and computer consuming. In the XANES region the path series do often not converge which makes it necessary to use the FMS approach. For the EXAFS region the series is convergent and the path-by-path expansion is the best method of choice because it allows to select the most relevant path contributions for the overall EXAFS and to fit them separately. Furthermore FMS is not accurate for high energies and therefore not useful for EXAFS where typically calculations up to $k = 20$ are done.

2.2.2. Calculation and Simulation of XAFS

The analyses of XANES and EXAFS are treated as two different problems due to the differences in their physics. One reason is that accuracy of XANES analysis is still worse than that of EXAFS analysis and it delivers more qualitative than quantitative results. Another reason is that calculations by programs are based on different approaches, as it is described in chapter 2.2.1 and thus they cannot work well for both, XANES and EXAFS at the same time. The scattering path expansion for example does usually not converge in XANES and on the other hand the FMS approach becomes impractical for EXAFS, since for large k also the matrices become large [60].

The goal of both, XANES and EXAFS calculations, is to establish a model and to compare it with experimental data including unknown parameters and/or functions. It is typical to intro-

duce a minimization function to approach the data by the proposed model in the best possible way. Theoretical programs calculate XAFS spectra for a given set of atomic positions and non-structural parameters such as cluster size for FMS, energy region, and the edge within a certain time - ranging from seconds to hours in dependence of the choice of parameters. Such calculations can include a fitting procedure, in which the calculated spectrum is compared to an experimental spectrum and an error gives a value for the discrepancy of the two spectra. By changing the parameters (structural and/or non-structural), calculating a new spectrum for the new set of parameters and subsequent calculation of the residual error, one can find a set of parameters, for which the residual errors become minimal. These steps can be repeated many times until the residual errors converge and the theoretical model is optimized for a given set of parameters [60].

Chi-Square Algorithm

A typical residual error function, which is also used by several EXAFS programs is the *chi-square algorithm* [71]:

$$\chi^2 = \sum_i \left[\frac{S_i - S_i^{model}(\omega_i)}{\sigma_i} \right]^2 \quad , \tag{2.14}$$

where S_i is the signal for the i^{th} measurement, $S_i^{model}(\omega_i)$ is the theoretical calculated value with respect to i parameters ω_i and σ_i is the statistical error of the i^{th} measurement. This value also depends on the data range over which the fit is performed and on the number of fitting parameters. Thus commonly the *reduced chi-square* $\chi^2_\nu = \chi^2/\nu$ is used, whereas $\nu = N - p - 1$ accounts for the number of fitting parameters p and the number of observations N corresponding to the data points for which the deviation $S_i - S_i^{model}$ is calculated. The ideal agreement between model and experiment causes a reduced χ^2/ν to be close to 1.0 which means the deviation of experiment and theory equals the statistical error of the measurement. If χ^2/ν is close to 0 then most probably the estimated uncertainties for the data (σ_i) are too large. The higher the value for χ^2/ν the poorer is the fit result.

FEFF

In this work calculations of XANES and EXAFS spectra were performed by the program FEFF [61, 72], whereas the newest version FEFF9 was used [73]. FEFF has its name from the spherical wave back scattering amplitude $f_{eff}(k;r)$ appearing in the EXAFS equation. FEFF uses the multiple scattering Green's function method and includes the self-energy correction added to the optical potential 2.10 which leads to the muffin-tin approximation as described in chapter 2.2.1. The Green's function can be calculated in two ways. The first includes the multiple scattering path expansion based on the Rehr-Albers multiple scattering formalism. This method is suitable for high energies above the absorption edge (for reasons described in the theory part above). Here the number of paths which is summed is finite and can be selected explicitly. The second method is appropriate for energies in the near edge region and executes a full multiple scattering calculation (FMS) for a cluster of atoms centered around the absorbing atom. FMS is

typically the most time consuming part whereas the computation time increases with the cluster size. The second method is provided by the latest versions of the code FEFF8 and FEFF9. FEFF calculates the absorption cross section for all atoms of a given atomic cluster specified by cartesian coordinates. It calculates the self-consistent scattering potentials taking into account the muffin tin approximation and in addition calculates the electronic structure including local densities of states (LDOS). The FEFF program is controlled by an input command file. Details are described in the FEFF manual [70].

FitIt

As mentioned in chapter 2.2.2 it is often necessary to calculate a high number of spectra in order to find an optimal model describing the data. Depending on the number of required spectra, number of atoms in the cluster and other non-structural parameters this can be a very time consuming process. Consequently computation time is a crucial factor which limits the interpretation of XANES. A solution for this problem is the software FitIt which is a program to fit XANES spectra by calculating a multidimensional interpolation polynomial for the approximation of a single spectrum [74, 75]. Hereby, the interpolation is a function of structural parameters which determine the geometrical structure of the sample molecule. The goal of the program is to find the set of parameters which correspond to the minimal discrepancy between a given experimental spectrum and the interpolated spectrum. Due to the interpolation it is not necessary to calculate a XANES spectrum for all parameter combinations which shall be tested. Instead for a given set of parameters an ab initio-spectrum is calculated by an external program (FEFF in our case). For a variation of parameters within physical reasonable values (about ± 0.2 Å for a bond length) the spectrum which corresponds to this variation is approximated by the interpolation polynomial. The mathematical description of the construction of the interpolation polynomial is the following [75]:

$$\mu_i(E, P_1 + \delta P_1, P_2 + \delta P_2, ..., P_n + \delta P_n) = \mu(E, P_1, P_2, ..., P_n) + \sum_n A_n(E)\delta P_n + \sum_{mn} B_{mn}(E)\delta P_m \delta P_n + ... \ , \tag{2.15}$$

where $\mu_i(E)$ is the interpolated X-ray absorption coefficient and $\mu(E)$ is the ab-initio calculated absorption coefficient by FEFF. For a starting set of parameters P_1, P_2,...,P_n and δP_1, δP_2,...,δP_n are the corresponding deviations. The energy dependent coefficients $A_n(E)$, $B_{mn}(E)$,... are known from the calculations of $\mu(E, P_1, ..., P_k)$ with equations for a given set of structural parameters solving linear systems of equations: $\mu(E, P_1, ..., P_k)_i = \mu(E, P_1, ..., P_k)$ whereas P_1,...,P_k is called the "interpolation node number k" [75, 76].

Beside the ab-initio calculation of the XANES spectrum by FEFF also the structural changes of the initial structure are performed by an external program named Prot2005 [77]. It allows geometrical changes of bond lengths and angles.

2.3. X-ray Fluorescence

The XAFS phenomenon is based on the photoelectric effect in which the absorption of an X-ray photon leads to the ejection of a core electron. In the previous sections it was described how the photoelectron's scattering off the neighboring atoms changes the absorption coefficient. The photoelectron escaping from the excited atom leaves a core hole which can be filled by two different mechanisms. The first mechanism is X-ray fluorescence where an electron of a higher lying core-level drops down and fills the inner core hole. An X-ray fluorescence photon is then emitted [78, 63]. Since this has an energy corresponding to the energy difference between atomic levels of an element, it can be used for the characterization of sample atoms. The fluorescence photons are named by the energy level of the dropping electron. L shell electrons which fill a hole in the innerst K-shell (n=1) create fluorescence photons named K_α. An electron from the next higher lying M-shell creates K_β radiation and so on.

The so called *Auger-Effect* is referred to the alternative mechanism for the de-excitation [78, 63]. Here, also an electron from a higher shell recombines with the core hole and releases energy which is dissipated non-radiatively by the excitation of a second electron to the continuum. This second electron is called *Auger electron*. The two processes compete with each other and the probability depends on the atomic number of the absorbing atom [59]. For light elements the Auger-effect is more favorable while the probability for fluorescence increases for heavier elements.

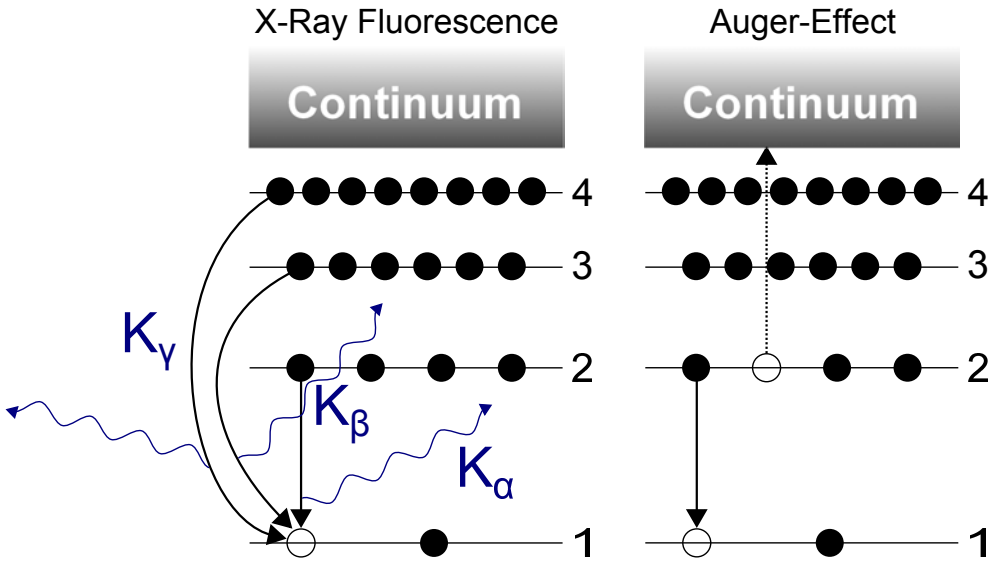

Figure 2.6.: *a) X-ray fluorescence: The absorption of a photon creates a core hole of an inner shell (in this case n=1) which is filled by a higher lying shell electron. As a consequence an X-ray photon is emitted. b) Auger-Effect: The core hole is also filled by a higher shell electron. However, the energy is used to the excite another electron. This figure is redrawn. It is based on [63].*

2.4. Statistical Aspects of a Laser-Pump X-ray-Probe Experiment

The purpose of a time-resolved laser-pump X-ray-probe experiment is to analyze the changes of a sample system induced by a laser pulse (photoexcitation) and after a certain time-delay probed by an X-ray pulse. The XAFS spectra are recorded in X-ray fluorescence detection mode. The transient pump-probe signal T_{fl} is the difference between the X-ray fluorescence signal of the pumped state I_{fl}^{pump} and the X-ray fluorescence signal of the unpumped ground state I_{fl}^{unpump}, normalized by the incident X-ray intensity I_0 [79]:

$$T_{fl} = \frac{I_{fl}^{pump} - I_{fl}^{unpump}}{I_0} \ . \tag{2.16}$$

However, the pump signal I_{fl}^{pump} is a mixed signal from sample molecules in the ground state and excited state, since only a fraction of the molecules can be excited. To obtain the full excited state spectrum for all molecules being in the excited state the following equation can be utilized [79, 51, 80, 49]:

$$T_{fl} = \underbrace{T_{EX}(E,t)}_{measured} = f(t) \underbrace{[A_{EX}^{ES}(E,t) - A_{EX}^{GS}(E)]}_{T_{EX}^{100}} \ , \tag{2.17}$$

where $T_{EX}(E,t)$ is the measured transient difference absorption spectrum containing all information about the changes between the two states, $A_{EX}^{ES}(E,t)$ is the excited state absorption spectrum at time instance t following the photoexcitation and $A_{EX}^{GS}(E)$ is the ground state absorption spectrum. The photoexcitation yield $f(t)$ delivers information of how efficient the excitation process is at a certain instant of time t. $T_{EX}^{100}(t = 0)$ is the experimental transient difference spectrum occurring for $100\ \%$ of the probed molecules being in the excited state.

2.5. Photoexcitation Yield

The photoexcitation yield f depends on the number of laser photons N_0^{ph} provided for the excitation process, the concentration of the sample solution c_{sam}, the excitation volume V_{ex} illuminated by the incident laser beam and the optical cross section σ_{opt} of the sample at the excitation wavelength of the laser. Figure 2.7 illustrates the photoexcitation process of the sample dissolved for a liquid micro-jet and pumped by a laser. Since f scales the transient signal $T(E,t)$, knowledge of f is the crucial quantity for quantitative analysis. Bressler et al. introduced an equation which allows calculation and optimization of f in dependence of the described parameters [81, 79]:

$$\boxed{f(c_{sam}, N_0^{ph}, \sigma_{opt}, t) = \frac{N_0^{ph}}{c_{sam} \cdot V_{ex}}(1 - e^{-c_{sam}\sigma_{opt}d})} \ , \tag{2.18}$$

where the excitation volume V_{ex} is defined by the focus beam size and the thickness of the jet. The number of photons N_0^{ph} depends on further beam properties of the pump laser e.g. pulse

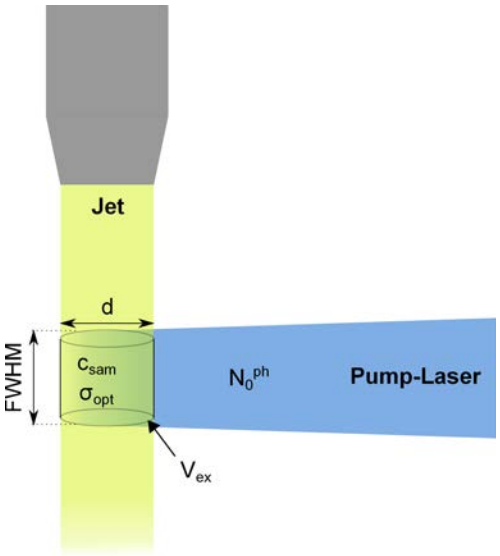

Figure 2.7.: *The sample is dissolved and provided in a liquid micro-jet, shown in yellow. A fraction of the jet V_{ex}, defined by the jet-diameter d and the laser focus size (FWHM), is excited by the pump laser, shown in blue. The photoexcitation yield f is the ratio of molecules in the ground and excited state. Parameters, which need to be known for the calculation of f are shown.*

energy, focus beam size and repetition rate. Basically the formula describes how f depends on the transmitted laser intensity within the jet volume obeying Lambert-Beer's law. Equation 2.18 gives the ratio of number of absorbed photons N_{abs}^{ph} and number of sample molecules $n_{sam} = c_{sam} \cdot V_{ex}$ and can be also written as:

$$f = \frac{N_{abs}^{ph}}{c_{sam} V_{ex}} \ . \tag{2.19}$$

The validity of equations 2.18 and 2.19 is based on a linear excitation process and multi-photon absorption processes are not considered i.e. $N_{abs}^{ph} = n_{sam}^{ES}$. Under this assumption the absorption of one photon consequently leads to one excited molecule and it must apply:

$$f = \frac{n_{sam}^{ES}}{c_{sam} V_{ex}} = \frac{c_{sam}^{ES}}{c_{sam}} \tag{2.20}$$

For an ideal excitation process, in which each sample molecule absorbs one photon, f would be 1. In a real absorption process only a fraction can be excited and the number of sample molecules is the sum of ground state molecules n_{sam}^{GS} and excited state molecules n_{sam}^{ES}:

$$n_{sam} = n_{sam}^{GS} + n_{sam}^{ES} \text{ and } c_{sam} = c_{sam}^{GS} + c_{sam}^{ES} \ . \tag{2.21}$$

Equations 2.18 and 2.19 do also not account for excited state absorptions. In principle also the excited state molecules have a cross section which differs from that one of the ground state molecule. This extinction coefficient is unknown and can be only determined in an additional

laser spectroscopic experiment.

However, we modified equation 2.18 for the fact that excited state molecules cannot absorb an additional photon. This fact becomes especially important for high laser intensities and for high photoexcitations, which occur when small diameter jets are used, as in this experiments. For this consideration equation 2.18 becomes

$$\boxed{f(c_{sam}, N_0^{ph}, \sigma_{opt}, t) = \frac{N_0^{ph}}{c_{sam} \cdot V_{ex}}(1 - e^{-c_{sam}(1-f)\sigma_{opt}d})}\,, \tag{2.22}$$

where the term $c_{sam}(1-f)$ assures that only molecules in the ground state are accounted for the absorption process. By usage of equation 2.20 and equation 2.21 it can be written:

$$c_{sam}(1-f) = c_{sam}^{GS}\ . \tag{2.23}$$

Equation 2.22 was solved numerically, whereas the number of laser photons in a gaussian profile incident on the jet, has been calculated by integration over the jet thickness. Some of the parameters in the formula like concentration, laser focus size and number of photons are adjustable, while the others like jet thickness and extinction coefficient are fixed.

2.6. Synchroton X-ray Source PETRA III

The descriptions of this section follow the books by G. Bunker [60] and J. A Nielsen [78] and for specific details refer to the PETRA III technical design report [82].

2.6.1. Basic Functioning Principle

Synchrotron Radiation (SR) is electromagnetic radiation, produced by radially accelerated charged particles and has its name from *Synchrotrons*, which are large machines originally built for high-energy experiments. Figure 2.8 shows a sketch of a synchrotron with its major components. In a synchrotron charged particles, like electrons or positrons (PETRA III runs with electrons, so this description is used in the following) are generated by an electron gun and accelerated by a linear accelerator (*LINAC*) [82]. This is equipped with *radio frequency cavities* (RF cavities) in which an electromagnetic wave is maintained, increasing the electron energy up to several MeV before they enter a booster-ring. In this circular pre-accelerator the electrons are accelerated up to very high velocities, almost reaching the speed of light. When the final energy of several GeV is reached the electron beam is injected into the *storage ring* where the electrons circulate for several hours producing SR. Adjacent to the storage ring the *beamlines* use the SR for manifold experiments. In the storage-ring the movement of the electrons is along straight paths until *bending magnets* force them into an arc-formed movement in the horizontal plane. After this arc another straight path follows. This is repeated until the path is closed. In the regions where the path is bended, the electrons are accelerated and therefore emit SR. The radiation is emitted into a small cone, which is vertically of about $1/\gamma$ in angular width with $\gamma = E/mc^2$ where E is

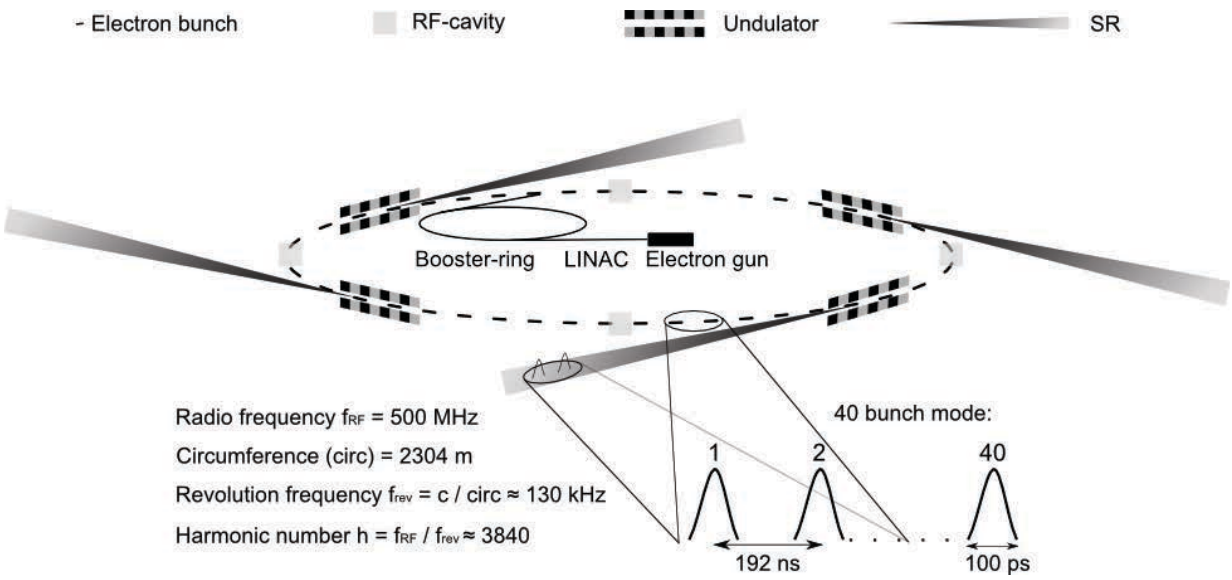

Figure 2.8.: *Synchrotron with basic components and parameters. Electrons are injected by an electron gun and linearly accelerated in the LINAC. A booster-ring increases the energy of the electrons up to several GeV before they enter the storage ring, where they circulate. In undulators the electrons pass a magnetic field, which forces them to oscillate and thus to emit high intensity SR. The temporal structure of the electron bunches translates directly into the temporal structure of the resulting SR bunches (see marked bunches).*

energy of the electron and mc^2 its rest energy [78]. The emission of SR causes loss of electron energy, which is compensated by continuous energy supply from the RF cavities. For PETRA III $50\ \%$ of the RF-cavity power is needed to compensate the SR losses, while the rest power is used for the generation of the cavity voltage [82]. In addition energy losses also occur due to scattering of the electrons with gas molecules, though the storage-ring is operated under ultra-high vacuum conditions. These losses accumulate in time and require a refilling of electrons into the ring. This occurs either by a larger injection with a time interval of several hours or by smaller injections every $70\ \mathrm{s}$ [82]. The latter case is called *top-up mode* and provides a much more constant beam current which is preferable for time-resolved pump-probe experiments. The radiation properties highly depend on the energy of the machine (several GeV for large synchrotrons). Quadrupole and sextupole magnets keep the electron on a stable beam orbit in longitudinal and transverse direction to the electron movement. *Insertion Devices* allow a much more efficient way to produce SR optimized for the very specific experimental requirements of the different beamlines. Such devices, which can be inserted into the straight sections of the storage-ring, are classified into two types: *Wigglers* and *Undulators*.

2.6.2. Wiggler and Undulator

In an insertion device dipole magnets are periodically stacked behind each other producing an alternating magnetic field along the device length. Electrons which pass the device are deflected

by the magnetic field and thus are forced onto an oscillating sinusoidal track with a phase corresponding to the distance λ_u of the single magnets. The deflection leads to an acceleration of the electrons at the deflection points and hence to emission of radiation. The difference of wigglers and undulators lies in the different period of the magnetic field, which is defined by the arrangement of the bending magnets. In a wiggler the magnets cause a relative large deflection and the radiation from different parts of the electron's path is accumulated incoherently leading to a continuous broad spectrum. In comparison to a single bending magnet, the enhancement of the radiation intensity is a factor of N, which is the number of bending magnets in the wiggler. In an undulator the magnets are arranged in a way that the angular excursion of the electrons is smaller than $1/\gamma$ so that for a given photon energy and its harmonics the electromagnetic wave emitted of an electron at one oscillation is in phase with radiation of the same electron from another oscillation. This leads to a coherent sum of amplitudes of radiated waves, whereas the radiation intensity approximately scales with N^2. The emitted spectrum has a bandwidth of ca. $1\ \%$. An important parameter which describes the movement of electrons in a periodic magnetic field is represented by the *Deflection Parameter* [78]:

$$K = \frac{eB_0\lambda_u}{2\pi m_e c} = 0.934 \cdot \lambda_u \cdot B_0 \ , \tag{2.24}$$

where m_e is the electron mass, B_0 is the maximum magnetic field and c the speed of light. For $K \ll 1$ the movement of electrons follows the one of an undulator and for $K \gg 1$ the movement of electrons is that of a wiggler.

2.6.3. Temporal Structure

The temporal structure of a synchrotron is of fundamental importance for time-resolved experiments. After the excitation by a laser pump pulse the sample is probed at instants of time which are defined by the flashes of the X-ray probe beam. The magnetic field of the RF cavities at PETRA III oscillates with a radio frequency of $f_{RF} = 500\ \mathrm{MHz}$ (referred to as *fundamental RF frequency*) and creates potential walls causing the electrons to travel in packages named buckets through the storage ring. These buckets are capable to be filled with electrons. The revolution frequency f_{rev} is the frequency of the electrons circulating in the storage ring. Thus it is defined by the circumference (circ) of the ring, which is $2304\ \mathrm{m}$ for PETRA III [82] and the electrons speed, almost reaching the speed of light c:

$$f_{rev} = \frac{\mathrm{c}}{circ} \approx 130\ \mathrm{kHz} \ . \tag{2.25}$$

The radio frequency is always an integer of the revolution frequency given by the harmonic number h:

$$h = \frac{f_{RF}}{f_{rev}} \approx 3840 \ . \tag{2.26}$$

PETRA III provides 3840 buckets [82], which potentially can be filled with bunches. The length of a bunch is directly related to the pulse duration of the emitted X-ray bunch and in case of

PETRA III it is about $100\ \mathrm{ps}$ FWHM (for measurement of the PETRA III bunch resolution see also [1]). PETRA III provides operation modes with 40, 60, 240 and 960 bunches [82]. Considering the revolution frequency of $130\ \mathrm{kHz}$, in case of 40 bunch mode the time gap between two adjacent bunches is $192\ \mathrm{ns}$ and the lifetime with this filling pattern is about 2 hours only. Operation at $100\ \mathrm{mA}$ with top-up injection, in which every $70\ \mathrm{s}$ a refilling takes place, ensures the current to be constant within $1\ \%$ [82]. For time-resolved experiments filling patterns with a small number of bunches with a high intensity are preferable.

2.6.4. Monochromator

The SR produced by the undulator is tangentially emitted from the path of the electron bunches into a radiation cone and finally reaches the beamline endstation. The beamline provides different devices and equipment for performing experiments. First step is the X-ray energy selection by a *monochromator*. This consists of one or more crystals which reflect the beam incident under a specific angle according to Bragg's law. Only those X-rays, which have the specific wavelength for which Bragg's law is satisfied will be reflected constructively. All other wavelengths undergo a destructive interference and do not leave the monochromator. By changing the reflecting angle of the crystal, specific X-ray wavelengths/energies can be selected. In order to resolve XANES features, the energy resolution should be at least $1\ \mathrm{eV}$, which nowadays can be realized by crystal monochromators without any difficulty. In addition the energy region should reach up to about $1\ \mathrm{keV}$ above the absorption edge for EXAFS measurements. Details of the monochromator, which was used for the experiments described in this thesis, are given in chapter 4.1.1.

2.6.5. Synchrotron Radiation Parameters

SR can be characterized by the following terms:

- The *photon flux* F is the overall number of photons in a beam per time interval [60]:

$$F = \frac{\textit{number of photons}}{s} \tag{2.27}$$

- The *intensity* I refers to the flux per area on which the photons hit [60]:

$$I = \frac{\textit{number of photons}}{s \cdot mm^2} \tag{2.28}$$

- The quality of synchrotron sources is commonly described by the *brilliance* which is defined as the flux per source area per opening angle for a given energy bandwidth (BW) [60, 78]

$$B = \frac{\textit{number of photons}}{(s \cdot mm^2 \cdot mrad^2 \cdot 0.1\%BW)}\ , \tag{2.29}$$

where the energy BW of the source is commonly defined as 0.1 % of the photon energy

$$\textit{Energy BW} = \frac{\Delta E}{E} = 10^{-3} = 0.1\% BW \ . \tag{2.30}$$

For an ideal optical system the quantity is an invariant. If the spatial size is reduced (enlarged) the angular divergence will be increased (decreased). Thus the brilliance is ideal to describe such complex optical systems as a synchrotron and it provides a mean to compare beam properties of different X-ray sources.

- Another important quantity, the *emittance*, is the product of opening angle and source size and thus connected to the brilliance. A low emittance means high brilliance and hence is desirable for generating high brightness synchrotron radiation [83].

2.6.6. Focusing of X-rays

One way to focus X-rays is by utilizing compound refractive X-ray lenses [84, 85]. The refractive index for hard X-rays in matter is slightly smaller than 1, so that the focusing optics have a concave form (in contrast to visible light with refractive index of 1.5 for glass lenses with convex form). A single compound refractive lens is shown in figure 2.9. Due to small refraction of

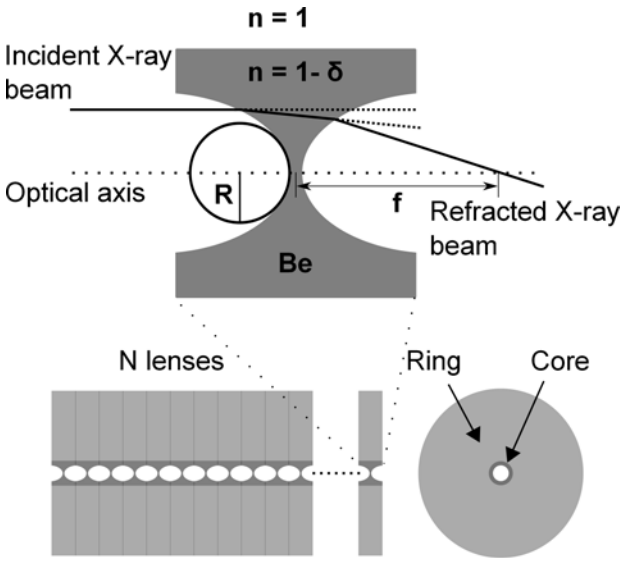

Figure 2.9.: *Top: Working principle of a singe refractive X-ray lense. Bottom: Array of single lenses to magnify refraction. The figure is adopted from [86].*

X-rays several of these lenses are stacked behind each other in a lens package preferably under ultra-high vacuum conditions [84]. The number of lenses depends on the X-ray energy and on the desired focus size. Because X-rays are also absorbed by the lenses, these are made of low-z materials such as beryllium, boron, carbon, or aluminum [85]. The ”Physikalisches Institut” of the RWTH Aachen provides an online tool which calculates, for a given source size, distance

from the source, X-ray energy and geometrical parameters of the lenses, the number of X-ray lenses to obtain a specific beam focus size in a certain focal distance [86].

2.6.7. APD-working Principle

All XAFS spectra were measured in X-ray fluorescence yield mode by using an *Avalanche Photo Diode (APD)*. The working principle of an APD is based on the photo electric effect where photons are converted into electrons. This is the principle of a conventional photodiode. In addition the APD has an internal gain which amplifies the created electrons. Thus, an APD can be regarded as a photomultiplier tube (PMT) with semiconducting properties [87].
When the energy of the incoming X-ray photon is higher than the band gap energy, an electron-hole pair is created. In case of silicon, the band gap is $1.1\ \mathrm{eV}$. However, not every photon fulfilling this requirement results in an electron-hole pair. The process depends also on the *quantum efficiency* (QE), which describes the ratio of the number of photons hitting the photo-reactive surface and the number of created electron-hole pairs. In the case of Si-APD the QE is ca. 0.7 at $\approx 10\ \mathrm{keV}$ (value is interpolated from QE=0.95 at $6\ \mathrm{keV}$ and QE=0.45 at $12\ \mathrm{keV}$ given in [88]). When a high reverse bias voltage of several hundred volts (up to $380\ \mathrm{V}$ for the APD from FMB Oxford used in this experiment) is applied to the depletion layer, the electrons are strongly accelerated and they collide with other electrons causing an electron cascade. A large number of these events results in high gains of 250 or more [87]. This effect is called *avalanche effect*.

3. Sample Preparation

The sample compounds Gaq3 and Alq3 were purchased from ABCR (www.abcr.de) and Sigma-Aldrich (www.sigmaaldrich.com) in form of a yellowish powder with a grain size of several micrometers. The quoted purity was $99\ \%$. For experiments the powders were transferred into different phases. The XAFS experiments are based on a liquid micro-jet system so that the sample compound had to be dissolved in an appropriate solvent. Spectroscopic investigations were obtained from Gaq3 and Alq3 dissolved in solution, from thin films, powders, and crystals. The latter represents the main applicable form for use in OLEDs. For single crystal X-ray diffraction it is necessary to grow crystals of appropriate size and quality. Different techniques for crystal growth of Gaq3 are presented in this chapter. For future perspective pump-probe X-ray diffraction experiments it is planned to use low roughness crystal slices of a few micrometers thickness and a few hundred micrometers diameter. For the production of these crystal slices a new surface treatment device was developed and built up (see chapter 3.4.1). One important requirement for the crystal surface treatment is a sufficient crystal size of about $1\ \mathrm{mm}$. Thus the crystal growth applications were optimized to obtain large crystals.

3.1. Solutions

For the XAFS experiments in solution a high sample concentration is desirable to achieve a high fluorescence signal. In order to find an appropriate solvent for Gaq3, the following solvents were tested: Ethanol, methanol, dimethylformamide (DMF), dimethyl sulfoxide (DMSO), water, chloroform, benzyl alcohol, acetonitrile. The by far best solubility was achieved in benzyl alcohol. At room temperature the highest solubility was $25\ \mathrm{mg/ml}$ corresponding to $50\ \mathrm{mmol/l}$. This concentration was used and kept constant during all XAFS-experiments. Beside the solubility also vapor pressure and toxicity play an important role for the experiment. A low vapor pressure leads to an evaporation of the solvent during experimental operation which can be hardly suppressed when using a liquid micro-jet system. To keep the sample concentration constant the solvent has to be refilled regularly. In case of benzyl alcohol, however, the boiling point of $204\ ^\circ$ is high enough, that evaporation is negligible. Benzyl alcohol is declared as harmful [89], however, the health hazards from the solvent under the given experimental conditions could be estimated as low.

3.2. Thin Film Growth

For the fabrication of OLEDs metal organic compounds are grown in form of thin films placed in a sandwich like structure between two electrodes. The film form presents therefore the most common and important form of metal-organic compounds. Thin films were grown with the *Physical Vapor Deposition (PVD)* technique. The setup[1] is shown in the appendix in figure A.1. In a vacuum chamber the sample powder is heated in a small oven up to the sublimation point. The gaseous sample is deposited as a film on a substrate which is horizontally placed above the oven. The oven consists of a copper heating apparatus which is wrapped by a heating wire. This can be operated via direct current of up to $2\ \mathrm{A}$ creating a temperature of $600\ ^{\circ}\mathrm{C}$. The temperature is measured by a Pt100-element. A cylindrical cup with a conical lid containing the sample is inserted into the apparatus. The lid has a small opening of ca. $200\ \mu\mathrm{m}$ only and works in this way similar to a jet nozzle. Its function is to assure that only gaseous sample can leave the cup. As substrate silicon wafers with a size of $20\ \mathrm{mm}$ x $20\ \mathrm{mm}$ were used. Before usage they were cleaned in an ultrasonic bath with acetone and afterwards washed with isopropanol and air dried. The vacuum inside the chamber had a pressure of down to $5 \cdot 10^{-5}\ \mathrm{mbar}$ and the sublimation temperature at the heating apparatus was between $380 - 420\ ^{\circ}\mathrm{C}$. A crucial parameter for the film properties is the distance from the substrate to the cup opening. For a relative homogenous film surface the distance was adjusted to ca. $5\ \mathrm{cm}$. A control mechanism for the film thickness was not included. Figure 3.1 shows a Gaq3 film on a silicon wafer. For UV-VIS absorption spectroscopic experiments UV-transparent optical glass slides were used instead of the silicon slices. However, the method described for the thin film growth was identical.

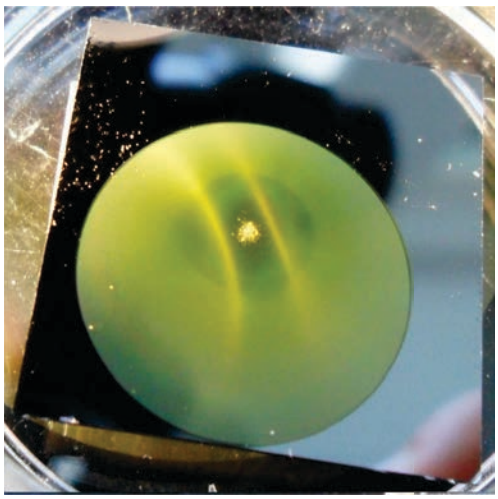

Figure 3.1.: *Gaq3 thin film grown on a* $20\ \mathrm{mm}$ *x* $20\ \mathrm{mm}$ *Si-wafer by using the PVD technique. In the center the film layer shows a small inhomogeneity consisting of Gaq3 powder. Such inhomogeneities occurred, when the heating rate was too high. In this case the pressure in the cup was high enough, that parts of the sample powder, which were not yet sublimated, were transported to the substrate by gaseous parts of the sample from hotter areas of the cup.*

[1] Courtesy of workgroup of M. Drescher from University of Hamburg.

3.3. Crystal Growth

Alq3 as well as Gaq3 crystals were grown by crystallization from solution and by sublimation. For both homologous compounds the methods were identical and slight quantitative deviations could be found only in the solubility and sublimation point.

3.3.1. Crystallization from Solution

Gaq3 and Alq3 crystals were grown by precipitating from solution. In this, molecules aggregate as a consequence of supersaturation and form nuclei which grow into macroscopic crystals. Crystal growth depends on the solubility, supersaturation rate, diffusivity, temperature and reactivity of substrate surfaces towards nucleation [90, 91, 92]. At first the solubility of the sample compounds was tested, because the solute should be easily soluble in the solvent for crystallization. These were water, ethanol, methanol, DMF, DMSO, toluol, chloroform, and benzyl alcohol. For crystal growth the supersaturation of a solution is the driving force. The power of a solvent is defined as the mass of solute that can be dissolved in a given mass of a solvent at a specified temperature [92]. Another important parameter is the temperature coefficient of the solubility. For most solids the solubility increases with increasing temperature [92]. That means one way for crystallization of a substance is the cooling of a nearly saturated solution in order to achieve supersaturation and consequently the formation of a crystal nucleus. Since in benzyl alcohol by far the largest amount of Alq3 and Gaq3 could be solved, this solvent was potentially suitable for a crystallization process. In fact large single crystals could be obtained from benzyl alcohol. At first a saturated Gaq3/benzyl alcohol solution was created at a temperature of $60\ ^{\circ}\mathrm{C}$. It was assured that the whole amount of substance was completely dissolved, so that a filtration was not necessary. Subsequently the solution was placed in a self-built crystallization chamber which allowed a temperature control with an accuracy of better than $0.2\ ^{\circ}\mathrm{C}$. The solution was slowly and continuously cooled down to room temperature within six to seven days. During this time, Gaq3 single crystals of high quality were grown to a size of up to $1\ \mathrm{mm}$ in length, $300\ \mu\mathrm{m}$ in width and $50\ \mu\mathrm{m}$ thickness. A light microscope image of a Gaq3 single crystal is presented in figure 3.2.

Alq3 and Gaq3 single crystals were also grown from ethanol and methanol. Due to its lower hazardous risks, crystals from ethanol were preferably used. The corresponding powder of the compound was added to ethanol at $60\ ^{\circ}\mathrm{C}$ until a supersaturation was reached (about $5 - 6\ \mathrm{mg/ml}$). Under a constant temperature of $60\ ^{\circ}\mathrm{C}$, small crystals were appearing within $10 - 20$ minutes and growing to larger crystals of about $100 - 200\ \mu\mathrm{m}$ due to Ostwald ripening, in which larger crystals grow at the cost of smaller ones [93]. Figure 3.3 presents light microscope image of the resulting Alq3 crystals.

3.3.2. Crystallization by Sublimation

Crystals of Alq3 and Gaq3 can also be obtained by sublimation [24], where the sample is directly transferred from the gas phase into the solid phase. This transition takes place at temperatures and pressures which are given by the sublimation point of a substance. In a phase diagram the

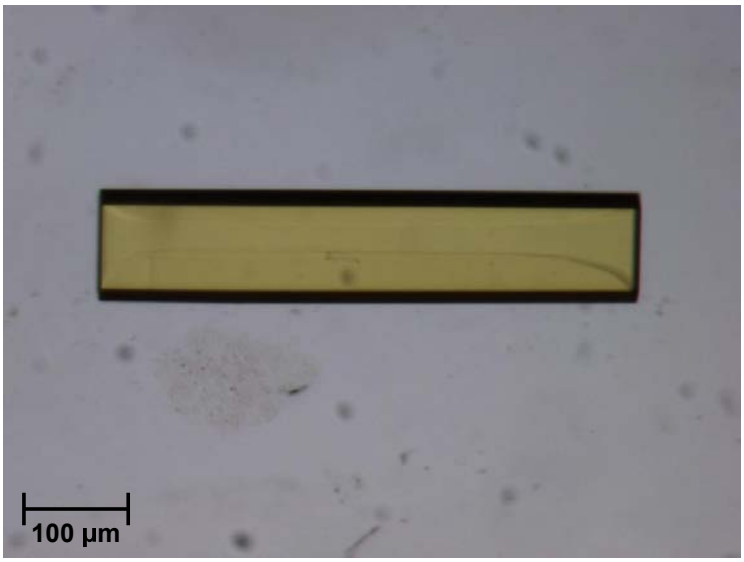

Figure 3.2.: *Gaq3 single crystal grown from benzyl alcohol. The size of the crystal is ca.* 620 μm *x* 110 μm *x* 30 μm *(length x width x thickness).*

Figure 3.3.: *Alq3 single crystals grown from ethanol.*

phase transition takes place at the sublimation curve which is part of the phase boundary below the triple point. For the metal-organic quinoline compounds pressures of below 10^{-6} mbar and temperatures above 360 °C are required. Under these conditions the compound is first gaseous and crystal growth can be obtained by a re-sublimation of the compound on an appropriate target. Coelle et al. showed that different phases of Alq3 grow at different temperatures [24]. For the sublimation technique an own sublimation tube was built. It consisted of a ca. 20 cm long glass tube with one closed and one open end. A vacuum of about 10^{-4} mbar was obtained by connecting a vacuum pump to the open end. The tube was heated by a heating wire winded around the glass tube. For the re-sublimation a temperature gradient along the tube was used, generated by an increasing distance between the single wire loops. Different phases of the compound appeared each at a favored temperature. The experimental procedure was the following:

- Placing of the sample compound in a little aluminum vessel inside of the glass tube.
- Connection of the pump and obtaining of a vacuum of ca. 10^{-4} mbar.
- Heating up of the compound to 400 °C.

The sublimate deposited on an aluminum target placed along the heated region of the glass tube. The crystals, which were obtained in this way are shown in figure 3.4. Two main types of crystals could be distinguished. One type, located in the hotter region of the tube, showed rectangular single crystals with a length of about 100 μm, a width and a thickness of about 10 μm, respectively. The other type appeared in a region directly adjacent to the first region and showed thin needle-like crystals with a length of up to 1 mm. Though Coelle et al. reported three different phases using this sublimation technique, I could only observe these two different phases by light microscopic investigation. A reason for this could be different temperature gradients within the sublimation tubes.

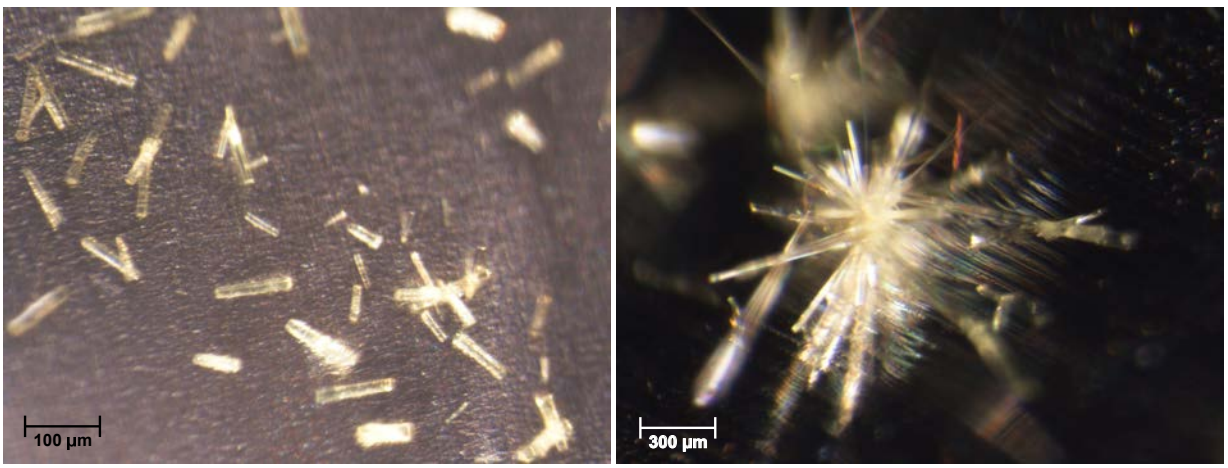

Figure 3.4.: *Two different Gaq3 crystal phases obtained by sublimation technique. Left: Single crystals with a size of about* 100 μm *x* 10 μm *x* 10 μm *(length x width x depth). Right: Needle-like crystals with a length of up to* 1 mm

3.4. Pump-Probe Experiments of Crystals

This chapter describes a sample preparation method for future perspective pump-probe X-ray diffraction experiments. Actual pump-probe experiments suffer from the fact that the penetration depth of the pump laser light into the sample material is limited. Due to the high extinction coefficient of the sample, most of the intensity of the incident laser light is absorbed within the first hundred nanometers of the sample [94]. For Alq3 thin films Mezyk et al. determined an average absorption coefficient of $\alpha = 4 \cdot 10^4\ \mathrm{cm}^{-1}$ for wavelengths between $351\ \mathrm{nm}$ and $363\ \mathrm{nm}$ [95]. It is reasonable to assume that in crystals the absorption coefficient is of the same order. In figure 3.5 the laser pulse energy incident on a crystal/film is plotted as function of the thickness according to Lambert-Beer's law. It shows that due to the very low penetration depth of $\delta_p = \alpha^{-1} = 250\ \mathrm{nm}$, where the laser intensity is decayed to $1/e$ of its surface value, nearly all of the laser intensity is absorbed after $1\ \mu\mathrm{m}$.

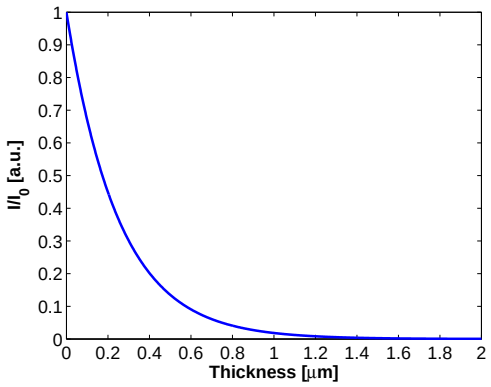

Figure 3.5.: *Ratio of incident and transmitted laser intensity as function of the sample thickness for an absorption coefficient of* $\alpha = 4 \cdot 10^4\ \mathrm{cm}^{-1}$ *for Alq3 films [95].*

Figure 3.6 shows a scheme for the experimental setup for a pump-probe X-ray micro-diffraction experiment, consisting of crystal slice, pump laser beam and probe X-ray beam. The pump laser beam is focused to a line focus of about $500\ \mu\mathrm{m}$ x $5\ \mu\mathrm{m}$ and allows efficient pumping of the crystal slice. The X-ray probe beam, focused to about $1\ \mu\mathrm{m}$ x $5\ \mu\mathrm{m}$ hits the crystal slice perpendicular to the optical axis of the laser, so that ideally only the excited state fraction close beneath the crystal surface is probed.

In contrast to the high absorption of the pump laser light, the interaction between the probing X-ray beam and the sample is much lower. A consequence of this mismatch of penetration depths of laser and X-ray is that only a fraction of the probed sample volume is in the excited state, if an X-ray focus $\gg 2\ \mu\mathrm{m}$ is used. In this case the probe signal is a mixture of ground and excited states. This illustrates the necessity of X-ray focusing close to the sub-micrometer range. Furthermore the photoexcitation process should be optimized. In solution XAFS spectroscopy the concentration and/or the jet diameter can be varied for this purpose. In case of a crystal these options are not given. In order to excite deeper lying sample layers by the pump laser, one possibility is to increase the laser intensity. However, this also raises the risk for damage of the crystal structure. Another approach is to tune the wavelength such that the absorption maximum

is not directly met. In this case one has to assure that the sample is still excited into the right desired excited state. An idea to overcome these difficulties is to polish or cut the crystals down to crystal slices with a height of a few micrometer and very low surface roughness. The low crystal thickness serves for a better conduction of heat, which is induced by the high intensive laser beam into the crystal structure. The slices should be then adjusted such that the pump laser beam irradiates the crystal slice with the optical axis perpendicular to the crystal surface. In this way it shall be assured that a constant fraction of the crystal close beneath the surface is homogeneously excited. The excited state fraction of the crystal is then capable to be probed by a sharply focused X-ray beam of about $1\ \mu\mathrm{m}$ x $5\ \mu\mathrm{m}$ (v x h). In this case it is assured that mainly excited states contribute to the probe signal.

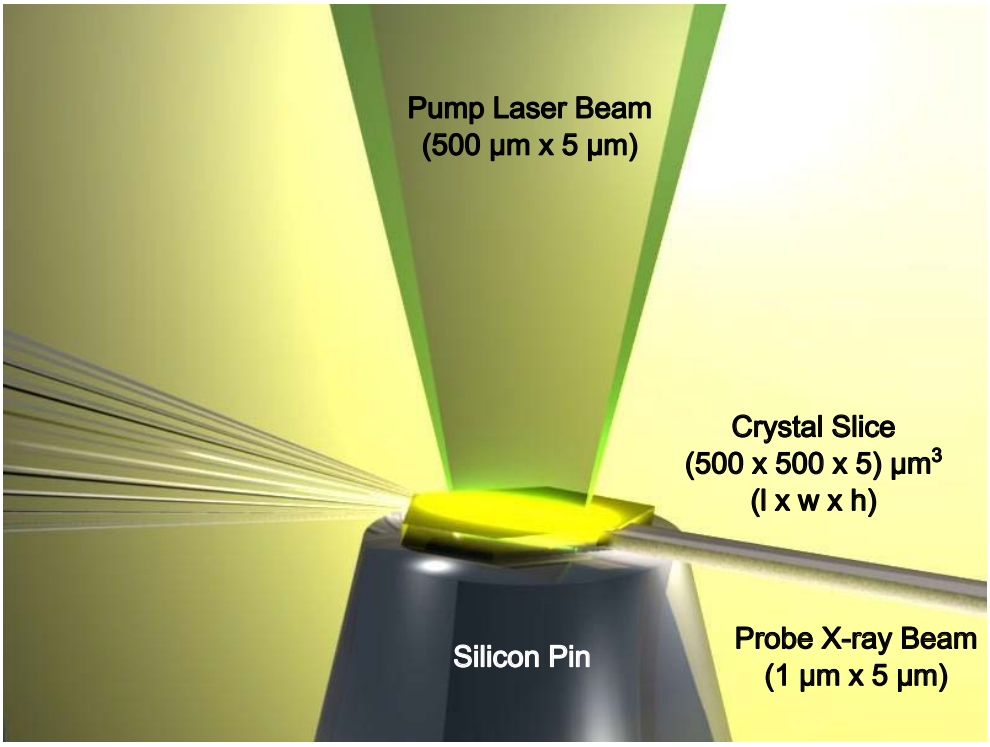

Figure 3.6.: *Beam and sample arrangement for a pump-probe X-ray micro-diffraction experiment, consisting of crystal slice, pump laser beam and probe X-ray beam. The pump laser beam is focused to a line focus with the longer axis parallel to the optical axis of the X-ray beam. The focused X-ray probe beam has a size of about* $1\ \mu\mathrm{m}$ *x* $5\ \mu\mathrm{m}$ *and hits the crystal slice close to its surface and perpendicular to the optical axis of the laser, so that ideally only the excited state fraction close beneath the crystal surface is probed.*

In the following section I introduce a newly developed method, which allows surface treatment of soft organic crystals with a size of less than $1\ \mathrm{mm}$.

3.4.1. Device for Surface Treatment of Soft Organic Crystals

A polishing device based on a motorized air bearing spindle from ESS Mikromechanik (www.ess-mikromechanik.de) with a tool holding device, which can be equipped with different turning tools has been developed in the framework of this thesis. The advantage of air bearings is the very low friction and the high precision. The setup of the device is illustrated in figure 3.7.

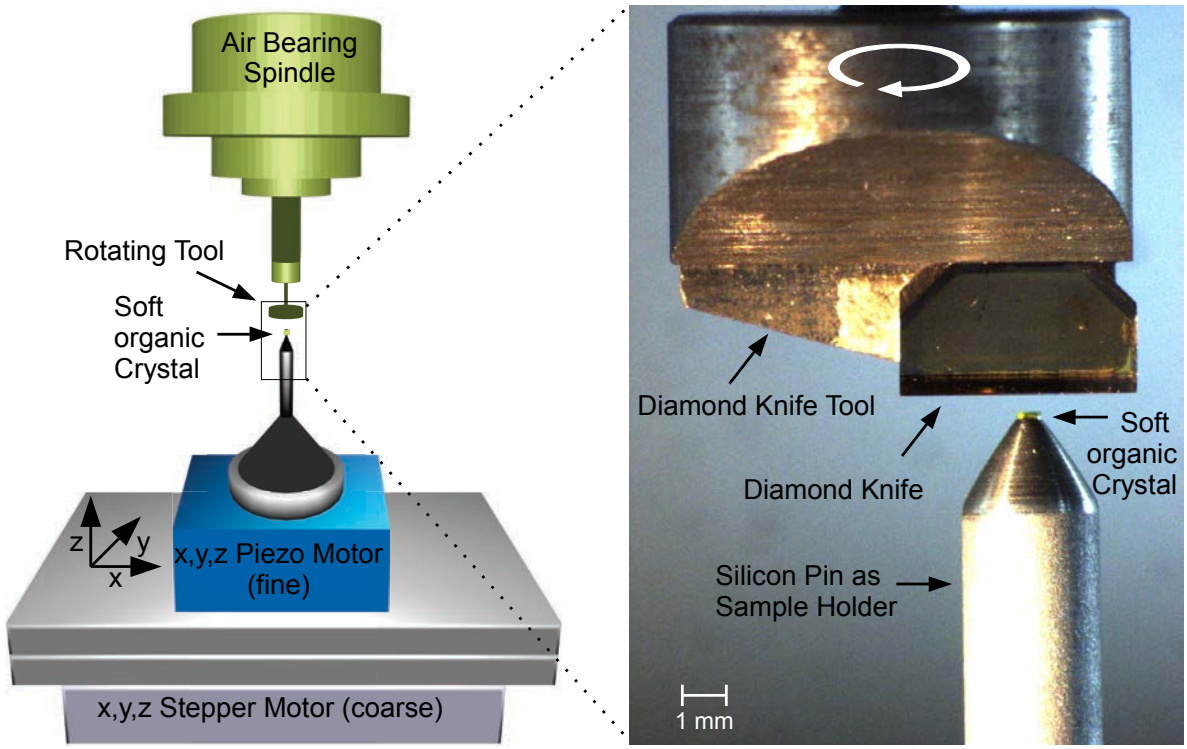

Figure 3.7.: *Left: Newly developed device for surface treatment of soft organic crystals. The device is based on an air bearing and two motor stages for sample control. It can be equipped with different polishing and cutting tools for various applications. Right: Diamond knife tool with diamond knife and sample crystal mounted on a silicon pin. For the cutting procedure the silicon pin is moved towards the rotating knife and in this way the crystal is cut layer by layer.*

The crystal is glued on the tip of a silicon pin, which can be fixed in a magnetic mount commonly used as standard sample holder in protein crystallography. In this way the crystal can be directly mounted at the beamline after polishing without changing the sample holder. This helps to prevent mechanical damage to the crystal during handling. The silicon pin with the crystal is mounted on top of two different x,y,z-motor stages. The first one is a stepper motor from xhuber (www.xhuber.com) with $1\ \mu$m-resolution, serving for larger movements. The second motor is a piezo based *nanocube* from *Physikintrumente* (www.physikinstrumente.de) and allows movements in x,y,z-direction with 1 nm-resolution and adjustment travels of $420\ \mu$m x

$420\ \mu\mathrm{m}$ x $300\ \mu\mathrm{m}$. Under real experimental conditions the resolution of the nanocube was not better than $50\ \mathrm{nm}$. For the polishing process the crystal is approached to the rotating polishing tool (movement of the crystal in z-direction), while a microscope camera, which is focused onto the crystal, allows an optical control of the distance. The result of the polishing depends on one hand on the structural properties of the crystal and on the other hand on parameters of the polishing process itself. These parameters are the properties of the polishing head, the rotating speed and the step size and velocity of the motor movement.

Dental Polishing Tool Various types of polishing heads from Leickert-Dental (www.leickert-dental.de), commonly used in dental technologic applications, were tested. These tools are available in great variety consisting of different materials with different grain sizes. All tested polishing heads for the new device were made of diamond. Apart from polishing heads with very low grain sizes, these polishing heads turned out to be unfeasible for the soft organic crystals and did not lead to satisfying results. Thus an own cutting tool was invented and then produced by Diatec-Diamanttechnik (www.diatec-pforzheim.de).

Diamond Knife Tool The tool consists of a monocrystalline diamond knife as it is also used for commercial microtomes. Using this tool the procedure is more precisely rather a cutting than a polishing process. The cutting face of the knife is parallel to the crystal surface. It rotates around the axis perpendicular to the crystal surface. The cutting procedure is conducted by a stepwise approach of the crystal to the rotating knife. In this way the crystal surface is cut layer by layer, whereas the layer thickness depends on the step size of the motor movement. Best results were achieved by step sizes of about $100\ \mathrm{nm}$. In any case the step size must be larger than the resolution of the piezo motor of $50\ \mathrm{nm}$ under experimental conditions. Steps below this size lead to poor results. The crystal was moved in z-direction only, while not being in contact with the rotating knife to avoid forces caused by the translational movement. In principle the motor of the air bearing allows rotating speeds of up to $16000\ \mathrm{rpm}$, but it could be shown that very low rotational speeds led to better results. Operation of the air bearing under high speed induces more forces into the crystal structure and increases the risk to crack the crystal.

Microtome The surface treatment device was compared to another method, in which the crystals were cut by a commercial rotational microtome[2] from Leica (www.Leica.com). A microtome is used to cut thin slices of a sample, named sections. Thus it is suitable for sample preparation for light and electron microscopy. The knife is fixed in a horizontal position and the sample, mounted on a flywheel, is bypassed. During the rotary motion of the flywheel, the distance of sample and knife is reduced until thin slices are cut. For the cutting of our crystals a diamond knife was used. In contrast to the usual procedure of a microtome we were not interested in the sections, but in the remaining crystal fixed on the sample holder.

[2]Courtesy of Heinrich-Pette-Institut Hamburg.

3.4.2. Analysis of the Polished Crystals

Light Microscopic Analysis

The polished crystals were first inspected under a light microscope. Figure 3.8 shows a crystal surface before (a)) and after the polishing procedure (b)) with a magnification of 500. In b) pieces of the removed crystal layers can be seen. These could be easily erased from the crystal by pressurized air. The polished surface is well defined and of lower roughness than the original surface.

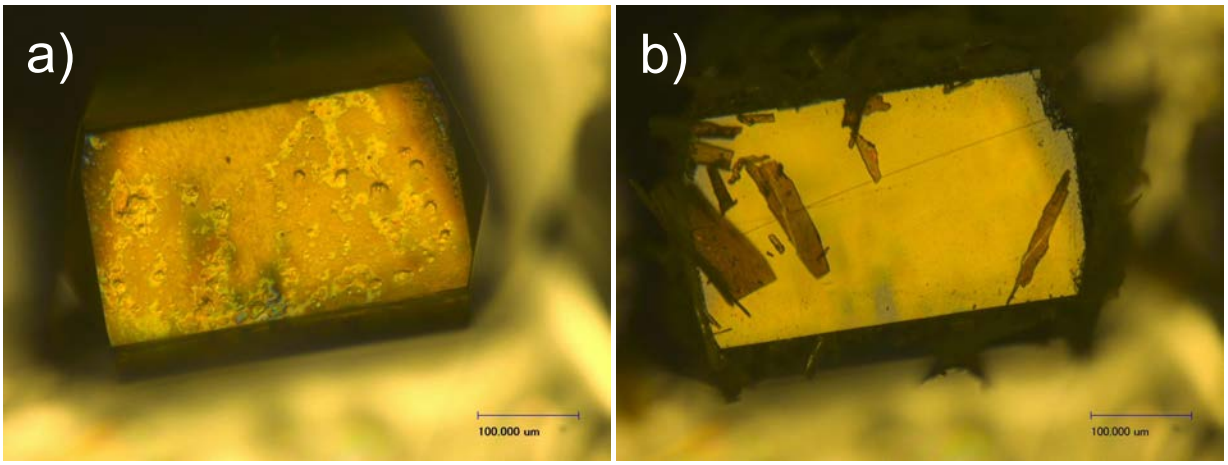

Figure 3.8.: *Light microscopical images with magnification of* 500. *a) Crystal surface before polishing. b) Crystal surface after cutting with the diamond knife tool with pieces of removed crystal layers.*

Atomic Force Microscopic Analysis

The generated crystal surfaces were further characterized using an *Atomic Force Microscope (AFM)*[3] [96]. This type of microscope is well suited for the analysis of many kinds of surfaces. It consists basically of a cantilever of about 100 μm length, which has a sharp tip at its end. This tip interacts with the sample and as a result of the occurring forces the cantilever is deflected according to *Hook's law*. An image is generated by scanning the sample surface whereas the deflection of the cantilever is measured as function of the position. This, most straightforward scanning mode, is called *Constant Height Mode*. A height image, which reveals detailed information about the topography of the surface, can be generated in *Constant Force Mode*. In this the z-scanner of the AFM is operated in closed loop such that deflections of the cantilever are instantly compensated by an appropriate height adjustment of the z-scanner. The voltage signal applied to the z-scanner is recorded as function of the position during scanning and an height image is created from this information. A statistical analysis of the height image allows to measure the surface roughness. The constant force mode was used for the generation of the images of

[3]Courtesy of S. Roth, HASYLAB, DESY.

the polished sample surfaces. Different scanning modes are usable and the question, which one is most recommendable depends on the type and properties of the sample as well as the specific application. For a more detailed introduction into AFM, the reader is referred to [97, 98].

Figure 3.9 shows an AFM height image of the crystal surface after treatment with the diamond knife tool presented in figure 3.8 b). In addition a histogram of the surface heights is displayed. The scan size was $20\ \mu\mathrm{m}$ x $20\ \mu\mathrm{m}$ with a resolution of 256 x 256. A statistical surface analysis

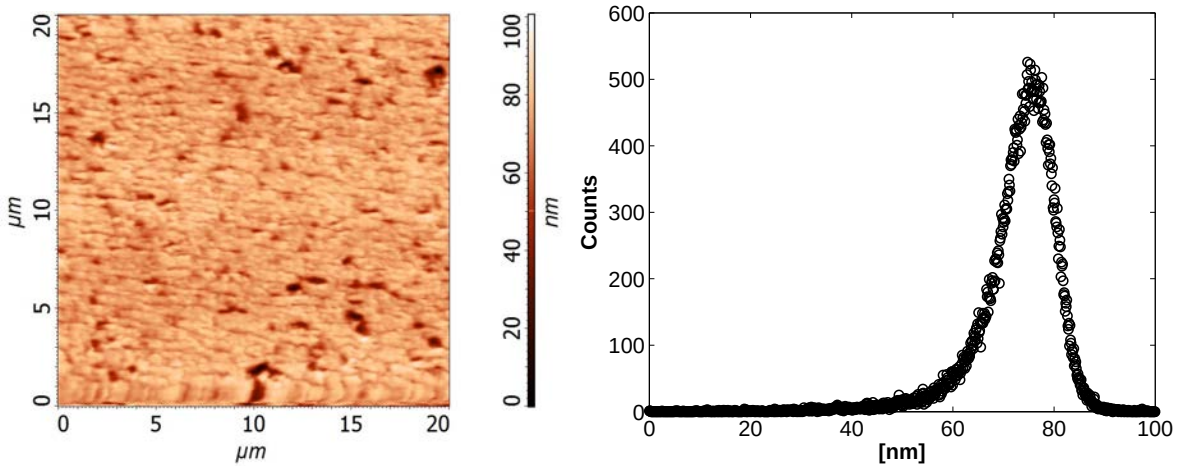

Figure 3.9.: *Left: AFM image of a crystal surface after treatment with the diamond knife tool. Right: Histogram of the corresponding height distribution.*

revealed a root-mean-square (rms) roughness of $8.0\ \mathrm{nm}$ and an average roughness of $5.6\ \mathrm{nm}$ whereas the difference between the minimum and the maximum height was $100.5\ \mathrm{nm}$ (peak-to-peak value). Crystal surfaces generated by the surface treatment device with a conventional polishing head and with the diamond knife tool, as well as surfaces obtained by the commercial microtome were analyzed. In table 3.1 the best results, in terms of lowest roughness, of each method are listed. The corresponding AFM images and histograms are presented in the appendix in figure A.2. For all crystal surfaces the same scan size of $20\ \mu\mathrm{m}$ x $20\ \mu\mathrm{m}$ and resolution of 256 x 256 were used. The dental polishing head provides only poor roughness. The corresponding AFM height image shows that the surface is roughened by the treatment of the polishing head.

Table 3.1.: *Results of the polished crystal surfaces analyzed by AFM.*

Type of Polishing	**Polishing device with dental polishing tool**	**Polishing device with diamond knife tool**	**Microtome**
Amount of sampling	256 x 256	256 x 256	256 x 256
Peak-to-Peak	$428,3\ \mathrm{nm}$	$110.8\ \mathrm{nm}$	$35.5\ \mathrm{nm}$
Average Roughness	$30,5\ \mathrm{nm}$	$4,6\ \mathrm{nm}$	$3.0\ \mathrm{nm}$
RMS Roughness	$39,1\ \mathrm{nm}$	$5.9\ \mathrm{nm}$	$3.8\ \mathrm{nm}$

The corresponding histogram shows a wide distribution of measured heights. The diamond knife tool improves the roughness significantly. The height image c) shows a much smoother surface and the histogram in d) is sharper reflecting a much lower roughness nearly seven times better than that one obtained by the dental polishing head. The knife cuts the crystal layer by layer similar to a microtome knife. The commercial microtome provides slightly better results. It is worth mentioning that the generated crystal surfaces nearly show the same quality concerning roughness as Alq3 films produced by vapor deposition: Jonda et al. reported about a monomeric layer of Alq3 vapor deposited on an ITO substrate for usage in OLEDs with a peak-to-peak roughness of $23.7\ \mathrm{nm}$ and a rms roughness of $2.7\ \mathrm{nm}$ [99].

It is important to mention that the new device was specifically designed for the surface treatment of soft organic crystals. The resulting crystal slices shall serve as samples in pump-probe X-ray diffraction experiments. Especially the easily removable sample mount ready for use at a synchrotron beamline was planned for this. In this way, the setup allows efficient preparation of sets of polished crystals. In contrast to that, handling of a crystal in a commercial microtome is less straightforward and much more time consuming. In addition it should be pointed out, that the diamond knife tool used in the polishing device has potential for improvements. The knife profile and blade angle for example could be optimized such that the angle between crystal surface and knife blade (inclination) of nearly $90\ ^\circ$ in our case, is less steep.

4. Experiments

All experiments in the framework of this thesis were performed at beamline P11 at the 3rd generation synchrotron source PETRA III (synchrotron and beamline specifications, described in this chapter are mainly from [100]). A new setup for Pump-Probe XAFS experiments was developed and built up at this beamline. The experiments were performed between December 2011 and January 2013. During this period the setup has been further developed and continuously improved. This chapter is structured in the following way: First beamline P11 and the XAFS setup itself are described including all experimental parts, such as laser, alignment setup with sample flow system, timing and data acquisition. In addition the experiments, which were necessary for the preparation and characterization of the sample-system, such as laser and UV-VIS spectroscopy are explained separately.

4.1. Pump-Probe XAFS Spectroscopy

In a pump-probe XAFS experiment a XAFS spectrum is recorded from the sample in the ground state (unpumped, laser off) and another spectrum is recorded from the excited state (pumped, laser on). For the excited state spectrum the sample molecules are pumped by a laser pulse into an excited energy state (photoexcitation). After a time delay shorter than the lifetime of the excited state, the X-ray probes the excited molecules. Therefore, laser and X-ray beam have to spatially overlap on the sample. Ideally the pump laser beam is larger than the X-ray beam so that only molecules within the pumped sample volume are probed by the X-rays. The difference of the pumped excited state spectrum A_{EX}^{ES} and the unpumped ground state spectrum A_{EX}^{GS} is the transient difference spectrum $T_{EX}^{100} = A_{EX}^{ES} - A_{EX}^{GS}$. Analysis of this transient signal allows to reveal structural and electronic changes of the sample upon photoexcitation. The XAFS technique applied in this thesis is based on the measurement of samples in solution. The sample, dissolved in an appropriate solvent, is pumped through a circular flow-system which ends into a glass nozzle. In this way a laminar, stable and rapidly flowing jet with sample solution is generated, which can be considered as a liquid sample beam. For these experiments the philosophy was to use a small jet diameter of $30\ \mu\mathrm{m}$ in order to achieve highest photoexcitation yields.

4.1.1. Beamline P11

The first optical element at beamline P11 is a liquid nitrogen cooled double-crystal monochromator (DCM) for selection of a specific wavelength. It has two Si-111 and Si-311 crystals with an energy resolution of $\Delta E/E = 1.3 \cdot 10^{-4}$ and $\Delta E/E = 0.28 \cdot 10^{-4}$, respectively. For XAFS

experiments the energy resolution is crucial since the absorption is measured as a function of energy. During a measurement the energy is scanned and the absorption signal is recorded at each energy step. Especially at the absorption edge, where changes of the absorption signal are large, a high energy resolution is required to resolve all features. Beamline P11 provides an energy range of $2.4 - 30$ keV and a maximum flux of $1.3 \cdot 10^{13}$ ph/s at 12 keV. The monochromatic X-ray beam can be focused by a *Kirkpatrick-Baez (KB)* mirror system which is located behind the monochromator. It consists of two horizontal deflecting and one vertical deflecting X-ray mirror. The mirrors can be bended dynamically and produce an intermediate focus with a size of 16 μm x 96 μm (v x h) and a divergence of 8 μrad x 15 μrad (v x h) at 65 m distance from the source.

4.1.2. Laser-System

Pulsed Laser PHAROS

The laser system used in the experiments is the femtosecond pulsed laser *PHAROS* from Light Conversion (www.lightcon.com) outfitted with special specifications needed for a synchronization of the system to the PETRA III synchrotron. The system consists of an oscillator with Kerr lens mode-locking [101], a regenerative amplifier and a stretcher-compressor unit. The system is based on a Yb:KGW crystal as active medium which is pumped by CW laser diodes. In addition a *phase-locked-loop (PLL)* serves for synchronization to the synchrotron. Figure 4.1 shows a sketch of the system, whose components and functioning principle are explained in the following. The oscillator provides laser pulses with 1030 nm wavelength, a power of ca. 1800 mW

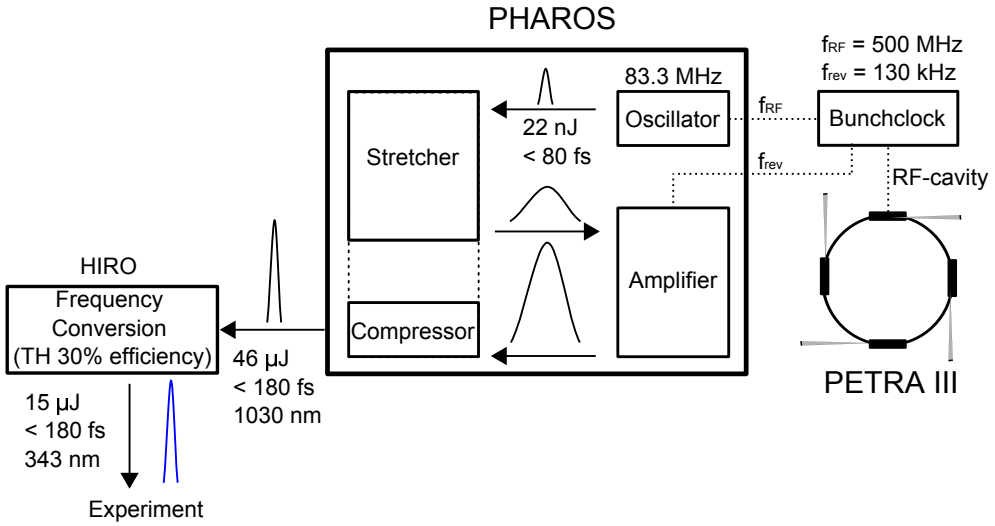

Figure 4.1.: *Block diagram of the PHAROS pump laser-system synchronized to the synchrotron via bunchclock (for details see text).*

and a repetition rate of 83.3 MHz, which corresponds to one sixth of the synchrotron master frequency of 500 MHz. Each pulse has an energy of 22 nJ and a duration of about 80 fs. To

generate higher pulse energies this laser light is seeded into the amplifier which is based on the *Chirped Pulse Amplification (CPA)* technique [101].

Pulse stretching and compression are based on a single high efficiency transmission grating, so that stretcher and compressor are enclosed in the same housing, which contributes to the compactness of the system. Changing the compression length allows to tune the output pulse duration to a maximum of about $10\ \mathrm{ps}$. In the amplifier, an intensity gain of about 10^7, depending on the gain medium, is obtained. Within the amplifier cavity a single Beta-barium-borate (BBO) pockels cell is used for injection of the seed and dumping of the amplified pulse. The pockels cell is triggered by the revolution frequency of $130\ \mathrm{kHz}$ from the bunchclock of PETRA III. The seed pulse is captured within the cavity where it oscillates and undergoes an amplification by passing the active medium. The laser pulse leaving the amplifier and the subsequent compressor has a pulse power of up to $46\ \mu\mathrm{J}$, a pulse duration of $< 180\ \mathrm{fs}$, a wavelength of $1030\ \mathrm{nm}$ and a repetition rate of $130\ \mathrm{kHz}$.

High Harmonic Generator HIRO

The PHAROS laser system is equipped with a harmonic generator called *HIRO*. In this the second, third and fourth harmonics (SH, TH, FH) of the fundamental wavelength are generated by using BBO crystals. Frequency conversion is based on nonlinear optical processes in which photons interact with a nonlinear crystal [101]. For example for second harmonic generation (SHG), two photons, with ordinary polarization with respect to the crystal structure result in a photon with extraordinary polarization, twice the energy of the incident photon and thus half of its wavelength. The TH is generated by interaction of the fundamental wavelength and the SH. The TH with $343\ \mathrm{nm}$ was used for the experiments described in this thesis. A detailed description of frequency conversion is given in [101].

Synchronization

For time resolved pump probe measurements a controlled variation of the relative delay between laser and X-ray pulses must be guaranteed. The laser pulses, pumping the sample into the excited state have to be in a controllable relation with respect to the X-ray pulses which probe the excited sample. The laser is synchronized to the synchrotron by phase-locking the oscillator frequency of $83.3\ \mathrm{MHz}$ to the master frequency of $500\ \mathrm{MHz}$ delivered by the PETRA III bunch clock. This timing device was developed and built up by Moritz Schlie and is described in detail in his thesis [1]. The minimal achievable timing jitter between laser and X-ray pulses is $\approx 4\ \mathrm{ps}$.

4.1.3. XAFS Setup

Figure 4.2 shows the XAFS setup installed on the granite block at beamline P11. For the measurement, the pump laser beam and the probe X-ray beam are focused on the jet such that the two beams are precisely spatially overlapping with the jet. The setup is mounted on a hexapod stage

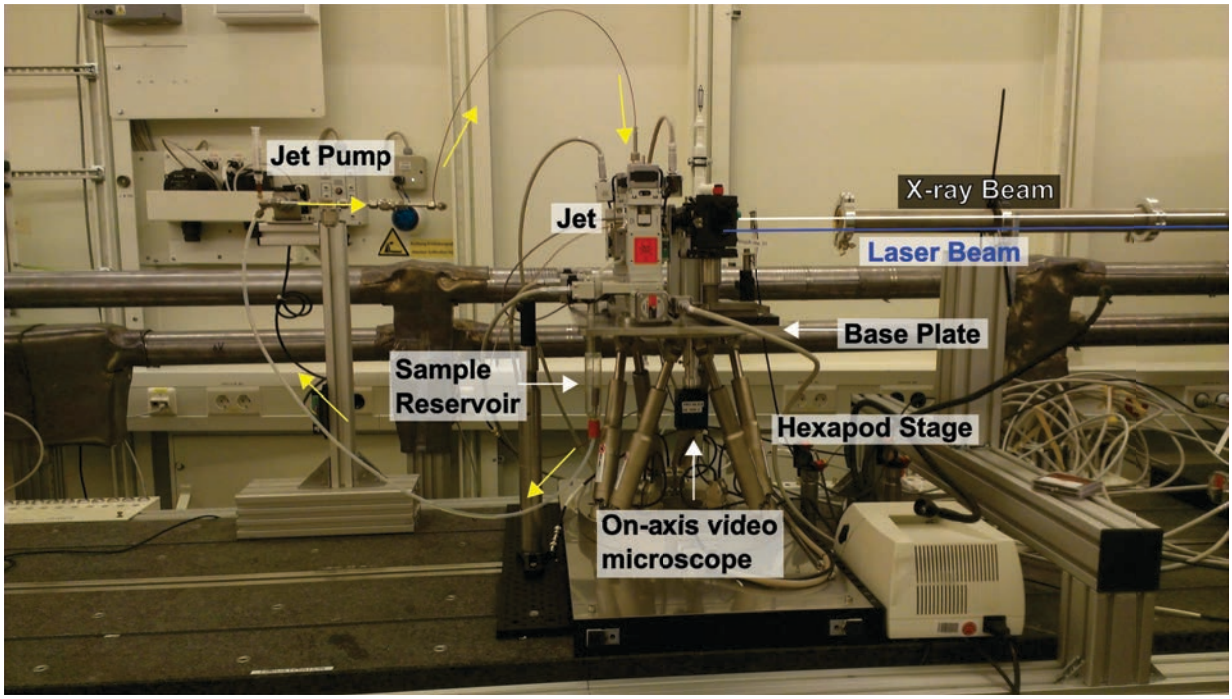

Figure 4.2.: *XAFS setup installed on the granite block at beamline P11. Laser and X-ray beams enter the optics of the XAFS setup from the right hand side and are focused onto the micro-jet sample. After passing the focus area of X-ray and laser beams, the sample is caught and refilled into the sample reservoir leading to a circular flow system, which is continuously pumped by the jet pump. An on-axis video microscope provides images of the sample jet, the laser beam and the X-ray beam and allows for their alignment with micrometer precision.*

with six degrees of freedom (3 rotational axis and 3 translational axis) allowing a very flexible and accurate alignment of the setup in the X-ray beam. On top of the hexapod a base plate is installed, which carries the jet, the optics, an APD for detection of fluorescence photons and an on-axis video microscope for alignment purposes. A detailed CAD-drawing of the base plate and the components is shown in figure 4.3. An equivalent photo-graphic image of the base plate and the pump laser beam hitting the jet is shown in the appendix in figure A.14.

The individual components and their functions are explained in the following:

- One motor tower consisting of three x,y,z translational motors with micrometer precision carries the APD. The APD is used to detect the fluorescence photons in X-ray fluorescence yield mode as described in chapter 4.1.9.
- An on-axis video microscope, consisting of a reflective objective (*Schwarzschild-objective* from Newport) and a CCD camera, allows to visualize the jet. Alternatively a fluorescent

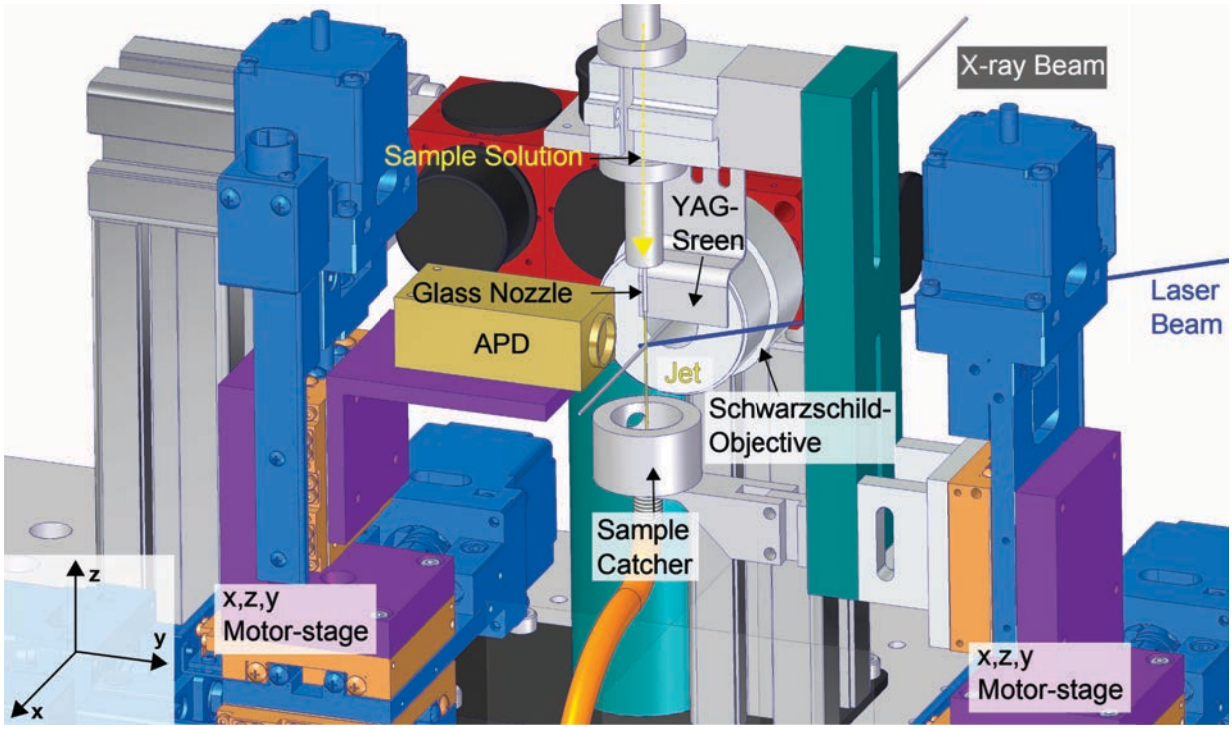

Figure 4.3.: *CAD-drawing of the components on the base plate. The X-ray beam passes a Schwarzschild-objective through a drill hole with* $1.5\ \mathrm{mm}$ *diameter (not visible under this angle) and hits the sample jet. The laser beam hits the jet at the same interaction point with an incident angle of about* $60\ ^{\circ}$ *(see also figure 4.5 d)). The Schwarzschild-objective generates a magnified image of the jet or of a Yttrium Aluminum Garnet (YAG) screen located at the focal point, into a CCD camera (for more details see text).*

Yttrium Aluminum Garnet (YAG) screen can be placed at the position of the jet, so that the video camera can be used for characterization and alignment of the laser and X-ray beams. The optical resolution of this setup is about $0.5\ \mu\mathrm{m}$.

- A second identical motor tower allows movement of the micro-jet system. The micro-jet is generated by pressing the sample solution through a glass nozzle with a pressure of several bar. The small opening of the nozzles allows for a laminar flow and a stable micro-jet. The nozzles are about $50\ \mathrm{mm}$ in length and have an outer diameter of about $1\ \mathrm{mm}$. Diverse types with different opening sizes are available. The inner lying channel with diameter between $230\ \mu\mathrm{m}$ and $500\ \mu\mathrm{m}$ narrows to the end and results in openings between $30\ \mu\mathrm{m}$ and $300\ \mu\mathrm{m}$ (depending on the type). The glass nozzles are fixed by a plastic ferrule to a *Swagelok system* and are in this way easily exchangeable. Figure 4.4 a) shows the glass nozzle mounted into the Swagelok adapter and in figure 4.4 b) a magnified image of the nozzle tip is shown.

- The jet pump (mzr-4605 HNP Mikrosysteme), shown in figure 4.2, delivers the sample solution from the reservoir through the circular flow system. The flow rate used in the experiment was about $1\ \mathrm{ml/min}$. The pump is a micro-angular gear pump in which two rotating gear wheels produce a small displacement volume of only $12\ \mu\mathrm{l}$. This pulseless pumping allows for constant flowing and stable jets.

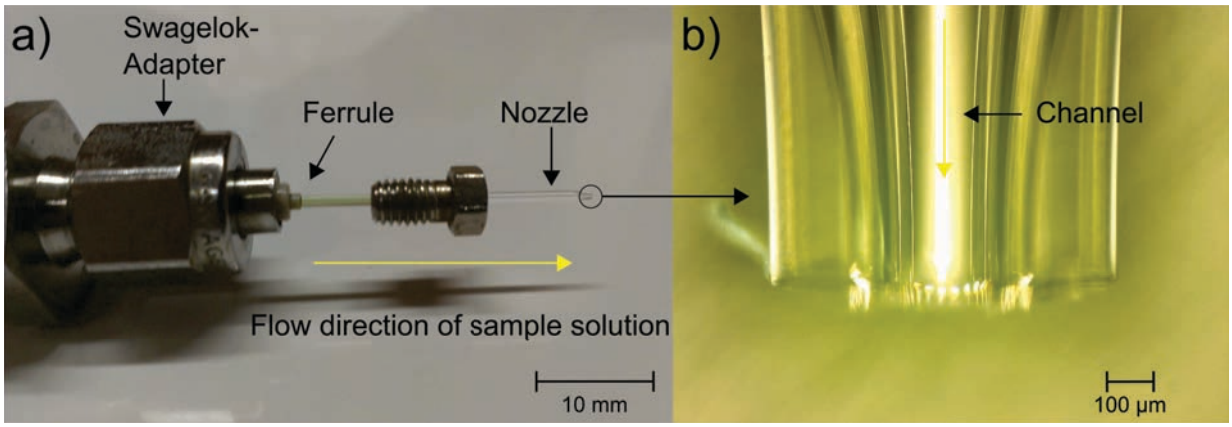

Figure 4.4.: *a) Glass nozzle mounted in swagelok adapter. b) Microscope image of a glass nozzle tip.*

4.1.4. Focusing and Characterization of Laser Beam

The laser system is placed at the beginning of the granite block and the laser beam is guided to the interaction point by mirrors. The last optical element is a lense mounted in an adjustable lense mount on top of the hexapod, which focuses the beam onto the jet. For geometrical reasons the laser beam hits the jet (respectively the YAG screen) with an incident angle of $90\ ^\circ - \alpha = 60\ ^\circ$ (see figures 4.3 and 4.5 d)). This causes a certain deformation of the laser focus image on the

screen in horizontal direction, which can be corrected mathematically by simple geometrical considerations. Figure 4.5 a) shows a video microscope image of uncorrected laser focus on the fluorescent YAG-screen located at the jet position. Along the black dashed lines a height profile was measured and fitted by a Gaussian functional form in order to extract the beam size. The spot size of the laser beam can be determined as

$$\begin{aligned} FWHM_{ver} &= 37.0\ \mu\mathrm{m} \\ FWHM_{hor} = FWHM_{hor}^{uncor} \cdot \sin(\alpha) &= 74.8\ \mu\mathrm{m} \cdot \sin(30\ ^\circ) = 37.4\ \mu\mathrm{m}. \end{aligned} \tag{4.1}$$

This laser focus setup was used for the XANES experiments with a $30\ \mu$m-jet. During the EXAFS experiments a jet with larger diameter was used (reasons are explained in the next section), and hence the laser spot size was increased to $110\ \mu$m x $110\ \mu$m (v x h).

4.1.5. Focusing and Characterization of X-ray Beam

The small jet requires to focus the X-ray beam to a size similar to the jet diameter. For X-ray beam focusing, compound refractive X-ray lenses [84, 85] were used, as described in chapter 2.6.6. For the measurements at the Ga-K-edge energy $E = 10367$ eV we used 25 Be lenses with $R = 0.2$ mm to obtain a $18\ \mu$m x $14\ \mu$m FWHM (v x h) focus in 1.20 m distance from the lens package at the jet position.

An image of the X-ray focus with the corresponding height profiles in horizontal and vertical direction is shown in figure 4.6. A drawback of X-ray lenses for XAFS is their chromaticity. In XAFS spectroscopy the energy is changed over a broad range of about 300 eV for XANES and $\gg 800$ eV for EXAFS. Due to the chromaticity the focus size of the X-ray beam changes as function of energy. Figure 4.7 shows CCD images of the X-ray focus on the YAG-screen located at the jet position for energies ranging from 10270 eV to 11070 eV. Such an energy range is typical for EXAFS measurements. The focus size strongly changes with energy, which make the X-ray lenses not the ideal focusing tool for EXAFS spectroscopy. From the images one can identify two main observations:

1. The focus size changes from $23.0\ \mu$m x $12.2\ \mu$m (v x h) at 10270 eV to $30.6\ \mu$m x $42.5\ \mu$m (v x h) at 11070 eV.

2. The shape of the beam changes. While at the starting energy of 10270 eV the vertical axis is elongated with respect to the horizontal axis this ratio goes into reverse with increasing energy.

The resulting problem is a changing X-ray photon flux on the sample jet, which negatively influences the signal-to-noise ratio during the measurements.

Modification of the XAFS Setup for EXAFS Measurements We conducted EXAFS measurements over a wider energy range of about 800 eV with refractive lenses, however, the results were not satisfying. Hence the X-ray optical setup was modified for EXAFS measurements over such an energy range. The refractive lenses were removed and the X-ray beam was focused

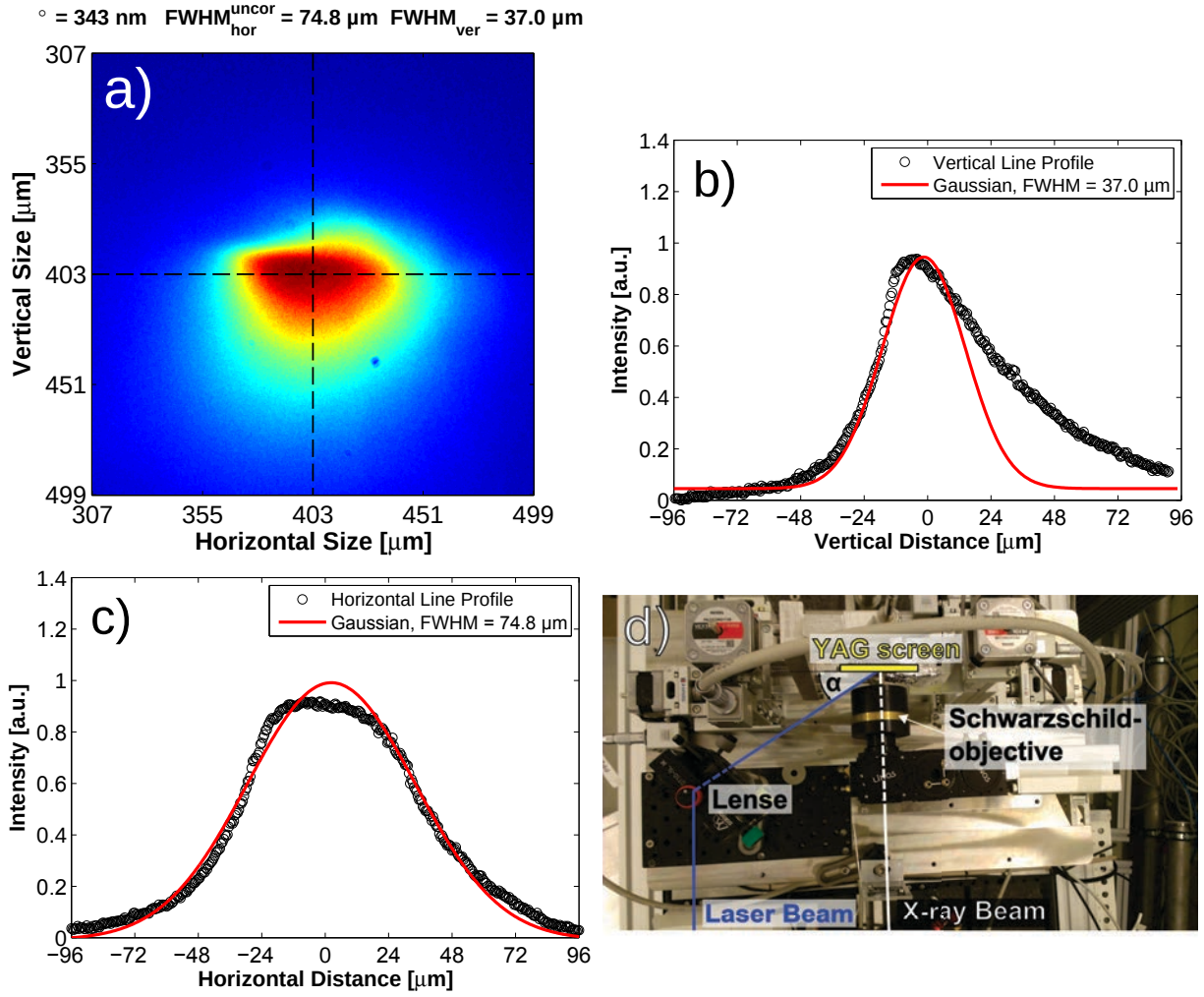

Figure 4.5.: *a) Video microscope image of the laser focus on the YAG-screen at the jet position. b) Vertical line profile of focus shown in a) with a* $FWHM_{ver}$ *of* $37.0\ \mu\mathrm{m}$*. c) Horizontal line profile of focus shown in a) with a* $FWHM^{uncor}_{hor}$ *of* $74.8\ \mu\mathrm{m}$*. d) Top view onto the base plate of the XAFS setup. The X-ray beam passes the Schwarzschild-objective of the video microscope and hits the YAG screen, located at the position, where the jet is placed during the measurements. The laser beam is focused by a lense in an adjustable lense mount and hits the YAG screen with an incident angle of* $90\,^\circ - \alpha = 60\,^\circ$*, where* α *is used as correction angle of the horizontal beam profile. The YAG screen in combination with the on-axis video microscope serve in this way as optical system for beam characterizations.*

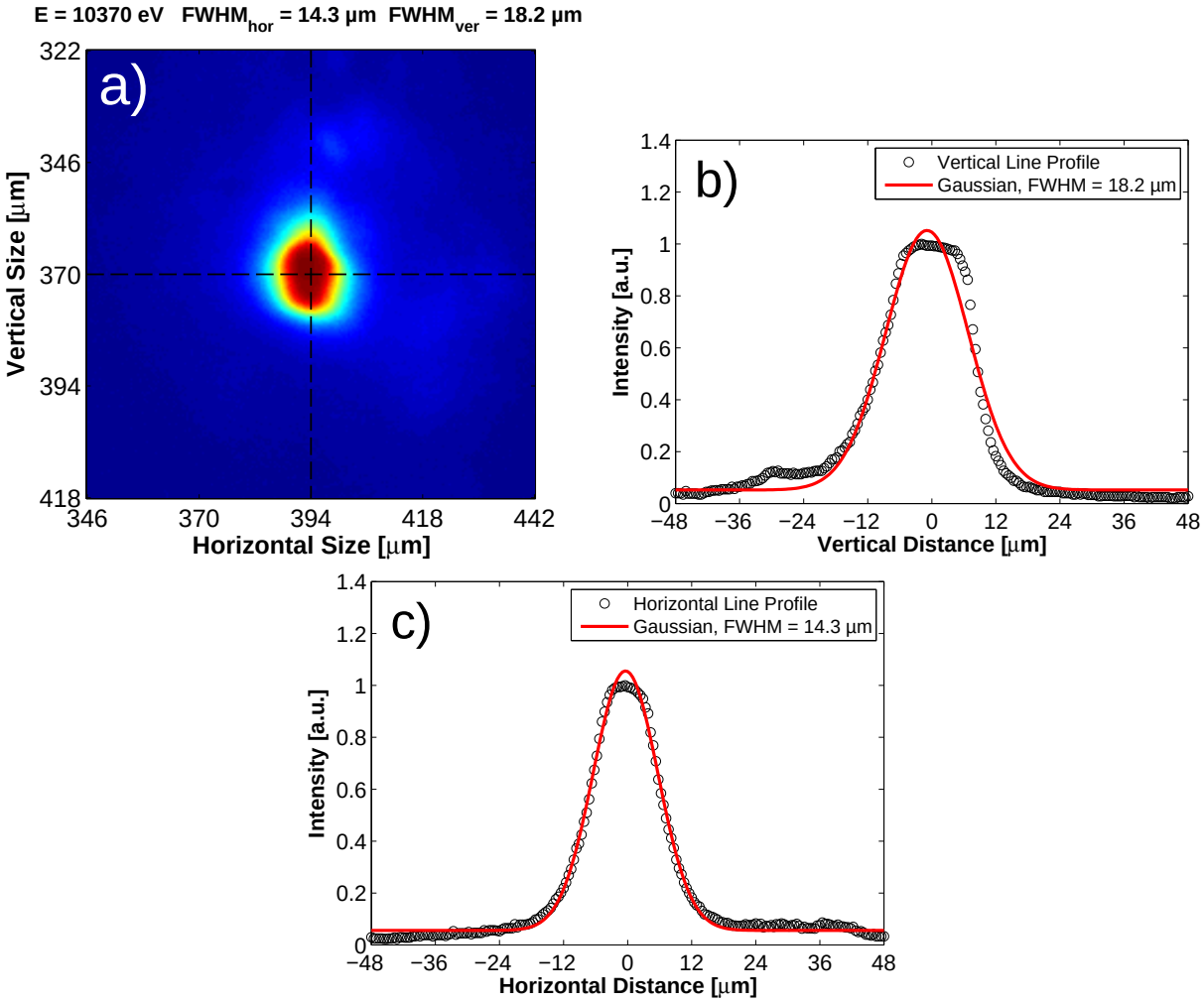

Figure 4.6.: *a) X-ray beam focus on the YAG-screen at the jet position for an energy of 10370 eV. b) Vertical line profile of focus shown in a) with a* $FWHM_{ver}$ *of* $18.2\ \mu\mathrm{m}$*. c) Horizontal line profile of focus shown in a) with a* $FWHM_{hor}$ *of* $14.3\ \mu\mathrm{m}$*.*

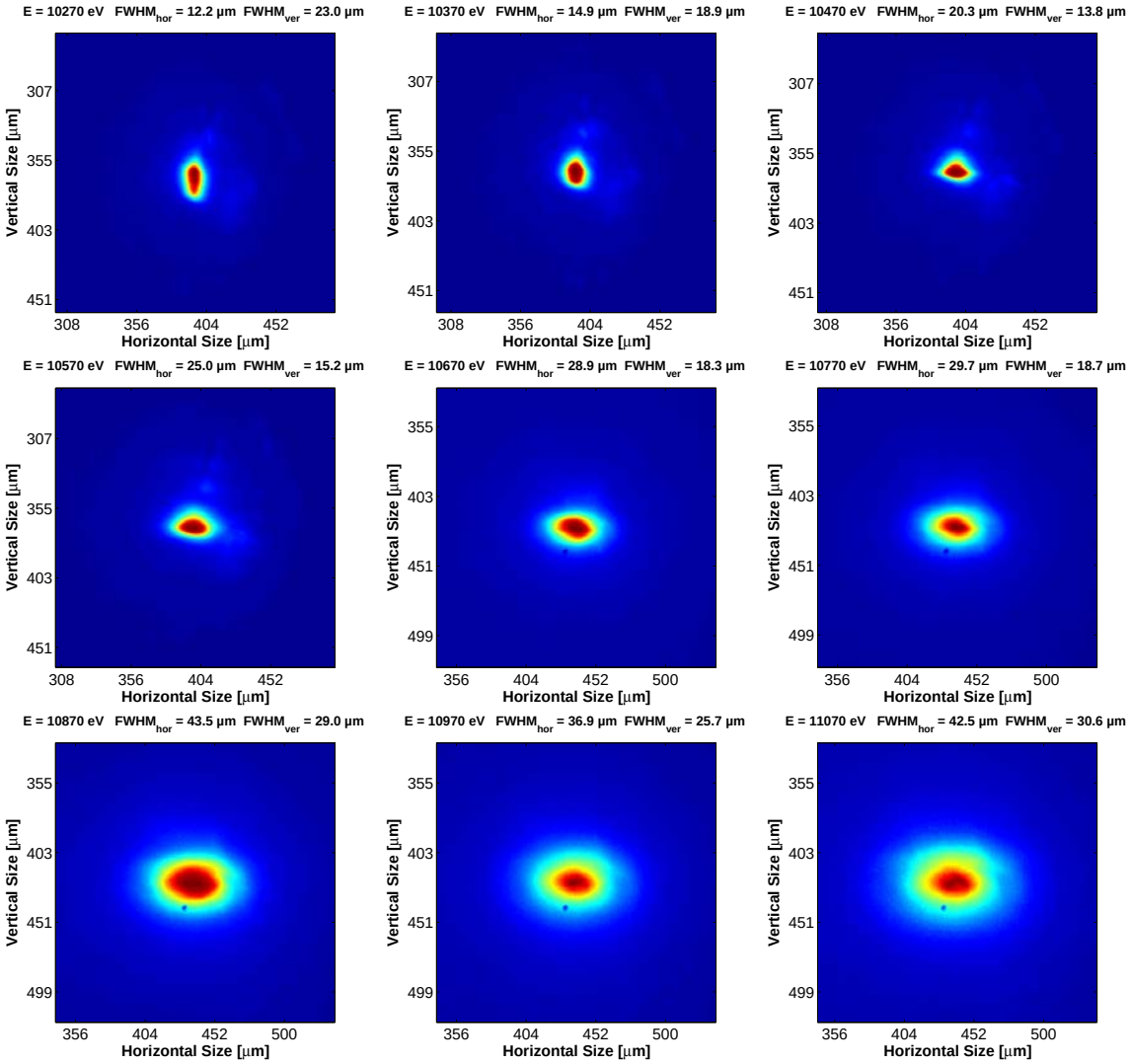

Figure 4.7.: *X-ray beam spots for energies ranging from* 10370 eV *to* 11070 eV *obtained at the jet position in* 1.20 m *distance from the lenses. The focus size changes from* 23.0 μm *x* 12.2 μm *(v x h) at* 10270 eV *to* 30.6 μm *x* 42.5 μm *(v x h) at* 11070 eV. *Beside the focus size also the beam shape is affected.*

by the KB mirrors, which are directly located behind the monochromator, to a size of 100 μm x 360 μm (v x h). The beam was then shaped by using a piezo-driven pinhole close to the micro-jet. In this way an X-ray beam with a focus size of 100 μm x 100 μm (v x h) was obtained, which was independent of the energy. To better fit the larger beam size a glass nozzle with a diameter of 70 μm instead of 30 μm as used for the XANES measurements was installed. As a consequence lower photoexcitation yields were obtained in this modified setup, but the same X-ray fluorescence count rates as in the XANES measurements could be maintained.

4.1.6. Spatial Overlap of Laser and X-ray Beams

A crucial requirement for pump-probe experiments is the spatial overlap of the laser and X-ray beams on the jet. Therefore, a precise alignment procedure needs to be performed before the start of the measurements. The following steps were taken: At first the X-ray beam was focused on the YAG-screen. Size and shape of the X-ray beam were optimized and characterized using the on-axis video microscope. Afterwards the jet was moved to the y,z focus plane of the X-ray (the coordinate system is depicted in figure 4.3). In order to find the ideal jet position with the highest fluorescence photon count rate, a so called jet-scan was performed where the APD signal was recorded as function of the jet-position in horizontal y-direction. A typical jet-scan plot of a 30 μm-jet is shown in figure 4.8. The plot represents the convolution of X-ray beam and jet and allows for an estimation of the jet width. To overlap the laser with the X-ray, we checked the X-ray beam position by moving the YAG screen to the jet-position and by marking the fluorescent spot on the camera image. Afterwards the jet was moved back in the beam. In this configuration the camera image shows the jet and the marked X-ray position. Since Gaq3 shows strong optical fluorescence, the jet fluoresces, where it is hit by the laser. This simplified the alignment of the laser and we adjusted the focus, so that the maximum fluorescence intensity was centered within the marked X-ray position on the jet. With this procedure a good spatial overlap was achieved.

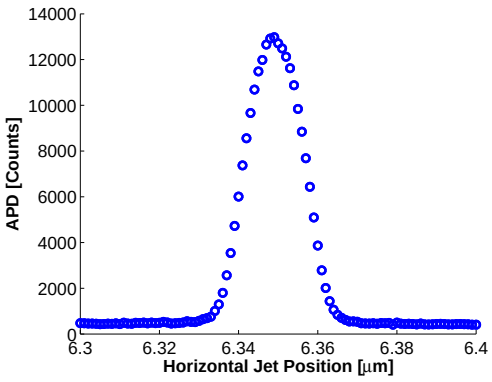

Figure 4.8.: *APD signal as function of the jet-position in horizontal direction. This scanning of the jet through the X-ray beam is used to find the ideal overlap. Furthermore it allows to determine the jet thickness as about* 30 μm *and shows the stability and symmetry of the jet.*

4.1.7. Temporal Overlap of Laser and X-ray Beams

Time resolved measurements also require temporal overlap of pump laser beam and X-ray probe beam. First, we performed a rough overlap by placing a fast photodiode at the jet position and recording the signals from both, the laser and the X-ray pulses on the same diode using a fast oscilloscope. The two pulses were adjusted in such way that the laser pulse arrived several hundred picoseconds before the X-ray pulse. This delay is small enough to assure that the transient signal is not fully decayed. Afterwards first pump-probe absorption spectra for ground and excited states were recorded. For the energy value at which the resulting transient spectrum $T_{EX}(E)$ shows a maximum, a delay-scan was recorded. Here, the $T_{EX}(E_0, t)$ was measured as function of the so far roughly adjusted time delay Δt. The overall time range was $12\ \mathrm{ns}$ with a step width of $50\ \mathrm{ps}$. This measurement allows for an optimal temporal overlap of laser pump and X-ray probe pulse and is shown in chapter 5.2.2.

4.1.8. Data Acquisition

A block scheme of the data acquisition process is shown in figure 4.9. The APD pre-amplifier

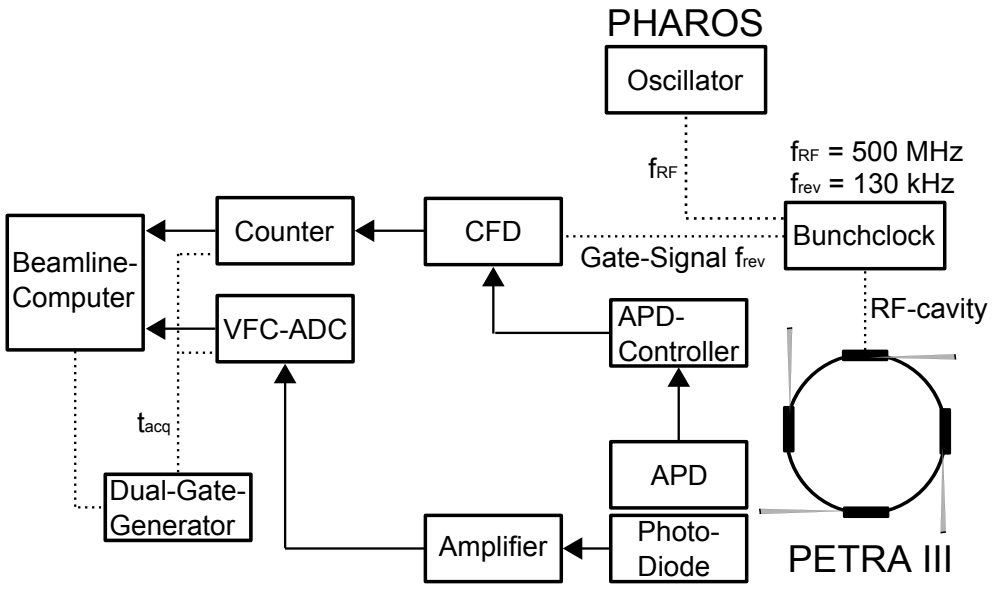

Figure 4.9.: *Block diagram of the data acquisition and synchronization processes (for details see text)*

converts the measured X-ray pulse intensity into a voltage. Typical pulse amplitudes from the APD head after the pre-amplifier are in the range of $-50\ \mathrm{mV}$ to $-400\ \mathrm{mV}$. This signal is amplified in the controller unit by a second amplifier with a gain factor of -8 resulting in a typical signal amplitude of $+400\ \mathrm{mV}$ to $+3.2\ \mathrm{V}$. A baseline restoration circuit removes any base line shift by a general offset of $200\ \mathrm{mV}$. The high bias voltage was set to $300\ \mathrm{V}$, which corresponds to about $80\ \%$ of the breakdown voltage. The APD was operated in *integral mode* where for every signal, which is above a low-level threshold an output-pulse is generated [102]. The signal (NIM) of the APD controller unit is led to a *Constant-Fraction Discriminator (CFD)* from Ortec

(www.ortec-online.com), which allows gating of the APD signal. The gate is defined by the PETRA III bunchclock, which delivers a bunch trigger signal with the bunch repetition frequency of $130\ \mathrm{kHz}$ and a width of $150\ \mathrm{ns}$. In 40 bunch mode the signal bunches have a temporal distance of $\approx 192\ \mathrm{ns}$. In this way only one of the 40 bunches is used for the experiments. The CFD selects a timing point on each input pulse independently from the pulse amplitude. The output pulse is generated for a point on the leading edge of the input pulse, which corresponds to $20\ \%$ of its maximum amplitude. Furthermore, a threshold discriminator allows for rejecting of low-level noise. The incoming signal is counted as 1 if the threshold is reached. Signals above the threshold are not further differentiated. This implies, that multi-photon events are counted as single-photon events. Hence the distance from sample to APD had to be adjusted in such way that the probability for single-photon events became maximum. The output signal from the CFD is further led to a counter, which counts the events occurring in a certain time window generated by a dual gate generator. The same gate is used to define the sample time for a Voltage-to-Frequency-Converter-Analog-to-Digital-Converter (VFC-ADC) [103]. This device digitizes the analog signal from a Si-photodiode S9724-019 from Hamamatsu Photonics (www.hamamatsu.com), which measures the flux of the X-rays near the sample position (in between an amplifier was used for the required amplification). In this way the counts from the APD and the flux from the Si-photodiode are

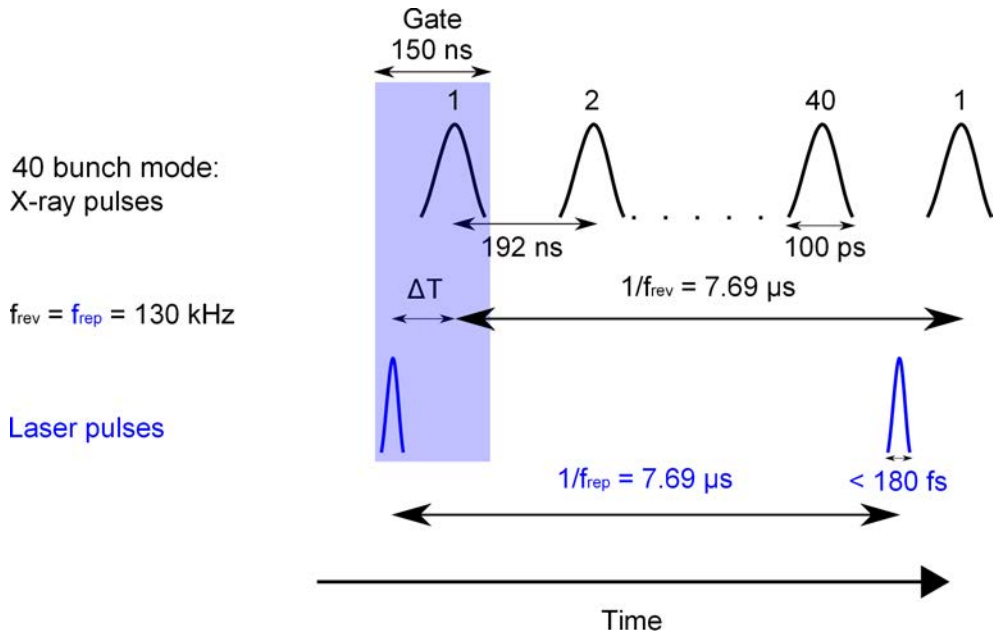

Figure 4.10.: *Timing structure of the X-ray and laser pulses. The laser pulse is synchronized to one of the 40 X-ray pulses within a timing gate for the data acquisition.*

measured within the same sample time t_{acq} and allow for normalization of the APD fluorescence signal to the flux of the incident X-ray photons. Thus fluctuations of the APD signal caused by lower flux e.g. at higher energies are corrected. The signals from the VFC and Counter were fed into the beamline computer and processed by the acquisition software. The acquisition time for the XAFS spectra was set to $t_{acq} = 16\ \mathrm{s}$. For each energy step the unpumped ground state signal

I_{fl}^{unpump} (laser off) was measured for 16 s and afterwards the pumped excited state signal I_{fl}^{pump} was measured for the same time. For the ground state signal the laser was blocked by a laser shutter based on a relay switch. In figure 4.10 the synchronization of the of X-ray pulses with the laser pulses is illustrated.

4.1.9. Measurement Modes

X-ray Transmission Mode

XAFS measures the absorption coefficient $\mu(E)$ which can be performed in different modes. The transmission mode is the most straightforward one since it directly measures $\mu(E)$, present in the Lambert-Beer Law 2.1. In an experiment the incident intensity I_0 and the transmitted intensity I of the X-ray beam are measured before and after the sample simultaneously and then $\mu(E)$ can be calculated by the following equation:

$$\mu(E)d = -\ln\left(\frac{I}{I_0}\right) \tag{4.2}$$

X-ray Fluorescence Yield Mode

For thin samples or lower concentrations i.e. $\mu(E)d \ll 1$, measuring the X-ray fluorescence yield is the preferred method. The fluorescence signal is proportional to the absorption coefficient and it corresponds to

$$I_{fl} \propto I_0 - I_0 \cdot e^{-\mu(E)d} \tag{4.3}$$

For $\mu(E)d \ll 1$ the term $e^{-\mu(E)d}$ is equal to $1 - \mu(E)d$ and it follows

$$\mu(E)d \propto \frac{I_{fl}}{I_0}. \tag{4.4}$$

In a fluorescence yield measurement the radiation emitted by an electron dropping down to fill the core hole is measured. Since a sample usually contains more than only one element, the signal includes the fluorescence line of interest and fluorescence lines from other elements. Moreover, it includes elastically and inelastically scattered X-rays. To suppress unwanted fluorescence lines and the scattered photons, an energy discrimination has to be applied. This can be done by using filters or by filtering the signal electronically after detection. In this experiment the latter was conducted. Equation 4.4, where I_{fl} is proportional to $\mu(E)$, is a simplification. In fact I_{fl} has to be corrected for geometrical considerations and fluorescence quantum efficiencies. The experimental setup for the X-ray fluorescence yield geometry of a liquid micro-jet is depicted in figure 4.11. Fluorescence photons are isotropically emitted in contrast to the scattered photons, which are not isotropically emitted, because the synchrotron radiation is polarized in the plane of the synchrotron. To minimize these scattering contributions, the fluorescence detector is placed perpendicular to the incident beam axis in the synchrotron plane. In this case the polarization factor for Thomson Scattering becomes 0. In the following the number of fluorescence photons I_{fl} emitted from the jet and reaching the APD detector for an incident X-ray beam with intensity

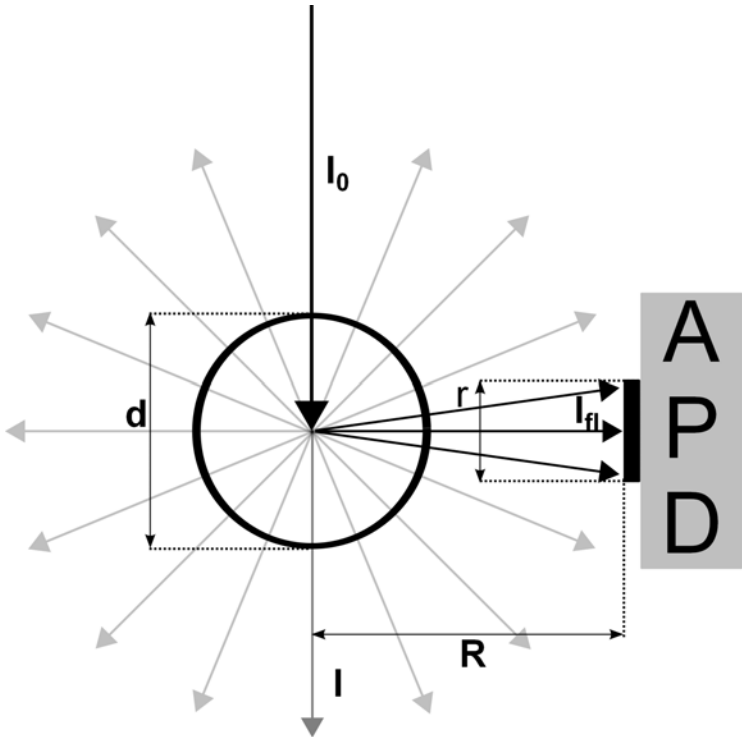

Figure 4.11.: *Top view onto the experimental setup for X-ray fluorescence yield geometry. The profile of the micro-jet with diameter $d = 30\ \mu\mathrm{m}$ is depicted as black circle. The X-ray beam with intensity I_0 hits the jet. While a huge fraction I from the incident intensity I_0 is transmitted through the sample volume, another fraction is absorbed according to Lambert-Beer's law and causes emission of fluorescence photons, which are isotropically emitted. The APD detector, located in a distance R with an angle of $90\ ^\circ$ with respect to the X-ray beam, detects only a small fraction of these photons.*

I_0 at the Gaq3 K-edge energy is calculated. This value will be compared to the measured value from the experimental spectrum. This allows answering the question of how well the experiment fits to theoretical expectations. At first the number of photons from a single bunch for an acquisition time of $t_{acq} = 16\ \mathrm{s}$ for the APD is considered. The intensity I_0 of X-rays at the K-edge energy incident on a Si-diode of given characteristics can be calculated via [104]:

$$I_0 = I_{cur} \frac{E_{eh}}{eE\left[1 - e^{-A_{pe} t_{Si} \rho_{Si}}\right]}, \tag{4.5}$$

where I_{cur} is the photo-induced current, Q is the charge created in the Si-diode by the incident X-rays of energy E, A_{pe} is the photoelectric cross section of silicon, e is the electronic charge, E_{eh} is the energy required for creation of an electron-hole pair, t_{Si} is the diode thickness and ρ_{Si} the density of silicon. This formula is included in an online-tool, available at [105]. This online-calculator, which only requires the X-ray energy and the thickness of the Si-diode to be specified, yields a flux of $1.35 \cdot 10^{12}$ photons per second. Since PETRA III was running in 40 bunch mode

during the experiment, this value has to be divided by 40 and multiplied by $t_{acq} = 16\,\mathrm{s}$ to obtain the number of photons of a single bunch per 16 seconds. Thus the incident intensity is $I_0 = 5.4 \cdot 10^{11}$. The detector sees only a small fraction of the X-rays emitted in a solid angle of 4π. The number of X-ray photons recorded by the detector depends on the distance R from the active area of the detector to the sample as well as on the active area radius r_{APD}. The active area is defined by an aperture in the shielding, which is directly placed in front of the APD window to reduce scattered radiation. The solid angle can be calculated via [79]:

$$\Omega = \frac{\text{Active Area}}{4\pi R^2} = \frac{\pi r_{APD}^2}{4\pi R^2} \tag{4.6}$$

Gawelda et al. calculated the fluorescence signal I_{fl}, which is emitted from a liquid micro-jet as [79]:

$$I_{fl} = \frac{I_0 \mu_A(E) \epsilon_A}{\mu_T + \mu_{fl}} \{1 - e^{-(\mu_T + \mu_{fl})d}\}, \tag{4.7}$$

where $\mu_A(E)$ is the absorption coefficient of the absorbing atom, μ_T is the total absorption coefficient including the solvent, atoms from the ligand and counter-ions at the incident beam energy E and μ_{fl} stands for the absorption coefficient at the fluorescence photon energy E_f. All three absorption coefficients μ_A, μ_T and μ_{fl} represent linear absorption coefficients for gallium at the K-edge at $E = 10367\,\mathrm{eV}$, for Gaq3 at the edge energy of the experimental spectrum at $E = 10373\,\mathrm{eV}$ and for Gaq3 at the main emission line of gallium at $E_f = 9251\,\mathrm{eV}$. The linear absorption coefficient $\mu_l[\,\mathrm{cm}^{-1}]$ is related to the mass absorption coefficient $\mu[\,\mathrm{cm}^2/\mathrm{g}] = \mu_l \rho$ via the density ρ. The absorption coefficients were computed via the program *XOP* [106, 107] by providing the densities of gallium and Gaq3 in the jet sample volume. The values computed were $\mu_A(10367\,\mathrm{eV}) = 0.78\,\mathrm{cm}^{-1}$, $\mu_T(10373\,\mathrm{eV}) = 0.82\,\mathrm{cm}^{-1}$ and $\mu_{fl}(9521\,\mathrm{eV}) = 0.21\,\mathrm{cm}^{-1}$. $\epsilon(A)$ in formula 4.7 is the fluorescence yield efficiency per unit solid angle Ω. The probability for the occurrence of fluorescence competing with other de-excitation processes like Auger effect is given by the fluorescence yield (FY). This represents the probability of filling a core hole through de-excitation of an electron from a higher shell by emission of a fluorescence photon. For gallium at the K-edge the fluorescence yield is $FY \approx 0.5$ [64]. The solid angle can be calculated by using equation 4.6 as $\Omega = 3.52 \cdot 10^{-4}$, whereas the jet distance to the APD during the experiment was $R = 40\,\mathrm{mm}$ and the radius of the active area is $r_{APD} = 1.5\,\mathrm{mm}$. For these values ϵ_A can be calculated as $\epsilon_A = 1.76 \cdot 10^{-4}$. Finally all values for parameters appearing in equation 4.7 are given and I_{fl} can be determined by integration over the jet-diameter d irradiated by the X-ray. Because APDs have a specific energy dependent quantum efficiency QE_{APD}, the number of photons has to be corrected for this quantity. For the silicon APD used in this experiment the QE_{APD} is 0.70 for $\approx 10\,\mathrm{keV}$, so that finally the number of fluorescence photons counted by the APD at the edge energy is:

$$I_{fl} = 1.39 \cdot 10^5\ \text{Photons} \tag{4.8}$$

In the experimental spectrum the number of measured counts is $1.88 \cdot 10^5$ for a monochromator energy of $10373\,\mathrm{eV}$. So it can be concluded that the theoretical considerations for the measure-

ment of XAFS spectra in fluorescence yield mode agree well with the experimental conditions of the XAFS setup.

4.2. Optical Spectroscopy

Absorption and emission spectra allow the characterization of the electronic system (see chapter 1.2) and the determination of the extinction coefficient of a sample. Optical spectroscopy also serves as an easy and reliable method to investigate differences between the different phases of a sample molecule. The optical experiments presented in this chapter were performed in order to obtain the following information:

- Determination of the extinction coefficient of Gaq3 in benzyl alcohol for the calculation of the photoexcitation yield.
- Determination of the optimal excitation energy, which is the maximum of the UV-Vis absorption spectrum.
- Characterization of the electronic states of the Gaq3 molecule.
- Revealing differences between diverse phases of Gaq3 (solution, powder, crystal, film).

4.2.1. UV-VIS Absorption and Fluorescence Spectra of Alq3 and Gaq3 in Solution

The emission spectra of the solutions were measured using a multimode plate reader M1000[1] from Tecan (www.Tecan.com). This monochromator based reader allows absorbance as well as fluorescence measurements and offers thereby wavelength selection without the need for optical filters. The measurement is performed by scanning a ca. $6\ \mathrm{cm}$ x $10\ \mathrm{cm}$ sized transparent plate containing multiple vessels, whereas each of them can be filled separately by sample solution. Each of the vessels is illuminated from top with the detector located beneath the plate. In this way a high number of sample solutions can be measured automatically within one scan period. For an absorption spectrum the wavelength is selected and tuned by the monochromator, whereas for each wavelength an absorption value is recorded separately. In figure 4.12 the UV-VIS spectrum and the corresponding fluorescence spectrum of Gaq3 dissolved in benzyl alcohol are plotted together. Gaq3 shows one broad absorption peak in the UV region centered at $\lambda_{abs} = 382\ \mathrm{nm}$ indicating an electronic $\pi \rightarrow \pi^*$ transition as discussed in chapter 1.3.2. In this an electron is moved from the HOMO to the LUMO level located on the quinoline-ring and a ligand localized excited state is formed [108, 21, 31]. This excited state decays under emission of broad fluorescence peak with the maximum located at $\lambda_{ex} = 546\ \mathrm{nm}$. The Stoke's shift of $164\ \mathrm{nm}$ is relatively large and on the one hand it indicates the existence of vibrational electronic states of the excited state and on the other hand it can be thought to arise from significant structural differences between the S_0 and S_1 state [28]. The black vertical arrow on the left side marks

[1] Courtesy of EMBL, Hamburg.

the pump wavelength $\lambda_{pump} = 343$ nm, which was used for the excitation of the sample during the pump-probe XAFS experiments. This wavelength corresponds to the third harmonic of the pump laser and does not optimally match to the $\pi \rightarrow \pi^*$ transition of the sample. This means the sample could have been pumped more efficiently during the XAFS experiments, if the laser wavelength could be tuned. The shorter wavelength means that more energy was deposited into the sample solution so that in this case an excitation to the higher vibrational levels of the S_1 excited state is probable. In order to analyze the influence of the central absorber atom on the

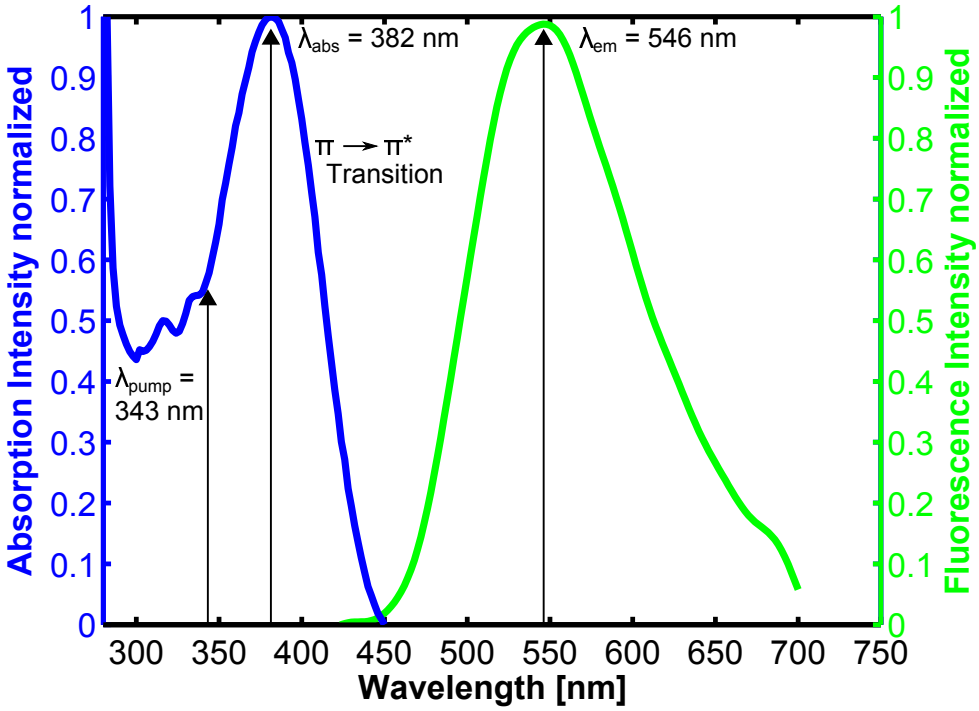

Figure 4.12.: *Absorption spectrum (blue) and fluorescence spectrum (green) of Gaq3 dissolved in benzyl alcohol. λ_{pump} marks the wavelength of the pump laser beam, used for the XAFS experiments. λ_{abs} corresponds to the absorption maximum of the $\pi \rightarrow \pi^*$ transition. λ_{em} corresponds to the fluorescence maximum. The difference of λ_{abs} and λ_{em} means a Stoke's shift of* 164 nm *for Gaq3 in benzyl alcohol.*

electronic energy states, absorption and emission spectra were also measured for Alq3 (see figure 4.13). In order to analyze the influence of the solvent on the optical properties of Gaq3 and Alq3, absorption and fluorescence spectra were also measured for the solvents DMSO and DMF. The plots are depicted in figure 4.14. Table 4.1 lists the wavelength for the maximum of the absorption band λ_{abs} and the wavelength for the maximum of the emission band λ_{em} as well as the Stoke's shift. λ_{abs} and λ_{ex} for Gaq3 dissolved in DMF are in very good agreement with other experimentally determined values: Humbs et al. investigated photoluminescence properties of Gaq3 in DMF and determined the lowest absorption band to $\lambda_{abs} = 385$ nm, while the emission band maximum is located at $\lambda_{em} = 549$ nm [21]. The corresponding spectra of Humbs et al. for Alq3 dissolved in DMF show absorption centered at $\lambda_{abs} = 379$ nm and an emission peak

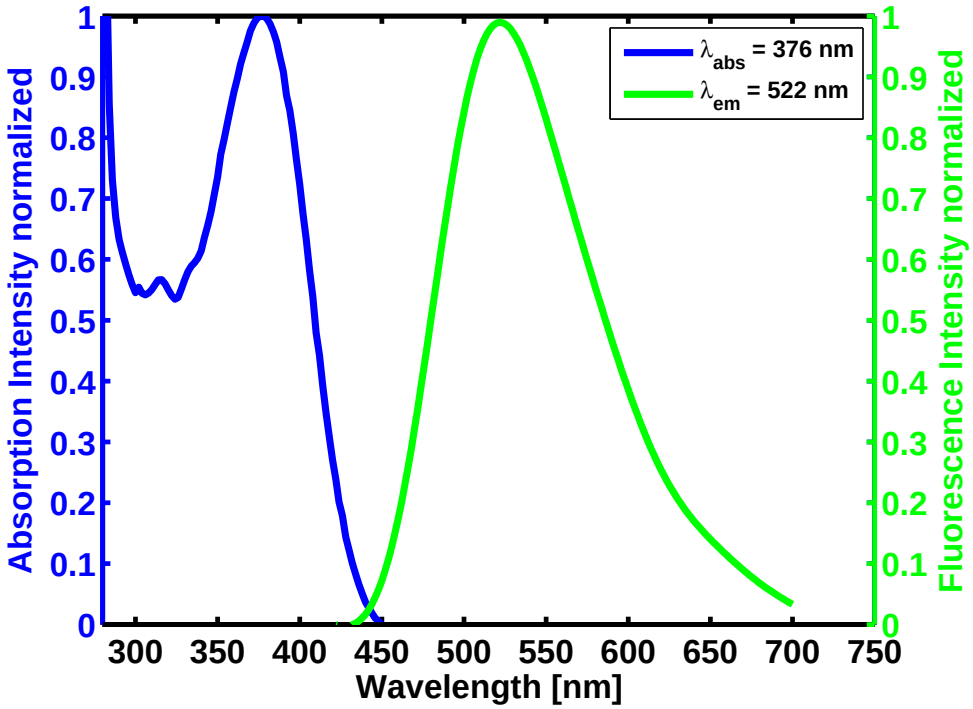

Figure 4.13.: *Absorption spectrum (blue) and fluorescence spectrum (green) of Alq3 dissloved in benzyl alcohol.*

Table 4.1.: *Experimentally derived λ_{abs}, λ_{em} and Stoke's shift for Gaq3 and Alq3 dissolved in benzyl alcohol, DMSO and DMF.*

Gaq3

Solvent	λ_{abs}	λ_{em}	Stoke's Shift
Benzyl alcohol	382 nm	546 nm	164 nm
DMSO	388 nm	550 nm	162 nm
DMF	388 nm	548 nm	160 nm

Alq3

Solvent	λ_{abs}	λ_{em}	Stoke's Shift
Benzyl alcohol	376 nm	522 nm	146 nm
DMSO	386 nm	526 nm	140 nm
DMF	386 nm	524 nm	138 nm

at $\lambda_{em} = 526$ nm. Even if the shifts between absorption and emission bands of the different solvents are small, they indicate that the solvent has some impact on the energetic states of the Gaq3 and Alq3 molecules. This is discussed in detail in chapter 6.1.1. Comparison of the Gaq3 and Alq3 absorption and fluorescence spectra reveal a blue shift of Alq3 spectra with respect to Gaq3 spectra, which confirms the impact of the central metal atom on the electronic structure of the Mq3 molecule.

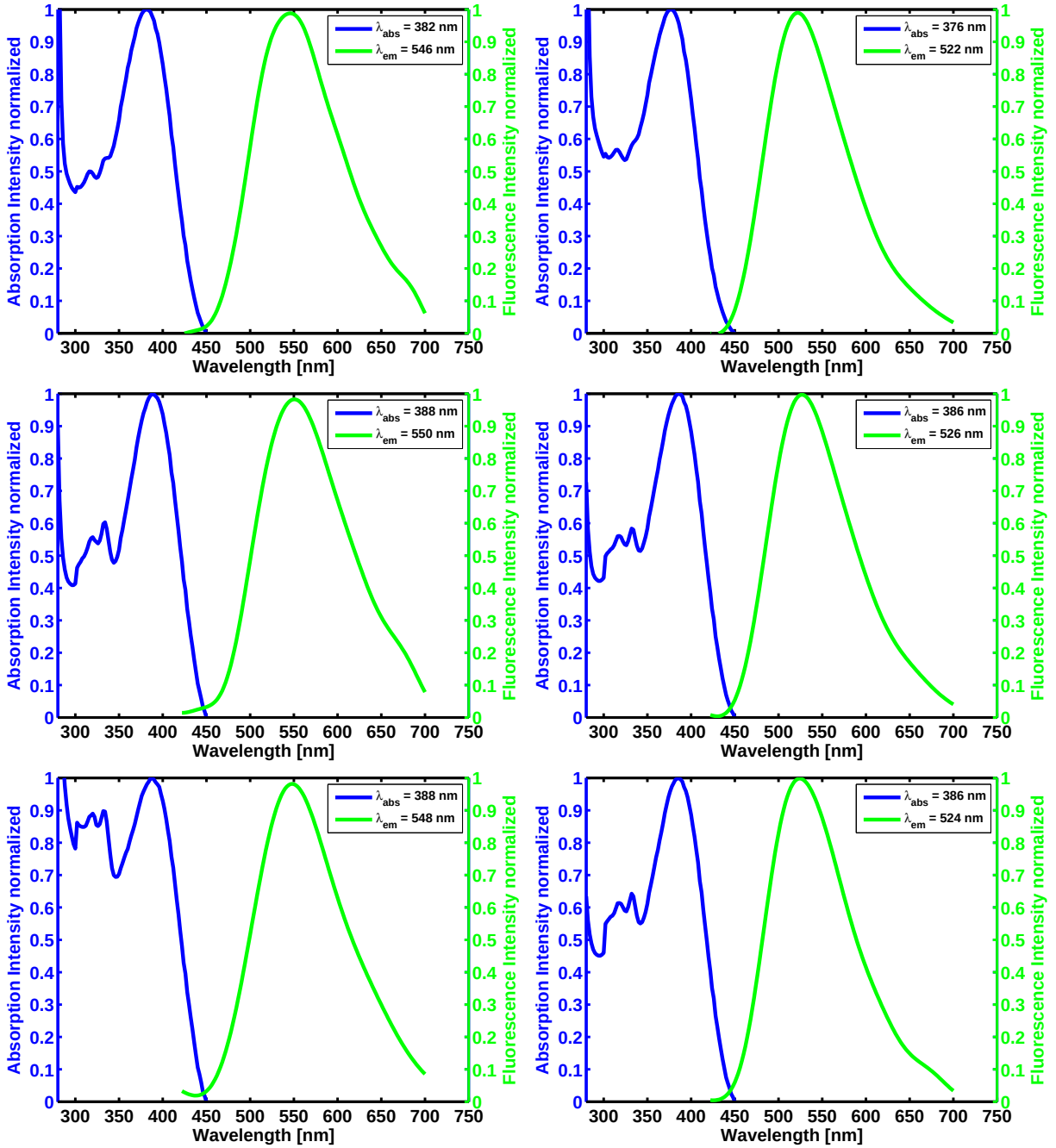

Figure 4.14.: *UV-VIS (blue) and fluorescence spectra (green) of Gaq3 (left column) and Alq3 (right column) dissolved in benzyl alcohol, DMSO, and DMF (from top to bottom).*

4.2.2. Extinction Coefficient of Gaq3 in Benzyl Alcohol

In order to determine the extinction coefficient of Gaq3 in benzyl alcohol, absorption spectra for different Gaq3 concentrations were recorded. These UV-VIS absorption spectra were performed with a commercial UV-VIS photospectrometer (Shimadzu UV 6700). The working principle is based on on a cuvette system, where the cuvette of defined width (usually $1\ \mathrm{cm}$) is irradiated by a broadband light source from the side. This principle is advantageous and promises more accurate results in comparison to the plate reader setup where the solution is illuminated from the top and thus the thickness of the sample solution is less well defined due to the meniscus effect. For photospectrometric analysis the sample is dissolved in a solvent and placed in the cuvette which is irradiated by a broadband light source. By measuring the intensities before (I_0) and after (I) the cuvette, the absorption coefficient α can be calculated according to Lambert-Beer's law [62]:

$$I = I_0 \cdot e^{-\alpha \cdot d} \tag{4.9}$$

In case of a liquid or a gas, the absorption coefficient α can be written as the product of a molar absorptivity ϵ, which is also called extinction coefficient, and the molar concentration c of the absorbing species in the material. In this way equation 4.10 can be written as [15]:

$$I = I_0 \cdot e^{-\epsilon \cdot c \cdot d} \tag{4.10}$$

The absorption or extinction is then[2]:

$$A = -\ln\left(\frac{I}{I_0}\right) = \alpha \cdot d = \epsilon \cdot c \cdot d \tag{4.11}$$

This equation implies that absorption and concentration are linearly correlated by the extinction coefficient. This way it is possible to determine the extinction coefficient for a given thickness d of the sample by measuring the absorption for different concentrations of the sample. In spectrophotometry d is defined by the width of the cuvette which is usually $10\ \mathrm{mm}$. The concentrations are expressed as mole fraction (mol/L). Extinction and absorption coefficients have the same units: $L \cdot mol^{-1} \cdot cm^{-1}$.

In figure 4.15 the optical UV-VIS absorption spectra of Gaq3 dissolved in benzyl alcohol are shown. Since we are interested in the $\pi \rightarrow \pi^*$ transition, only the first broad absorption peak is shown here. Spectra were recorded from Gaq3/benzyl alcohol solutions with different concentrations. In order to determine the wavelength dependent extinction coefficient ϵ, the absorption values A for the wavelength $\lambda_{pump} = 343\ \mathrm{nm}$ used for the pump-probe XAFS experiments (taken from figure 4.15) were plotted separately as function of the Gaq3 concentration in benzyl alcohol c as shown in figure 4.16. The experimental data (blue circles) can be fitted by a linear regression line, whose slope is $\epsilon \cdot d$. The width of the cuvette used in the photospectrometer is $d = 1\ \mathrm{cm}$ and so the extinction coefficient can be directly determined to $\epsilon = 2851\ \mathrm{L \cdot mol^{-1} cm^{-1}}$.

[2]Sometimes, for example for light absorption in a liquid, also the decadic logarithm is used, so one has to pay attention to the different base conventions.

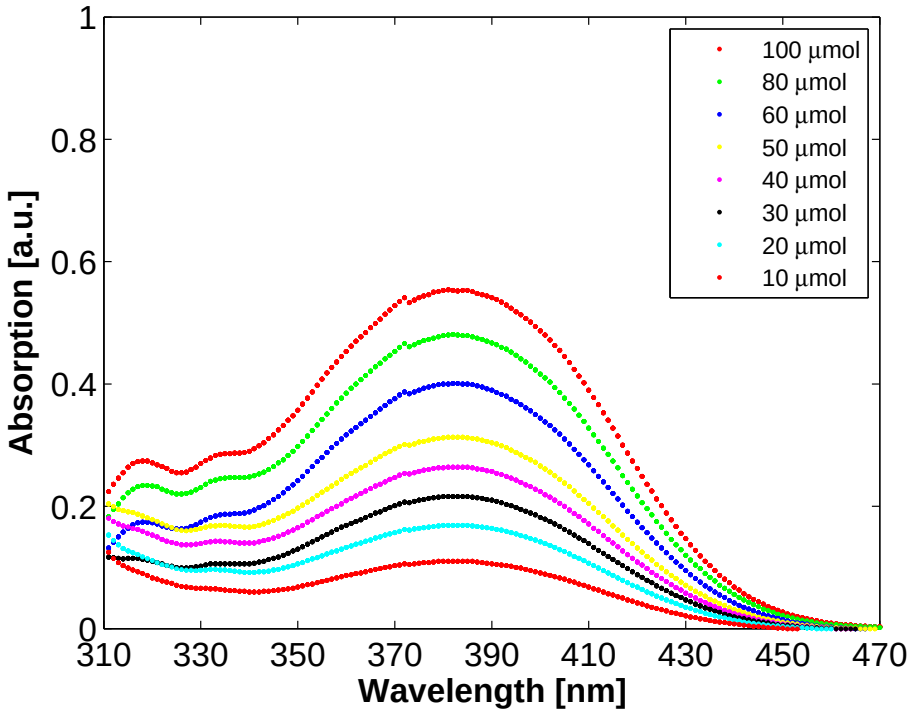

Figure 4.15.: *UV-VIS Absorption spectra of Gaq3 in benzyl alcohol for different concentrations.*

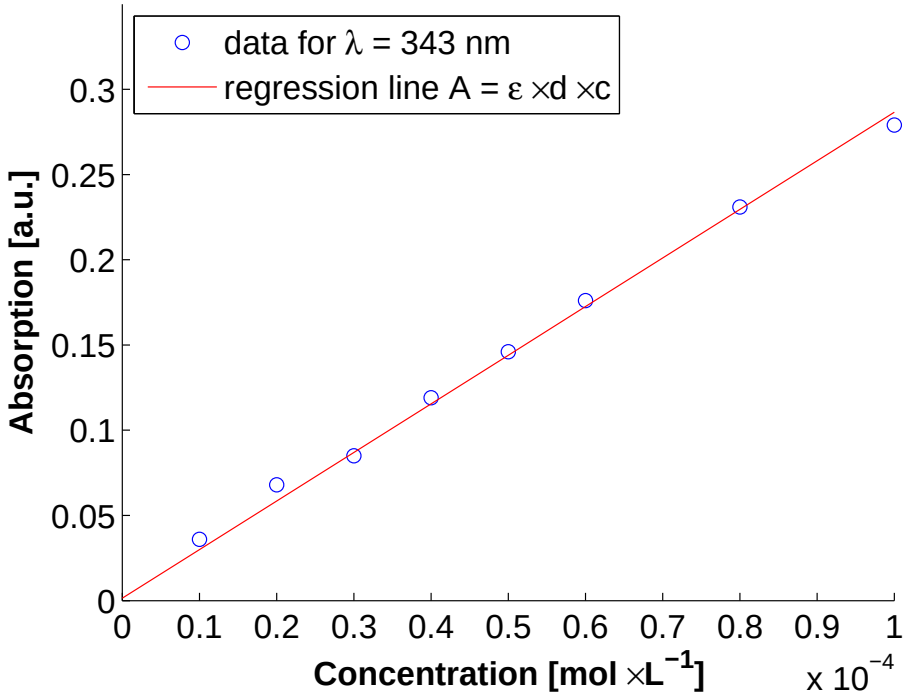

Figure 4.16.: *Absorption for a wavelength of* $\lambda = 343$ nm *as function of the Gaq3 concentration in benzyl alcohol. The extinction coefficient is determined from the slope of the linear fit function.*

4.2.3. Fluorescence Spectra of Different Phases of Gaq3

The photoluminescence properties of Gaq3 were investigated for different phases, which are powder, film and crystal. The powder form is the form, in which Gaq3 is purchased by the chemical distributor ABCR (www.abcr.de). The thin films were produced by vapor deposition as described in chapter 3.2. The crystals were grown by techniques presented in chapter 3.3. For the fluorescence measurements of these samples the following experimental setup was used: The sample was illuminated by a blue laser diode with wavelength $\lambda_{ex} = 405\ \mathrm{nm}$, which was focused onto the sample. The fluorescence was collected by using a microscope objective which was aligned in a $90\ ^\circ$ angle with respect to the optical axis of the incident laser beam. Adjusting the focal point of the objective into the small illuminated part of the sample reduced any contributions from scattering light. The fluorescence light was collimated and led into the spectrometer via a glass fiber. In figure 4.17 the fluorescence spectra of Gaq3 are shown for powder, film and crystal. The spectra of the the three phases show small but clear differences. The film sample exhibits

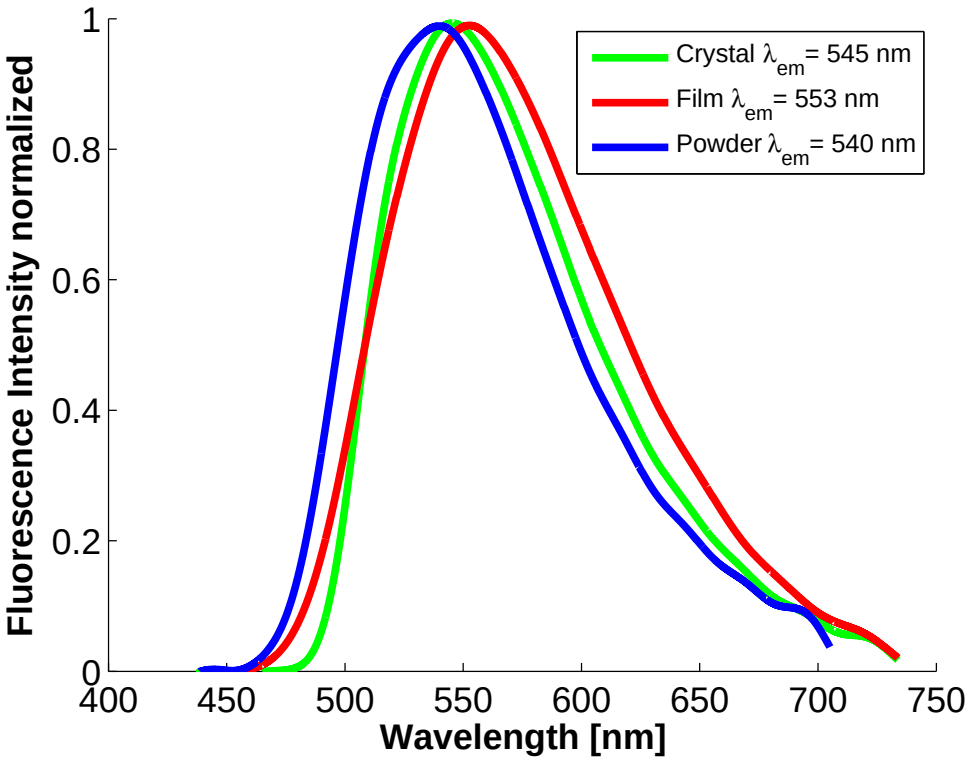

Figure 4.17.: *Fluorescence emission spectra of Gaq3 in form of crystal, film, and powder show shifted fluorescence spectra.*

redshifted emission and the emission maximum of the crystalline sample lies between those of powder and film. The emission wavelengths are listed in table 4.2. Recalling the emission maximum of Gaq3 dissolved in benzyl alcohol solution of $546\ \mathrm{nm}$ it is in the same region as emission from the crystal.

Table 4.2.: *Experimentally derived λ_{em} for Gaq3 in different phases.*

Solvent	λ_{em}
Powder	540 nm
Solution (benzyl alcohol)	546 nm
Crystal	545 nm
Film	553 nm

4.2.4. Calculation of the Photoexcitation Yield

In this section the photoexcitation yield f is calculated using equation 2.22, introduced in chapter 2.5. For the calculation at first the parameters used in the XANES experiments have to be identified. The extinction coefficient of Gaq3 in benzyl alcohol was determined by photospectrometric analysis to be $\epsilon = 2851\ \mathrm{L \cdot mol^{-1} cm^{-1}}$, as presented in chapter 4.2.2. Instead of the extinction coefficient the optical cross section σ_{opt} is appearing in equation 2.22. The two quantities are related by Avogadro's number $N_A = 6.02 \cdot 10^{23}\ \mathrm{mol^{-1}}$, which gives the number of constituent particles in one mole of a substance, [3]:

$$\sigma_{opt} = \frac{2303 \cdot \epsilon}{N_A} = 3.81 \cdot 10^{-21} \cdot \epsilon\ \mathrm{cm^2}. \tag{4.12}$$

Hence, the optical cross section σ_{opt} is $1.09 \cdot 10^{-17}\ \mathrm{cm^2}$. The laser focus was characterized by using the YAG-screen and the on-axis camera as described in chapter 4.1.4 and is 37 μm x 37 μm (v x h). The pump laser power at the jet position was determined by using a power meter. Its maximum value was $882\ \mathrm{mW}$. For a repetition rate of $130\ \mathrm{khz}$ this relates to a pulse energy E_{pulse} of about $6.78\ \mu\mathrm{J}$. The energy of a single photon is given by the Planck relation

$$E_{\text{photon}} = h \cdot \frac{c}{\lambda}, \tag{4.13}$$

where $h = 6.626 \cdot 10^{-34}$ is the *Planck's constant*, c is the speed of light and λ is the photon's wavelength. In case of the excitation wavelength $\lambda_{abs} = 343\ \mathrm{nm}$, the energy E_{ph} is $5.79\ \cdot 10^{-19} J$. Thus the number of photons per pulse N^{ph}_{pulse} can be calculated via

$$N^{ph}_{pulse} = \frac{E_{pulse}}{E_{ph}} = 1.17 \cdot 10^{13}, \tag{4.14}$$

whereas the maximum pulse power of $6.78\ \mu\mathrm{J}$ was used here. The pump volume is defined by the fraction of the jet, which is illuminated by the laser (see figure 2.7). The jet has a diameter of $d_{jet} = 30\ \mu\mathrm{m}$. In this way the sample volume is approximately a cylindrical fraction of the jet with diameter d_{jet} and the height h of the laser focus corresponding to its $FWHM_{ver} = 37\ \mu\mathrm{m}$.

$$V_{ex} = \pi \cdot \left(\frac{d_{jet}}{2}\right)^2 \cdot h = 2.12 \cdot 10^4\ \mu\mathrm{m}^3 = 2.12 \cdot 10^{-11}\ \mathrm{L}. \tag{4.15}$$

Since the laser focus is slightly larger than the jet diameter, not all of the photons N_{pulse}^{ph} hit the jet. In order to precisely determine the number of photons N_0^{ph} incident on the jet, a gaussian distribution for N_{pulse}^{ph} was accounted and integrated over the jet-diameter. For a concentration c_{sam} of the Gaq3 sample solution of $0.0498\ \mathrm{mol \cdot L^{-1}}$ the number of Gaq3 molecules in V_{ex} is

$$n_{sam} = c_{sam} \cdot V_{ex} = 0.0498\ \mathrm{mol \cdot L^{-1}} \cdot 2.12 \cdot 10^{-11}\ \mathrm{L} = 1.06 \cdot 10^{-12}\ \mathrm{mol}. \tag{4.16}$$

With the Avogadro's number $N_A = 6.02 \cdot 10^{23}\ \mathrm{mol^{-1}}$ the number of Gaq3 molecules in the jet sample volume illuminated by the laser can be calculated as

$$n_{sam} = 1.06 \cdot 10^{-12}\ \mathrm{mol} \cdot 6.02 \cdot 10^{23}\ \mathrm{mol^{-1}} = 6.36 \cdot 10^{11}\ . \tag{4.17}$$

Finally all parameters of equation 2.22 are determined and the photoexcitation yield f can be calculated. We calculated f as a function of the pump laser pulse energy. Figure 4.18 shows the plot for the modified formula 2.22 and in comparison the plot for formula 2.18 for three different jet diameters. The calculations were performed for a $30\ \mu$m-jet (solid curves), a $150\ \mu$m-jet

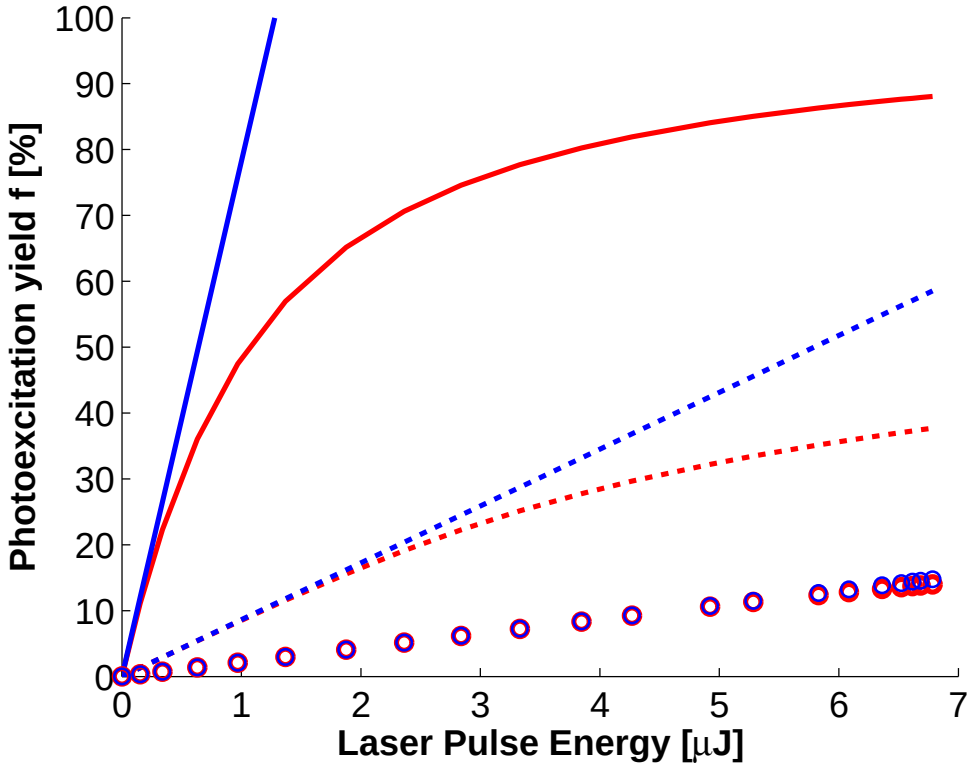

Figure 4.18.: *Photoexcitation yield f as function of the laser pulse energy, calculated for equation 2.18, obtained by [81, 79] (blue), and for the modified equation 2.22 (red). The calculations were performed for three different jet-diameters:* $30\ \mu$m*-jet (solid curves),* $150\ \mu$m*-jet (dashed curves) and* $300\ \mu$m*-jet (circles).*

(dashed curves) and a $300\ \mu$m-jet (circles). While formula 2.18 has a linear progression, the

modification leads to a saturation progression for increasing laser powers. This is due to the fact that with increasing laser power less and less sample molecules in the ground state are available for excitation. However, this fact plays only a role when high excitation yields are obtained as for a small $30\ \mu$m-jet diameter, which was used for the XANES experiments (see chapter 5.2.1). The larger the jet diameter, the more sample molecules in the sample volume have to be pumped. Consequently the excitation yields are lower for equivalent laser pulse energy ranges and differences between equations 2.18 and 2.22 become negligible. In case of a $30\ \mu$m-jet a photoexcitation yield of nearly $90\ \%$ can be achieved in the pump volume V_{ex} for high laser pulse energies between $5.5 - 7\ \mu$J.

The probe volume V_{probe}, probed by the X-ray beam has also to be taken into account for the photoexcitation yield. It is defined by the X-ray beam focus size. If $V_{probe} \geq V_{ex}$ the photoexcitation yields in V_{probe} and V_{ex} are equal. If $V_{probe} \approx V_{ex}$, the averaged yield in the whole probe volume can exceed the one in the pump volume, because the excitation densities are higher in the center of the jet due to the gaussian profile of the laser beam. The jet was divided into slices parallel to both optical axis and jet flow direction. For each slice the photoexcitation yield was calculated separately. The result is graphically illustrated in figure 4.19.

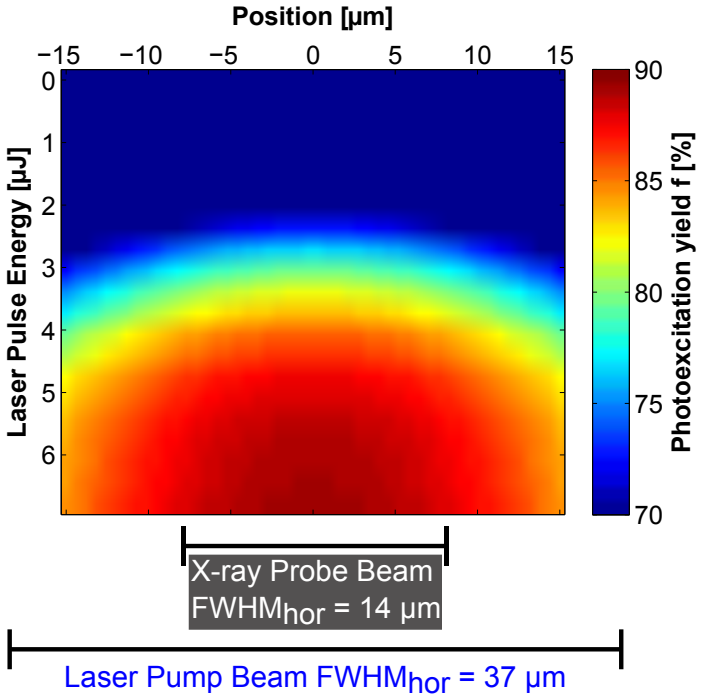

Figure 4.19.: *The Colormap shows the photoexcitation yield as function of the pulse energy of the incident pump laser beam on a* $30\ \mu$m*-jet. The x-axis represents the position within the jet. Since the* $FWHM_{hor}$ *of the X-ray beam is smaller than* $FWHM_{hor}$ *of the laser beam and the jet diameter, the volume* V_{probe} *probed by the X-ray shows higher excitation densities than the pump volume* V_{ex}*.*

The colormap shows the photoexcitation yield in V_{ex} (indicated by color) as function of the

pulse energy of the incident pump laser beam (y-axis) on the jet. The x-axis represents the position within the jet and for each position a specific value for f can be determined. For pulse energies beyond ca. $5.5\ \mu\mathrm{J}$ used in the XANES experiments, the yield exceeds $85\ \%$ over the whole jet width. The X-ray focus of the X-ray beam was $18\ \mu\mathrm{m}$ x $14\ \mu\mathrm{m}$ (v x h) (see chapter 4.1.5). This means the probe volume was smaller than the pump volume. The scale bar in figure 4.19 shows the horizontal beam size of the pump laser, indicating V_{ex} and the horizontal size of the X-ray probe beam indicating V_{probe}. This corresponds to the marked area of the jet width from ca. $-7\ \mu\mathrm{m}$ to ca. $+7\ \mu\mathrm{m}$, where the photoexcitation yield is about $90\ \%$. This value was assumed for the analysis of the XANES experiments in this thesis.

5. Results

This work concentrates on bond-distance changes of the metal organic compound Gaq3 induced by photoexcitation. The gallium atom in Gaq3 has no unoccupied d-orbitals into which photoelectrons can be excited. Thus no charge transfers and no intermolecular transitions are expected. Therefore, the interpretation of the Gaq3 XANES is based on multiple scattering events. The ground state structure of the Gaq3 molecule is well known due to crystallographic data and agrees well with quantum chemical calculations using the Density Functional Theory (DFT) approach and the Hartree-Fock (HF) approach. The experimentally determined excited state structure remains unknown until now.

5.1. X-ray Diffraction of Gaq3 Crystal

The molecular ground state structure of Gaq3 was determined by single crystal X-ray diffraction. For a detailed description of experimental methods and the theory of (single crystal) X-ray diffraction, the reader is referred to the books by Woolfson [109] and Nielsen [78]. The measurements were conducted at the DORIS beamline BW7A. The dataset was processed with XDS [110] and structure solution as well as refinement were performed with SHELX [111].

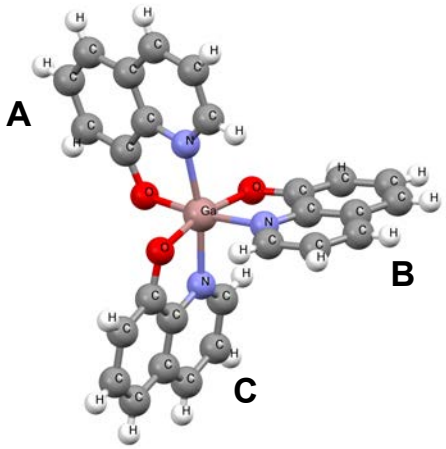

Figure 5.1.: *Gaq3 crystal structure. The letters A, B, C refer to the three coordinated quinoline-rings. The atoms of the molecule are Ga = Gallium, N = Nitrogen, O = Oxygen, C = Carbon, H = Hydrogen.*

The methods for Gaq3 and Alq3 crystal growth are presented in chapter 3.3. The compound

forms monoclinic crystals: $a = 11.163(2)$ Å, $b = 13.224(3)$ Å, $c = 16.631(3)$ Å, $\alpha = 90.00\,^{\circ}$, $\beta = 94.30\,^{\circ}$ and $\gamma = 90.00\,^{\circ}$ with space group $P2_1/n$ and one $[Ga(C_9H_6N_1O_1)_3]$ molecule. Figure 5.1 shows the structure of the Gaq3 molecule determined by X-ray crystallography in the asymmetric unit. This structure corresponds to the meridional isomer (mer-Gaq3) in which the sixfold-coordinated Ga^{3+} is surrounded by three equal quinoline-rings, referred to as A,B and C. The results of the crystal structure analysis are summarized in table 5.1.

Table 5.1.: *X-ray diffraction data of Gaq3*

Parameter	Value (this work)	Value([112])
Crystal	yellowish rectangular	yellowish rectangular
	0.10 x 0.03 x 0.01 mm^3	0.60x0.36x0.28 mm^3
Cell constants		
a	11.163(2) Å	11.0233(13) Å
b	13.224(3) Å	13.2751(7) Å
c	16.631(3) Å	16.920(4) Å
α	90.00 °	–
β	94.30 °	98.049(12) °
γ	90.00 °	–
Cell volume	2448.2(8) $Å^3$	2451.6(6) $Å^3$
Space group	$P2_1/n$	$P2_1/n$
R-value	0.0486	0.117
Temperature	293 K	293 K
Radiation wavelength	0.8123 Å	0.71073 Å
Number of reflections (total)	4946	–
Number of reflections (gt)	4465	–
Z	4	4

5.2. Pump-Probe XANES Spectroscopy of Gaq3

5.2.1. Transient Difference Signal as Function of Laser Power

The fraction of excited state molecules within the probe volume can be determined using 2.22 for the photoexcitation yield f as introduced in chapter 2.5. In chapter 4.2.4 f was calculated for a 30 μm-jet and all other experimental parameters determined for the XANES experiments like laser beam size (see chapter 4.1.4), sample concentration and extinction coefficient of Gaq3 in benzyl alcohol (see chapter 4.2.2). The result of f as function of the laser pulse energy is replotted in figure 5.2 (red curve). To compare this result with the XANES pump-probe measurements, we measured the transient absorption signal $T_{fl} = (I_{fl}^{pump} - I_{fl}^{unpump})/I_0$ (see chapter 2.4) for a time delay of 50 ps and for the energy E_0 as function of the pump laser pulse energy. The only power quantity which could directly be controlled during the experiment is the power

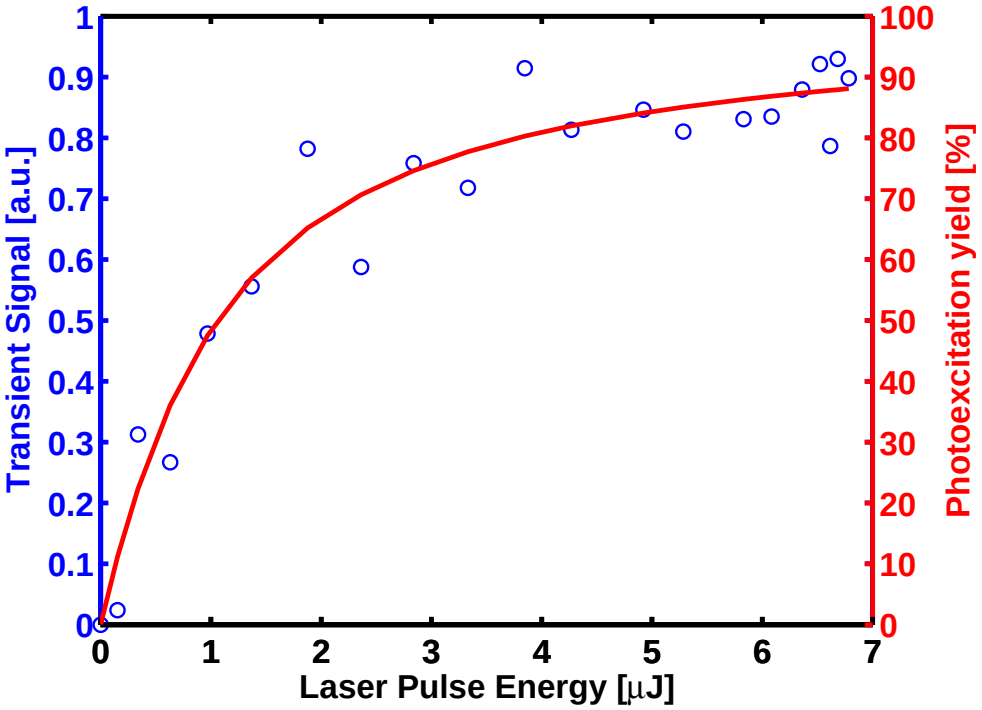

Figure 5.2.: *Experimentally obtained transient difference signal (blue circles) and photoexcitation yield (red curve) calculated by formula 2.22, as function of the pulse energy of the pump laser (for details see text).*

of the laser amplifier, which has been varied in increments of 50 mW. The pump power for each power setting of the laser amplifier was measured at the jet position using a laser power meter. Due to nonlinear processes the real laser power at the jet position does not scale linearly with the amplifier power and thus the laser pulse energy increments in the saturation scan are not equidistant. For each pulse energy the X-ray fluorescence signal of the pumped state I_{fl}^{pump} and the X-ray fluorescence signal of the unpumped ground state I_{fl}^{unpump} were measured for 16 s.

The resulting measurement of T_{fl}, referred to as *Excitation-Scan* is plotted in figure 5.2 (blue circles).

The curve shows a typical saturation progression as function of the pump laser pulse energy such that beyond 5.5 μJ the transient signal does not increase any further with an increase in laser power. This experimentally determined values were fitted with the formula 2.22 for the photoexciation yield by scaling the transient signal to the function of f. The fact that the measured saturation curve agrees well with the theoretical values supports the assumptions of the theoretical calculations above. In combination with formula 2.22 the excitation scan allows an estimate of the excited state fraction and it provides a strong indication that a higher excitation yield can not be achieved.

5.2.2. Transient Difference Signal as Function of Temporal Delay

Figure 5.3 shows a time delay scan of the transient difference signal between laser pulse and X-ray pulse. Several crucial information can be extracted from this measurement:

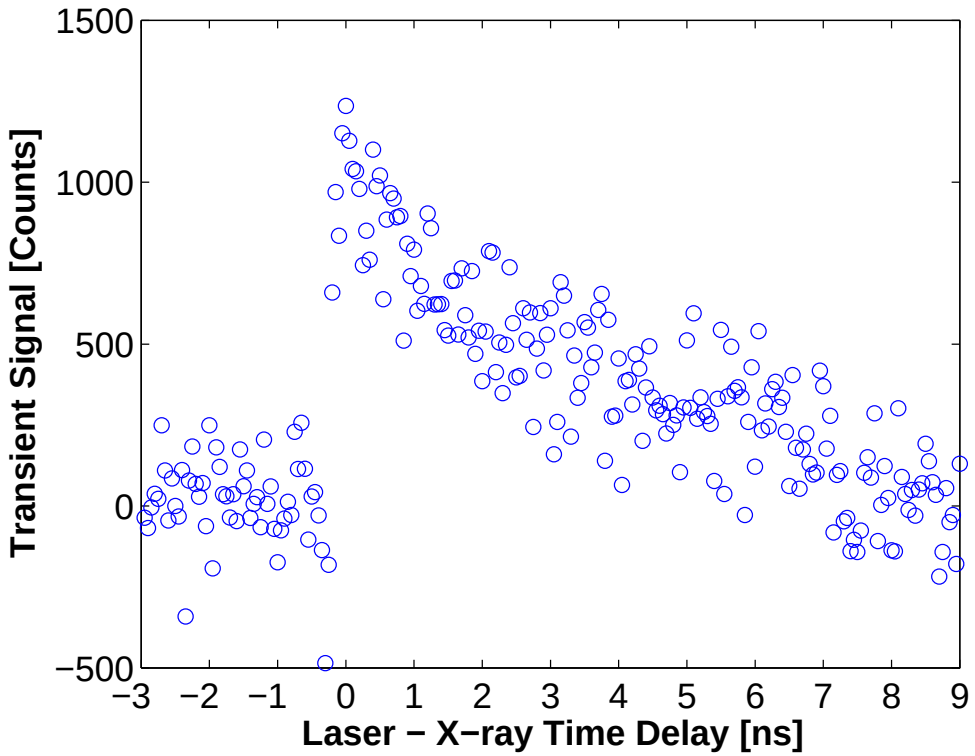

Figure 5.3.: *Transient difference signal as function of the time delay between pump laser pulse and probe X-ray pulse.*

- Fine-adjustment of the temporal overlap between laser pulse and X-ray pulse for a maximum transient signal (see also chapter 4.1.7).

- Detection of the temporal decay, which allows the determination of the excited state lifetime of the sample molecules (see [1]).
- Determination of the X-ray pulse width (see [1]).

Regarding this measurement, for the acquisition of the pump-probe XAFS spectra, presented in the following sections, the delay was chosen to an optimal value of $\Delta t \approx 50$ ps.

5.2.3. Ground State Absorption Spectrum

The experimental K-edge spectrum of Gaq3 dissolved in benzyl alcohol was measured in total X-ray fluorescence yield and the raw spectrum is shown in figure 5.4. The energy was

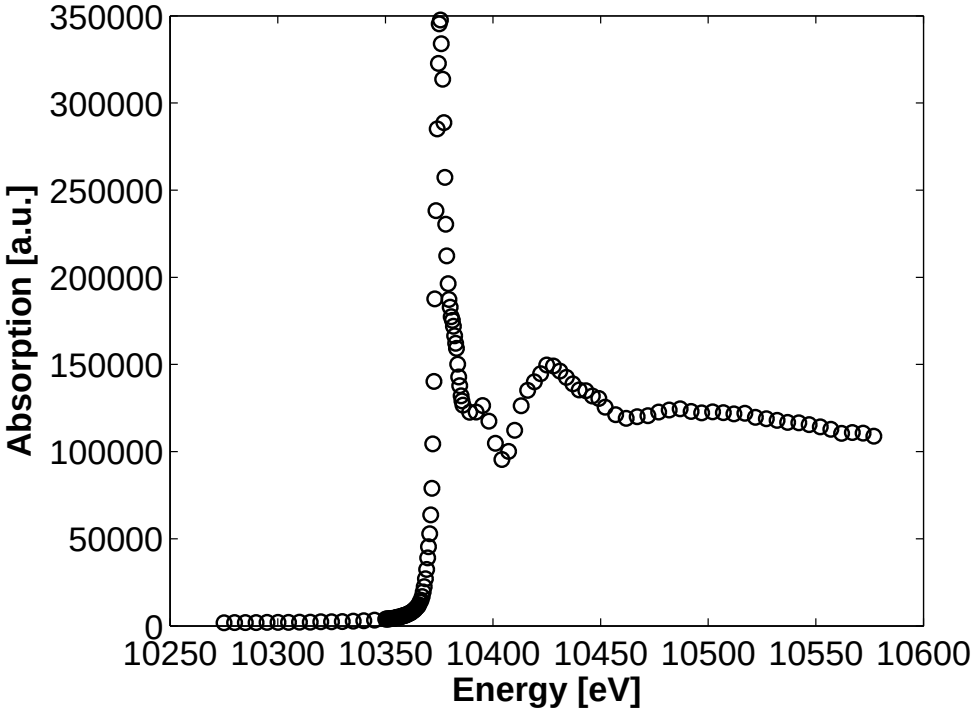

Figure 5.4.: *Gaq3 absorption spectrum measured in total X-ray fluorescence yield.*

increased in increments of 0.5 eV near the absorption edge and in $2-5$ eV steps below and far above the edge. At each energy step the signal was counted for 16 s. The maximum count-rate occurred at the whiteline with $348000\,\mathrm{counts}/16\,\mathrm{s}$. Considering the PETRA III bunch revolution frequency of 130 kHz, the average count rate per bunch and per second is $348000\,\mathrm{counts}/16\,\mathrm{s}/130\,\mathrm{kHz} \approx 0.17\,\mathrm{counts}$. Assuming that the measurement of the X-ray fluorescence signal I_{fl} obeys a Poisson-distribution and excluding systematic errors, the statistical error of the signal is equal to the square root of the number of measured counts:

$$\sigma(I_{fl}) = \sqrt{I_{fl}}\ . \tag{5.1}$$

For the whiteline with 348000 counts the absolute error is 590 counts resulting in a relative error of 0.17 %. Possible systematical errors however, are not considered here.

5.2.4. Pump-Probe Absorption Spectrum

Figure 5.5 shows the normalized experimental ground state absorption spectrum A_{EX}^{GS} of Gaq3 in red color. The normalized experimental excited state spectrum A_{EX}^{ES} in green color is deduced from the experimental transient difference spectrum T_{EX} in blue color applying equation 2.17. For the normalization of the raw data I_{fl}^{pump} and I_{fl}^{unpump} the program Athena [113] was used

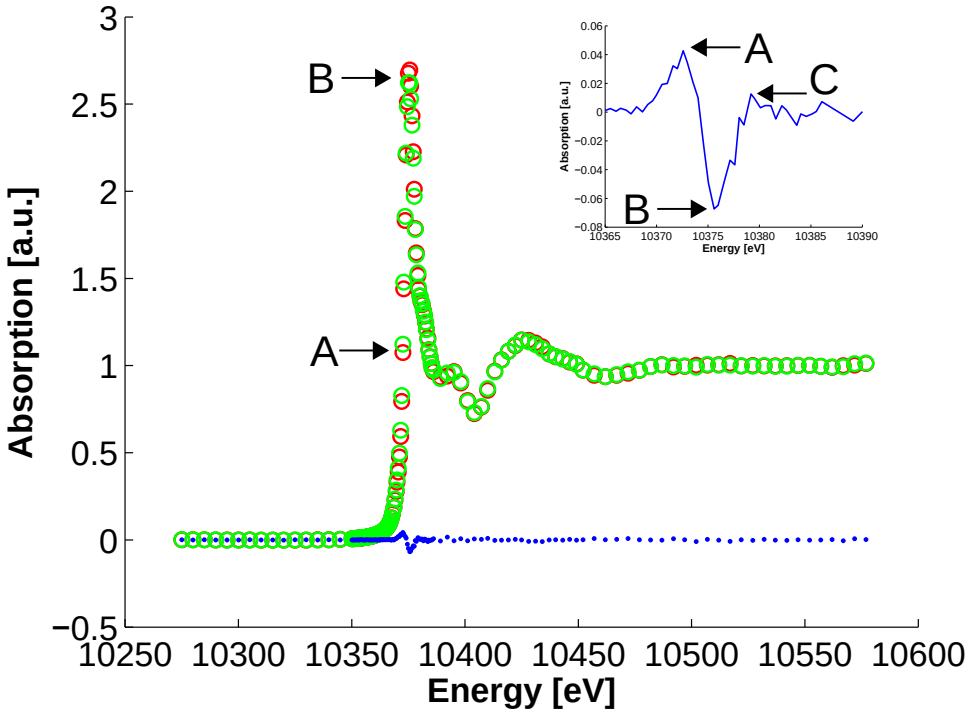

Figure 5.5.: *Experimental GS spectrum A_{EX}^{GS} (red circles), experimental ES spectrum A_{EX}^{ES} (green circles) and transient difference spectrum $T_{EX} = f[A_{EX}^{ES} - A_{EX}^{GS}]$. Features A, B and C refer to the main differences between A_{EX}^{ES} and A_{EX}^{GS}. The inset shows a magnified section of T_{EX} with features A, B and C.*

in the way that the pre-edge area is 0 and the post edge area is 1. The normalization accounts for background absorption below the absorption edge (pre-edge) and above the absorption edge (post-edge) and is performed by subtracting a polynomial fit function, called spline function from the two contributing data areas. The ES spectrum was recorded with a time delay of $\Delta t \approx 50$ ps of the X-ray pulse with respect to the laser pulse. Though the spectra are identical over a broad energy range, two main differences, in the following named feature *A* and feature *B*, are observed. At feature A the absorption signal of the ES is above the GS signal leading to a relative change of 4.0 % and at feature B the excited state signal is lower than the GS signal leading to a whiteline

suppression of $2.7\ \%$. A third difference, lower than the two aforementioned features, occurs at the falling edge as a small increase, which is named feature C. This is better recognizable in the inset in figure 5.5 showing a magnified plot of T_{EX}. This pump-probe absorption spectrum of Gaq3 was many times reproduced in several beamtimes.

5.2.5. Analysis Approach for Pump-Probe Absorption Spectra

Since XANES spectroscopy is not a direct measurement of structural changes, the following approach was used for data analysis: For the interpretation theoretical spectra for both the GS structure and the ES structure were calculated by FEFF and the theoretical transient spectrum obtained was compared with the experimental transient spectrum (as denoted in chapter 2.2.2 the reduced chi-square algorithm was used here as criterion). For the calculation of a XANES spectrum, FEFF requires the atomic coordinates of the molecule. For the GS this information was taken from X-ray crystallography (see chapter 5.1 and table 5.1) and from computational calculations using the Hartree-Fock (HF) theory and the Density Functional Theory (DFT) [31, 40]. For the ES the structural information predicted by calculations based on the single Configuration Interaction (CIS) method was used [31]. In addition a structural model is introduced in which the atomic coordinates are optimized for the Gaq3 molecule in the ES.

5.2.6. Calculation of the Gaq3 Ground State Spectrum

Figure 5.6 shows the experimental ground state spectrum of Gaq3 (red circles) and the optimal FEFF simulation (solid black trace) with the structural input from crystallographic data. The calculation is in good agreement over a wide energy range. In consideration of the transient spectrum especially the regions containing features A, B and C are of high importance. This is the case since especially the whiteline is in good agreement with the experimental data. Non-structural parameters were stepwise optimized until the best agreement between theoretical and experimental data was obtained. As criterion for the agreement the reduced chi-square algorithm, described in chapter 2.2.2 was used. In order to minimize the reduced chi-square value, different parameters were varied and their influence on the spectra was checked. The most crucial parameters with large impact on the spectra turned out to be the *FMS* parameter, which defines the cluster size, the *lmax* which limits the angular momentum bases of the self-consistent potentials (*SCF*) and of the full multiple scattering calculations (*FMS*) and the S_0^2 amplitude reduction factor. Their influence on the fit results is illustrated in figure 5.7. The optimized value for S_0^2 is 0.94 . For a FMS cluster size below 3.2 Å FEFF was not capable to calculate spectra or the results were very poor and did not reflect the experimental spectrum. The results for different cluster sizes in figure 5.7 show, that above a FMS cluster size of 6.9 Å no further improvement for the χ_ν^2 value could be achieved, which is reasonable since the distance from the absorber atom to the farthest intermolecular atom is 6.141 Å. The high values for the reduced chi-square do not directly indicate a bad agreement between theoretical and experimental spectra but accommodate for an underestimation of the statistical error. Systematical errors are not considered by the chi-square criterion. The resulting optimized values for the non-structural parameters were used for all further calculations. The GS structure derived from X-ray diffraction for which the non-

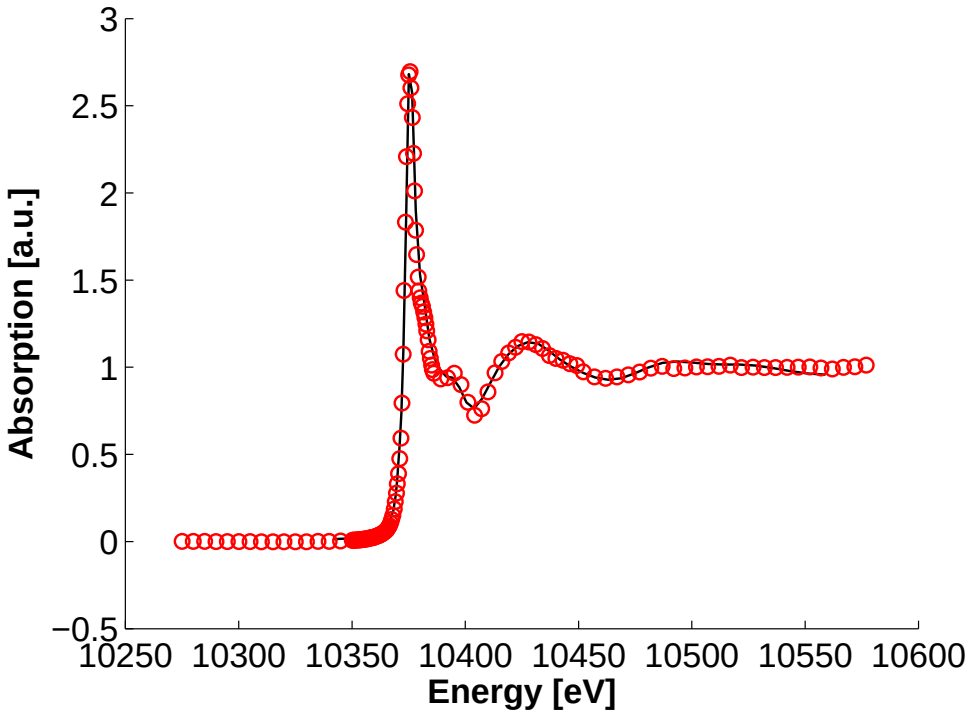

Figure 5.6.: *Experimental ground state spectrum of Gaq3 (red circles) and theoretical ground state spectrum calculated by FEFF (solid black trace).*

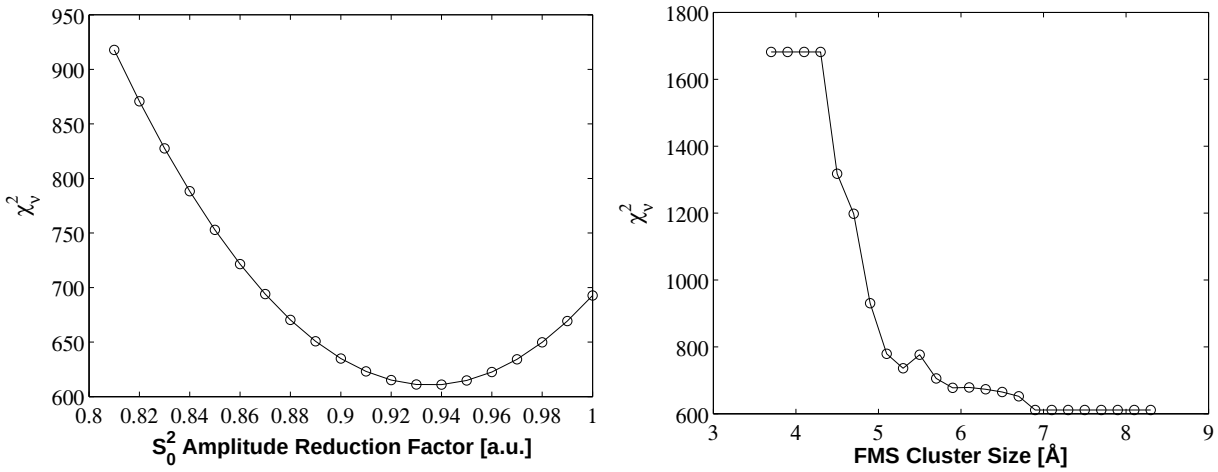

Figure 5.7.: *Left: χ^2_ν-value as function of the S_0^2 amplitude reduction factor. Right: χ^2_ν-value as function of the FMS cluster size.*

structural FEFF parameters were optimized and which serves as basis for the structural model will be named GS_{cryst1} in the following.

5.2.7. Gaq3 Structures of Ground State and Excited State

Molecular Geometry of Gaq3 Predicted by Means of Theoretical Calculations

Gahungu et al investigated the structural changes associated with electronic excitations from the ground state S_0 to the first excited state S_1 of Gaq3 using quantum chemical methods such as DFT, ab initio HF, and CIS [31]. They found that upon $S_0 \rightarrow S_1$ transition a structural shift occurs, which is mainly located on the A-quinoline-ring, while the two other quinoline-rings B and C remain mainly unaffected (figures 5.1 and 5.8 show the structures of the molecule and the A-quinoline-ring). According to their calculations the $Ga - N_A$ bond distance is contracted by -0.099 Å, while the $Ga - O_A$ bond distance is elongated by 0.090 Å in the excited state (the subscripted letter A denotes the A-quinoline-ring). Beside this alternate shortening and lengthening of these two bonds, also intraligand bond length changes of the A-quinoline-ring atoms occur. The largest change of $+0.073$ Å occurs between the N_A atom and the C_2 atom. In addition the $Ga - N_B$ bond of the B-quinoline-ring is shortened by -0.027 Å and the $Ga - N_C$ bond of the C-quinoline-ring is elongated by 0.023 Å. A very small modification of 0.003 Å is predicted for the $Ga - O_B$ bond and -0.004 Å for the $Ga - O_C$ bond. At the time of writing this thesis this paper was found to be the only one reporting about the S_1 excited state structure of Gaq3. Bond angle changes upon the $S_0 \rightarrow S_1$ transition of Gaq3 are not predicted in this work. Figure 5.8 shows the A-ligand of Gaq3 with the denoted atoms according to reference [31]. More theoretical calculations have been performed for the homologue molecule aluminum(tris8-

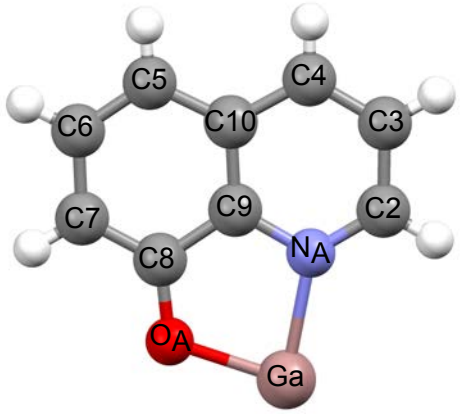

Figure 5.8.: *The A-quinoline-ring of the Gaq3 molecule. The atoms are named according to denotation of atoms in paper [31] and in table 5.2.*

(hydroxyquinoline))(Alq3) [108, 114, 115, 40], where the gallium atom is replaced by an aluminum atom. This replacement has some influence on geometrical and electronic properties, but the mechanism described for the structural changes upon photoexcitation is the same. In their work about theoretical calculations for the Alq3 molecular structure, J. Zhang and G. Frenking also report a structural shift upon $S_0 \rightarrow S_1$ transition, which is predominantly localized on the A-quinoline-ring while the other two quinoline-rings are mainly unaffected [32]. In addition the

authors report about bond angle changes on the A-ligand with the largest difference of $3.7\,^{\circ}$, but do not describe explicitly which bond angle is affected. Nevertheless this gives a hint that changes of bond angles should be also considered for the Gaq3 excited state structure.

Table 5.2 lists bond distances of the Gaq3 molecule from two different theoretical calculations [31, 40] and from experimental crystallographic data taken from [112] and those performed within the framework of this thesis (see chapter 5.1). The names of the calculated structures are given by the methods and basis sets (HF/6-31G* for S_0 and CIS/6-31G* for S_1 [31] and B3LYP/6-31G(d) for S_0 [40]). The crystallographic determined S_0 structure of this work is named GS_{cryst1} and the crystallographic determined structure taken from [112] is called GS_{cryst2}.

Table 5.2.: *Gaq3 bond lengths for the ground state S_0 ([31, 40, 112] and from this work) and the excited state S_1 as well as their difference $\Delta(S_1 - S_0)$ [31]. Bond lengths considered in the structural model for the XANES analysis are printed in bold. A,B and C refer to the three quinoline-rings of the molecule with X as placeholder for A,B,C. The atomic positions within a quinoline-ring are depicted in figure 5.8. All numbers are given in Å.*

Theoretical Calculations HF/6-31G* for S_0 and CIS/6-31G* for S_1 [31]

	Ground State S_0			Excited State S_1			$\Delta S_1 - S_0$		
Bond	A	B	C	A	B	C	A	B	C
$N_X - C_2$	1.298	1.300	1.297	1.371	1.299	1.297	0.073	-0.001	0.000
$C_2 - C_3$	1.408	1.410	1.410	1.359	1.409	1.410	-0.049	-0.001	0.000
$C_3 - C_4$	1.361	1.363	1.362	1.415	1.363	1.362	0.054	0.000	0.000
$C_4 - C_{10}$	1.416	1.417	1.417	1.405	1.417	1.417	-0.011	0.000	0.000
$C_{10} - C_5$	1.416	1.417	1.418	1.409	1.417	1.418	-0.007	0.000	0.000
$C_5 - C_6$	1.363	1.364	1.363	1.416	1.364	1.363	0.053	0.000	0.000
$C_6 - C_7$	1.411	1.413	1.414	1.359	1.413	1.414	-0.052	0.000	0.000
$C_7 - C_8$	1.373	1.373	1.371	1.441	1.373	1.371	0.068	0.000	0.000
$C_8 - C_9$	1.433	1.430	1.431	1.435	1.431	1.430	0.002	0.001	- 0.001
$C_9 - C_{10}$	1.399	1.397	1.396	1.406	1.397	1.396	0.007	0.000	0.000
$N_X - C_9$	1.356	1.352	1.352	1.341	1.353	1.351	-0.015	0.001	- 0.001
$C_8 - O_X$	1.295	1.297	1.302	1.253	1.298	1.301	-0.042	0.001	-0.001
$\mathbf{Ga - O_X}$	1.896	1.912	1.915	1.986	1.915	1.911	**0.090**	**0.003**	**-0.004**
$\mathbf{Ga - N_X}$	2.112	2.136	2.088	2.013	2.109	2.111	**-0.099**	**-0.027**	**0.023**
Theoretical Calculations B3LYP/6-31G(d) [40]									
$\mathbf{Ga - O_X}$	1.934	1.951	1.950	-	-	-	-	-	-
$\mathbf{Ga - N_X}$	2.090	2.111	2.077	-	-	-	-	-	-
Crystallographic data GS_{cryst1}(this work)									
$\mathbf{Ga - O_X}$	1.930	1.951	1.981	-	-	-	-	-	-
$\mathbf{Ga - N_X}$	2.099	2.111	2.075	-	-	-	-	-	-
Crystallographic data GS_{cryst2} [112]									
$\mathbf{Ga - O_X}$	1.937	1.940	1.965	-	-	-	-	-	-
$\mathbf{Ga - N_X}$	2.093	2.112	2.092	-	-	-	-	-	-

A comparison of the ground state structures listed in table 5.2 reveals a maximum discrepancy of bond lengths between calculated HF/6-31G* and GS_{cryst2} of 0.041 Å for the $Ga - O_A$ bond. Additionally, there is also a discrepancy concerning the geometry between the methods and basis sets used for the theoretical calculations [31]. The results differ from each other with a maximum deviation of 0.1 Å between HF/6-31G* and B3LYP/3-21G [31] (latter basis set not shown here). Given the fact that bond length changes of 0.1 Å upon the $S_0 \rightarrow S_1$ transition are investigated, this has to be considered as a large discrepancy.

Theoretical Transient Spectrum Based on Calculated Basis Sets

In chapter 5.2.5 it is mentioned that the determination of the excited state structure is based on comparing the experimental transient spectrum T_{EX}^{100}, which is the difference between the experimental excited state spectrum A_{EX}^{ES} and ground state spectrum A_{EX}^{GS}, with the theoretical transient difference spectrum T_{TH}. If the experimental spectra agree well with the calculated spectra A_{TH}^{ES} and A_{TH}^{GS} for excited and ground state, respectively, the following relation must be satisfied:

$$\begin{aligned} A_{TH}^{ES} - A_{TH}^{GS} &= A_{EX}^{ES} - A_{EX}^{GS} \\ T_{TH} &= T_{EX}^{100} \ . \end{aligned} \tag{5.2}$$

Due to the discrepancies of the different GS structures for Gaq3 it is important to specify for which geometrical molecular structure a spectrum is calculated. To elucidate this matter the transient signal for different ground state structures (GS_{cryst1}, GS_{cryst2}, B3LYP/6-31G(d), HF/6-31G*) and the excited state structure CIS/6-31G* were compared. Though the paper [31] lists bond lengths for the S_0 and S_1 states, the atomic positions of the molecule are not published. The authors provided these coordinates upon request for the S_0 HF/6-31G* basis set and for the S_1 CIS/6-31G* basis set. In this way it was possible to calculate the transient spectrum based on the theoretical calculations including the small structural shifts within the A-quinoline-ring. For comparison the transient spectrum between the S_1 CIS/6-31G* and S_0 B3LYP/6-31G(d) and the transient spectrum between the S_1 CIS/6-31G* and GS_{cryst1} were calculated. Thereby the non-structural parameters as determined in chapter 5.2.6 were used for all calculations. The results are depicted in figure 5.9. Firstly none of the theoretical transients (black) fits well to the experimental transient (cyan). Thus the structural differences between each of the ground state and excited state do not directly reflect the structural change in the sample which lead to the measured transient spectrum. Secondly the calculated spectra clearly depend on the structural input for the ground state spectrum (Note that for all three transients the excited state S_1 CIS/6-31G* basis set was used). The S_0 B3LYP/6-31G(d) state is in better agreement with GS_{cryst1} than S_0 HF/6-31G* and thus their corresponding transient spectra show a very similar curve progression. It can be concluded that the FEFF simulations based on the theoretical predictions do not fit well to the data. Consequently I tried to optimize the molecular structure for the S_1 state in such a way that the FEFF simulations agree better with the experimental transient spectrum. For this a structural model was developed, which will be explained in the next chapter. Assuming that X-ray crystallography provides the most reliable information about the ground state structure,

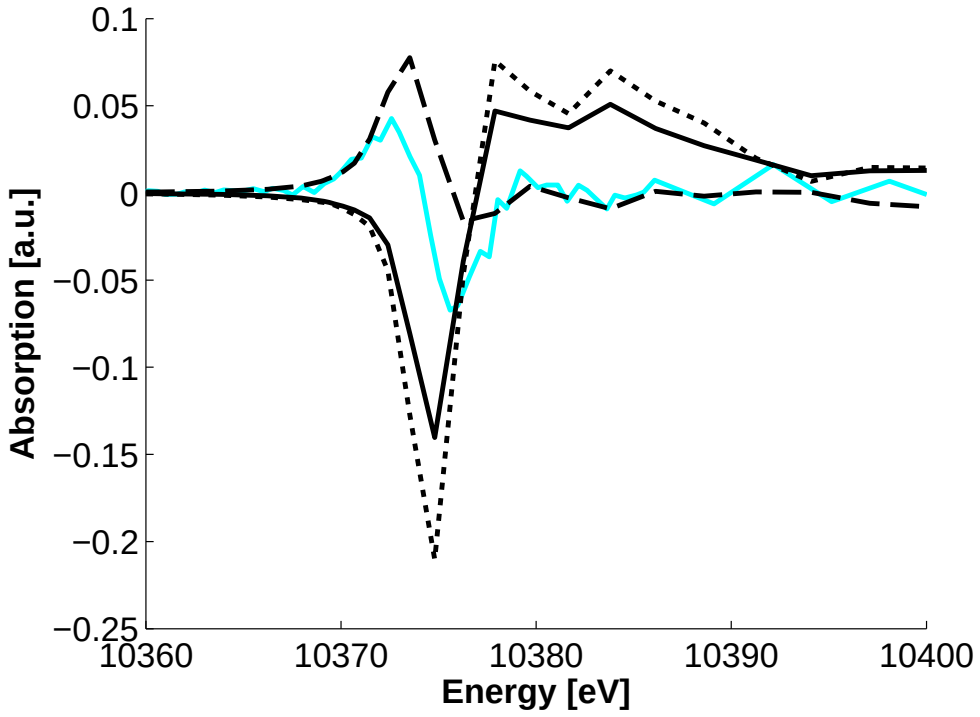

Figure 5.9.: *The experimental transient spectrum (cyan) plotted together with the theoretical transient spectra between the S_1 CIS/6-31G* state and the S_0 HF/6-31G* state (dashed curve), the GS_{cryst1} (dotted curve) and the S_0 B3LYP/6-31G(d) state (solid curve).*

the calculated ground state spectrum A_{TH}^{GS} for the structure GS_{cryst1} was used in the following.

5.2.8. Optimization of Structural Parameters for the S_1 Excited State

In order to precisely determine the S_1 excited state structure, several specific structural parameters were varied incrementally according to a model of the Gaq3 molecule shown in figure 5.10. The yellow arrows present structural changes such as bond length contractions and elongations, respectively, as well as bond angle changes. This model assumes that bonds between the gallium atom and the directly coordinating atoms are changed. The remaining carbon and hydrogen atoms of one quinoline-ring are grouped together with the nitrogen atom of the same ring. That means a bond length change between the nitrogen atom of one of the ligand rings and the gallium atom causes a change of the whole ring except of the oxygen atom which is considered independent. This is a reasonable assumption since the $O_A - C_8$ bond is not rigid, but is shortened when the $Ga - O_A$ bond is elongated (see figure 5.8 and table 5.2). Intraligand structural changes apart from the $O_A - C_8$ bond are in this way completely neglected. A graphical illustration of the movement of the A-quinoline-ring as consequence of the bond length changes is shown in figure 5.11 A). Each of the six atoms, coordinated to the gallium atom, can undergo a

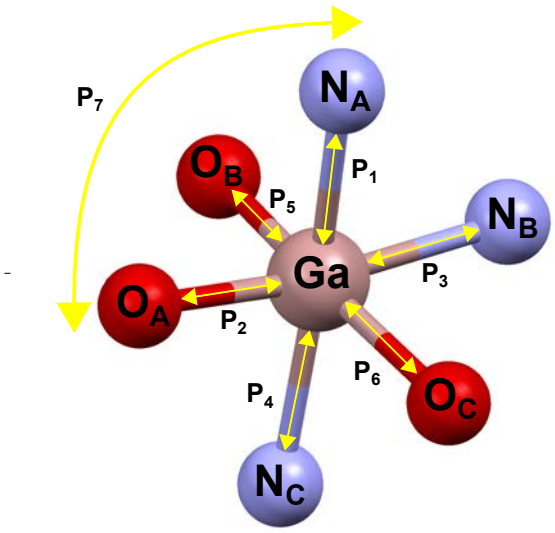

Figure 5.10.: *Model for possible structural changes upon photoexcitation of Gaq3. For better clearness only the nearest neighbor atoms are shown. The straight yellow arrows illustrate a possible bond length expansion respectively contraction and the curved yellow arrow indicates a possible rotation of the whole A-ligand in the O_A-Ga-N_A-plane. Each of these structural changes are allocated to single parameters, named P_1 to P_7.*

change along the bond length direction and a rotation perpendicular to its gallium bond axis in three spatial directions. This means four parameters for each atom. For each set of parameters an ES spectrum is calculated. The calculations showed, that even small bond length changes of smaller than $\Delta L = 0.01$ Å and bond rotations of below $\Delta R = 0.2\,^\circ$ influence the calculated spectra significantly. Expectable bond length changes, predicted by theoretical models for metal organic compounds are in the range of $0.1 - 0.2$ Å [31]. That means for covering an adequate length region of $L = 0.4$ Å (from -0.2 Å to $+0.2$ Å) with sufficient resolution $\Delta L = 0.01$ Å the number of calculated spectra is $L/\Delta L = 0.4/0.01 = 40$.

For bond angles changes a range of about $R = \pm 5^\circ$ in increments of $\Delta R = 0.2\,^\circ$ can be expected. Thus for a rotation parameter the calculation of $R/\Delta R = 5 - (-5)/0.2 = 50$ spectra seems to be a reasonable number. Considering one length parameter and three rotation parameters for each of the six neighboring atoms, the number of spectra, which have to be calculated in order to describe each theoretical possible parameter combination is

$$N_{spectra} = {N_{trans}}^{N_{atom}} \cdot {N_{rot}}^{N_{atom} \cdot 3} = 40^6 \cdot 50^{6 \cdot 3} \approx 1.56 \cdot 10^{40} \ , \tag{5.3}$$

where N_{trans} is the number of spectra for translational changes, N_{rot} is the number of spectra for rotational changes and N_{atom} is the number of atoms coordinating the gallium atom. This is a huge number of freedom degrees and for the model one has to concentrate on a limited number of these parameter combinations in a physical meaningful range. This range is provided by the theoretical calculations presented in chapter 5.2.7. In this way we accounted those parameters predominantly, which are expected to undergo the largest change due to the theory. Furthermore

the N atom and the O atom of one quinoline-ring are more rigidly connected and consequently the $Ga-N$ and $Ga-O$ bonds can be expected to undergo dependent rotational changes. In order to apply the structural changes to the molecule a *Matlab* [116] code was written, which changes the atomic positions by mathematical transformations according to the parameters. At the end the code delivers the molecular structure in form of a pdb-file and also generates a FEFF input file. For each molecular structure with specific bond lengths and angles, potentially presenting the correct description of the excited state structure of the molecule, a FEFF calculation is performed and a theoretical excited state spectrum is produced. If the model describes the structural shift correctly, there is a theoretical ES spectrum matching the experimental ES spectrum. Assuming, the calculated GS spectrum for the structure GS_{cryst1} agrees well with the experimental GS spectrum, the differences of the theoretical spectra should be the same as the differences of the experimental spectra and equation 5.2 is fulfilled.

In addition a variation of this model was tested. In this, the quinoline-ring is grouped together with both, the nitrogen and the oxygen atom of one ring. An elongation of the gallium-nitrogen bond is compensated by a shortening of the gallium-oxygen bond, and vice versa. In this way the

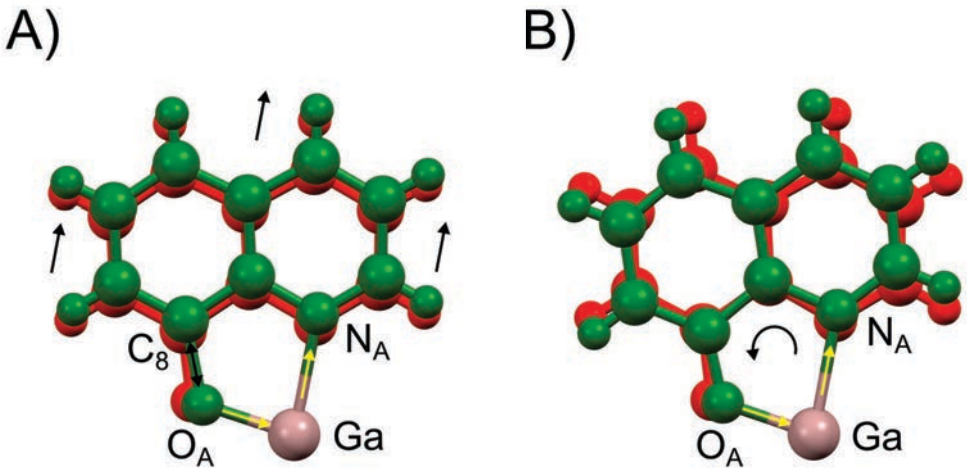

Figure 5.11.: *Illustration of two different models for the determination of the S_1 excited state structure of Gaq3. For better visibility only one quinoline-ring is shown. The red atoms represent the ground state structure and the green colored atoms represent the optimized structure for the excited state. A) Model 1: The quinoline-ring is fixed to the nitrogen atom only. Changes of the $Ga-N_A$ bond length (here $\Delta(Ga-N_A) = +0.200$ Å, marked by a yellow arrow) lead to a translational movement of the quinoline-ring along the $Ga-N_A$ axis (black arrows). The $Ga-O_A$ bond is optimized independently (here $\Delta(Ga-O_A) = -0.200$ Å, marked by a yellow arrow). Thus the O_A-C_8 bond is flexible and the only bond of the quinoline-ring, for which changes are allowed (black double arrow). B) Model 2: The quinoline-ring is rigidly fixed to both, the nitrogen and the oxygen atom. The $Ga-N_A$ and the $Ga-O_A$ bonds are changed contrariwise (here $\Delta(Ga-N_A) = +0.200$ Å and $\Delta(Ga-O_A) = -0.200$ Å), which leads to a rotation of the quinoline-ring (curved arrow) in the plane spanned by the Ga-, N-, O- atoms.*

rigid quinoline-ring undergoes a rotation in the plane spanned by the gallium, the nitrogen, and the oxygen atoms. The difference between the two models is the movement of the quinoline-ring, which is fixed to the nitrogen atom only (model 1, described above) and fixed to the nitrogen atom and the oxygen atom (model 2, variation). A graphical illustration of the two models is presented in figure 5.11. The graphics show the A-quinoline-ring structure in the ground state (red) and the optimized structure, which potentially represents the excited state structure of the A-quinoline-ring (green). To emphasize the differences between the two models the maximum bond length changes of $\Delta(Ga-N_A) = +0.200$ Å and $\Delta(Ga-O_A) = -0.200$ Å, used for the optimizations, were applied here. For small structural changes the difference is very small. The results obtained by the two different models were qualitatively and almost quantitatively the same. Model 1 leads to slightly better results, so that the resulting calculations presented and discussed in this thesis are based on this model. However, for comparison chapter 5.2.10 presents the results obtained for model 2. To optimize the excited state structure usually a large number of spectra has to be calculated, whereas the number highly depends on how many parameters are taken into account. In order to find the spectrum, which shows the best agreement with the data a fitting process was applied.

5.2.9. Fitting of Spectra (Model 1)

Based on the large number of calculated spectra a criterion is needed, which allows an estimation of how "good" a fit is. The fit, which fulfills the criterion best, is the *best-fit* and the molecular structure, related to this best-fit, is the *best-fit structure*. The criterion used for this estimation is the reduced chi-square algorithm, introduced in chapter 2.2.2.

The direct fitting of the transient spectrum is advantageous in comparison to a separate fitting of the ground state and excited state spectra because the discrepancy of the fits and data are larger than the discrepancy between ground and excited state spectra. A structural optimization of first the ground and subsequent the excited spectrum would lead to structural changes, which are already larger for the ground state than the changes induced by photoexcitation. Due to the very large number of possible parameter combinations in the present work, this number was limited to those parameters, for which theoretical predictions showed significant changes. Furthermore an optimization process was used, in which parameters were optimized stepwise. In each of these steps one or two parameters were optimized separately. After each parameter optimization the best-fit structure(s) of the previous step was/were optimized for the next parameter(s). In the best case this process leads to a convergence of the chi-square function. The optimization process is illustrated in figure 5.12. The next chapter shows the results of several different optimizations, in which the chronological order of the parameter to be optimized was varied. In this way it shall be examined if another order and the choice of starting values influence the final best-fit structure. In the first optimization the chronological order, in which the single parameters are optimized, is based on their expected changes due to the theoretical calculations. This means, the parameters which are supposed to undergo the largest changes and thus with the largest impact on the theoretically calculated spectrum are changed at first and the next parameters are consecutively optimized due to their level of expected structural changes.

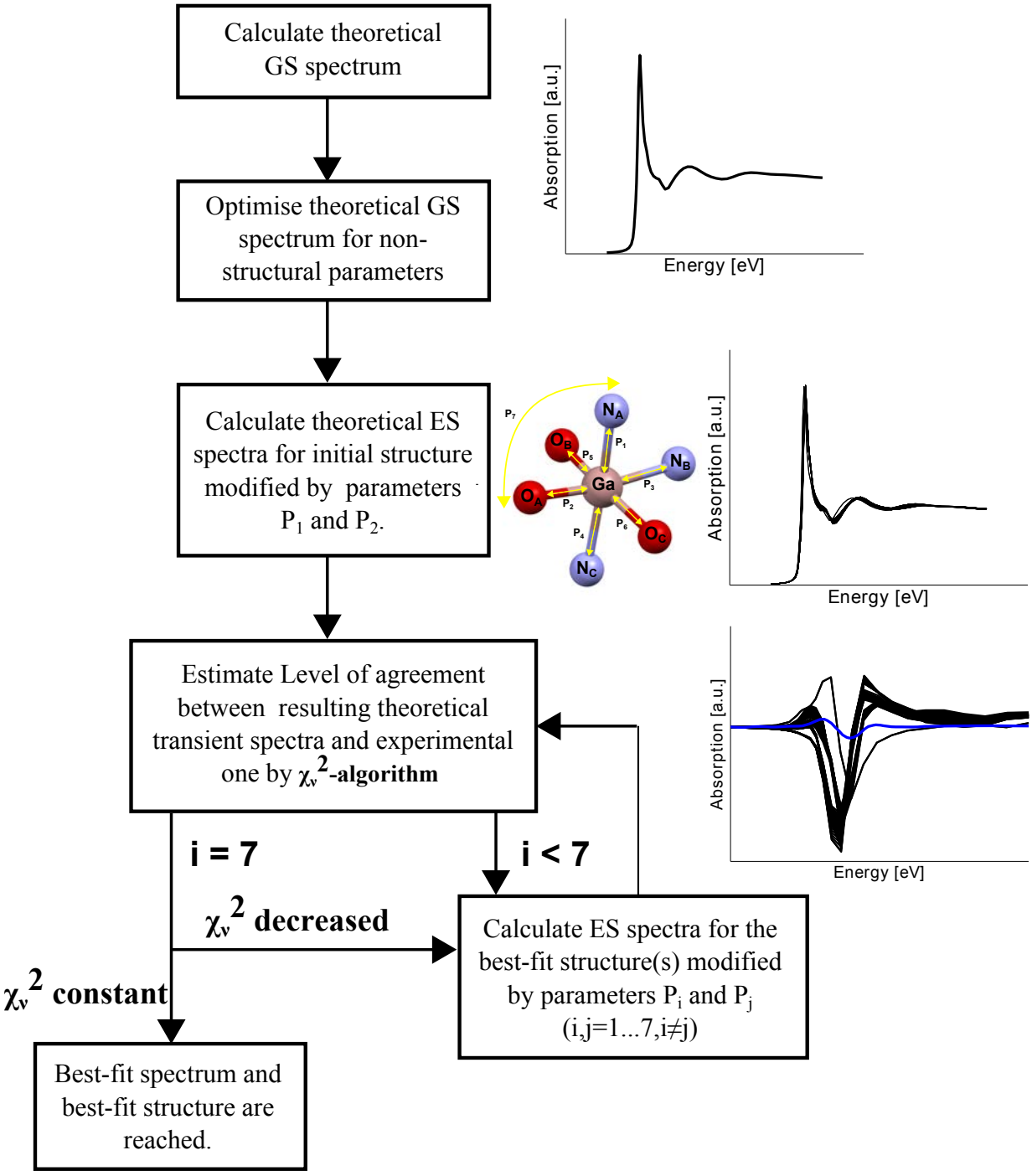

Figure 5.12.: *Different steps of the Gaq3 structure optimization.*

Optimization 1

Optimization of parameters P_1 and P_2

The parameters P_1 and P_2 are referred to the bonds $Ga - N_A$ and $Ga - O_A$ which are expected to have the largest impact on the excited state structure according to the theoretical predictions. Thus, first of all these two parameters were tested by changing each of the two bonds from -0.200 Å to 0.200 Å in increments of 0.010 Å along the bond direction (bond angles stay constant). This implies 41 lengths for each bond (the 0, indicating no change, is included) and $41 \cdot 41 = 1681$ different combinations. Hence on the first level of parameter optimization 1681 FEFF calculations were performed. Figure 5.13 shows the experimental excited state spectrum (green circles) and a selection of 60 spectra calculated by FEFF (black solid lines). These spectra derive from small structural changes of 0.010 Å and therefore their differences are small leading to an overlap of the spectra and an appearance as one single spectrum. At the B feature and at the first maximum after the whiteline this spectrum is smeared out which implies a sensitivity of the FEFF simulations to structural changes in these regions. These theoretical spectra A_{TH}^{ES} sub-

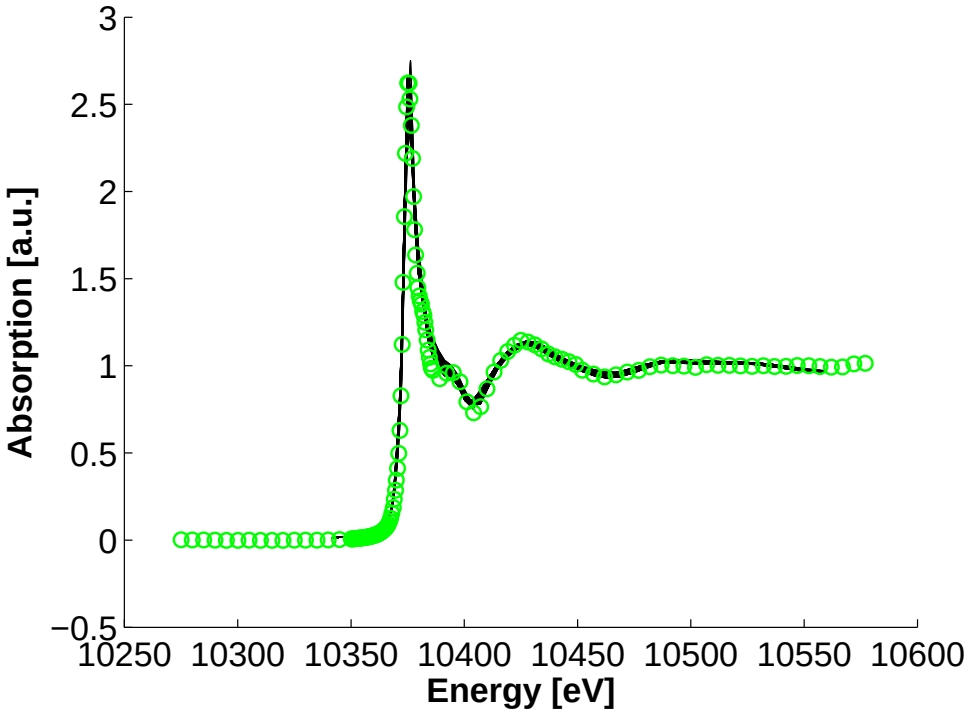

Figure 5.13.: *Experimental excited state spectrum of Gaq3 (green circles) and* 61 *calculated spectra (black solid lines) referred to* Ga_{N_A} *and* Ga_{O_A} *bond length differences of* -0.010 *Å. Structural changes mainly influence the white line height and the progression of the spectrum near the first maximum after the whiteline.*

tracted by the theoretical spectrum A_{TH}^{GS} lead to a set of theoretical transient difference spectra:

$$T_{TH} = [A_{TH}^{ES} - A_{TH}^{GS}] \ , \tag{5.4}$$

which are compared with the experimental transient spectrum T_{EX}^{100}. T_{EX}^{100} can be derived from the measured transient spectrum $T_{EX}(E,t)$ by applying equation 2.17. In chapters 4.2.4 and 5.2.1 the photoexcitation yield f was calculated and it was shown that about $90\ \%$ of the sample molecules are excited during the experiment. Thus it must apply

$$\begin{aligned} \underbrace{T_{EX}(E,t)}_{measured} &= f(t)\,\underbrace{[A_{EX}^{ES}(E,t) - A_{EX}^{GS}(E)]}_{T_{EX}^{100}} \\ T_{EX}^{100} &= \frac{1}{f}(t)\cdot T_{EX}(E,t) = \frac{100}{90}\cdot T_{EX}(E,t)\ . \end{aligned} \tag{5.5}$$

In the following the experimental transient difference spectra shown, are always referred to T_{EX}^{100} unless otherwise stated. Figure 5.14 shows the experimental transient spectrum T_{EX}^{100} (cyan colored curve) and the theoretical transient spectrum calculated by FEFF (black curve). The experimental spectrum was fourier-filtered, thus higher frequencies were cut off to eliminate noise allowing a better comparison between fit and experiment. In the following plots only the filtered spectrum (blue trace) will be shown. The theoretical transient is the best-fit (with respect to

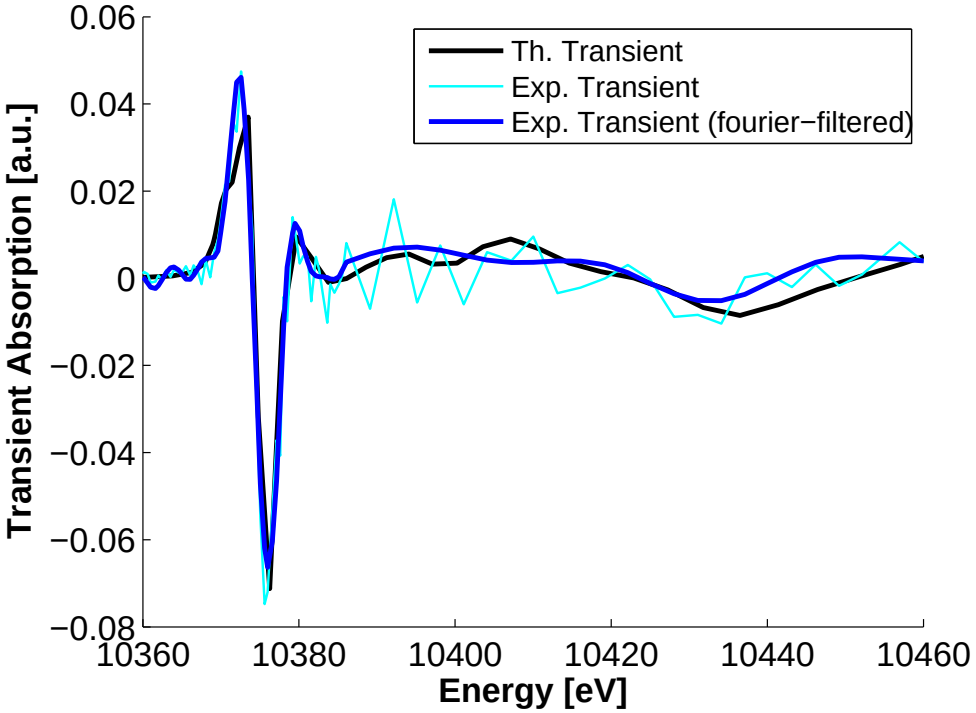

Figure 5.14.: *Experimental transient spectrum (cyan curve), fourier-filtered experimental transient spectrum (blue curve) and the simulated best-fit for optimization of parameters P_1 and P_2, which represent the $Ga - N_A$ and $Ga - O_A$ bond distance changes, respectively.*

parameters P_1 and P_2) concerning the criterion given by the reduced chi-square algorithm (see equation 2.14). Here S_i is the experimental transient spectrum $T_{EX}^{100} = A_{EX}^{ES}(E,t) - A_{EX}^{GS}(E)$ and

$S_i^{model}(\omega_i)$ is the theoretical transient spectrum $T_{TH} = A_{TH}^{ES}(E,t) - A_{TH}^{GS}(E)$, while ω_i stands for parameters P_1 and P_2, and σ_i for the statistical error. For the calculation of the statistical error σ_i we assume a Poisson distribution and thus the error can be calculated from the signals I^{pump} and I^{unpump}, which are equal to the square root of the number of measured photons (compare section 5.2.3):

$$\sigma(I_{fl}^{pump,unpump}) = \sqrt{I_{fl}^{pump,unpump}} \ . \tag{5.6}$$

The transient fluorescence signal T_{fl} is the difference of I_{pump} and I_{unpump} and their errors contribute to the error of T_{fl} according to Gauss' propagation of uncertainty:

$$\sigma(T_{fl}) = \frac{\sqrt{I_{fl}^{pump} + I_{fl}^{unpump}}}{I_0} \ . \tag{5.7}$$

Furthermore the errors of the normalized spectra A_{EX}^{ES}, A_{EX}^{GS} and T_{EX}^{100} were multiplied by an energy dependent factor which accounts for the spline function applied during the normalization process. The fitting parameters are in this case P_1 and P_2. For each of the 1681 theoretical spectra a χ_ν^2 value was determined and plotted in a contour plot as function of the $Ga - N_A$ and $Ga - O_A$ bond lengths changes. The result is depicted in figure 5.15. In this illustration the x-axis presents the $Ga - O_A$ bond distance change and the y-axis presents the change of the $Ga - N_A$ bond. The values of χ_ν^2 are allocated to colors, whereas blue means a very low value presenting a good agreement between theoretical and experimental spectrum and red means a high value. Due to a better clearness the scalebar ranges from 36 to 96 only. Thus for most combinations of bond length changes the χ_ν^2 is beyond 96, whereas the maximum value is 27511. From the plot one can derive the following information:

- There is only one parameter combination, which causes a minimum of the reduced χ_ν^2-function ($\chi_\nu^2 = 37.00$).
- According to this parameter combination, which is the best-fit structure with respect to the parameters P_1 and P_2, the molecule undergoes a structural change of $\Delta(Ga - N_A) = 0.050$ Å and $\Delta(Ga - O_A) = -0.020$ Å.
- The result is in discrepancy to the theoretical prediction of $\Delta(Ga - N_A) = -0.099$ Å and $\Delta(Ga - O_A) = 0.090$ Å.

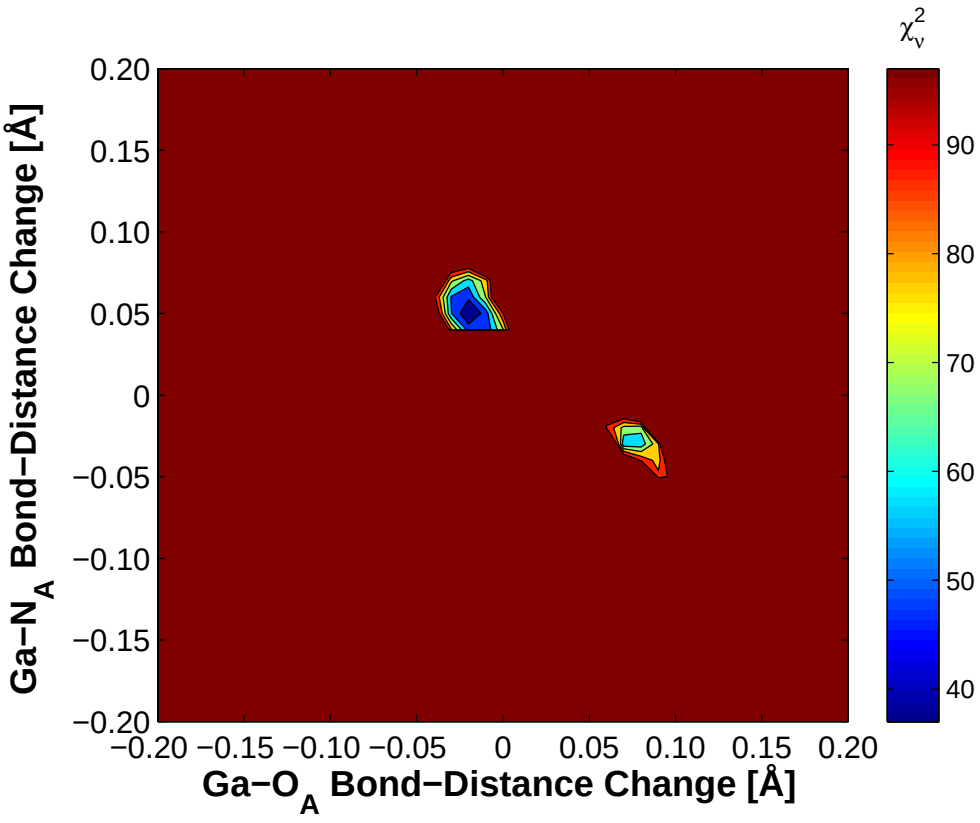

Figure 5.15.: χ^2_ν *as function of the bond length changes. Blue color presents a good agreement of theoretical and experimental spectra. Here the best-fit was obtained for* $\Delta(Ga - N_A) = 0.050$ *Å and* $\Delta(Ga - O_A) = -0.020$ *Å.*

Optimization of Parameters P_3 and P_4

The next set of parameters P_3 and P_4 refers to changes of the $Ga-N_B$ and $Ga-N_C$ bonds, which undergo according to the theory, the second largest changes. Therefore, the best-fit structure of the first optimization level was taken and the aforementioned bond lengths were changed from -0.050 Å to 0.050 Å in increments of 0.010 Å. This implies 121 possible combinations of P_3 and P_4 and thus the same number of FEFF calculations. For a change of these parameters no improvement of the fit could be achieved. The structure with $\Delta(Ga - N_B) = 0.000$ Å and $\Delta(Ga - N_C) = 0.000$ Å caused the best-fit of the corresponding spectrum. Hence the best-fit structure remains the same as after the first optimization process.

Optimization of Parameters P_5 and P_6

The next optimization level refers to changes of the $Ga - O_B$ and $Ga - O_C$ bonds in the range from -0.050 Å to 0.050 Å in increments of 0.010 Å. Therefore the parameters P_5 and P_6 are changed equally to P_3 and P_4. In this case the fit could be improved for a change of $\Delta(Ga - O_B) = 0.020$ Å and $\Delta(Ga - O_C) = -0.010$ Å resulting in a goodness of fit of $\chi^2_\nu = 36.81$. The new improved fit is presented in figure 5.16. The improvement of this fit compared to the fit in figure 5.14 is marginal, but recognizable and reflects the slight improvement of the chi-square value.

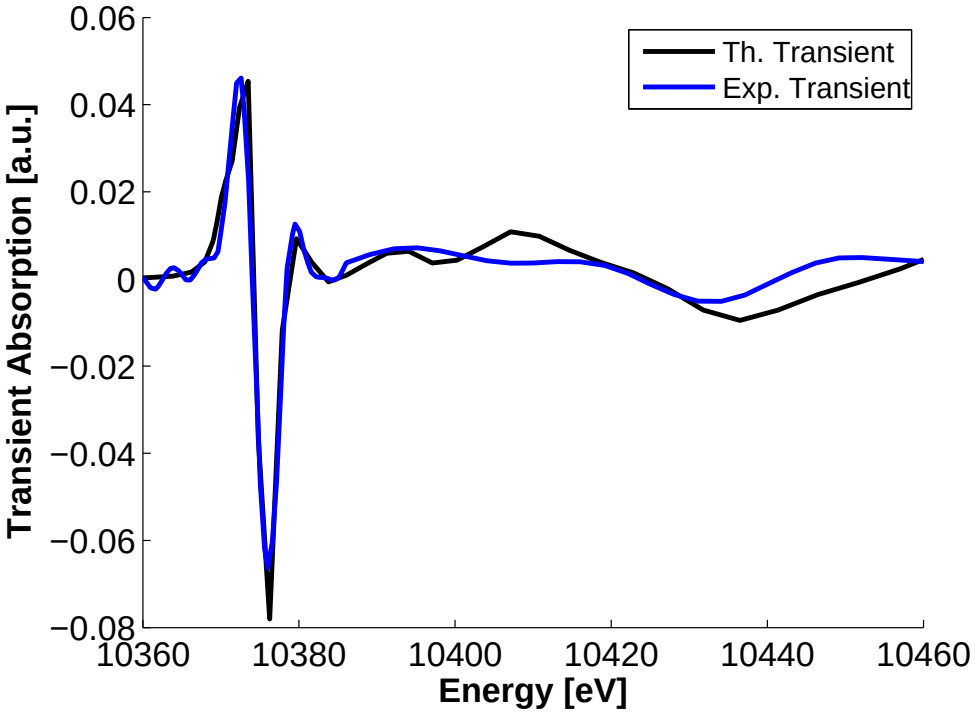

Figure 5.16.: *Best-fit after optimization of parameters P_5 and P_6, representing the $Ga-O_B$ and $Ga-O_C$ bond distance changes.*

Optimization of Parameter P_7

In the last optimization level the whole A-quinoline-ring of the new best-fit structure was rotated around the gallium atom in the plane spanned by the atoms Ga, N_A and O_A (compare figure 5.10) by an angle varying from $-5.0\,^\circ$ to $5.0\,^\circ$ in increments of $0.2\,^\circ$. This implies a variation of the N_A-Ga-N_B angle. The best-fit was achieved for an angle change of $-0.200\,^\circ$ resulting in a $\chi^2_\nu = 36.39$. The final fit results of the three optimization levels, which improved the fit are plotted together in figure 5.17. The fits differ only slightly but especially the changes of

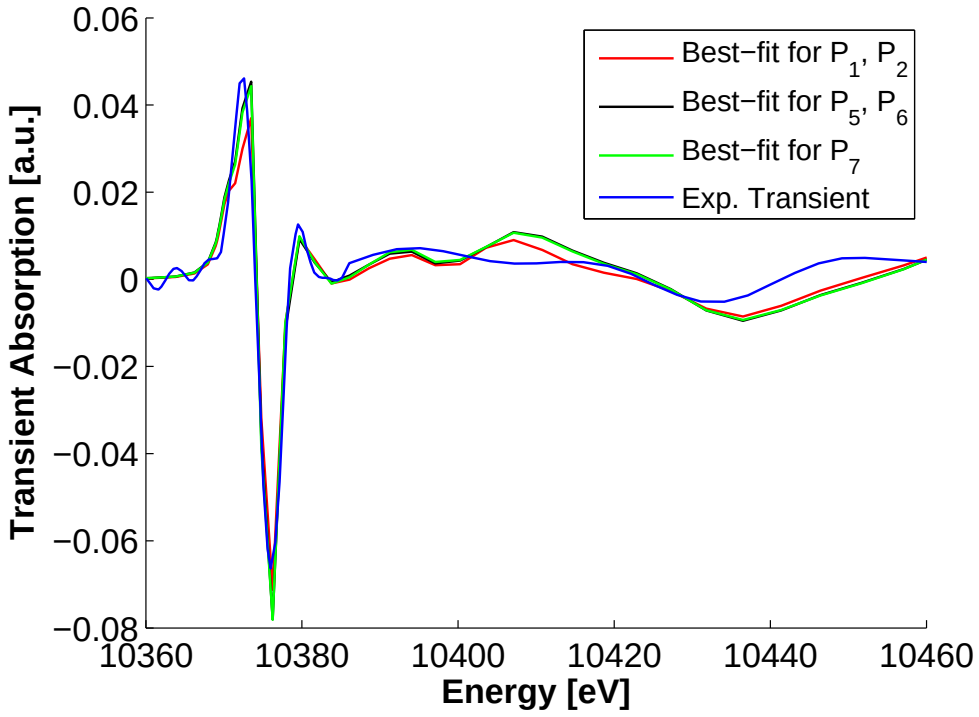

Figure 5.17.: *Experimental transient spectrum and the best-fits of the three steps of optimization 1. The second step leads to a better agreement at the first maximum. The third step, where P_7 for the N_A-Ga-N_B angle is optimized, has only low impact on the fit result.*

parameters P_5 and P_6 result in an improvement in the region of the first peak (feature A) of the transient while parameter P_7 has only minor impact and can nearly be neglected. In table 5.3 the structural changes of the specific bonds and the fit result of the first optimization process are listed.

So far a best-fit for the experimental spectrum was found and the best-fit structure causing this spectrum is assumed to be the excited state structure of the Gaq3 molecule. However, one has to keep in mind that this spectrum is based on parameters, which are chosen to be minimized firstly, and on the initial values of these parameters. The optimization process used so far accounted only a limited number of parameter combinations and thus the actual minimum might be just a local minimum.

Influence of Chronological Order on Parameter Optimization

During the first optimization process the A-quinoline-ring of the molecule was changed at first, since structural changes of large impact were expected due to the theory. It is in principle conceivable that another combination of parameter optimizations leads to another minimum, for which the $\Delta(Ga-N_A)$ and $\Delta(Ga-O_A)$ changes are different to those of this first optimization. Consequently optimization processes were also conducted for other chronological orders. The results of five of these processes are presented in the following sections. Table 5.3 summarizes the results. In optimizations 3,4 and 5 four parameters and in optimization 6 only two parameters were optimized. The corresponding transient spectra and the contour plots of these optimizations are presented in appendix A.3.

Optimization 2 In this optimization process the parameters were optimized in the order P_7, P_5 and P_6, P_3 and P_4 and P_1 and P_2. This is the reversed chronological order in comparison to the first optimization. The high χ^2_ν of 138.42 for the initially optimized parameter P_7 points to a bad fit agreement and means that the structure merely varied by the angle does not lead to a good fit result. The next parameter variations improve the fit clearly, but are not in agreement with the

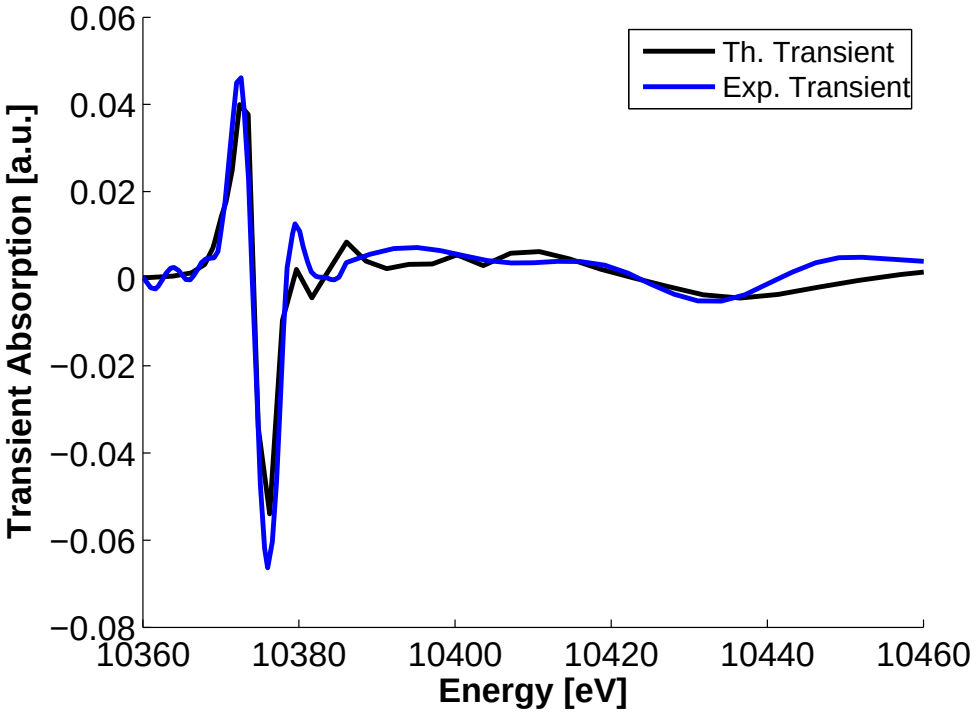

Figure 5.18.: *Overall best-fit of optimization 2 with* $\chi^2_\nu = 32.65$.

parameters from the first optimization process, though the resulting fit shows a very similar χ^2_ν value. After the third optimization level with P_3 and P_4 the lowest χ^2_ν of 32.65 is reached already. Changes of P_1 and P_2 do not further improve the structure since the contour plot in figure 5.19

shows a minimum χ^2_ν for $\Delta(Ga-N_A) = 0$ Å and $\Delta(Ga-O_A) = 0$ Å. In figure 5.18 the overall best-fit structure of this optimization procedure is depicted.

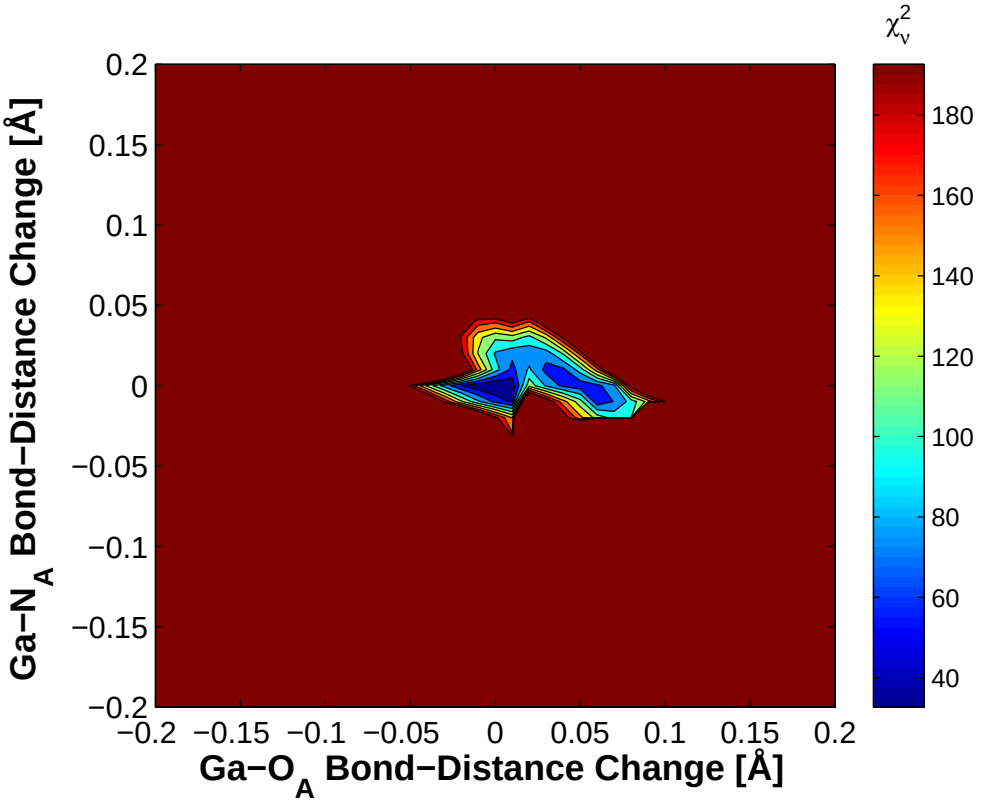

Figure 5.19.: *Contour plot of the last step of optimization 2 in which the parameters P_1 and P_2 were varied. χ^2_ν is minimal for $Ga - N_A = 0$ Å and $Ga - O_A = 0$ Å, which means that the structure from the previous optimization level could not be further improved. The result is also in contrast to the optimization 1 (for comparison see figure 5.15).*

Optimization 3 The first optimized parameters are P_3 and P_4 referring to the $Ga - N_B$ and $Ga - N_C$ bonds. The corresponding contour plot in figure A.3 shows a minimum for $\Delta(Ga - N_B) = -0.040$ Å and $\Delta(Ga - N_C) = 0.050$ Å with a χ^2_ν of 67.46. The transient plot for this parameter combinations is shown in figure A.4. Afterwards the parameters P_1 and P_2 were optimized resulting in a best-fit structure for $\Delta(Ga - N_A) = -0.040$ Å and $\Delta(Ga - O_A) = 0.050$ Å. The best-fit with $\chi^2_\nu = 60.46$ is depicted in figure A.5 in appendix A.3.

Optimization 4 The first optimized parameters are P_5 and P_6 referring to the $Ga - O_B$ and $Ga - O_C$ bonds. The corresponding contour plot in figure A.6 shows a minimum for $\Delta(Ga - O_B) = 0.090$ Å and $\Delta(Ga - O_C) = -0.050$ Å with a χ^2_ν of 94.55. The subsequent optimization of parameter P_1 and P_2 results in a χ^2_ν of 59.46 for $\Delta(Ga - N_A) = -0.020$ Å and $\Delta(Ga - O_A) = 0.050$ Å and improves the fit by about 37 %.

Optimization 5 This optimization process relates to parameters P_3, P_5, P_1 and P_2. P_3 and P_5 refer to the B-quinoline-ring and the purpose to optimize these two parameters primarily is to check if XANES is sensitive to distinct between different quinoline-rings. From a chemical point of view the three quinoline-rings are almost identical, but show different bond lengths to the central gallium atom - a fact which is shown by crystallographic data and theoretical calculations consistently (see table 5.2). The initial structure of this optimization is the ground state structure and the bond lengths $Ga-N_B$ and $Ga-O_B$ were changed congruently to $Ga-N_A$ and $Ga-O_A$ in the first optimization process.

The best-fit structure for P_3 and P_5 shows the bond length changes $\Delta(Ga-N_B) = 0.050$ Å and $\Delta(Ga-O_B) = -0.020$ Å, which are identical to those determined for the optimization of parameters P_1 and P_2 for the A quinoline-ring. The resulting χ^2_ν value is 49.68. The contour plot in figure A.9 for $Ga-N_B$ and $Ga-O_B$ exhibits exactly the same features as the contour plot for P_1 and P_2. The minimum is at the same position. The only difference is the absolute χ^2_ν-value which is about $34\ \%$ higher than for the first optimization with $\chi^2_\nu = 37.00$. This structure was hereafter optimized for P_1 and P_2, whereas the minimum χ^2_ν of 33.06 was achieved for $\Delta(Ga-N_A) = -0.010$ Å and $\Delta(Ga-O_A) = 0.020$ Å.

Optimization 6 This optimization process relates to parameters P_4 and P_6, which correspond to the $Ga-N_C$ and $Ga-O_C$ bonds of the C-quinoline-ring. The idea for the optimization of these bonds is to analyze if the result for both, the A-quinoline-ring and the B-quinoline-ring, showing identical bond length changes, can also be observed for the C-ring. The best-fit structure for P_4 and P_6 exhibits the bond length changes $\Delta(Ga-N_C) = 0.060$ Å and $\Delta(Ga-O_C) = -0.040$ Å. The resulting χ^2_ν value is 69.00, which is an increase of about $86\ \%$ with respect to optimization 1 ($\chi^2_\nu = 37.00$) and of about $39\ \%$ with respect to optimization 5 $\chi^2_\nu = 49.68$. The bond changes are slightly larger than those optimized for the A- and B-ring, but the tendency - an increase of the $Ga-N$ bond and a shrinking of the $Ga-O$ bond - is the same. The corresponding contour plot for $\Delta(Ga-N_C)$ and $\Delta(Ga-O_C)$ is depicted in the appendix in figure A.12. It reveals the same features known from the two previous optimizations 1 and 5. The best-fit with $\chi^2_\nu = 69.00$ is shown in figure A.13.

Results of Optimization Processes

Parameter	Structural Change	Value	χ^2_ν
1. Optimization Process			
P_1	$\Delta(Ga - N_A)$	0.050 Å	37.00
P_2	$\Delta(Ga - O_A)$	−0.020 Å	
P_3	$\Delta(Ga - N_B)$	0.000 Å	37.00
P_4	$\Delta(Ga - N_C)$	0.000 Å	
P_5	$\Delta(Ga - O_B)$	0.020 Å	36.81
P_6	$\Delta(Ga - O_C)$	−0.010 Å	
P_7	$\Delta(N_A\text{-}Ga\text{-}N_B)$	−0.200 °	36.39
2. Optimization Process			
P_7	$\Delta(N_A\text{-}Ga\text{-}N_B)$	0.800 °	138.42
P_5	$\Delta(Ga - O_B)$	0.070 Å	46.14
P_6	$\Delta(Ga - O_C)$	−0.040 Å	
P_3	$\Delta(Ga - N_B)$	−0.030 Å	32.65
P_4	$\Delta(Ga - N_C)$	0.020 Å	
P_1	$\Delta(Ga - N_A)$	0.000 Å	32.65
P_2	$\Delta(Ga - O_A)$	0.000 Å	
3. Optimization Process			
P_3	$\Delta(Ga - N_B)$	−0.040 Å	67.46
P_4	$\Delta(Ga - N_C)$	0.050 Å	
P_1	$\Delta(Ga - N_A)$	−0.040 Å	60.46
P_2	$\Delta(Ga - O_A)$	0.050 Å	
4. Optimization Process			
P_5	$\Delta(Ga - O_B)$	0.090 Å	94.55
P_6	$\Delta(Ga - O_C)$	−0.050 Å	
P_1	$\Delta(Ga - N_A)$	−0.020 Å	59.46
P_2	$\Delta(Ga - O_A)$	0.050 Å	
5. Optimization Process			
P_3	$\Delta(Ga - N_B)$	0.050 Å	49.68
P_5	$\Delta(Ga - O_B)$	−0.020 Å	
P_1	$\Delta(Ga - N_A)$	−0.010 Å	33.06
P_2	$\Delta(Ga - O_A)$	0.020 Å	
6. Optimization Process			
P_4	$\Delta(Ga - N_C)$	0.060 Å	69.00
P_6	$\Delta(Ga - O_C)$	−0.040 Å	

Table 5.3.: *Fit results of the structure optimizations.*

Influence of the Photoexcitation Yield on Parameter Optimization

All optimizations shown in the previous section were performed for a photoexcitation yield of $90\ \%$ as determined in chapters 4.2.4 and 5.2.1. In this chapter the influence of different excitation yields on the parameter optimization is analyzed. As described in chapter 5.2.9 the measured transient has to be corrected for the photoexcitation yield by usage of equation 5.5 in order to obtain the transient spectrum T_{EX}^{100} for $100\ \%$ probed molecules in the excited state. Here the analysis of the parameters P_1 and P_2 was performed for assuming $f = 90\ \%$, $f = 75\ \%$, $f = 50\ \%$ and $f = 33\ \%$. Contour plots for the χ^2_ν as function of parameters P_1 and P_2 in dependence of the photoexcitation yields are shown in figure 5.20. It can be observed that with increasing

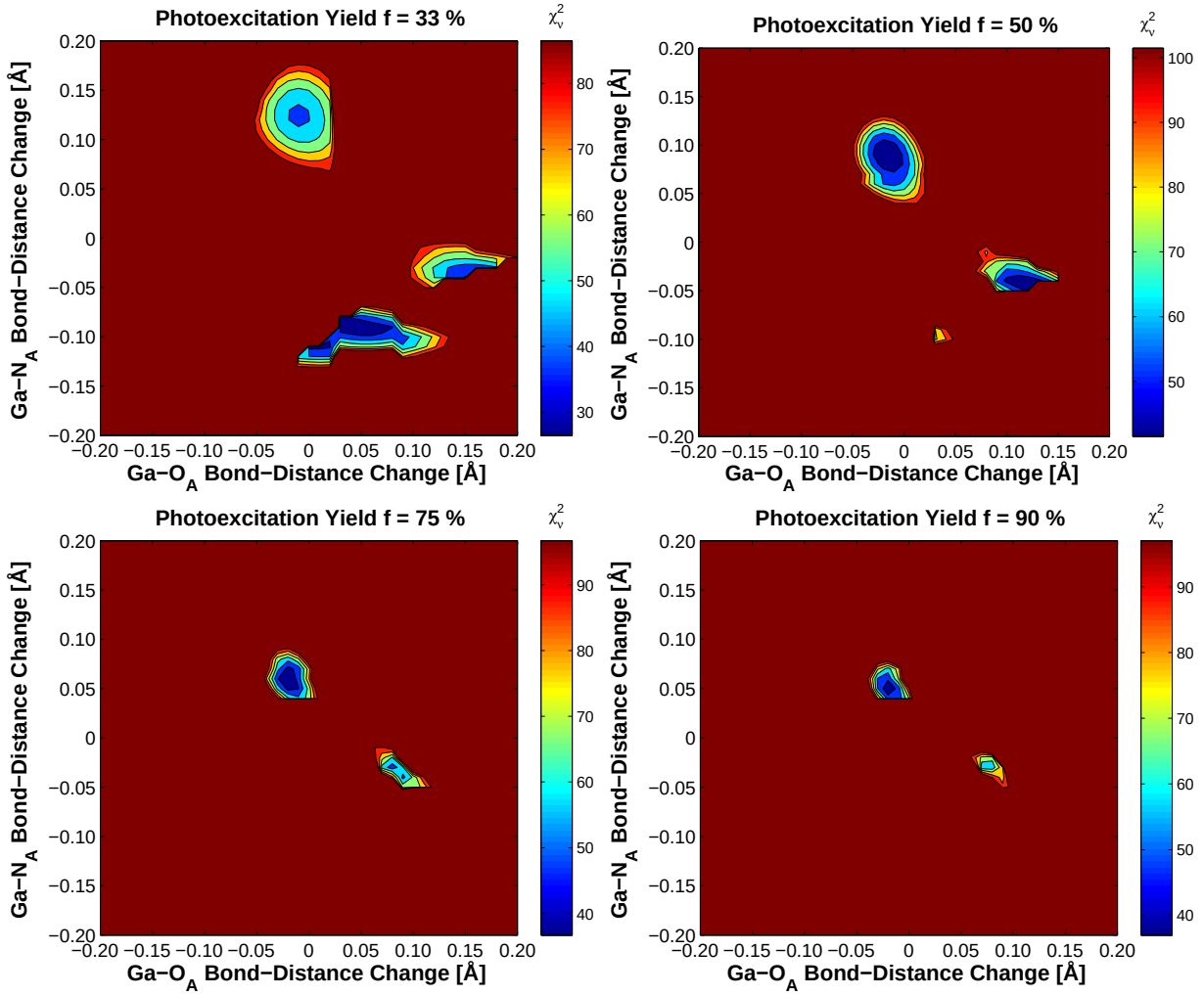

Figure 5.20.: *χ^2_ν contour plots for the optimization of the $Ga-O_A$ and $Ga-N_A$ bonds of the A-quinoline-ring in dependence of different photoexcitation yields. The smaller the yield, the larger are the expected bond length changes.*

photoexcitation yield lower χ^2_ν values are reached for shorter bond distance changes. This can be explained by the fact that the corrected transient spectrum $T_{EX}^{100} = \frac{1}{f} \cdot T_{EX}(E,t)$ scales inversely

proportional to f. The higher the yields the smaller is the scaling factor and thus the resulting transient spectrum has a smaller amplitude which leads in the end to good fit results for shorter bond distance changes. For $f = 33\ \%$ the best-fit is reached for the bond distance changes $\Delta(Ga - N_A) = -0.090$ Å and $\Delta(Ga - O_A) = 0.040$ Å. This means, in this case an elongation of the $Ga - O_A$ bond and a shrinking of the $Ga - N_A$ bond is observed. This is in strong contrast to the best-fit structure of $\Delta(Ga - N_A) = 0.050$ Å and $\Delta(Ga - O_A) = -0.020$ Å for $f = 90\ \%$. However, for low excitation yields a unique result can not be obtained, even though only two parameters are considered here. This is shown by the relatively large bluish colored areas in the contour plots, indicating several possible solutions with good chi-square values. In contrast for $f = 90\ \%$ only one differentiated solution can be found. This analysis shows how crucial the precise determination of the excited state molecule fraction for qualitative and quantitative correct conclusions is.

5.2.10. Fitting of Spectra (Model 2)

This chapter presents the results based on optimization model 2 described in chapter 5.2.8. In order to compare this model with model 1, which led to the previously presented results, the parameters P_1 and P_2 referring to the $Ga-N_A$ and $Ga-O_A$ bond length changes were optimized in the same increment of 0.010 Å from -0.100 Å to $+0.100$ Å. This optimization process is equivalent to optimization 1 of model 1 (see chapter 5.2.9). The contour plots are shown in figure 5.21. The left contour plot shows χ^2_ν values for bond elongations of the $Ga - N_A$ bond

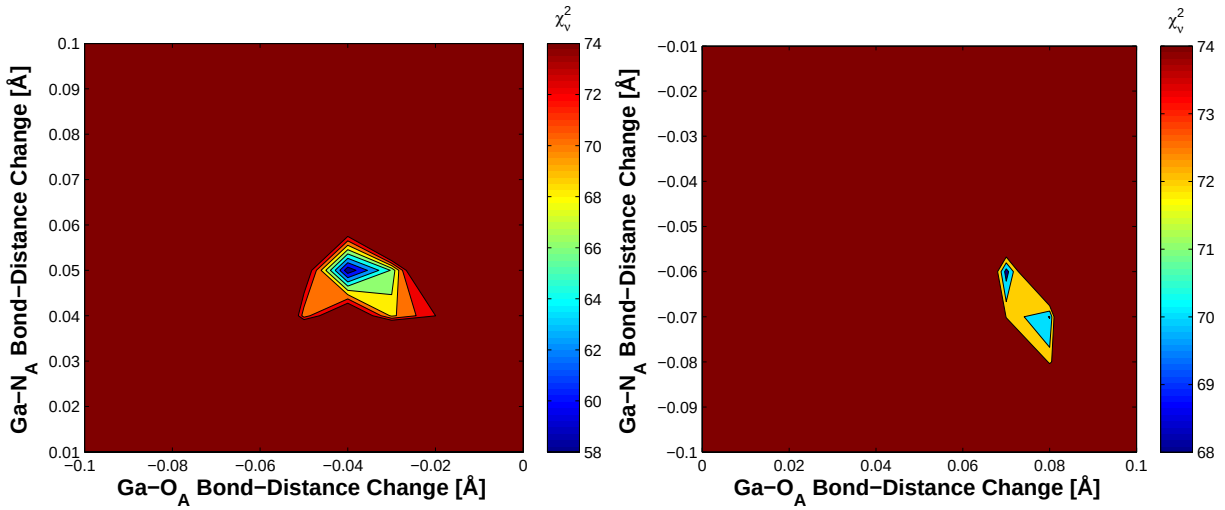

Figure 5.21.: *χ^2_ν contour plots for the optimization of the $Ga-O_A$ and $Ga-N_A$ bonds of the A-quinoline-ring. Left: χ^2_ν for elongation of the $Ga - N_A$ bond and shortening of the $Ga - O_A$ bond. Right: χ^2_ν for opposite bond distance changes.*

and contractions changes of the $Ga - O_A$ bond. The right contour plot shows χ^2_ν values for the opposite bond length changes. Similar to model 1 in this model an elongation of the $Ga - N_A$ bond and a shortening of the $Ga - O_A$ bond leads to the best-fit agreement (see blue colored

island in the left contour plot). The lowest χ^2_ν value of 58.56 could be reached for $\Delta(Ga-N_A) = 0.050$ Å and $\Delta(Ga-O_A) = -0.040$ Å. Hence, the bond distance changes are almost the same as obtained for model 1 with $\Delta(Ga-N_A) = 0.050$ Å and $\Delta(Ga-O_A) = -0.020$ Å, but the $\chi^2_\nu = 58.56$ is 58% larger than the $\chi^2_\nu = 37.00$ for the best-fit of model 1. For this reason model 1 is considered to be the superior model for the optimization of the Gaq3 excited state structure. Figure 5.22 shows for comparison the best-fits of model 1 and 2 together with the experimental transient spectrum.

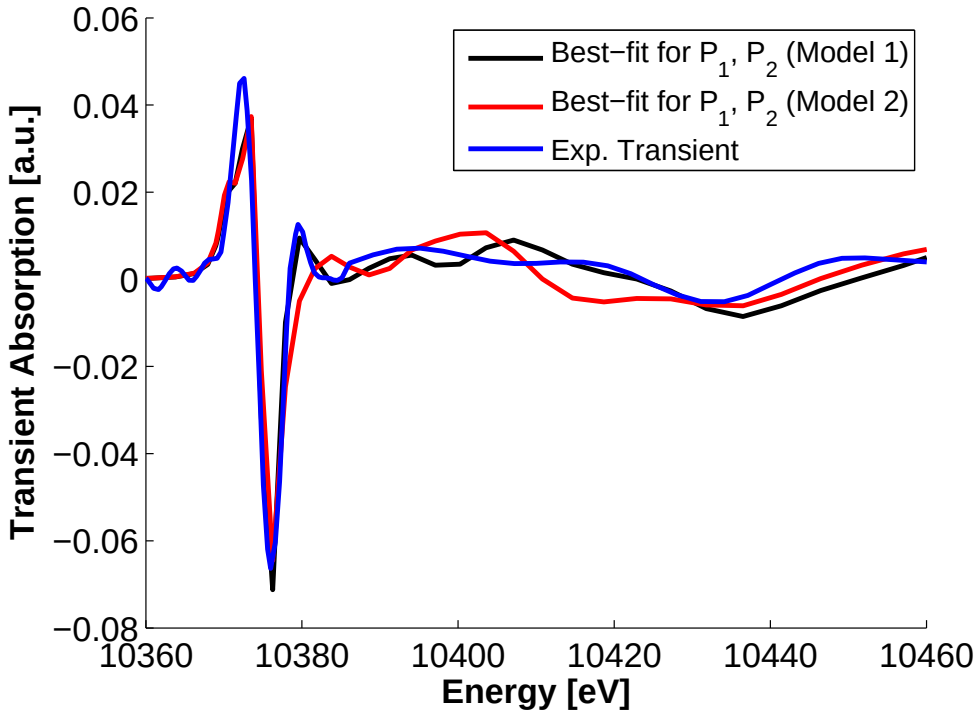

Figure 5.22.: *Best-fits for optimization of parameters P_1 and P_2 for model 1 (black curve) with $\chi^2_\nu = 37.00$ and for model 2 (red curve) with $\chi^2_\nu = 58.56$. The experimental transient spectrum is plotted in blue.*

5.2.11. Analysis with FitIt

Fitting of XANES allows a quantitative determination of the geometrical structure of the sample molecule and it was shown that fitting of XANES spectra depends on a large number of structural parameters which can be combined in many ways, whereas the single parameters are heavily dependent from each other. Each parameter combination results in a specific structure for which a full XANES spectrum was calculated. As explained in chapter 2.2.2 the program FitIt provides to calculate a spectrum by approximation of an interpolation polynomial for a given set of parameters. In this way a huge number of spectra can be calculated in much less computation time. The program was used to fit the experimental transient spectrum T^{100}_{EX} of Gaq3, presented in the

previous sections. In figure 5.23 a fit performed by FitIt for parameters P_1 and P_2 is compared to the fit from optimization process 1, shown in chapter 5.2.9. Both fits refer to the same bond distance changes of $\Delta(Ga - N_A) = 0.050$ Å and $\Delta(Ga - O_A) = -0.020$ Å. The agreement

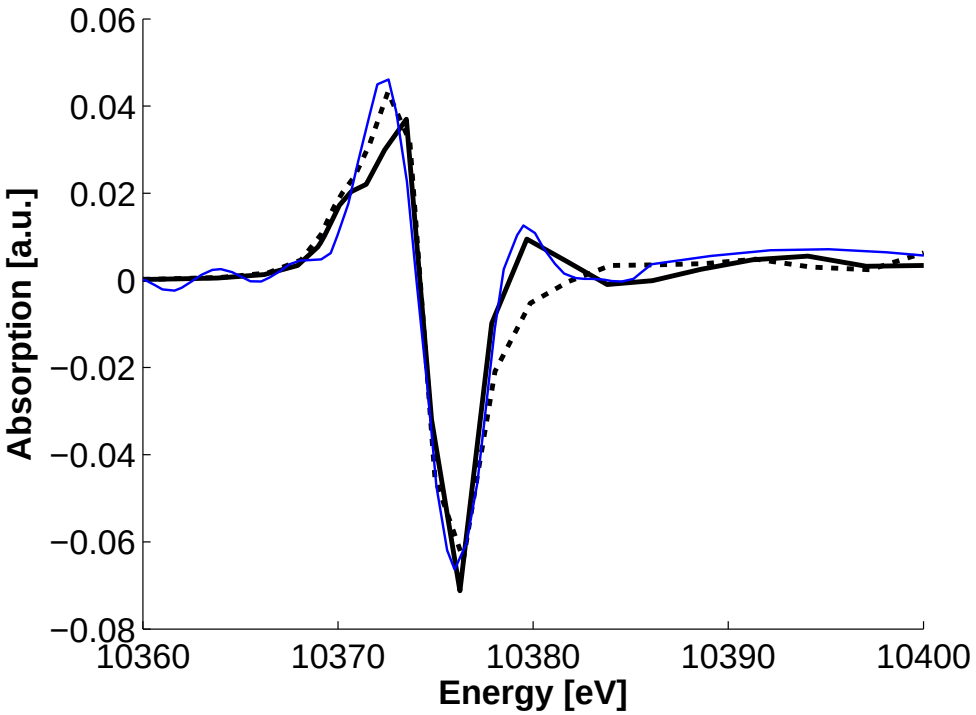

Figure 5.23.: *Fit results with best-fit performed by FitIt (black dashed line) and best-fit of the FEFF calculated spectra (black solid line). Both fits belong to a change of the parameters P_1 and P_2 of $\Delta(Ga - N_A) = 0.050$ Å and $\Delta(Ga - O_A) = -0.020$ Å. The FitIt transient reflects slightly better the first peak (A-feature) of the experimental transient (blue line), but does not fit to the little third small peak (C-feature), which is resolved by the FEFF fit.*

with the experimental transient spectrum of both fits is good, however, they show differences at the first (feature A) and third peak (feature C) of the experimental transient. The fits performed by FitIt highly depend on the construction of the interpolation polynomial and are therefore less accurate than the FEFF calculation which calculates a full spectrum. Different usage of terms for the interpolation polynomial reflects into completely different results. Reliability for the results is ensured only for a correctly defined interpolation polynomial.

5.2.12. Summary and Conclusion

The different optimization processes show that the variation of structural parameters leads to several best-fit transient spectra which are in sense of the reduced chi-square criteria in good agreement with the experimental measured spectrum. During the different optimization processes a convergence of the reduced chi-square algorithm could be obtained. It was shown that

in dependence of the starting parameters and the chronological order, in which the parameters are optimized, good fits for completely different parameter constellations can be achieved (see table 5.3). Though the overall best-fit agreement is $\chi^2_\nu = 32.65$ for the structure optimized in process 2, several further minima with similar χ^2_ν were found, which also present solutions for structural changes of the excited Gaq3 molecule. This means for such a large parameter space, in which the three quinoline-rings and their atoms are treated equally, the optimization model did not provide an unique result.

Hence the theoretical calculations were used to make physical meaningful assumptions for the parameter optimizations i.e. a limitation of the parameter space to the $Ga-N$ and $Ga-O$ bonds only. A comparison of the optimizations of the initial parameters P_1 and P_2 in optimization 1 and of the initial parameters P_3 and P_5 in optimization 5 shows clearly that the resulting fits are very similar and the absolute bond distance changes are equal, no matter if the A-quinoline-ring or the B-quinoline-ring is changed. A similar observation can be also made for the C-quinoline-ring in optimization 6. This means for the limitation of the parameters to the $Ga-N$ and $Ga-O$ bonds, all three optimizations show by trend an elongation of the nitrogen-gallium bond and an shrinking of the oxygen-gallium bond. The best χ^2_ν-value for the initial optimization of the $Ga-N$ and $Ga-O$ bonds is reached for the A-quinoline-ring with $\chi^2_\nu = 37.00$. This value is $\sim 26\ \%$ lower than the $\chi^2_\nu = 49.68$ for the B-quinoline-ring and it is $\sim 46\ \%$ lower than the $\chi^2_\nu = 69.00$ for the C-quinoline-ring. From this it can be inferred that most probably the A-quinoline-ring changes, which is in agreement with the theoretical calculations.

It should be noted that intraligand changes except for the $O-C$ bond were not considered by the optimization model. Theoretical calculations predict also relatively large changes for the C-atoms of the A-ligand (see table 5.2). In view of the sensitivity of the theoretical transient spectra towards little atomic bond distance changes of 0.010 Å for the $Ga-N$ and $Ga-O$ bonds, also intraligand atomic bond distances can be expected to have some impact on the fitting procedure. However, this impact will be much lower since these atoms correspond to the second shell coordination sphere. An inclusion of these changes in the model would strongly increase the already high number of possible parameter combinations and cannot be considered as a promising approach for the structure determination of the first excited state of Gaq3.

The following results can be concluded:

- The experimental transient spectrum can be fitted by theoretically calculated difference spectra.
- Several different parameter combinations lead to good fit results and hence a global unique result for the best-fit structure cannot be determined in the large parameter space.
- Under physical meaningful assumptions provided by theoretical calculations, it can be shown that most probably the A-quinoline-ring is changed during the $S_0 \rightarrow S_1$ transition.
- The theoretically predicted shortening of the nitrogen-gallium bond and the alternating elongation of the oxygen-gallium bond of the A-quinoline-ring (see chapter 5.2.7) can not

be confirmed. In contrast to this, all good fit results show an elongation of the nitrogen-gallium bond and a shrinking of the oxygen-gallium bond. This observation could be made for all three quinoline-rings A,B and C in the optimization processes 1,5 and 6. The best-fit structure with $\chi^2_\nu = 37.00$ is very close to the overall best-fit structure with $\chi^2_\nu = 32.65$.

- The theoretical transient spectra are sensitive to little atomic bond length changes of 0.010 Å.
- A change of the bond angle has only minor impact on the theoretical transient spectrum.
- The photoexcitation yield has a strong impact on the analysis of bond distance changes in the excited state.

5.3. Pump-Probe EXAFS Spectroscopy of Gaq3

EXAFS can be utilized for reliable measurements of the first shell atomic distances from the absorber atom and is much more sensitive to bond distance changes than XANES, which - as it was shown - does not deliver an unique result for the bond length changes of Gaq3.
The quantitative analysis of EXAFS by using the EXAFS equation developed by Stern, Sayers and Lytle [69] is nowadays a well proven and standard method. The equation was introduced and described already in chapter 2.1.2:

$$\chi(k) = S_0^2 \sum_j \frac{N_j e^{-2\sigma_j^2 k^2} e^{-2R_j/\lambda(k)} f_j(k)}{kR_j^2} \sin[2kR_j + 2\delta_c + \Phi] \ . \tag{5.8}$$

This parameterized form of the EXAFS $\chi(k)$ can be used to fit the measured EXAFS and to extract information about the local atomic arrangement around the central absorber atom. In the next section the procedure for EXAFS data analysis is explained.

5.3.1. Analysis of EXAFS

In an EXAFS data set the absorption coefficient is given as function of the energy. The EXAFS is defined by equation 2.5. Before starting the analysis using the EXAFS equation 5.8, a data reduction to the meaningful parts has to be conducted. This procedure is done using the software Athena [113], which uses the IFEFFIT code [117] and provides a graphical user interface. The procedure includes separate steps as in [63], which are explained in the following and illustrated in figure 5.24.

1. Conversion of measured intensities to $\mu(E)$.
2. Subtraction of a smooth pre-edge function from $\mu(E)$.
3. Identification of the threshold energy E_0 which is the energy of the maximum of the first derivative of $\mu(E)$.

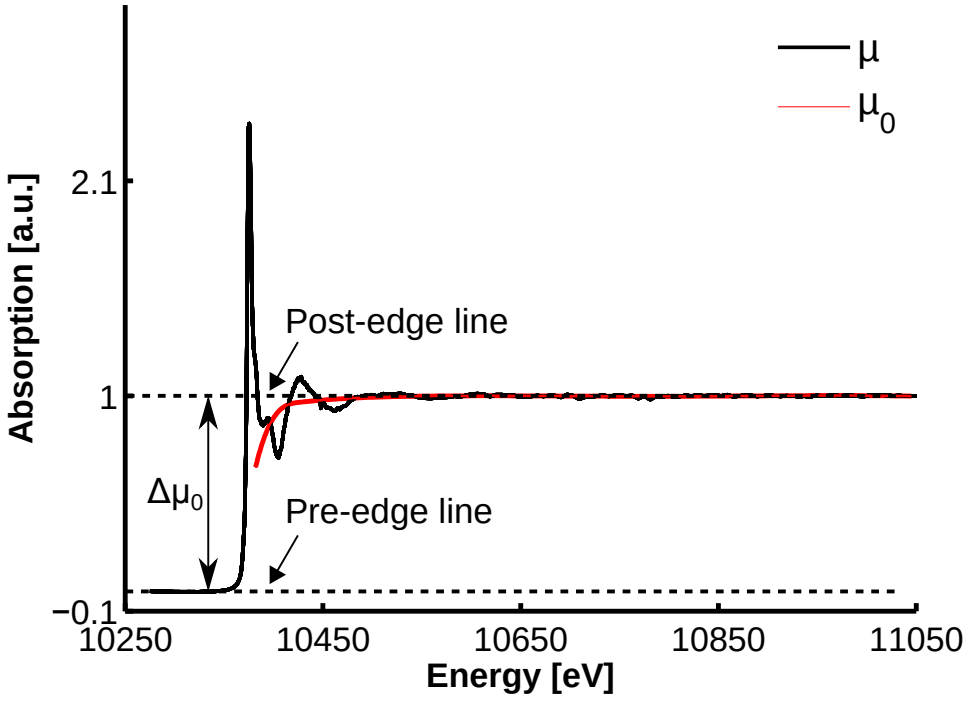

Figure 5.24.: *Absorption spectrum of Gaq3. Several steps (see text) have to be carried out to extract the EXAFS from the measured absorption data. The raw spectrum is normalized such that the pre-edge is 0 and that the post-edge is 1. $\Delta\mu_0(E)$ is the edge jump and the difference of pre-edge line and post-edge line.*

4. Normalization of $\mu(E)$ in the way that the pre-edge is 0 and the post-edge is 1.
5. Removing of the background of the post-edge by fitting a smooth function to the spectrum.
6. Identification of the edge jump $\Delta\mu_0(E)$ which is at this point the difference between post-edge line and pre-edge line.
7. Transfer of the spectra from energy to k-space using equation 2.6: $k = \sqrt{2m_e(E - E_0)/\hbar^2}$.
8. Weighting of the resulting EXAFS $\chi(k)$ by k^n, where $n = 1, 2, 3$.
9. Fourier transformation of $\chi(k)$ into R-space.

After performing step 7, data reaches the form matching to the EXAFS equation described by equation 2.5. Since it is convenient to express the EXAFS equation in terms of k one switches from the energy into the k-space. The background function simulates the absorption μ_0, which an isolated atom without neighboring atoms would have. In this way the low frequency part of the spectrum is removed but not the EXAFS signal itself. In order to reinforce also smaller oscillations at higher k-values it is common to weight the raw $\chi(k)$ by a factor of k^n whereas n is between 1 and 3. By use of a window function a special k-range of the $k^n\chi(k)$ spectrum

can be selected for further analysis such that only contributions from the spectrum within the window will be accounted. In this way the high frequency noise, appearing for higher k-values can be cut off. A very important step of the EXAFS analysis, which makes it so powerful is the Fourier transformation of the EXAFS spectrum $\chi(k)$. It provides a *Radial Distribution Function (RDF)*, in which the frequencies correspond to the distances between the absorber atom and its neighboring atomic shells. A peak at position R of the RDF corresponds to the average radial distance R_j of the j^{th} atom. However, this is not a direct measurement of the real distance because the distance in the fourier transformation is about 0.2 Å to 0.5 Å shorter than the actual distance due to a phase shift $2\delta_c + \Phi$ [61, 118]. To extract correct information about the bond distances and also other EXAFS parameters the data have to be compared to accurate theoretical or experimental standards. A theoretical approach is provided by XAFS programs like FEFF and ARTEMIS [113], which were used for this work (see chapter 2.2.2). The software ARTEMIS adjusts the non k-dependent parameters S_0^2, N_j, σ_j^2 and R_j^2 appearing in the EXAFS equation to fit the experimental data, while the k-dependent parameters $2\delta_c + \Phi$ (total phase) and $f_j(k)$ (backscattering amplitude) are calculated by FEFF. The latter are not varied during the fitting procedure. For the non k-dependent parameters the user can provide the software with a starting value for the variation to carry out. The software tries to adjust the parameters such that the mathematical best-fit agreement is reached (ARTEMIS also uses the reduced chi-square algorithm as a quantity for fit agreement). But it is up to the user to decide if the parameters are in a physical meaningful frame.

An absolute crucial requirement for a successful EXAFS experiment, which is tailored to measure precisely bond distances is an adequate k-range. An often quoted formula for the best achievable resolution for the distinction of two bond distances is given in the following equation [119]:

$$\Delta R \geq \pi / 2\Delta k \ . \tag{5.9}$$

This means for a given k-range Δk the ability to distinguish between two bonds with a length difference of ΔR can be estimated. The accuracy to measure a single bond distance is usually much better and depends on the noise of the data and on the precision of the phase shift calculation by FEFF.

5.3.2. Pump-Probe EXAFS Spectra of Gaq3

The Pump-Probe EXAFS spectra were measured in analogy to the previous XANES spectra. To account for the longer energy range of 800 eV, a modification of the setup was used, in which the X-ray beam was not focused by refractive lenses, but with an achromatic KB-system (see chapter 4.1.5). The before mentioned analysis procedure was applied to the GS EXAFS spectrum as well as to the ES EXAFS spectrum. Thereby all normalization ranges and spline functions were kept constantly for the GS and the ES to assure that data reduction is equal and prospective differences can be fully accounted to the photoexcitation of the pump laser. The resulting normalized EXAFS spectra are shown in figure 5.25.

The red curve presents the GS spectrum A_{EX}^{GS} of Gaq3, whereas the green curve stands for

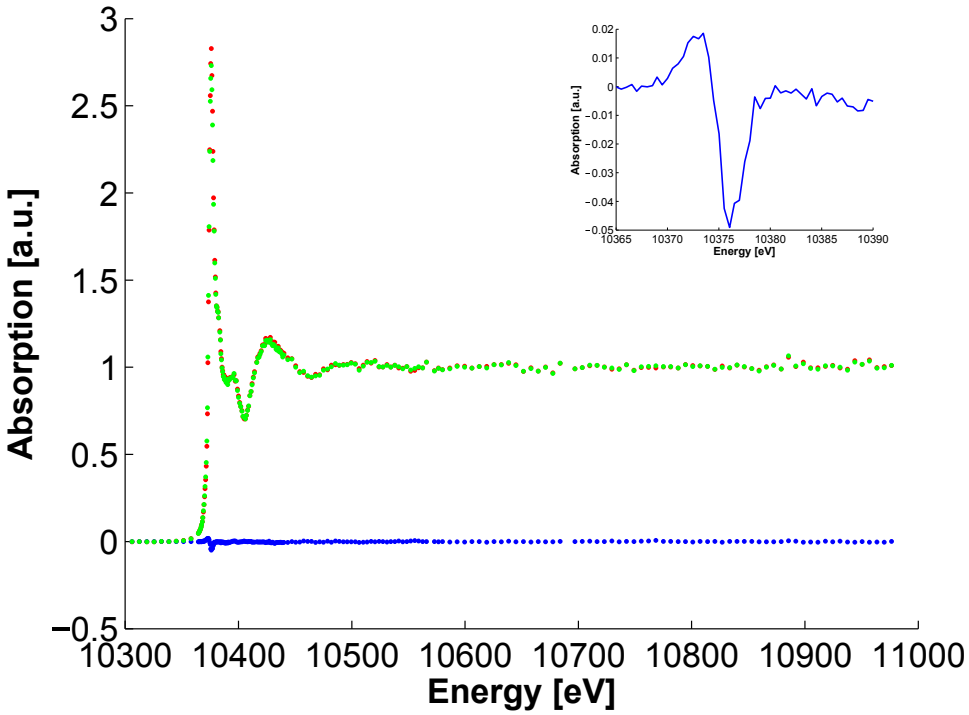

Figure 5.25.: *Normalized Gaq3 EXAFS spectra. The red data points refer to the ground state spectrum A_{EX}^{GS} and the green data points present the excited state spectrum A_{EX}^{ES}. The transient spectrum T_{EX} in blue reveals the same features known from the XANES measurements, while for higher energies the transient signal is constant. The inset shows a magnified section of T_{EX}.*

the normalized ES spectrum A_{EX}^{ES} deduced from the experimental transient difference spectrum T_{EX} in blue color applying equation 2.17. Here the photoexcitation yield was determined by comparison with the XANES measurement presented in chapter 5.2.4: We showed that the edge of the ES spectrum A_{EX}^{ES} is increased by $4.0\ \%$, while the whiteline is supressed by $2.7\ \%$ with respect to the GS spectrum A_{EX}^{GS}, whereas a photoexcitation yield of $f = 90\ \%$ was assumed. In reverse the corresponding transient T_{EX}^{100} can now be used to determine the photoexcitation yield of this new EXAFS measurement according to equation 5.5:

$$T_{EX}^{100} = \frac{1}{f} \cdot T_{EX}(E,t)\ , \tag{5.10}$$

where $T_{EX}(E,t)$ is the measured transient of the new EXAFS measurements. In this way we obtained a photoexcitation yield of about $f = 50\ \%$. This can be estimated as a reasonable value since the jet diameter was increased from $30\ \mu$m to $70\ \mu$m and the laser focus size of about $110\ \mu$m x $110\ \mu$m (v x h) was adapted to the larger jet size. Apart from the lower amplitude of the transient difference spectrum around the edge, the EXAFS measurement reveals the same features as the XANES measurement. Beyond the so far presented energy region of the XANES

spectra the transient difference signal is almost 0 and shows no further differences between the GS and ES spectra. In figure 5.26 the $\chi(k)$ functions for the GS (red curve) and the ES (green curve) as well as the corresponding RDFs for a k-weighting of 3, both obtained during the data reduction, are depicted. The $\chi(k)$ functions weighted by k^3 do not show significant differences

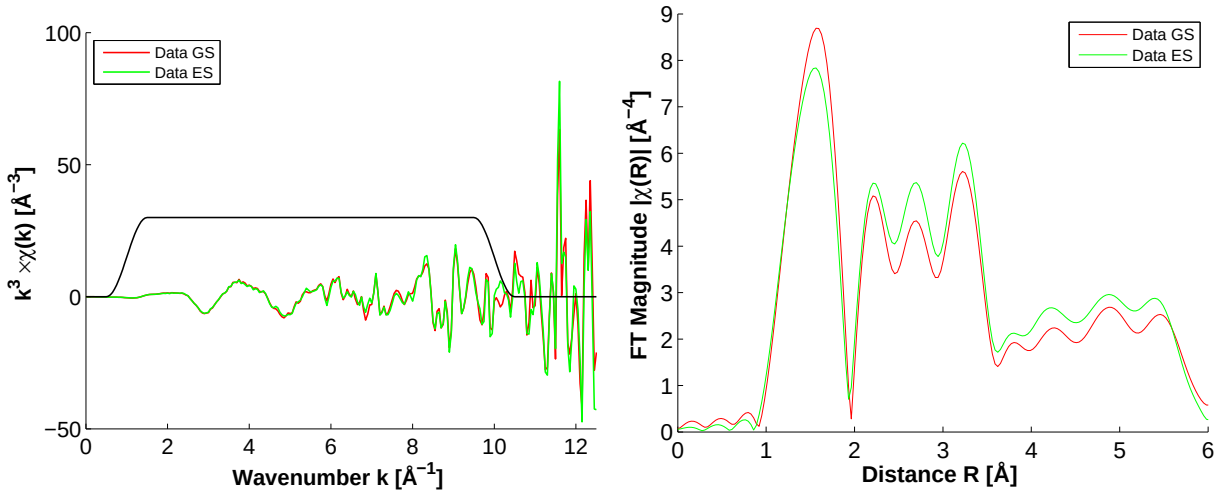

Figure 5.26.: *Left side: $\chi(k)$ for ground state (red) and excited state (green) of Gaq3 weighted by k^3. The window-function (black) is called Hanning-window. Right side: Fourier transformation of $\chi(k)$ delivers the corresponding RDFs for ground state (red) and excited state (green) weighted by k^3.*

between GS and ES for the first $4-5$ oscillations at lower k-values. Each $\chi(k)$ function was convoluted with a window function (Hanning) ranging from $k = 1-10$ to eliminate the noise at higher k and then fourier transformed in order to create the RDF. The first peak of the RDFs weighted by k^3 is the most interesting one providing the local arrangement of the next neighbors around the gallium atom. A slight shift of $R = 0.030$ Å of the ES RDF with respect to the GS RDF can be determined (see also figure 5.31).

5.3.3. Fitting of EXAFS

FEFF was used to calculate the theoretical amplitudes and phases for the GS and ES in order to fit the data in k and in R-space. As geometrical input for both states the crystallographic GS data GS_{cryst1} measured in X-ray diffraction experiments was taken. The GS and ES spectra were analyzed separately and independently from each other. Afterwards the structural information was extracted and compared. Here we present at first the GS spectrum together with the corresponding fits and afterwards the same for the ES. Figure 5.27 shows $\chi(k)$ weighted by k^3 together with its fit and the Hanning window giving the range for the fourier transformation into the R-space. Due to the large oscillations for high k only a limited k-range between $1-10$ delivered an analyzable RDF. The choice of the fourier transformation range is a compromise. A longer k-range allows a much better bond length resolution and includes generally more information. But large oscillations of $\chi(k)$ for high k result in several local maxima of

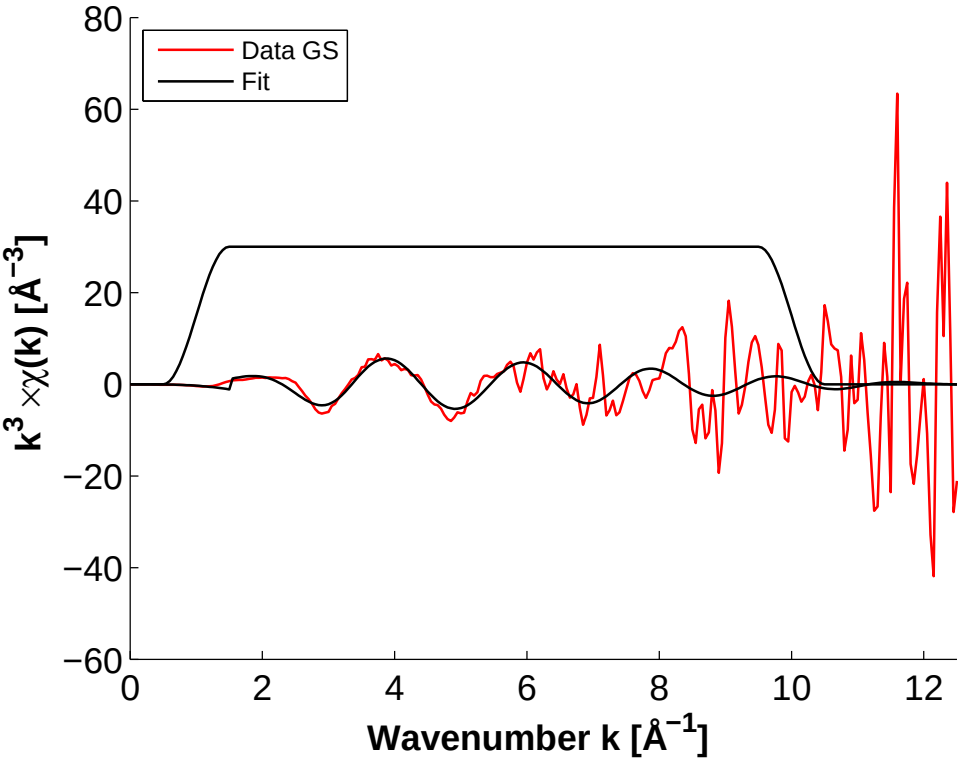

Figure 5.27.: *$\chi(k)$ of the Gaq3 ground state weighted by k^3 (red) and fit (black), performed within the Hanning window.*

the RDF whereas the single peaks cannot be unambiguously allocated to specific shells. Thus a k-range was chosen which delivered a RDF where the first peak was clearly distinguishable and the following peaks at higher R showed much less intensity. In figure 5.28 the RDF (red circles) is shown together with its best-fit (black curve) and the contributions from the first four single scattering paths presenting the photoelectron's scattering off the six nearest neighboring oxygen and nitrogen atoms. Two of these paths are degenerated and each counted twice (FEFF uses a so called degeneracy checker to identify equivalent paths (based on similar geometry, path reversal symmetry, and space inversion symmetry) [70]. Thus FEFF assigns the N_A atom and the N_C atom to the same path (N_C path) and counts it twice. The same applies to the O_A atom and the O_B atom which have the common O_A path. The contributing paths can be distinguished by their R-distance. So the N_B and N_C paths are slightly shifted towards higher R in comparison to the O_A and O_C paths. However, this difference is too short to be resolved in the resulting RDF. The fit was performed within the Hanning window from $R = 1-2$. Since we are primarily interested in the nearest neighboring bond distances only the single scattering paths of these atoms were taken into account. The fit result agrees very well with the experimental RDF and proves that the first large peak can be allocated to exactly these atoms. The RDF is not phase corrected and thus the peak appears for a too low R. The corrected final results for the fit are depicted in table 5.4. The relative high values for χ^2_ν of 151 for GS is presumably due to an underestimation of the statistical error and a relative high number of variables. The R-factor gives the relative missfit

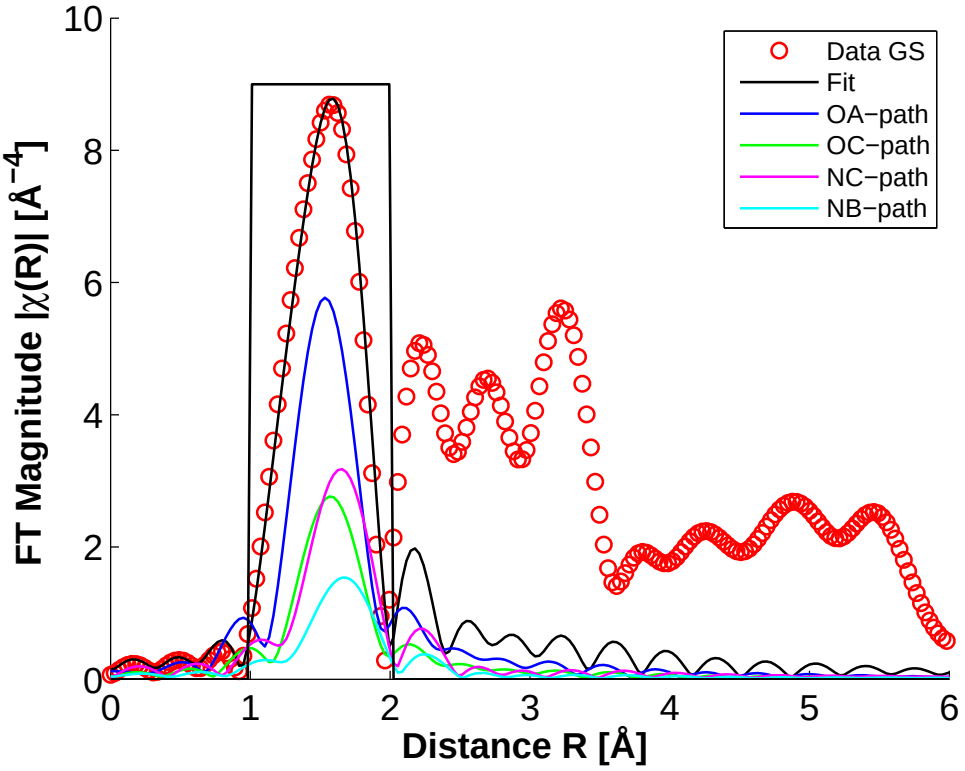

Figure 5.28.: *RDF of the Gaq3 ground state (red circles) together with the fit (black line) and the contributions from the single scattering-paths of the nearest neighbor atoms (different colors). Please note the FT magnitudes are not phase corrected and therefore they appear at shorter distances than the values obtained in Artemis and shown in table 5.4.*

and is independent from the statistical error as well as from the number of variables. A R-factor of 0.005 indicates that the fit agrees very well with the data. The same procedure was done for the ES state spectrum of Gaq3, whereas the same crystallographic data for the FEFF computation were used. This means the paths were kept constant with respect to the GS. Normalization and fitting range as well as type of window were also the same to the GS, so that all changes could be fully allocated to the photoexcitation. In figure 5.29 the $\chi(k)$ function is shown and in figure 5.30 the ES RDF for the Gaq3 is presented. The resulting best-fit within the Hanning window delivers nearly equal results for the bond distances.

Spectrum	$Ga - O_A$	$Ga - O_C$	$Ga - N_C$	$Ga - N_B$	χ^2_ν	$R - factor$
GS	1.97 ± 0.14 Å	2.01 ± 0.14 Å	2.12 ± 0.15 Å	2.15 ± 0.15 Å	151	0.005
ES	1.97 ± 0.10 Å	2.01 ± 0.10 Å	2.12 ± 0.11 Å	2.14 ± 0.11 Å	363	0.011

Table 5.4.: *Fit Results for the ground state S_0 and the first excited state S_1 of Gaq3.*

The fit agreement for the ES is slightly worse (factor ≈ 2) than for the GS. Apart from that the same considerations as for the GS can be made for the evaluation of the fitting results.

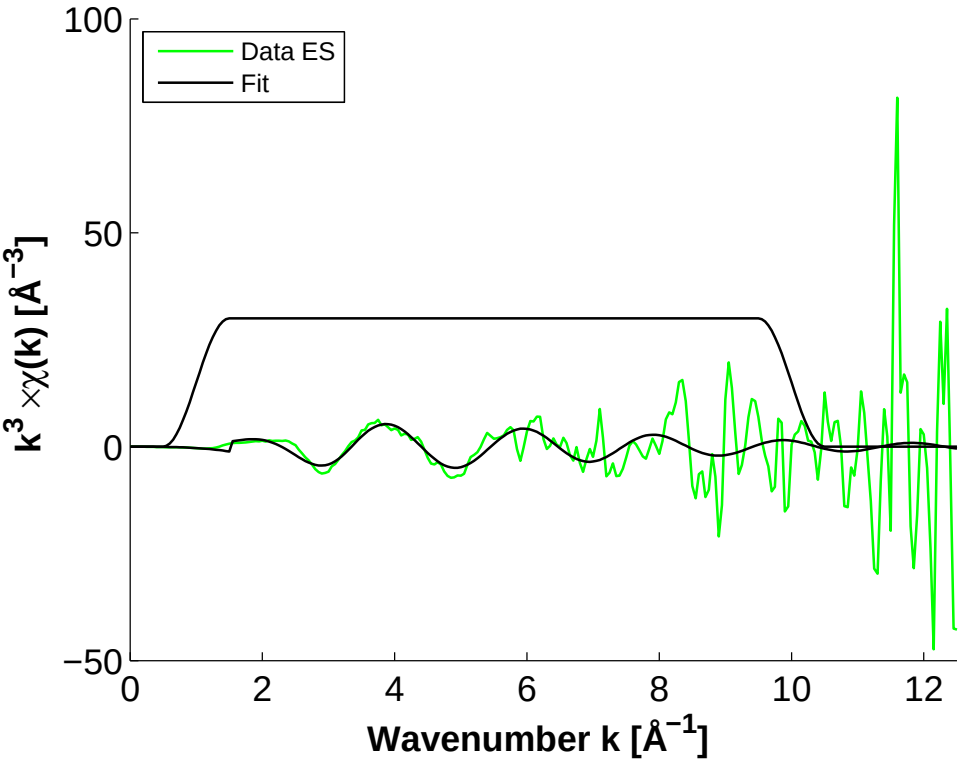

Figure 5.29.: *$\chi(k)$ of the Gaq3 excited state weighted by k^3 (green) and fit (black), performed within the Hanning window.*

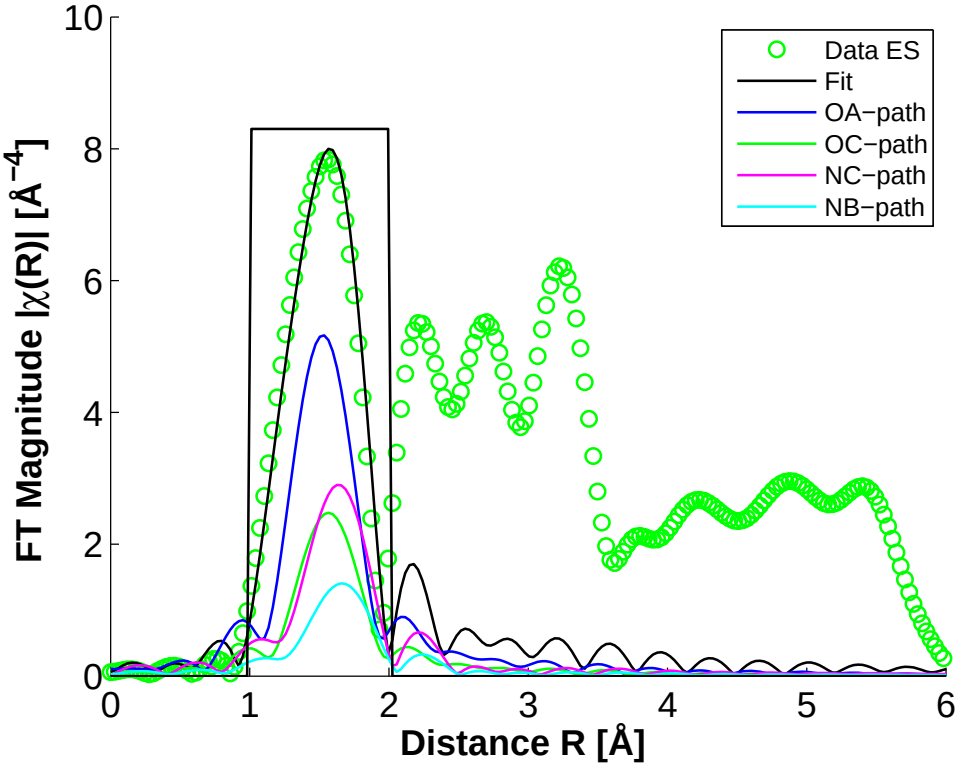

Figure 5.30.: *RDF of the Gaq3 excited state (green circles) together with the fit (black line) and the contributions from the single scattering-paths of the nearest neighbor atoms (different colors). The fit, by trend slightly redshifted, is the best-fit which could be obtained using ARTEMIS. Please note the FT magnitudes are not phase corrected and therefore they appear at shorter distances than the values obtained in ARTEMIS and shown in table 5.4.*

5.3.4. Influence of the Photoexcitation Yield on the Analysis

In the XANES analysis in chapter 5.2.9 it was shown, that the fitting of the transient signal highly depends on f, which scales the measured pump spectrum and the hence the transient signal. The assumption of different photoexcitation yields leads to different results of the analysis. The same holds for the EXAFS analysis, which is performed by the separate fitting of the GS and ES RDF functions. The RDF function is obtained by extracting the $\chi(k)$-spectrum of the measured absorption spectrum A_{EX} and a subsequent fourier transformation into the R-space. Since the ES EXAFS depends on the photoexcitation yield, also the corresponding ES RDF function is coupled to it. Here it is shown how the assumption of different photoexcitation yields influences the analysis. Figure 5.31 presents the ES RDFs obtained from the f-scaled ES EXAFS spectra A_{EX}^{ES} corresponding to selected fractions of excited molecules. The R-shift of the excited RDFs

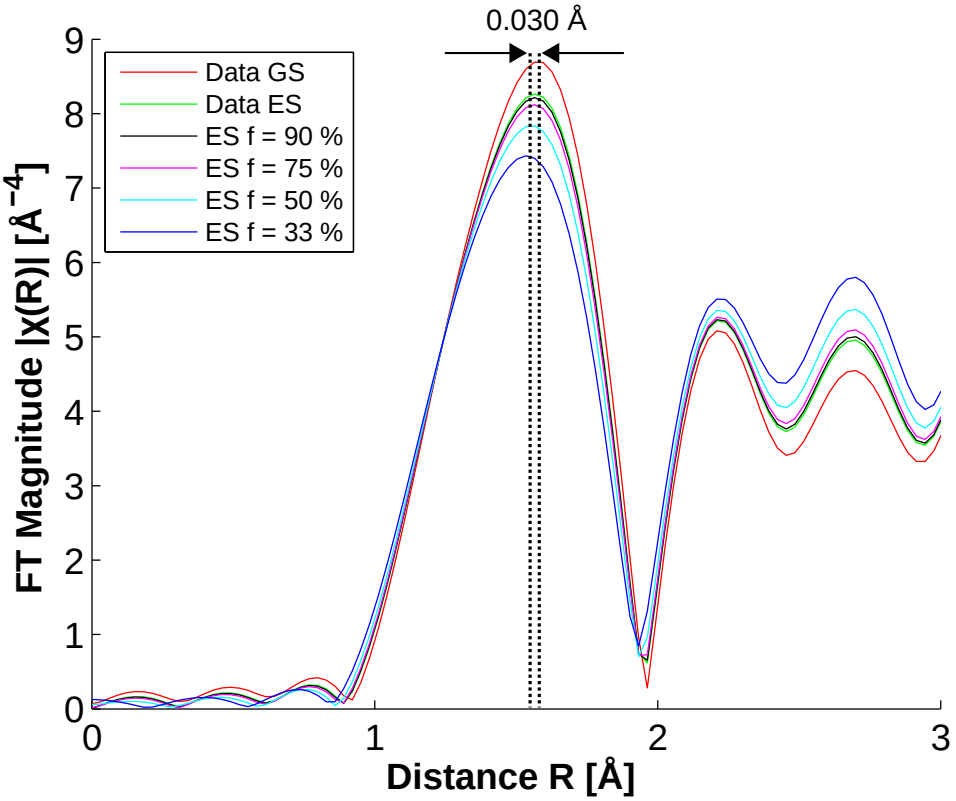

Figure 5.31.: *RDF for the ground state of Gaq3 and the excited state RDFs obtained from the f-scaled excited state EXAFS spectra. The shift of the ES RDFs with respect to the GS RDF decreases with increasing f. The arrows indicate a R-shift of 0.030 Å between ES RDF for $f = 50$ % and GS RDF.*

with respect to the GS RDF decreases with increasing f. For $f = 90$ % the (black) peak is nearly identical to the RDF obtained from the directly measured EXAFS pump spectrum (green color). A shift of the ES RDF with respect to the GS RDF of about 0.030 Å can be observed for a photoexcitation yield of $f = 50$ % as determined and analyzed in the previous chapter. For

higher photoexcitation yields the shift becomes so marginal, that a quantitative analysis of GS and assumed ES RDFs cannot reveal any bond length changes.

5.3.5. Summary and Conclusion

The experimental $\chi(k)$ and RDFs, extracted from the EXAFS data, were fitted by the ARTEMIS software using the paths, phase and backscattering amplitude information calculated by FEFF. The fits agree well with the data within the fitting range defined by the Hanning window and it could be clearly shown by the theoretical calculation of the scattering paths that the first peak of the RDF can be allocated to the distance from the gallium atom to the nearest neighbor atoms. The small shift of the ES RDF with respect to the GS RDF depicted in fig. 5.31 is a direct measurement of the change of the local geometry around the Ga-atom. It gives strong evidence that the bond distances of the next neighboring atoms changed due to the excitation by the laser. The problem in this analysis lies in the fact that the first peak of the RDF is the average distance of the nearest neighboring atoms. In case of the Gaq3 molecule the central absorber atom gallium is surrounded by three nitrogen atoms and three oxygen atoms. A close look to the bond distances of these six atoms (crystallographic GS data) shows an average distance for the oxygen atoms of $Ga - O_{avg} = 1.9540$ Å and for the nitrogen atoms $Ga - N_{avg} = 2.095$ Å. Their difference is $\Delta R_{cryst} = 0.1410$ Å. Such a difference can be only distinguished with very good data (high signal to noise) over a broad k-range. An adequate k-range is an absolute crucial requirement for a successful EXAFS experiment which is tailored to measure precisely bond distances. The best achievable resolution for the distinction of two bond distances is given by equation 5.9. Using this equation the minimal length difference for a k-range of 9 Å^{-1} can be calculated as $\Delta R = 0.174$ Å. Since $\Delta R > \Delta R_{cryst}$, it is not possible to distinguish the average lengths of nitrogen and oxygen atoms within the Gaq3 molecule. In addition nitrogen and oxygen are adjacent elements in the periodic table and thus have nearly the same electronic configuration. Calculations by FEFF (respectively ARTEMIS) of the atomic potentials are exactly based on this electronic configuration and thus treat the two atomic types nearly identically. Hence it is not possible to distinguish these two types of atoms, which have about the same distance from the central absorber atom. For the photoexcitation yield determined as 50 % a small shift of 0.030 Å can be observed between the RDFs of GS and ES. Such a small shift does not mean that no larger bond length changes of the single bonds occur. The theoretical calculations predict mainly a bond length change of $Ga - N_A = -0.099$ Å and $Ga - O_A = 0.090$ Å, which means that the $Ga - N_A$ bond shrinks, while the $Ga - O_A$ bond increases by almost the same value [31]. Since EXAFS is not sensitive for the distinction of the two atoms this structural change will not change the RDF significantly. In fact the shift is so marginal that ARTEMIS is capable to deliver a good fit with the same input data resulting in nearly equal bond distances. For these reasons such structural changes are almost impossible to determine by EXAFS spectroscopy.

6. Conclusions and Outlook

In this section the most important results for the absorption and fluorescence spectroscopic measurements for Gaq3 and Alq3 are discussed and from this conclusions are drawn for the XAFS results. Afterwards, the approach chosen to determine the photoexcitation yield f is discussed under consideration of further processes, which could potentially play an important role for the determination of the photoexcitation yield. At the end the results for the experimentally determined S_1 excited state structure are summarized and an outlook for future experiments is given.

6.1. Absorption and Fluorescence Spectroscopy of Mq3

6.1.1. Solvent Effects

Absorption and fluorescence spectra of Gaq3 and Alq3 were measured in different solvents which are shown in figure 4.14 in chapter 4.2.1. Spectra of Alq3 are blue shifted to those of Gaq3 indicating the role of the central metal atom for the structural and electronic properties of the molecule (see also chapter 1.3). The different electronic configurations of the two metal-quinolines influence the charge distribution of the ligands resulting in slightly different HOMO-LUMO levels.

For the three solvents benzyl alcohol, DMSO and DMF the absorption spectra of DMSO and DMF are nearly the same. For benzyl alcohol however, Alq3 showed a blue shifted absorption spectrum with a shift of $10\,\mathrm{nm}$ and for Gaq3 a blue shift of $6\,\mathrm{nm}$ could be observed. The fluorescence spectra were less strongly affected. Here blue shifts of $2-4\,\mathrm{nm}$ for both, Alq3 in benzyl alcohol and Gaq3 in benzyl alcohol were measured. These shifts clearly reveal that the solvent has an impact on the arrangement of the molecules in the solution.

The dipole moments of the solvents can interact with the dipole moments of the Alq3 and Gaq3 molecules. Both, DMSO and DMF have a higher polarity index than benzyl alcohol [120] and thus the solvent-solute interaction is increased. The higher polarity lowers the energy of the $\pi \rightarrow \pi^*$ transition, thus changing the wavelength of the absorbing photon and consequently leading to slightly red-shifted emission.

The effect of solvents is emphasized by comparison of absorption spectra from the solvents with the absorption spectrum of Gaq3 in film form, which is shown in figure 1.7 in chapter 1.3.2. The corresponding absorption maximum for the film is redshifted by $12\,\mathrm{nm}$ with respect to the absorption maximum of Gaq3 in benzyl alcohol. The influence of the solvent on the excited state lifetime was not analyzed. But investigations by Humbs et al. showed a correlation between fluorescence dynamics and choice of solvents [21].

6.1.2. Effects on Fluorescence Spectra Related to Different Phases

Fluorescence spectra of different phases of Gaq3 exhibit different fluorescence maxima (see chapter 4.2.3). The largest shift was observed for the film sample which was redshifted by $13\ \mathrm{nm}$ with respect to the spectrum of the powder and by $8\ \mathrm{nm}$ with respect to the crystal. This is in good agreement with spectroscopic studies of different Alq3 phases from Guo et al, where photoluminescence spectra of a polycrystalline powder, an amorphous film and a nano-structured film were recorded [121]. They also report that the amorphous film spectrum was redshifted with respect to the powder spectrum ($31\ \mathrm{nm}$) and the nano-structured film spectrum ($13\ \mathrm{nm}$) [121].

An explanation for the shifts of the different phases was given by Brinkmann et al: "The spectral position of fluorescence is found to be correlated with both the molecular density of the packing and the length of interligand contacts between neighboring Alq3 molecules as a consequence of different dispersive and dipolar interactions as well as different $\pi\pi$ orbital overlaps (the shorter the contacts, i.e., the denser the crystal, the more the fluorescence is red-shifted)"[19]. This means that in case of the measurements for this thesis the density of Gaq3 molecules within the particular phase increases from powder to crystal to film. The fact that the shifts are smaller than observed by Guo et al. could be caused by different degrees of crystallinity appearing in the generated samples as a consequence of variations in the processing methods.

In chapter 4.2.3 the fluorescence spectrum for Gaq3 in benzyl alcohol solution was found to have nearly the same maximum as the spectrum from the crystal. This suggests that the arrangement and conformation of the molecules in benzyl alcohol solution and in the crystal structure are similar. Structural information derived for the Gaq3 molecule in benzyl alcohol thus should be also transferable to the Gaq3 structure in crystal form. The correctness of the spectrum in benzyl alcohol can be indirectly confirmed by our result that the shift between the spectrum of Gaq3 in benzyl alcohol solution with respect to the Gaq3 film spectrum is $7\ \mathrm{nm}$, because a similar observation for photoluminescence spectra of Alq3 films and Alq3 solutions was made by Hopkins et al. They determined a redshift of $5\ \mathrm{nm}$ for the film spectrum with respect to the spectrum from solution [122].

The different phases and forms of Alq3 and Gaq3 exhibit different electronic and optical properties due to different molecular packings. This effect should be also considered for the interpretation of the molecular structure of the S_1 excited state of Gaq3. It can not be excluded that experimentally derived results for structural changes of the Gaq3 molecule in solution differ from theoretically predicted changes, based on computational methods, as a consequence of such effects.

6.2. Effects on the Determination of the Photoexcitation Yield

In chapter 4.2.4 the photoexcitation yield for Gaq3 in the XAFS experiment, based on a liquid jet system, was calculated by a modified formula introduced in chapter 2.5. The yield as function of the laser pulse energy was determined and it was shown that a maximum of about $f = 90\ \%$ could be reached, when all crucial parameters of the experiment were considered. In chapter

5.2.1 this calculation was compared to a measurement of the transient difference absorption signal as function of the laser pulse energy. The progressions of the resulting curves agree well, which gives evidence that the theoretical assumptions describe the processes involved in the excitation process correctly. Nevertheless, the formula was based on several assumptions and simplifications. In a real excitation process especially at high laser intensities further physical processes have to be considered, whereas the two most crucial are expected to be:

- Stimulated Emission, and
- Two-photon absorption.

In the following paragraphs the possible impact of these two processes for the presented pump-probe measurements will be discussed.

Stimulated Emission Stimulated emission is a process competing with spontaneous emission. When a laser photon strikes an electron in the excited state, the electron can be transferred to the ground state under emission of a further photon with the same energy and direction as the incident photon. Thereby the wavelength of the incident photon has to match the energy difference $E_1 - E_0$ between the excited S_1 and the ground state S_0. The condition

$$\Delta E = E_1 - E_0 = h \cdot c/\lambda \tag{6.1}$$

is the same condition to be fulfilled for the absorption of an electron from the ground state into an excited state (see chapter 1.2). In a two niveau system the cross sections and Einstein coefficients, which give the rate constants for stimulated emission A_{10} and absorption A_{01} are equal [62, 87, 18] (the same obeys for the corresponding cross sections σ_{10} and σ_{01}). This means in a pure two niveau system population densities of maximal $50\ \%$ can be reached in principle: Since both cross sections for absorption σ_{01} and stimulated emission σ_{10} are equal both energy niveaus are populated equally in the equilibrium. In this context the question arises if stimulated emission permits photoexcitation yields of a about $90\ \%$ as determined for $Gaq3$ in this thesis.

For the discussion it is important to consider the transition rates between the single electronic and vibrational states as well as the wavelength, pulse duration and repetition rate of the pump laser. An energy scheme of Mq3 is shown in figure 1.7, which can be used in case of Gaq3. Here we only consider the singlet states since the triplet state is not directly involved into the excitation process. Gaq3 in benzyl alcohol solution shows a large Stoke's shift of $164\ \mathrm{nm}$ between absorption wavelength and emission wavelength (see chapter 4.2.1). This shift is a clear indication for structural changes upon the S_0 and S_1 transition [28] and in general for vibrational levels. In the following it is now examined how the processes involved in photoexcitation, take place in detail. Illustrations of the discussion are displayed in figure 6.1.

When the pump laser pulse hits the Gaq3 molecules in the sample volume almost all electrons are in the lowest vibrational level of the S_0 ground state. During the absorption process which occurs in $< 1 \cdot 10^{-15}\ \mathrm{s}$ [3], a photon with the excitation wavelength $\lambda_{pump} = 343\ \mathrm{nm}$ interacts

with an electron, which is excited into a higher vibrational level S_1^* of the first excited singlet state S_1, thereby depopulating the ground state S_0, which is shown in figure 6.1 a) (since the excitation wavelength λ_{pump} is below the absorption maximum $\lambda_{abs} = 382\ \mathrm{nm}$ of Gaq3, shown in figure 4.12, it is assured that a higher vibrational level is reached). At this point a distinction of cases is made, since it can be thought of two different decay pathways:

1. **First case:** The S_1^* state decays non-radiatively to the lowest vibrational level of the S_1 singlet state. For a dye molecule this is a very efficient process and takes place within 10^{-13} s to 10^{-11} s [123]. For some molecules even higher rates of ca. $1 \cdot 10^{14}\ \mathrm{s}^{-1}$ have been reported [124, 3]. This means for the vibrational state a lifetime $\tau_{vib} = 10^{-14} - 10^{-11}$ s can be assumed. From the lowest vibrational level of the S_1 state the electron decays to any of the vibrational levels of the S_0 ground state under emission of fluorescence with a lifetime τ_{fl} of about $4 - 16$ ns (see chapter 1.3.2 and [1]), which is at least three orders of magnitude slower than VR. Consequently the S_1 state is the state with the highest population and source of fluorescence photons. In fact Kasha's rule states that emission originates only from the lowest excited state independent from the initially excited states [17] (see figure 6.1 a)). Generally it can be found that SE always takes place from this state because of the very fast and high efficient VR[6]. In our case the lowest S_1 state cannot be depleted by SE because the wavelength of the pump laser λ_{pump} does not match the $S_1 \rightarrow S_0$ transition as illustrated in figure 6.1 b).

2. **Second case:** So far the pulse duration $\tau_{pump} < 180$ fs of the pump laser was not taken into account (see chapter 4.1.2). In case of $\tau_{pump} < \tau_{vib}$ the probability is given that a second photon of the pump pulse strikes an excited state electron in the S_1^* level inducing a $S_1^* \rightarrow S_0$ transition before it is decayed non-radiatively. This is illustrated in figure 6.1 c). Examples for SE from higher vibrational levels have been reported [126]. In fact this scenario could potentially lead to a depletion of the excited state population by the pump laser pulse. However, it can be estimated that the cross section σ_{SE} of this process is much lower than the cross section for ground state absorption σ_{opt}, since a single excited state electron has to be struck twice by a laser photon within the time window τ_{pump}. It is worth mentioning here that an arriving pump pulse always sees Gaq3 molecules in the ground state because the pulse separation with $1/f_{rep} = 7.69\ \mu$s is much longer than the excited state lifetime τ_{fl}, so that all Gaq3 molecules decay to the ground state in between two arriving laser pulses.

It is difficult to estimate which scenario is more probably because most of the rates for the transitions involved in this processes have not been determined yet. One needs to measure the rate k_{vib} for the vibrational decay and the cross section σ_{SE} for stimulated emission. Such measurements are usually conducted by ultrafast transient absorption spectroscopy [18]. Nevertheless, the influence of the second scenario can be estimated as minor so that in conclusion stimulated emission does not seem to play an important role for the excitation process and a photoexcitation yield of $90\ \%$ is realistic.

[6] In *Stimulated Emission Depletion (STED)-fluorescence microscopy* SE is used to suppress fluorescence by depleting the lowest excited state and therefore presents its basic principle [125].

Two-photon absorption This process, illustrated in figure 6.1 d) for Gaq3, describes the simultaneous absorption of two photons within a time window of about 10^{-17} s [123]. The two photons thereby provide an energy which allows to transfer an electron into a higher excited state S_N. Thus a transition to such a state would correspond to the energy difference $E_2 - E_0 = 2 \cdot h \cdot c \cdot \lambda_{pump}$, where E_2 is the energy of a vibrational level of the S_N singlet state and E_0 is the energy of the S_0 ground state. This energy translates into a wavelength of $\lambda_{pump}/2 \approx 170$ nm. The absorption spectra in solution could not be measured down to a wavelength of 170 nm. The absorption spectra of Gaq3 films were measured at least down to 200 nm and showed a high absorption in this region. However, absorption at wavelengths $\ll 200$ nm is generally high due to the high photon energy capable to induce bond cleavage. Consequently two-photon absorption processes under high density excitation conditions used in this experiment could play a role. However, the same final remarks as for SE are also valid here: The cross section for two-photon absorption has to be measured in an ultrafast transient absorption spectroscopic experiment to allow for more quantitative statements.

In conclusion I want to point out that the calculation for the photoexcitation yield of $f = 90$ % should be considered as an upper limit, which is achievable. The curve progression agrees well with the curve progression of the transient difference signal as function of the laser pulse energy in chapter 5.2.1 and presented in figure 5.2. It shows that the theoretical considerations leading to formula 2.22 are correct. The deviation from the linear region of the excitation process at pulse energies beyond ca. 1 μJ is an indication for processes apart from one-photon absorption. The effects previously discussed and maybe further effects could take place at these high density excitation conditions. However, the contributions of these effects are defined by the specific rate constants, which can be only determined via optical transient spectroscopy.

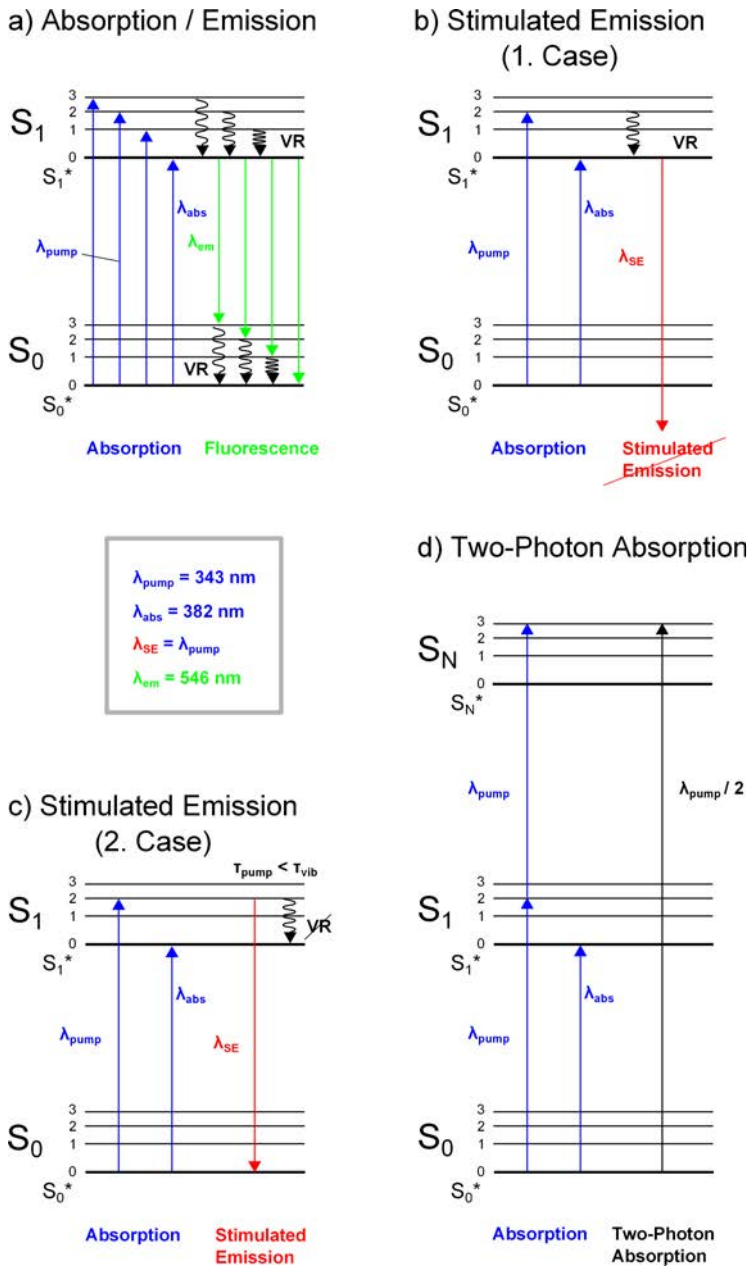

Figure 6.1.: *Models for the excitation and de-excitation processes involving the ground state S_0 and the first excited state S_1 as well as the vibrational levels S_0^* and S_1^*. All transitions obey the selection rules. λ_{abs} and λ_{em} are the maxima for absorption and fluorescence, respectively. λ_{pump} corresponds to the pump wavelength of the pulse laser, which was used for excitation. λ_{SE} is the pulse wavelength of possible stimulated emission (SE) and is identical with λ_{pump}. Straight arrows stand for radiative transitions, while curled arrows describe the radiationless vibrational relaxation (VR). a) Absorption and fluorescence; b) Stimulated emission from the lowest vibrational level of S_1 is not possible due to previously occurring VR; c) Stimulated emission from a higher vibrational level of S_1; d) Two-photon absorption where the population of a possible second excited state S_N with vibrational levels S_N^* is assumed.*

6.3. Excited State Structure of the Gaq3 Molecule

For the determination of the S_1 excited state structure of Gaq3 two different approaches were applied:

- Pump-Probe XANES spectroscopy (see chapter 5.2);
- Pump-Probe EXAFS spectroscopy (see chapter 5.3).

Both approaches have in common the measurement of a pump-probe absorption spectrum, whereas in case of EXAFS this is measured over a broader energy range of $800\ \mathrm{eV}$. The difference lies in the analysis of the spectra.

XANES For XANES the transient difference signal occurring in the vicinity of the absorption edge was analyzed. Thereby a new model for the Gaq3 molecule in the excited state was applied. By changes of structural parameters multiple possible excited state structures were created and for each of them the corresponding transient spectrum was calculated. These theoretical transient spectra were fitted to the experimental transient spectrum. The best-fit structure as judged by the chi-square criteria, was assumed to be the excited state structure. As it was shown in chapter 5.2.9 and discussed in chapter 5.2.12 several optimizations of structural parameters resulted in similar chi-square values. Each of these optimized structures can be considered as a possible solution for the S_1 excited state structure. For the large parameter space, in which the three quinoline-rings and their atoms are treated equally, the optimization model did not provide an unique result.

In consequence the parameter space was limited to those parameters, which are physically most meaningful according to theoretical calculations and to physico-chemical considerations. The photoexcitation is a ligand centered process. This means that mainly one of the three quinoline-rings is affected, whereas for the other two only minor changes are expected. In addition XAFS is most sensitive to changes in the first coordination shell. Combining these assumptions XAFS spectroscopy, in the specific case of Gaq3 should be most sensitive to changes of the $Ga-N$ and $Ga-O$ bond distances of one specific ligand. By limiting the parameter space to these two parameters a physically meaningful model with a small χ^2_ν value could be obtained. From the optimization processes with such a limited parameter space, two main results could be obtained:

1. An initial optimization of the $Ga-N$ and $Ga-O$ bonds of each of the three quinoline-rings A, B, and C showed that the best chi-square value was reached for the A-quinoline-ring. In these optimizations the $Ga-N$ and $Ga-O$ bond lengths of the other two quinoline-rings were kept constant upon photoexcitation and they were not optimized. The chi-square value for the optimization of the A-quinoline-ring was $\chi^2_\nu = 37.00$ and $\sim 16\ \%$ lower than the $\chi^2_\nu = 49.68$ for the optimization of the B-quinoline-ring and $\sim 46\ \%$ lower than the $\chi^2_\nu = 69.00$ for the optimization of the C-quinoline-ring. This is a strong hint, that changes most probably occur only at the A-quinoline-ring - a result which agrees well with the theoretical calculations.

2. The same optimization of the $Ga-N$ and $Ga-O$ bonds of the three quinoline-rings A, B, and C showed that all good fits result in an elongation of the nitrogen-gallium bond and an shrinking of the oxygen-gallium bond. This observation, which could be made for all three quinoline-rings A,B and C in the optimization processes 1,5 and 6 is in discrepancy to the theoretical calculations, which predict in opposite a shrinking of the nitrogen-gallium bond and an elongation of the oxygen-gallium bond.

According to these findings I propose a final model for the structural changes of the Gaq3 molecule upon photoexcitation from the ground state S_0 to the first excited state S_1. In this model, presented in figure 6.2, the $Ga - N_A$ bond is elongated by 0.050 Å and the $Ga - O_A$ bond is shortened by -0.020 Å. It is based on the specific conditions of our experiment and several assumptions for the analysis. It is noteworthy that Gaq3 was dissolved in benzyl alcohol with a concentration of $50\ \mathrm{mmol/l}$. The sample form has influence on the electronic and structural arrangement of Gaq3, as it was previously discussed in detail. Thus the model proposed here might not be matching to Gaq3 in other forms, though it was shown that Gaq3 in benzyl alcohol solution and Gaq3 in crystalline form exhibit very similar optical features, indicating similar structural properties. Furthermore the model is based on the following assumptions for the analysis:

- The photoexcitation is a ligand centered process and affects only one quinoline-ring.
- Intraligand structural changes of the molecule are neglected.
- The photoexcitation yield during the pump-probe XANES experiments was $90\ \%$.

The discrepancy between the bond length changes, proposed by this model, and the bond length changes of $\Delta(Ga - N_A) = -0.099$ Å and $\Delta(Ga - O_A) = 0.090$ Å predicted by theoretical calculations would mean that electron charge is most probably not partially transferred from the phenoxide side to the pyridyl side (see figure 1.8), but vice versa. This is a surprising result, because it contradicts the actual acknowledged theory about the locations of HOMOs and LUMOs on the quinoline-ring of Mq3. Even though our experiments were performed very carefully and the transient spectrum T_{EX} was reproduced several times, one or a combination of the following points might lead to the discrepancy between the proposed model of this thesis and the calculated structure using quantum chemical methods:

- The molecular structures (GS and ES) of Gaq3 in benzyl alcohol solution differ significantly from the Gaq3 molecular structures (GS and ES) in other sample forms and from those obtained by theoretical calculations.
- Intraligand structural changes have stronger impact on the optimized structure than expected and can not be neglected for the optimization model.
- The theoretical assumptions and approaches of the program FEFF, which was used in this thesis for the calculation of theoretical spectra of Gaq3, differ from those of the other theoretical calculations (DFT, HF, CIS).

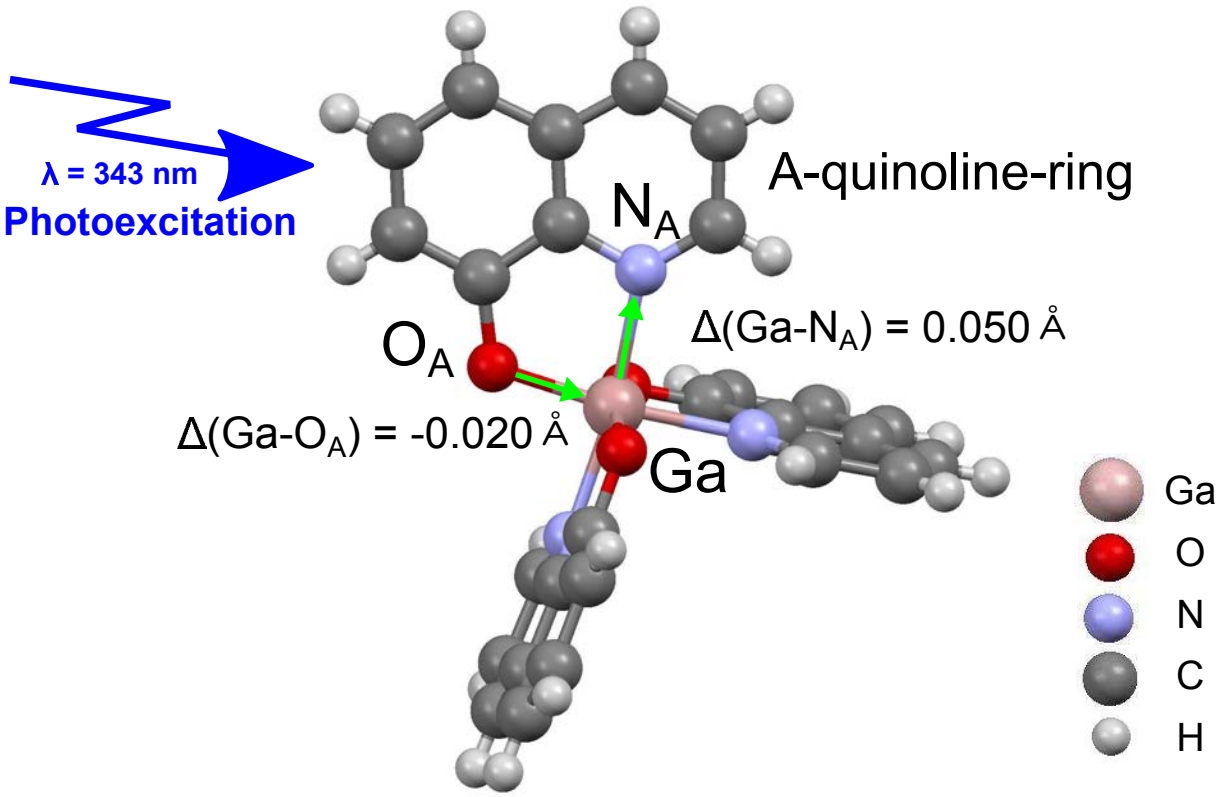

Figure 6.2.: *Final proposed model for the structural changes of the Gaq3 molecule in benzyl alcohol solution upon photoexcitation from the S_0 ground state to the S_1 excited state. Only the A-quinoline-ring is affected. The green arrows illustrate bond length elongation and contraction of the $Ga - N_A$ bond by 0.050 Å and the $Ga - O_A$ bond by -0.020 Å, respectively.*

- The theoretical calculations (DFT, HF, CIS) are not accurate enough.
- The photoexcitation yield f, assumed for the analysis in this thesis was not correct.

EXAFS The EXAFS analysis was based on using the EXAFS equation and this approach is a well proven and a standard method for structure determination. W. Gawelda presented in his thesis the successful excited state structure determination of $[Fe^{II}(bpy)_3]^{2+}$ by analysis of pump-probe EXAFS spectra via the EXAFS equation and could show that a $Fe-N$ bond length change of 0.2 Å occurs upon photoexcitation [79]. One difference of the $[Fe^{II}(bpy)_3]^{2+}$ molecule in comparison to the Gaq3 molecule is the coordination of the central metal atom. In case of $[Fe^{II}(bpy)_3]^{2+}$ Fe is coordinated by six nitrogen atoms which undergo a relative large average shift of 0.2 Å upon photoexcitation. Consequently the first peak of the excited state RDF providing the averaged distance of the six shifted nitrogen atoms shows a significant 0.2 Å shift with respect to the first peak of the ground state RDF. In case of Gaq3 alternating bond length changes of 0.090 Å and -0.099 Å for two of the six ligand atoms, coordinating the central gallium atom were predicted (see chapter 5.2.7). Since the RDF gives the average distance of the first shell atoms, the two alternating bond length changes in the Gaq3 molecule do not lead to a significant shift of ground state and excited state RDFs. A structural change as it is expected for the Gaq3 molecule can not be resolved with the current technical capabilities.

6.4. Outlook

The strength of XANES lies in the sensitivity to oxidation states and valency of atoms. Thus it is a powerful tool for the detection of charge transfers. Metal organic compounds, in which a *Metal to Ligand Charge Transfer (MLCT)* or a *Ligand to Metal Charge Transfer (LMCT)* can be induced by an optical pump pulse are excellent examples for sample systems appropriate for measurements with the pump-probe XANES technique (see for example [49]). In such a measurement the pumped absorption spectrum shows an edge shift (E_0) with respect to the unpumped absorption spectrum, which can be directly related into a quantitative change of the oxidation state of the central metal atom. Sample systems with such properties are well suited for future pump-probe XAFS experiments.

The XAFS setup developed at P11 with the small micro-jet allows high photoexcitation yields, as we have shown. In combination with the high flux X-ray beam provided by the PETRA III synchrotron source it allows to detect very small changes by time-resolved pump-probe XANES. This could be shown for the Gaq3 molecule. However, a quantitative bond length analysis as in the case of Gaq3 turned out to be challenging and reveals the limitations of this technique.

The measurement of the transient difference signal as function of the time delay between laser pump pulse and X-ray probe pulse at a specific energy E_0 where the largest changes occur, can be used to determine the temporal decay of the excited state. It would be very interesting to measure pump and unpumped absorption spectra of different time-delays. This would not only allow

to retrieve information about the temporal decay (excited state lifetime), but also provide insight into the dynamical behavior of structural and electronic changes as function of time ("molecular movies"). Such a measurement of course would be much more time consuming. The measurement as function of the time delay, shown in this thesis, took about $10\ \mathrm{h}$ for one fixed energy. To conduct the same measurement over a broader energy range with usable energy resolution would require $10\ \mathrm{h}$ scaled by the number of energy steps. For an acceptable time frame such experiments would be possible only by using much faster data acquisition.

The setup used at beamline $P11$ is performing very well already but also has potential for further improvements. As it was described in chapter 4.1.8 one of 40 bunches could be used for the experiment only, because the laser repetition rate was limited to $130\ \mathrm{kHz}$. Under the precondition of the same pulse energies, a pulsed MHz-laser system would allow to use all 40 bunches. The current data acquisition system is already capable of handling this higher data rates.

Another important experimental improvement would be the capability of tuning the pump laser wavelength. For the pump-probe experiments presented in this thesis $\lambda_{pump} = 343\ \mathrm{nm}$ was used. As described previously this wavelength does not perfectly match the absorption maximum $\lambda_{abs} = 382\ \mathrm{nm}$ of Gaq3 in benzyl alcohol. Thus by tuning the pump wavelength to or close beneath λ_{abs} the $\pi \rightarrow \pi^*$ transition could be activated much more efficiently. The measurement of the transient difference signal as function of the pump laser wavelength could reveal in detail how structural changes as a result of electronic transitions could be induced in the most efficient way. Since structural changes are expected for the S_1 excited state only, the transient difference signal strongly related to these changes should disappear as soon as the pump wavelength does not match to the corresponding $\pi \rightarrow \pi^*$ transition into the S_1 state. In future an *Optical Parametric Amplifier (OPA)* for the laser-system will be available at P11 and hence allow for tuning the wavelength in 1-nanometer steps.

Although EXAFS spectroscopy provides a well proven standard method for bond length determinations, neither EXAFS spectroscopy nor XANES spectroscopy allow direct measurements of atomic coordinates. For this reason time-resolved micro-crystallography presents a promising technique to analyze structural changes expected for the Gaq3 molecule upon photoexcitation. In contrast to X-ray absorption, crystallography provides direct $3d$ information on atomic coordinates of a crystalline lattice. A crystallographic experiment could help to clarify the discrepancies between the experimental results, obtained by XANES spectroscopy in this thesis and the theoretical calculations. Furthermore, it would show if pump-probe XANES spectroscopy and pump-probe crystallography can be used as complementary techniques for the analysis of the excited state structure of such sample systems. Some preparation work has been made already by the generation of low roughness single crystal slices. These allow to build up laser-induced, high excited state population densities close beneath the crystal surface, which can be probed with a micrometer sized X-ray beam.

Danksagung

Ich möchte mich bei Prof. Dr. E. Weckert bedanken, der mich in die Arbeitsgruppe aufgenommen und mir damit die Möglichkeit zur Bearbeitung dieses Projekts gegeben hat. Meinem Betreuer Dr. A. Meents, von dem ich viel - vor allem über experimentelles Arbeiten - lernen durfte, danke ich für die Betreuung und Unterstützung. Prof. Dr. M. Drescher danke ich dafür, dass er die Sublimationskammer zur Herstellung der Quinolatfilme zur Verfügung gestellt hat, sowie für die Übernahme des Zweitgutachtens.

Die Röntgenstrahl-Experimente, die in dieser Arbeit beschrieben sind, wurden an der PETRA III Beamline P11 zusammen mit Dennis Göries und Moritz Schlie durchgeführt. Im besonderen danke ich diesen beiden für die sehr gute Zusammenarbeit in vielen und langen Messzeiten.

Desweiteren möchte ich dem ganzen P11 Team für die Unterstützung während der Experimente danken. Insbesondere sei hierbei Nicolas Stübe erwähnt, der die CAD-Zeichnungen für den XAFS-Aufbau erstellt hat.

Andrej Singer, Dennis Göries, Desiree Heintz, Resmi Raghunandan, Philip Roedig, Sebastian Bommel und Anja Burkhardt danke ich für viele hilfreiche Diskussionen rund um die Doktorarbeit und andere Themen.

Grigory Smolentsev danke ich für die Ratschläge und Tipps bei der Benutzung des Programms “FitIt”. Wojciech Gawelda danke ich für hilfreiche Diskussionen im Rahmen der XAFS Auswertungen. Andre Rothkirch danke ich für freundliche Unterstützung bei Software-Fragen und Shell-Scripten. Jens Viefhaus danke ich für sein Interesse an unseren Experimenten und seine hilfreichen Ratschläge während der Messzeiten. Der HASYLAB Werkstatt um Jens Brehling danke ich für die Fertigung von Bauteilen für verschiedene Experimente und die Flexibilität bei Entgegenahme kurzfristig eingereichter Aufträge. Ein Dank auch an Manfred Spiwek für die stete Hilfsbereitschaft bei der Präparation und Vorbereitung von Proben.
Mit Andrej, Dennis und Christopher verband mich nicht nur die Arbeit am DESY, sondern darüberhinaus auch eine Freundschaft, für die ich ihnen sehr dankbar bin. Bei Voica bedanke ich mich für ihre Unterstützung, das Lesen der Arbeit und für viele fachliche und sprachliche Tipps.

Meiner ganzen Familie und besonders meinen Eltern danke ich für die moralische Unterstützung während der gesamten Doktorarbeitszeit.

A. Appendix

A.1. Sublimation Setup for Thin Film Growth

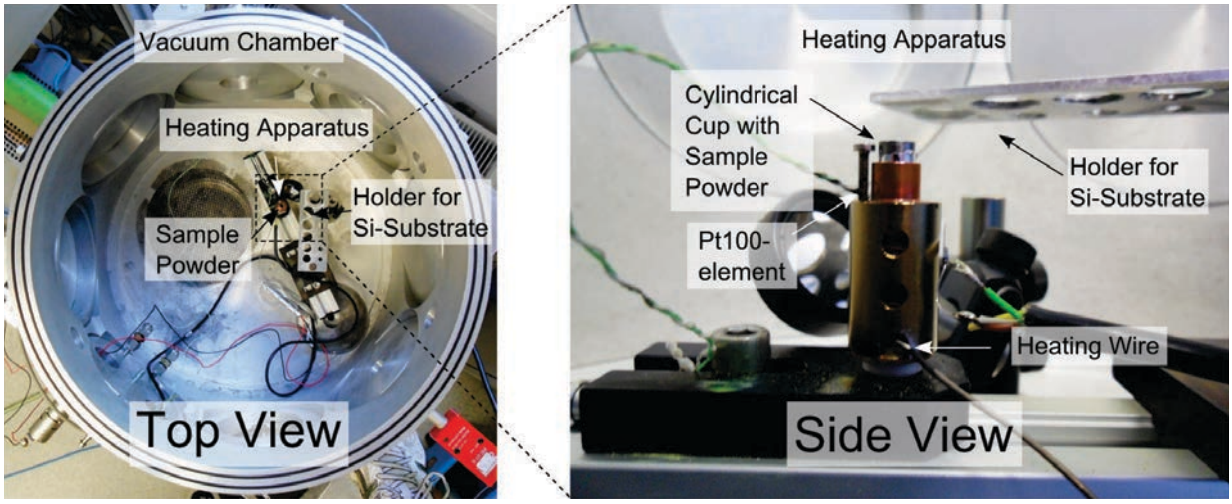

Figure A.1.: *Left: Vacuum chamber with sublimation setup for thin film growth. Right: The sample powder is placed in a cup, inserted into a heating apparatus. At temperatures between* $380 - 420\ ^{\circ}\mathrm{C}$ *and a pressure of* $5 \cdot 10^{-5}$ mbar *the sample is transferred to the gas phase and then deposited on a Si-substrate, horizontally placed over the cup opening. For temperature control a Pt100-element is used.*

A.2. Crystal Surface Analysis by Means of AFM

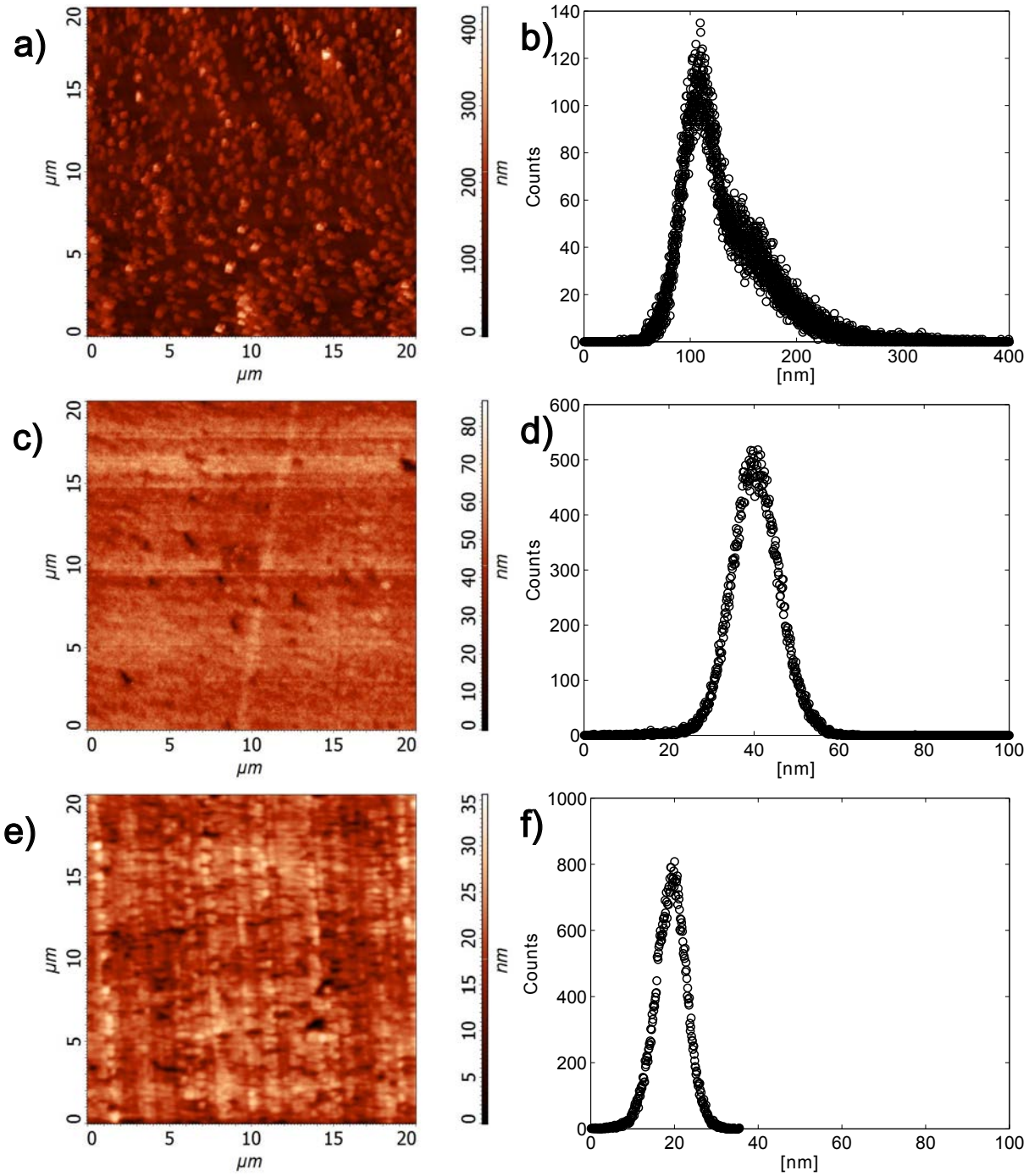

Figure A.2.: *AFM height images and corresponding histograms of crystal surfaces polished by means of different methods: a) and b) Polishing device with polishing head, c) and d) Polishing device with diamond knife tool, e) and f) microtome.*

A.3. Plots of the Pump-Probe Optimization Processes

A.3.1. Optimization 3

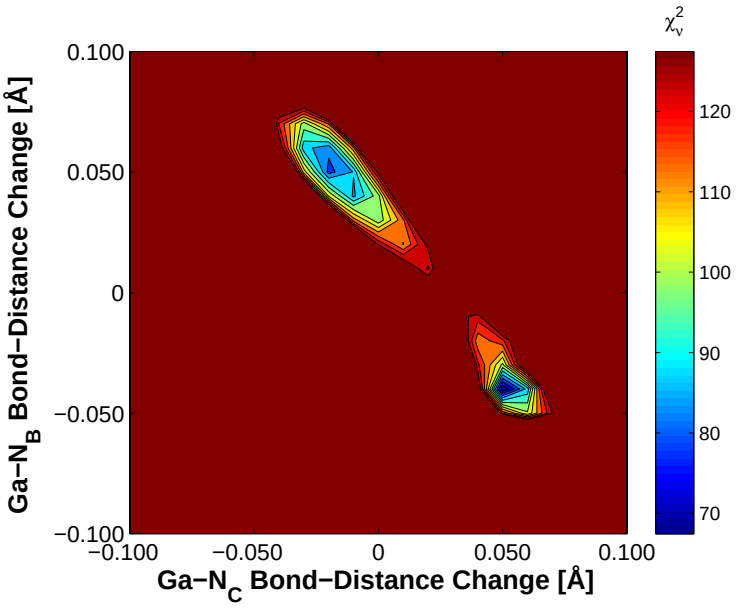

Figure A.3.: *Optimization of P_3 and P_4: A minimum of $\chi^2_\nu = 67.46$ is reached for $\Delta(Ga - N_B) = -0.040$ Å and $\Delta(Ga - N_C) = 0.050$ Å.*

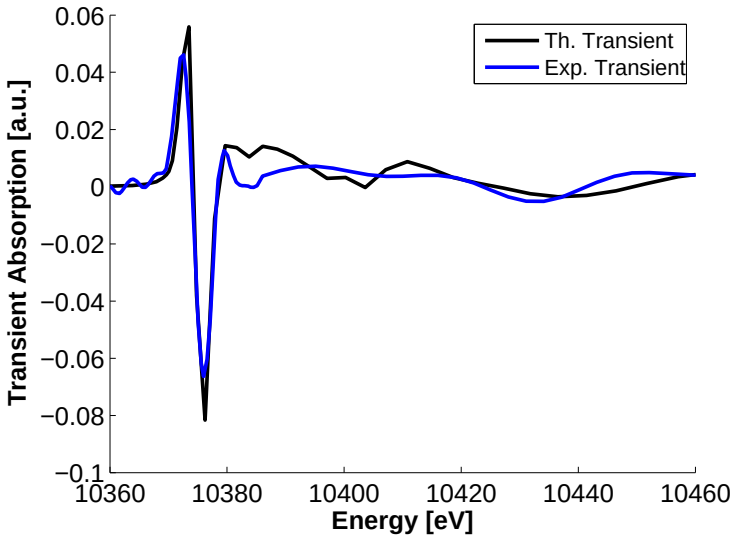

Figure A.4.: *Best-fit with $\chi^2_\nu = 67.46$ obtained for parameters P_3 and P_4.*

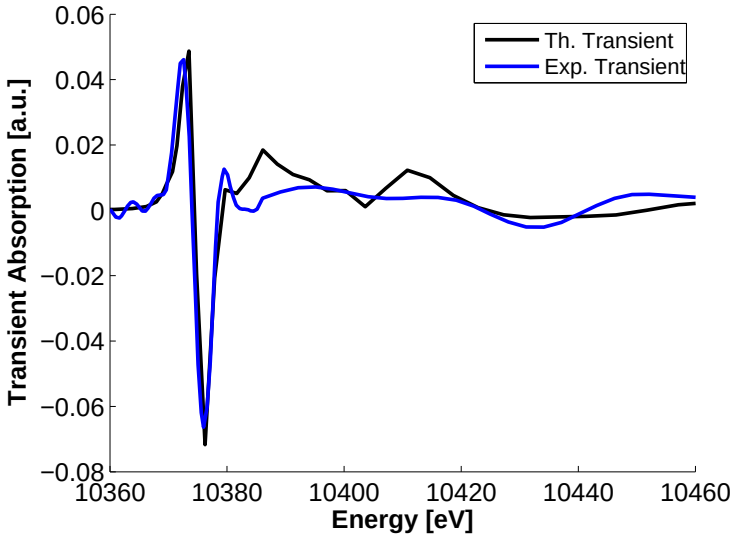

Figure A.5.: *Overall best-fit with* $\chi^2_\nu = 60.46$ *obtained for parameters* P_3 *and* P_4*, and* P_1 *and* P_2*.*

A.3.2. Optimization 4

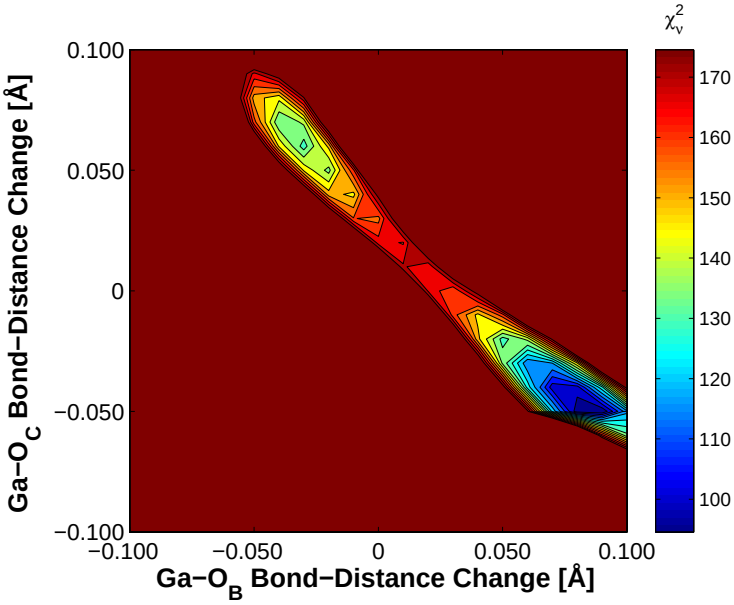

Figure A.6.: *Optimization of* P_5 *and* P_6*:* χ^2_ν *as function of* $\Delta(Ga - O_B)$ *and* $\Delta(Ga - O_C)$ *bond distance changes. A minimum of* $\chi^2_\nu = 94.55$ *is found for* $\Delta(Ga - O_B) = 0.090$ *Å and* $\Delta(Ga - O_C) = -0.050$ *Å.*

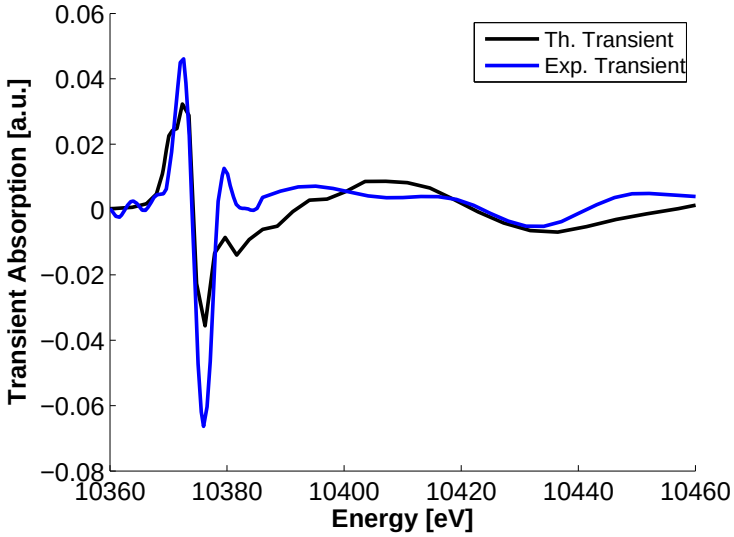

Figure A.7.: *Best-fit with* $\chi^2_\nu = 94.55$ *obtained for parameters* P_5 *and* P_6.

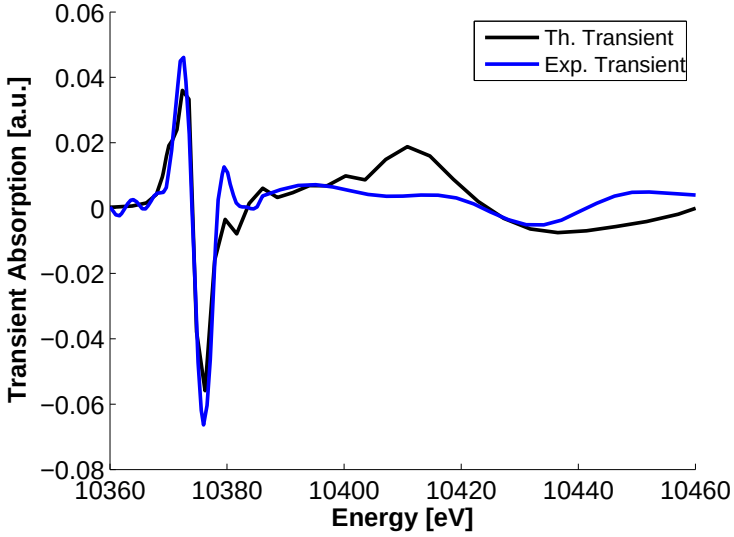

Figure A.8.: *Overall best-fit with* $\chi^2_\nu = 59.46$ *obtained for parameters* P_5 *and* P_6*, and* P_1 *and* P_2.

A.3.3. Optimization 5

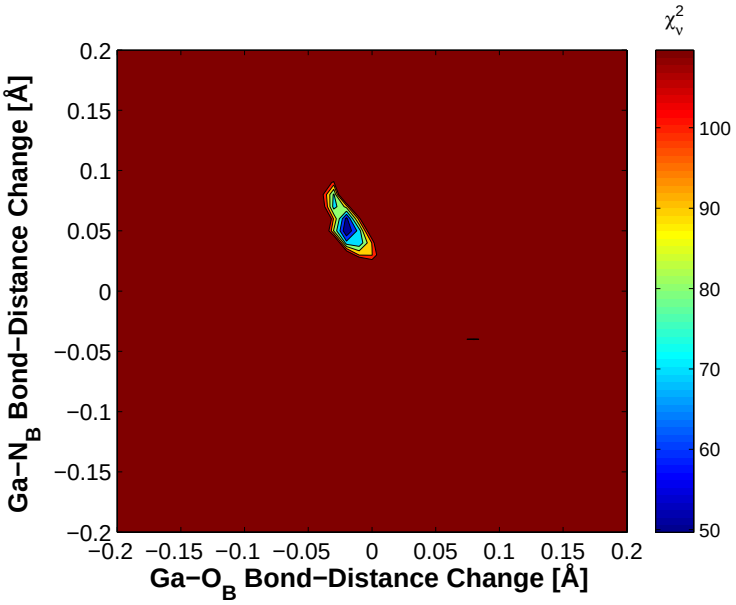

Figure A.9.: *Optimization of P_3 and P_5: χ^2_ν as function of the bond length changes of $Ga - N_B$ and $Ga - O_B$ with a minimum of $\chi^2_\nu = 49.68$ for $\Delta(Ga - N_B) = 0.050$ Å and $\Delta(Ga - O_B) = -0.020$ Å.*

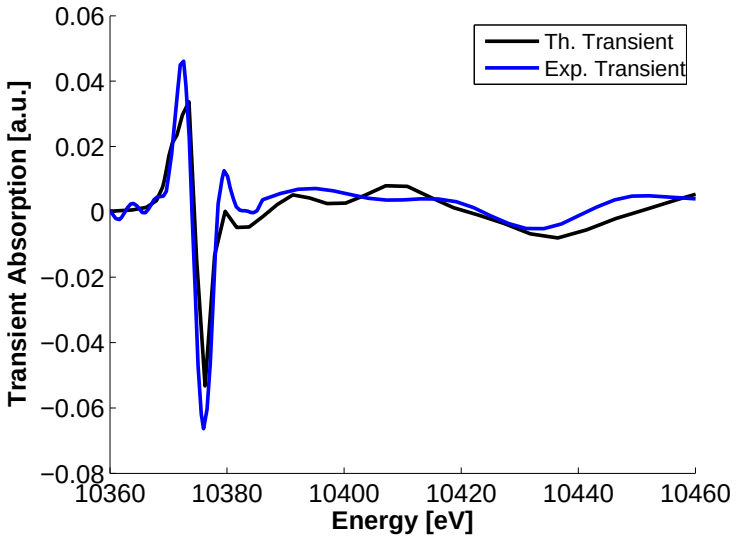

Figure A.10.: *Best-fit with $\chi^2_\nu = 49.68$ obtained for parameters P_3 and P_5.*

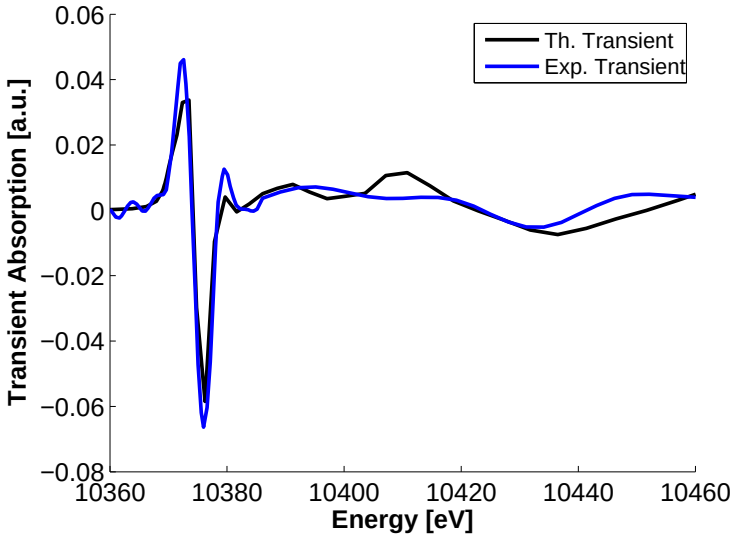

Figure A.11.: *Overall best-fit with* $\chi^2_\nu = 33.06$ *obtained for parameters* P_3 *and* P_5*, and* P_1 *and* P_2*.*

A.3.4. Optimization 6

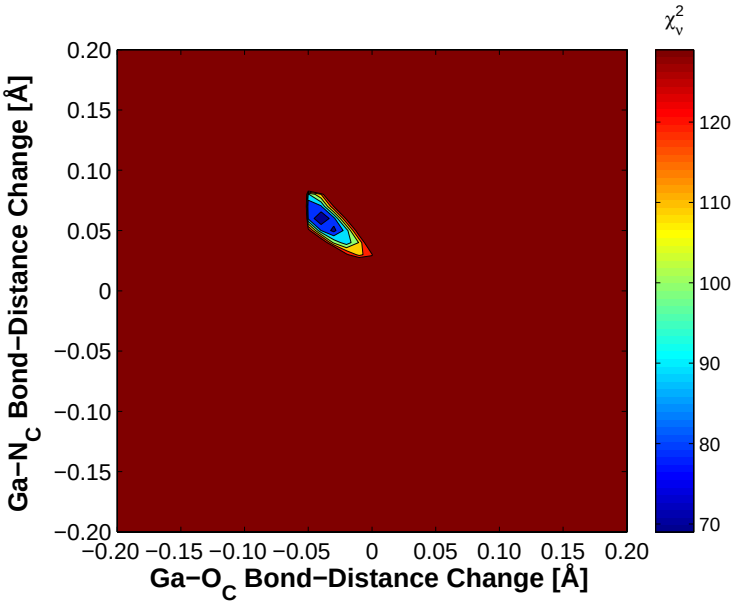

Figure A.12.: *Optimization of* P_4 *and* P_6*:* χ^2_ν *as function of the bond length changes of* $Ga - N_C$ *and* $Ga - O_C$ *with a minimum of* $\chi^2_\nu = 69.00$ *for* $\Delta(Ga - N_C) = 0.060$ *Å and* $\Delta(Ga - O_C) = -0.040$ *Å.*

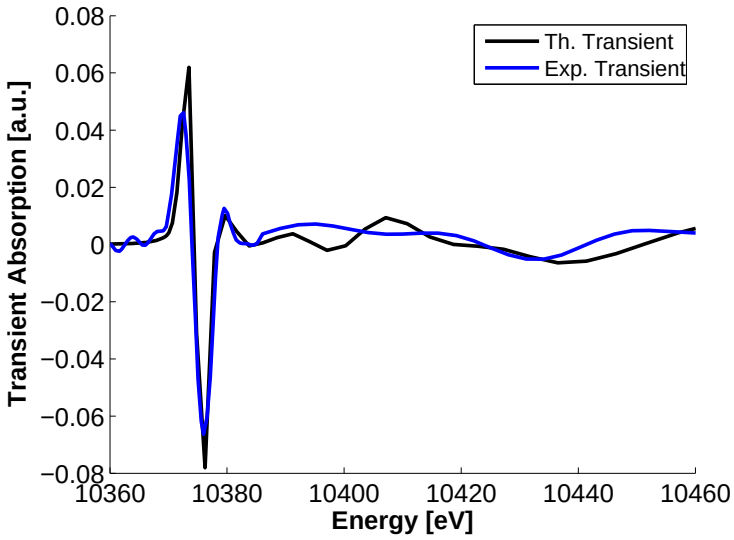

Figure A.13.: *Best-fit with* $\chi^2_\nu = 69.00$ *obtained for parameters* P_4 *and* P_6.

A.4. Liquid Micro-Jet Hit by Pump Laser

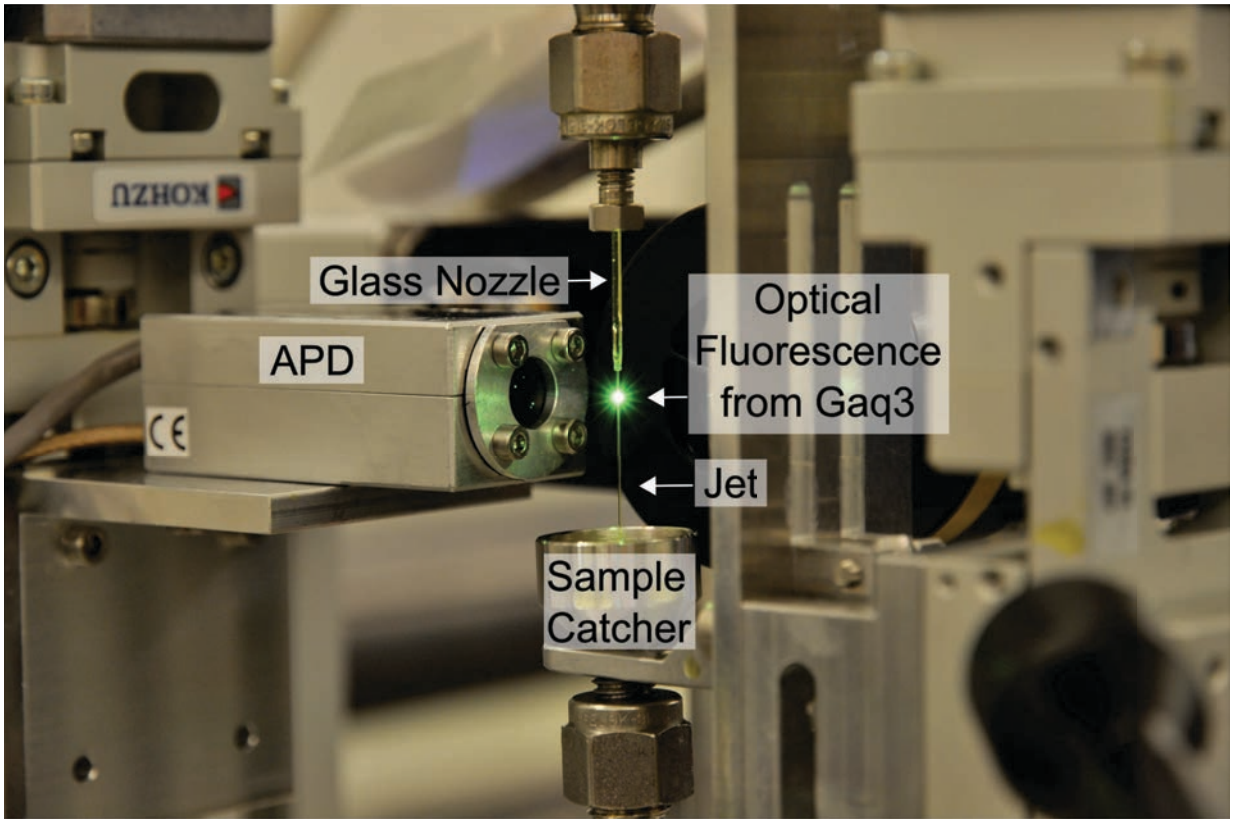

Figure A.14.: *The pump laser beam hits the liquid* $30\ \mu\mathrm{m}$*-jet with Gaq3 sample solution. Gaq3 exhibits a strong optical fluorescence after photoexcitation. The APD detects the fluorescence photons in X-ray fluorescence yield mode.*

Bibliography

[1] M. Schlie. *Time-resolved studies at PETRA III with a synchronized lasersystem*. Ph.D. thesis, Universität Hamburg (2013).

[2] E. A. Silinsh. *Organic Molecular Crystals*. Springer-Verlag Berlin Heidelberg New York, 2. edition (1980).

[3] M. Pope and C. E. Swenberg. *Electronic Processes in Organic Crystals and Polymers*. Oxford University Press, Oxford, 2. edition (1999).

[4] C. W. Tang and S. A. VanSlyke. Organic electroluminescent diodes. *Applied Physics Letters*, **51**, 913 (1987).

[5] C. W. Tang, S. A. VanSlyke, and C. H. Chen. Electroluminescence of doped organic thin films. *Journal of Applied Physics*, **65**, 3610 (1989).

[6] S. A. VanSlyke, C. H. Chen, and C. W. Tang. Organic electroluminescent devices with improved stability. *Applied Physics Letters*, **69**, 2160 (1996).

[7] C. W. Tang. Two-layer organic photovoltaic cell. *Applied Physics Letters*, **48**, 183 (1986).

[8] C. Reese, M. Roberts, M. Ling, and Z. Bao. Organic thin film transistors. *Materials Today*, **7**, 20 (2004).

[9] `http://www.iapp.de/orgworld/?Basics:What_are_organic_semiconductors`. Accessed: 19/04/2013.

[10] W. Brütting. *Physics of Organic Semiconductors*. WILEY-VCH (2005).

[11] G. Gahungu, J. Zhang, V. Ntakarutimana, and N. Gahungu. Combined Effects of One 8-Hydroxyquinoline/Picolinate and CH/N Substitutions on the Geometry, Electronic Structure and Optical Properties of mer-Alq3. *The Journal of Physical Chemistry A*, **114**, 652 (2010).

[12] G. Gahungu and J. Zhang. CH/N Substituted mer-Gaq3 and mer-Alq3 Derivatives: An Effective Approach for the Tuning of Emitting Color. *The Journal of Physical Chemistry B*, **109**, 17762 (2005). PMID: 16853272.

[13] R. Pohl and P. Anzenbacher. Emission Color Tuning in AlQ3 Complexes with Extended Conjugated Chromophores. *Organic Letters*, **5**, 2769 (2003).

[14] H. Yersin and W. J. Finkenzeller. *Triplet Emitters for Organic Light-Emitting Diodes: Basic Properties*, 1–97. Wiley-VCH Verlag GmbH & Co. KGaA (2008).

[15] M. Sauer, J. Hofkens, and J. Enderlein. *Handbook of Fluorescence Spectroscopy and Imaging*. Wiley-VCH, Weinheim (2011).

[16] M. Schrader, F. Meinecke, K. Bahlmann, *et al.* Monitoring the excited state of a fluorophore in a microscope by stimulated emission. *Bioimaging*, **3**, 147 (1995).

[17] M. Kasha. Characterization of electronic transitions in complex molecules. *Discuss. Faraday Soc.*, **9**, 14 (1950).

[18] R. Berera, R. Grondelle, and J. Kennis. Ultrafast transient absorption spectroscopy: principles and application to photosynthetic systems. *Photosynthesis Research*, **101**, 105.

[19] M. Brinkmann, G. Gadret, M. Muccini, *et al.* Correlation between Molecular Packing and Optical Properties in Different Crystalline Polymorphs and Amorphous Thin Films of mer-Tris(8-hydroxyquinoline)aluminum(III). *Journal of the American Chemical Society*, **122**, 5147 (2000).

[20] M. Rajeswaran, T. N. Blanton, and K. P. Klubek. Refinement of the crystal structure of the δ-modification of tris(8-hydroxyquinoline)aluminum(III), δ-$Al(C_9H_6NO)_3$, the blue luminescent Alq3. *Z. Kristallogr. NCS*, **218**, 439 (2003).

[21] W. Humbs, E. van Veldhoven, H. Zhang, and M. Glasbeek. Sub-picosecond fluorescence dynamics of organic light-emitting diode tris(8-hydroxyquinoline) metal complexes. *Chemical Physics Letters*, **304**, 10 (1999).

[22] P. E. Burrows, Z. Shen, V. Bulovic, *et al.* Relationship between electroluminescence and current transport in organic heterojunction light-emitting devices. *Journal of Applied Physics*, **79**, 7991 (1996).

[23] A. Kimyonok, X. Wang, and M. Weck. Electroluminescent Poly(quinoline)s and Metalloquinolates. *Journal of Macromolecular Science, Part C: Polymer Reviews*, **46**, 47 (2006).

[24] M. Cölle and W. Brütting. Thermal, structural and photophysical properties of the organic semiconductor Alq3. *physica status solidi (a)*, **201**, 1095 (2004).

[25] M. Brinkmann, B. Fite, S. Pratontep, and C. Chaumont. Structure and Spectroscopic Properties of the Crystalline Structures Containing Meridional and Facial Isomers of Tris(8-hydroxyquinoline) Gallium(III). *Chemistry of Materials*, **16**, 4627 (2004).

[26] Y.-W. Yu, C.-P. Cho, and T.-P. Perng. Crystalline Gaq3 Nanostructures: Preparation, Thermal Property and Spectroscopy Characterization. *Nanoscale Research Letters*, **4**, 820 (2009).

[27] R. J. Curry, W. P. Gillin, J. Clarkson, and D. N. Batchelder. Morphological study of aluminum tris(8-hydroxyquinoline) thin films using infrared and Raman spectroscopy. *Journal of Applied Physics*, **92**, 1902 (2002).

[28] M. D. Halls and H. B. Schlegel. Molecular Orbital Study of the First Excited State of the OLED Material Tris(8-hydroxyquinoline)aluminum(III). *Chemistry of Materials*, **13**, 2632 (2001).

[29] F. F. Muhammad, A. I. A. Hapip, and K. Sulaiman. Study of optoelectronic energy bands and molecular energy levels of tris (8-hydroxyquinolinate) gallium and aluminum organometallic materials from their spectroscopic and electrochemical analysis. *Journal of Organometallic Chemistry*, **695**, 2526 (2010).

[30] M. Ghedini, M. L. Deda, I. Aiello, and A. Grisolia. Synthesis and photophysical characterisation of soluble photoluminescent metal complexes with substituted 8-hydroxyquinolines. *Synthetic Metals*, **138**, 189 (2003).

[31] G. Gahungu and J. Zhang. Molecular geometry, electronic structure and optical properties study of meridianal tris(8-hydroxyquinolato)gallium(III) with ab initio and DFT methods. *Journal of Molecular Structure*, **131**, 19 (2005).

[32] J. Zhang and G. Frenking. Quantum chemical analysis of the chemical bonds in tris(8-hydroxyquinolato)aluminum as a key emitting material for OLED. *J. Phys. Chem.*, **108**, 10296 (2004).

[33] G. P. Kushto, Y. Iizumi, J. Kido, and Z. H. Kafafi. A Matrix-Isolation Spectroscopic and Theoretical Investigation of Tris(8-hydroxyquinolinato)aluminum(III) and Tris(4-methyl-8-hydroxyquinolinato)aluminum(III). *The Journal of Physical Chemistry A*, **104**, 3670 (2000).

[34] I. Sokolik, R. Priestley, A. D. Walser, R. Dorsinville, and C. W. Tang. Bimolecular reactions of singlet excitons in tris(8-hydroxyquinoline) aluminum. *Applied Physics Letters*, **69**, 4168 (1996).

[35] R. Ballardini, G. Varani, M. T. Indelli, and F. Scandola. Phosphorescent 8-quinolinol metal chelates. Excited-state properties and redox behavior. *Inorganic Chemistry*, **25**, 3858 (1986).

[36] H. D. Burrows, M. Fernandes, J. Seixas de Melo, A. P. Monkman, and S. Navaratnam. Characterization of the Triplet State of Tris(8-hydroxyquinoline)aluminium(III) in Benzene Solution. *Journal of the American Chemical Society*, **125**, 15310 (2003).

[37] J. C. Koziar and D. O. Cowan. Photochemical heavy-atom effects. *Accounts of Chemical Research*, **11**, 334 (1978).

[38] M. A. Baldo and S. R. Forrest. Transient analysis of organic electrophosphorescence: I. Transient analysis of triplet energy transfer. *Phys. Rev. B*, **62**, 10958 (2000).

[39] T. Hoshi, K. Kumagai, K. Inoue, *et al.* Electronic absorption and emission spectra of Alq3 in solution with special attention to a delayed fluorescence. *Journal of Luminescence*, **128**, 1353 (2008).

[40] J. Zhang and G. Frenking. Quantum chemical analysis of the chemical bonds in Mq3 (M=Al^{III},Ga^{III}) as a emitting material for OLED. *J. Chem. Phys.*, **394**, 120 (2004).

[41] S. Schenkl, G. Zgrablic, F. Mourik, S. Haacke, and M. Chergui. Ultrafast spectroscopy of biological systems. In B. Bartolo and O. Forte, editors, *Advances in Spectroscopy for Lasers and Sensing*, 119–127. Springer Netherlands (2006).

[42] A. H. Zewail. Femtochemistry: Atomic-Scale Dynamics of the Chemical Bond. *The Journal of Physical Chemistry A*, **104**, 5660 (2000).

[43] W. C. Roentgen. Eine neue Art von Strahlen. *Sitzungsberichte der Würzburger Physik.-medic. Gesellschaft* (1895).

[44] C. Rischel, A. Rousse, I. Uschmann, *et al.* Femtosecond time-resolved X-ray diffraction from laser-heated organic films. *Nature*, **390**, 490 (1997).

[45] R. W. Schoenlein, S. Chattopadhyay, H. H. W. Chong, *et al.* Generation of Femtosecond Pulses of Synchrotron Radiation. *Science*, **287**, 2237 (2000).

[46] R. Schoenlein, H. Chong, T. Glover, *et al.* Femtosecond X-ray Pulses from a Synchrotron. In *Ultrafast Phenomena XII*, volume 66 of *Springer Series in Chemical Physics*, 271–275. Springer Berlin Heidelberg (2001).

[47] M. R. Chance, M. D. Wirt, E. M. Scheuring, *et al.* Time-resolved x-ray absorption spectroscopy on microsecond timescales: Implications for the examination of structural motions. *Review of Scientific Instruments*, **64**, 2035 (1993).

[48] D. J. Thiel, P. Livins, E. A. Stern, and A. Lewis. Microsecond-resolved XAFS of the triplet excited state of $Pt_2(P_2O_5H_2)_4^{4-}$. *Nature*, **362**, 40 (1993).

[49] M. Saes, C. Bressler, R. Abela, *et al.* Observing Photochemical Transients by Ultrafast X-Ray Absorption Spectroscopy. *Phys. Rev. Lett.*, **90**, 047403 (2003).

[50] M. Saes, F. Van Mourik, W. Gawelda, *et al.* A setup for ultrafast time-resolved x-ray absorption spectroscopy. *Review of Scientific Instruments*, **75**, 24 (2004).

[51] W. Gawelda, M. Johnson, F. M. F. de Groot, *et al.* Electronic and Molecular Structure of Photoexcited $[Ru^{II}(bpy)_3]^{2+}$ Probed by Picosecond X-ray Absorption Spectroscopy. *Journal of the American Chemical Society*, **128**, 5001 (2006).

[52] W. Gawelda, A. Cannizzo, V.-T. Pham, *et al.* Ultrafast Nonadiabatic Dynamics of $[Fe^{II}(bpy)_3]^{2+}$ in Solution. *Journal of the American Chemical Society*, **129**, 8199 (2007).

[53] M. Benfatto, S. Della Longa, K. Hatada, *et al.* A Full Multiple Scattering Model for the Analysis of Time-Resolved X-ray Difference Absorption Spectra. *The Journal of Physical Chemistry B*, **110**, 14035 (2006).

[54] C. Bressler, C. Milne, V.-T. Pham, *et al.* Femtosecond XANES Study of the Light-Induced Spin Crossover Dynamics in an Iron(II) Complex. *Science*, **323**, 489 (2009).

[55] H. T. Lemke, C. Bressler, L. X. Chen, *et al.* Femtosecond X-ray Absorption Spectroscopy at a Hard X-ray Free Electron Laser: Application to Spin Crossover Dynamics. *The Journal of Physical Chemistry A*, **117**, 735 (2013).

[56] F. W. Lytle. *In Physics of Non-Crystalline Solids*. J. A. Prins (1965).

[57] F. W. Lytle. The EXAFS family tree: A personal history of the development of extended X-ray absorption fine structure. *Journal of Synchrotron Radiation*, **6**, 123 (1999).

[58] Stumm von Bordwehr, R. A History of X-ray absorption fine structure. *Ann. Phys. Fr.*, **14**, 377 (1989).

[59] D. Koningsberger and R. Prins. *X-Ray Absorption: Principles, Applications, Techniques of EXAFS, SEXAFS and XANES*. John Wiley & Sons (1988).

[60] G. Bunker. *Introduction to XAFS - A Practical Guide to X-ray Absorption Fine Structure Spectroscopy*. Cambridge University Press, Cambridge, 1. edition (2010).

[61] J. J. Rehr and R. C. Albers. Theoretical approaches to x-ray absorption fine structure. *Rev. Mod. Phys.*, **72**, 621 (2000).

[62] J. Eichler and J. Eichler. *Laser - Bauformen, Strahlführung, Anwendungen*. Springer Berlin Heidelberg New York, 6. edition (2006).

[63] M. Newville. Fundamentals of XAFS. `http://xafs.org/Tutorials`. Accessed: 30/04/2013.

[64] A. Thompson and D. Vaughan. *X-ray data booklet*. Lawrence Berkeley, National Laboratory, University of California, 2. edition (2001).

[65] J. J. Rehr, R. C. Albers, C. R. Natoli, and E. A. Stern. New high-energy approximation for x-ray-absorption near-edge structure. *Phys. Rev. B*, **34**, 4350 (1986).

[66] A. Bianconi. Surface X-ray absorption spectroscopy: Surface EXAFS and surface XANES. *Applications of Surface Science*, **6**, 392 (1980).

[67] J. E. Penner-Hahn. X-ray Absorption Spectroscopy. `http://www.umich.edu/~jphgroup/XAS_Course/CCC2_XAS.pdf`. Accessed: 31/10/2012.

[68] E. A. Stern. Theory of the extended x-ray-absorption fine structure. *Phys. Rev. B*, **10**, 3027 (1974).

[69] D. E. Sayers, E. A. Stern, and F. W. Lytle. New Technique for Investigating Noncrystalline Structures: Fourier Analysis of the Extended X-Ray Absorption Fine Structure. *Phys. Rev. Lett.*, **27**, 1204 (1971).

[70] User's Guide, feff version 9.6.4. `http://leonardo.phys.washington.edu/feff/html/documentation.html`. Accessed: 19/06/2012.

[71] J. Kas. *Toward quantitative calculation and analysis of x-ray absorption near edge spectra*. Ph.D. thesis, University of Washington (2009).

[72] J. J. Rehr, J. J. Kas, M. P. Prange, *et al.* Ab initio theory and calculations of X-ray spectra. *Comptes Rendus Physique*, **10**, 548 (2009).

[73] J. J. Rehr, J. J. Kas, F. D. Vila, M. P. Prange, and K. Jorissen. Parameter-free calculations of X-ray spectra with FEFF9. *Phys. Chem. Chem. Phys.*, **12**, 5503 (2010).

[74] G. Smolentsev and A. Soldatov. Quantitative local structure refinement from XANES: Multi-dimensional interpolation approach. *Journal of Synchrotron Radiation*, **13**, 19 (2006).

[75] G. Smolentsev and A. Soldatov. FitIt: New software to extract structural information on the basis of XANES fitting. *Computational Materials Science*, **39**, 569 (2007).

[76] G. Smolentsev and A. Soldatov. Multidimensional interpolation approach.

[77] G. Smolentsev and A. Soldatov. FitIt short user's guide. `http://www.nano.sfedu.ru/files/FitIt_Guide.pdf` (2006). Accessed: 20/10/2012.

[78] J. Als-Nielsen and D. McMorrow. *Elements of Modern X-ray Physics*. John Wiley & Sons, Ltd (2001).

[79] W. Gawelda. *Time-resolved x-ray absorption spectroscopy of transition metal complexes*. Ph.D. thesis, ÉCOLE POLYTECHNIQUE FÉDÉRALE DE LAUSANNE (2006).

[80] C. Bressler and M. Chergui. Ultrafast X-ray Absorption Spectroscopy. *Chemical Reviews*, **104**, 1781 (2004). PMID: 15080712.

[81] C. Bressler, M. Saes, M. Chergui, R. Abela, and P. Pattison. Optimizing a time-resolved X-ray absorption experiment. *Nuclear Instruments & Methods in Physics Research Section A-Accelerators Spectrometers Detectors and Associated Equipment*, **467-468**, 1444 (2001).

[82] K. Balewski, W. Brefeld, W. Decking, *et al.* PETRA III: A Low Emittance Synchrotron Radiation Source, Technical Design Report. Technical report, DESY (2004).

[83] H. Wiedemann. Low emittance storage ring design. In M. Month and S. Turner, editors, *Frontiers of Particle Beams*, volume 296 of *Lecture Notes in Physics*, 390–439. Springer Berlin Heidelberg (1988).

[84] A. Snigirev, V. Kohn, I. Snigireva, and B. Lengeler. A compound refractive lens for focusing high-energy X-rays. *Nature*, **384**, 49 (1996).

[85] A. Snigirev, V. Kohn, I. Snigireva, A. Souvorov, and B. Lengeler. Focusing High-Energy X Rays by Compound Refractive Lenses. *Appl. Opt.*, **37**, 653 (1998).

[86] P. Institut. RWTHAachen Compound Refractive Lenses. `http://www.institut2b.physik.rwth-aachen.de/xray/imaging/crl.html`. Accessed: 20/03/2013.

[87] D. Meschede. *Optik, Licht und Laser*. Vieweg+Teubner, 3. edition (2008).

[88] `http://www.fmb-oxford.com/uploads/files/Detectors09.pdf`. Accessed: 25/08/2013.

[89] Material Safety Data Sheet Benzyl Alcohol. `http://www.sigmaaldrich.com/catalog/product/sial/402834?lang=de&region=DE`. Accessed: 18/05/2013.

[90] J. M. Coulson and J. F. Richardson. *Chemical Engineering*. Butterworth Heinemann, 5. edition (2006).

[91] N. Rodríguez-hornedo and D. Murphy. Significance of controlling crystallization mechanisms and kinetics in pharmaceutical systems. *Journal of Pharmaceutical Sciences*, **88**, 651 (1999).

[92] J. W. Mullin. *Crystallization*. Butterworth Heinemann, 4. edition (2001).

[93] W. Ostwald. *Lehrbuch der Allgemeinen Chemie*, volume 2. W. Engelmann (1896).

[94] S. O. Mariager, F. Pressacco, G. Ingold, *et al.* Structural and Magnetic Dynamics of a Laser Induced Phase Transition in FeRh. *Phys. Rev. Lett.*, **108**, 087201 (2012).

[95] J. Mezyk, J. Kalinowski, F. Meinardi, and R. Tubino. Singlet exciton interactions in solid films of Alq3. *Chemical Physics Letters*, **395**, 321 (2004).

[96] G. Binnig, C. F. Quate, and C. Gerber. Atomic Force Microscope. *Phys. Rev. Lett.*, **56**, 930 (1986).

[97] R. W. Carpick and M. Salmeron. Scratching the Surface: Fundamental Investigations of Tribology with Atomic Force Microscopy. *Chemical Reviews*, **97**, 1163 (1997).

[98] An introduction to AFM. `http://hansmalab.physics.ucsb.edu/afmhistory.html`. Accessed: 20/05/2013.

[99] C. Jonda, A. Mayer, U. Stolz, A. Elschner, and A. Karbach. Surface roughness effects and their influence on the degradation of organic light emitting devices. *Journal of Materials Science*, **35**, 5645 (2000).

[100] PETRA III and Beamline Specifications. `http://photon-science.desy.de/facilities/petra_iii/index_eng.html`. Accessed: 18/04/2013.

[101] J.-C. Diels and W. Rudolph. *Ultrashort Laser Pulse Phenomena*. Elsevier, 2. edition edition (2006).

[102] APD-ACE, Pulse Processing Unit, Operating & Service Manual. `http://fmb-oxford.com`. Accessed: 14/04/2013.

[103] T. Kracht and H. Zink. The VFC-ADC, a Programmable AD Converter. `http://hasyweb.desy.de/science/annual_reports/2005_report/part1/contrib/27/15460.pdf`. Accessed: 09/04/2013.

[104] R. L. Owen, J. M. Holton, C. Schulze-Briese, and E. F. Garman. Determination of X-ray flux using silicon pin diodes. *Journal of Synchrotron Radiation*, **16**, 143 (2009).

[105] X-ray photon flux calculator. `http://x10sa.web.psi.ch/diode-calc.php`. Accessed: 04/03/2013.

[106] R. J. Dejus and M. S. del Rio. XOP: A graphical user interface for spectral calculations and x-ray optics utilities. *Review of Scientific Instruments*, **67**, 3356 (1996).

[107] XOP. `http://www.esrf.eu/computing/scientific/xop2.1/`. Accessed: 20/05/2013.

[108] A. Curioni, M. Boero, and W. Andreoni. Alq3: ab initio calculations of its structural and electronic properties in neutral and charged states. *Chemical Physics Letters*, **294**, 263 (1998).

[109] M. M. Woolfson. *An Introduction to X-ray Crystallography*. Cambridge University Press, 2. edition (1997).

[110] W. Kabsch. *XDS*. *Acta Crystallographica Section D*, **66**, 125 (2010).

[111] G. M. Sheldrick. A short history of *SHELX*. *Acta Crystallographica Section A*, **64**, 112 (2008).

[112] Y. Wang, W. Zhang, Y. Li, L. Ye, and G. Yang. X-ray Crystal Structure of Gallium Tris- (8-hydroxyquinoline): Intermolecular $\pi - \pi$ Stacking Interactions in the Solid State. *Chemistry of Materials*, **11**, 530 (1999).

[113] B. Ravel and M. Newville. *ATHENA*, *ARTEMIS*, *HEPHAESTUS*: Data analysis for X-ray absorption spectroscopy using *IFEFFIT*. *Journal of Synchrotron Radiation*, **12**, 537 (2005).

[114] A. Curioni, W. Andreoni, R. Treusch, *et al.* Atom-resolved electronic spectra for Alq3 from theory and experiment. *Applied Physics Letters*, **72**, 1575 (1998).

[115] N. Johansson, T. Osada, S. Stafström, *et al.* Electronic structure of tris(8-hydroxyquinoline) aluminum thin films in the pristine and reduced states. *The Journal of Chemical Physics*, **111**, 2157 (1999).

[116] MATLAB. *version 7.5.0 (R2007b)*. The MathWorks Inc., Natick, Massachusetts (2007).

[117] M. Newville. *IFEFFIT*: Interactive XAFS analysis and *FEFF* fitting. *Journal of Synchrotron Radiation*, **8**, 322 (2001).

[118] A. Mishra, N. Parsai, and B. D. Shrivastava. Simplified analysis of EXAFS data and determination of bond length. *IJPAP*, **49**, 25 (2011).

[119] P. A. Lee, P. H. Citrin, P. Eisenberger, and B. M. Kincaid. Extended x-ray absorption fine structure—its strengths and limitations as a structural tool. *Rev. Mod. Phys.*, **53**, 769 (1981).

[120] T. Skotheim and J. Reynolds. *Conjugated Polymers: Theory, Synthesis, Properties, and Characterization*. CRC Press, 3. edition (2006).

[121] Y. Guo, Z.-B. Wang, Y.-P. Cui, J.-Y. Zhang, and Y.-H. Ye. Tris (8-Hydroxyquinoline) Aluminium Nanostructure Film and Its Fluorescence Properties. *Chinese Physics Letters*, **25**, 4428 (2008).

[122] T. A. Hopkins, K. Meerholz, S. Shaheen, *et al.* Substituted Aluminum and Zinc Quinolates with Blue-Shifted Absorbance/Luminescence Bands: Synthesis and Spectroscopic, Photoluminescence, and Electroluminescence Characterization. *Chemistry of Materials*, **8**, 344 (1996).

[123] P. Bianchini, B. Harke, S. Galiani, G. Vicidomini, and A. Diaspro. Single-wavelength two-photon excitation-stimulated emission depletion (SW2PE-STED) superresolution imaging. *Proceedings of the National Academy of Sciences*, **109**, 6390 (2012).

[124] T. Cordes, S. Malkmus, J. A. DiGirolamo, *et al.* Accelerated and Efficient Photochemistry from Higher Excited Electronic States in Fulgide Molecules. *The Journal of Physical Chemistry A*, **112**, 13364 (2008).

[125] S. W. Hell and J. Wichmann. Breaking the diffraction resolution limit by stimulated emission: stimulated-emission-depletion fluorescence microscopy. *Opt. Lett.*, **19**, 780 (1994).

[126] H.-H. Fang, Q.-D. Chen, J. Yang, *et al.* Amplified spontaneous emission in the cyano-substituted oligo(p-phenylenevinylene) organic crystals: Effect of excitation wavelength. *Applied Physics Letters*, **96**, 103508 (2010).